# General properties of ionic complex fluids

Habilitationsschrift
zur Erlangung der Lehrbefugnis
für das Fach Theoretische Physik
an der Universität Stuttgart

Vorgelegt von

**Markus Bier**

Max-Planck-Institut für Intelligente Systeme,
Stuttgart

und

Institut für Theoretische Physik IV,
Universität Stuttgart

2016

# Summary

Various types of ionic complex fluids, e.g. dilute electrolyte solutions, room temperature ionic liquids (RTILs), ionic liquid crystals and colloidal suspensions, are described theoretically in order to infer general, i.e. material-independent, properties. A classification of ionic complex fluids in terms of the relevant length scales is suggested, including the Debye length, the molecular size and the size of colloidal particles.

For dilute electrolyte solutions the Debye length is competing with the bulk correlation length of the solvent. Far away from a critical point of the solvent the Debye length is the largest length scale so that the ionic complex fluid exhibits plasma-like behaviour with a screening of electric fields and correlations on the length scale of the Debye length. Non-trivial consequences are the Jones-Ray effect due to unequal partitioning of ions at liquid-liquid interfaces as well as the general occurrence of first-order wetting transitions for short-ranged interactions, irrespective of the order of wetting transitions of the pure, i.e. salt-free, solvent. Furthermore, the effect of electrowetting is discussed in terms of density functional theory, which reveals a severe misconception underlying the traditional interpretation in terms of electrocapillarity. Close to a critical point of the solvent an ionic complex fluid exhibits the universal critical behaviour of the pure solvent because then the Debye length appears as a "microscopic" length scale, so that ions contribute only to sub-leading order. Both regimes are separated in the bulk phase diagram by a narrow region, where the Debye length and the bulk correlation length of the solvent are similar, where damped oscillatory instead of monotonic asymptotic decay of the pair correlation function is present and which is bounded by Kirkwood crossover lines.

In room temperature ionic liquids (RTILs), and particularly in ionic liquid crystals, no solvent is present and the properties are determined by an interplay between the Debye length and molecular length scales of the particles. For dense RTILs the Debye length is (much) smaller than the molecular size so that these systems behave to a large extent similar to non-ionic complex fluids with genuine short-ranged interactions due to, e.g., material-specific chemical bonding which can give rise to the formation of microheterogeneities and mesophases. However, general plasma-like properties are observed in dense RTILs at length scales larger than the particle size. In dilute RTILs the Debye length is (much) larger than the particle size, because RTILs exhibit a tiny vapour pressure close to the triple point, which leads to a behaviour similar to a plasma of point-like particles.

In colloidal suspensions typically the size of the colloidal particles, the Debye length as well as the bulk correlation length of the solvent are relevant in decreasing order. Size and shape of the colloidal particles is material-independent but geometry-dependent and these properties give rise to characteristic phases of colloidal crystals and liquid crystals. Similarities to RTILs and electrolyte solutions occur in colloidal suspensions far away from critical points of the solvent, where screening of the colloidal surface charge on the

scale of the Debye length provides the leading correction to the hard particle behaviour. Close to the critical point of the solvent the critical Casimir force on the scale of the bulk correlation length dominates over the electrostatic interaction. However, the effective interaction between colloidal particles can be influenced by ion-solvent couplings, e.g. due to the unequal partitioning of ions in composition gradients of the solvent at the colloidal surface or at the fluid-fluid-colloid three-phase contact region of colloids trapped at fluid-fluid interfaces.

The ionic complex fluids considered in detail here, besides being important for modern applications, form an exhaustive set of representatives of the various regimes in terms of the relevant length scales. However, such a general, i.e. material-independent, classification is only possible for static properties of complex fluids, whereas dynamic properties are governed by system-spcific time scales which preclude such generality.

# Zusammenfassung

Theoretische Beschreibungen verschiedener ionischer komplexer Fluide, z.B. verdünnte Elektrolytlösungen, “room temperature ionic liquids” (RTILs), ionische Flüssigkristalle und kolloidale Suspensionen, werden gegeben, um daraus auf allgemeine, d.h. materialunabhängige, Eigenschaften zu schließen. Es wird eine Klassifikation ionischer komplexer Fluide vorgeschlagen, basierend auf der Debye-Länge, der molekularen Gößе und der Größe kolloidaler Teilchen.

In verdünnten Elektrolytlößungen konkurriert die Debye-Länge mit der Korrelationslänge des Lösungsmittels im Volumen. Weit weg von kritischen Punkten des Lösungsmittels is die Debye-Länge die dominante, sodass das ionische komplexe Fluid plasmaähnliches Verhalten mit Abschirmung elektrischer Felder und Korrelationen auf der Längenskala der Debye-Länge. Nichttriviale Konsequenzen hiervon sind der Jones-Ray-Effekt auf Grund einer ungleichmäßigen Partitionierung von Ionen an Grenzflächen zwischen zwei Flüssigkeiten sowie für kurzreichweitige Wechselwirkungen das allgemeine Auftreten von Benetzungsübergängen 1. Ordnung , unabhängig von der Ordnung des Benetzungsübergangs des reinen, d.h. salzfreien, Lösungsmittels. Darüberhinaus wird der Effekt der Elektrobenetzung im Rahmen der Dichtefunktionaltheorie diskutiert und so ein konzeptioneller Fehler der tranditionellen Interpretation als Elektrokapillarityätseffekt aufgedeckt. In der Nähe eines kritischen Punkts des Lösungsmittels zeigt ein ionisches komplexes Fluid das universelle kritische Verhalten des reinen Lösungsmittels, weil dann die Debye-Länge als “mikroskopische” Längenskala fungiert, sodass Ionen nur Korrekturen höherer Ordnung bewirken können. Beide Extremfälle sind im Phasendiagramm durch eine schmale Region getrennt, wo die Debye-Länge und die Korrelationslänge des Lösungsmittels ähnlich groß sind, wo die Paarkorrelationsfunktion mit abklingenden Oszillationen statt mit monoton abfällt und welche durch Kirkwood-Übergänge begrenzt sind.

“Room temperature ionic liquids” (RTILs), und insbesondere ionische Flüssigkristalle, enthalten kein Lösungsmittel, und ihre Eigenschaften sind durch das Wechselspiel zwischen der Debye-Länge und der molekularen Größe der Teilchen bestimmt. In dichten RTILs ist die Debye-Länge (viel) kleiner als die molekulare Größe, sodass sich diese Systeme großteils ähnlich verhalten wie nicht-ionische komplexe Fluiden mit ausschließlich kurzreichweitigen Wechselwirkungen, z.B. auf Grund von materialspezifischen chemischen Bindungen, welche zur Bildung von Mikroheterogenitiäten und Mesophasen führen können. Allgemeine plasmaähnliche Eigenschaften sind bei dichen RTILs dagegen auf Längenskalen größer als die Teilchengröße zu beobachten. In verdünnten RTILs ist die Debye-Länge (viel) kleiner als die Teilchengröße, da RTILs in der Nähe des Tripelpunkts einen verschwindend kleinen Dampfdruck zeigen, was zum Verhalten eines Plasmas punktförmiger Teilchen führt.

In kolloidalen Suspensionen sind gewöhnlich die Größe der kolloidalen Teilchen, die

Debye-Länge und die Korrelationslänge des Lösungsmittels in absteigender Reihenfolge relevant. Größe und Form der kolloidalen Teilchen sind materialunabhängig aber geometrieabhängig und diese Eigenschaften führen zu charakeristischen Phasen kolloidaler Krisalle und Flüssigkristalle. Ähnlichkeiten zu RTILs und Elektrolytlösungen treten in kolloidalen Suspensionen weit weg von kritischen Punkten des Lösungsmittels auf, wo die Abschirmung der kolloidalen Oberflächenladung auf der Skala der Debye-Länge die führende Korrektur zum Verhalten harter Teilchen liefert. Nahe einem kritischen Punkt des Lösungsmittels dominiert die kritische Casimir-Kraft auf der Skala der Korrelationslänge über die elektrostatische Wechselwirkung. Die effektive Wechselwirkung zwischen kolloidalen Teilchen kann jedoch beeinflusst werden durch Kopplungenen von Ionen und Lösungsmittel, z.B. durch ungleichmäßige Partitionierung von Ionen in Konzentrationsgradienten des Lösungsmittels an Kolloidoberflächen oder in der Dreiphasenkontaktregion von Kolloiden an Fluid-Fluid-Grenzflächen.

Die hier betrachteten ionischen komplexen Fluide sind nicht nur wichtig für moderne Anwendungen, sondern sie bilden auch einen vollständigen Satz von Repräsentanten der verschiedenen Regime der relevanten Längenskalen. Eine solche allgemeine, d.h. materialunabhängige, Klassifikation is nur für statische Eigenschaften komplexer Fluide möglich, wohingegen dynamische Eigenschaften durch systemspezifische Zeitskalen bestimmt sind, die keine solche Allgemeinheit zulassen.

# Contents

# Chapter 1

# Introduction

Amongst the vast variety of complex fluids it is those containing ionic constituents which are of primary importance. Ionic complex fluids encompass, e.g., electrolyte solutions, room temperature ionic liquids (RTILs), ionic liquid crystals, colloidal suspensions and polyelectrolytes. The omnipresence of ionic complex fluids in nature and technology is most probably due to the abundance of liquid water, which is a highly polar solvent that leads to an immediate dissociation of cations and anions.

The formation of freely moving ions in dilute electrolyte solutions, e.g. in physiological fluids such as the cytoplasm, is essential for many natural processes, e.g. the citric acid cycle of the aerobic cellular metabolism. Life on earth would not be as it is today without the primordial soup having been an ionic complex fluid. The complex fluid character of dilute electrolyte solutions is generated by the presence of a large number of constituents, whose typically imperfect mutual miscibility gives rise to demixing transitions and microheterogeneities. By definition the Debye length of dilute electrolyte solutions is much larger than the molecular sizes of the constitutents so that these ionic complex fluids exhibit many material-independent properties (see Secs. 2.1, 3.1, 3.2, 4.1, 4.2, 4.3 and 4.4).

Chemical processes involving redox reactions, e.g. in batteries, fuel cells, dye-sensitised solar cells, electrolysis and metal deposition, take place in ionic complex fluids composed of the reactants. A current trend in catalysis research is to study RTILs, i.e. (typically organic) fused salts with melting temperatures around room-temperature [457], as reaction media, which provide highly polar fluid environments for such applications [7, 165, 464, 470, 481, 483]. RTILs are also used in chemical sythesis as advanced solvents which can dissolve some water-insoluble materials, e.g. wood (cellulose), stabilise enzymes [463] or serve in biomass processing [427]. Due to features such as a remarkable thermal stability and a negligible vapour pressure [31, 273, 346, 467] many applications are conceivable, e.g. as liquid media under ultrahigh vacuum conditions [31, 273, 425, 459]. All these properties of RTILs can be viewed as those of ionic complex fluids which exhibit a unique combination of the electrostatic interaction with the steric interaction of highly unsymmetric particles. Since RTILs are no solutions but melts, they do not contain a solvent so that, in contrast to dilute electrolyte solutions, the ionic strength is very high, and hence the Debye length is much smaller than the particle size. General, i.e. material-independent, properties of these ionic complex fluids derive from the high charge density (see Secs. 2.2, 3.3 and 3.4).

Whereas the widely studied imidazolium- and pyridinium-based RTILs with short alkyl chains are isotropic fluids in the bulk, there exist also ionic liquid crystals, i.e. RTILs

which exhibit mesogenic behaviour. Due to their self-organised structures, the latter have attracted some attention for applications as anisotropic conductors [1, 225, 332, 485] or as templates to synthesize nanoparticles [429, 430]. Various types of ionic liquid crystals have been prepared [19, 50], which exhibit, e.g., smectic [61, 177, 193, 405], columnar [404, 486] or even cubic [318, 319] mesophases. As for isotropic RTILs, ionic liquid crystals exhibit high thermal and electrochemical stability [61, 103, 160, 237, 256, 419], which is advantageous in certain applications. However, the shape-induced complex fluid properties of ionic liquid crystals as compared to isotropic RTILs are more pronounced, as the anisotropic particle shapes not only lead to low melting temperatures, but also to the formation of mesophases (see Secs. 2.3).

Another class of ionic complex fluids whose particles are larger than the Debye length are colloidal suspensions. By appropriate preparation procedures and experimental conditions one is able to tune the colloidal interactions in a wide range [169, 269, 368, 428]. Consequently many parameters of a colloidal suspension are to be fixed, e.g. the size and the shape of the colloids as well as strength and functional form of the interaction potential [112, 260, 413, 484]. Moreover, the number of parameters increases dramatically when mixtures of different colloidal species are considered. There are two different perspectives on colloidal suspensions in the context of ionic complex fluids: On the one hand, one can consider the colloidal subsystem *as* an ionic complex fluid and treat the solvent as a structureless, inert and uniform medium, e.g. within the DLVO theory of the stability of colloidal dispersions [209, 385]. It is discussed in Sec. 2.4 that even binary mixtures of charged colloidal spheres of equal radii exhibit an extremely rich phase behaviour tuned merely by the length scale of the screened electrostatic interaction and in Sec. 4.5 that colloidal platelets share general properties with dilute electrolyte solutions and ionic liquid crystals. On the other hand, one can consider colloidal particles suspended *in* an ionic complex fluid medium, e.g. liquid-liquid emulsions, suspensions of viruses or clay and macromolecules such as DNA strands or proteins. This point of view raises the question of the effective interaction between colloidal particles in dependence on the properties of the ionic complex fluid medium; prominent examples are the effect of the screening of electric charges by mobile ions [75, 91, 92, 161, 162] and the salt-specific salting-in or salting-out of proteins in electrolyte solutions (Hofmeister effect) [243]. Frequently occurring situations in soft matter systems whose properties are determined by ionic complex fluid media and which are to be discussed here are the formation of electrostatically stabilised liquid-liquid emulsions (see Sec. 4.1), the interaction of colloidal particles in an electrolyte solution close to and far away from a critical point of the solvent (see Sec. 4.6) and the interaction of colloidal particles trapped at a fluid-fluid interface (see Sec. 4.7).

In the light of all these important systems, which are subjects of numerous research fields and technological applications, it is decisive to understand the properties of the ionic complex fluids, which form integral parts of them. Although there is a wide variety of ionic complex fluids they share general, i.e. material-independent, properties related to the coupling of mobile ions to additional degrees of freedom of the complex fluids. A particularly useful scheme, which has already been used above, is the classification in terms of relevant length scales, one of which is the Debye length related to the ionic strength of the charged entities. The combination of the ionic character with, e.g., orientational degrees of freedom, size polydispersity or conformational degrees of freedom leads to a rich phenomenology of ionic complex fluids, the understanding of which has progressed enormously in recent years due to improvements in the theoretical descriptions, computer

simulation techniques and experimental methods. The aim of this thesis is to provide an exposition of the author's own contributions to the topic of general properties of ionic complex fluids from Refs. [24, 35–37, 39–45, 96, 203, 204, 236, 283, 487, 491] and to put them into the context of contemporary research in this field. From the countless possible ways to discuss general properties of the various types of ionic complex fluids mentioned above, the categories "phase behaviour", "bulk structure" and "interfacial properties" are addressed in the following chapters. Each chapter begins with a discussion of dilute electrolyte solutions followed by ionic complex fluids of high charge density (RTILs) and/or of large particles (colloids).

The influence of the presence of ionic constituents on the phase behaviour of complex fluids is discussed in Ch. 2. The considered liquid-liquid demixing transitions of electrolyte solutions in complex solvents (Sec. 2.1) and the vapour phase of RTILs (Sec. 2.2) represent the situation of a low ionic strength, i.e. of a Debye length larger than the constituting molecules. The complementary situation of the particle size being larger than the Debye length gives rise to the mesogenic properties of ionic liquid crystals (Sec. 2.3) and the rich phenomenology of crystalline phases of charged colloids (Sec. 2.4).

The influence of ions onto the bulk structure of complex fluids is described in Ch. 3. The key observation for dilute electrolyte solutions is that the bulk structure of these ionic complex fluids is usually determined by the Debye length, except close to a critical point of the solvent, where the diverging bulk correlation length leads to an interesting crossover from electrolyte-like to critical solvent-like behaviour (Sec. 3.1). An interesting general observation to be discussed is that ionic impurities, in contrast to non-ionic ones, can alter the bulk structure of the solvent (Sec. 3.2). For dense ionic fluids a competition of the electrostatic interaction and the steric interaction due to size and shape of the particles leads to a crossover between a plasma-like and a dipolar-fluid-like behaviour which is discussed in terms of the static dielectric function (Sec. 3.3). Commonly it is the long range of the bare Coulomb interaction which is considered to be the origin of the peculiar phase behaviour and structural features of ionic systems. However, it can be shown that at least for dense ionic fluids this is not true in the sense that the same phase behaviour and structure can also be generated by an appropriate short-ranged interaction (Sec. 3.4).

Interfacial properties of ionic complex fluids are of particular importance for various applications so that Ch. 4 is devoted to an extensive discussion of interfaces. General features of interfaces of ionic complex fluids are related to the interfacial tension (Sec. 4.1), wetting behaviour (Sec. 4.2), critical adsorption (Sec. 4.3) and electrowetting (Sec. 4.4) in electrolyte solutions. Again, the phenomenology in this type of systems exhibits a wide material-independence, as the Debye length is the dominant length scale which exceeds the molecular size of the constituents. On the other hand, the interfacial struture of colloidal suspensions is dominated by the particle geometry and the Debye length merely leads to a correction. Nonetheless, the wetting properties of colloidal suspensions turn out to be similar to those of dilute electrolyte solutions and ionic liquid crystals (Sec. 4.5). However, colloidal suspensions can reveal a much richer phenomenology if several length scales contribute simultaneously. Examples are discussed of non-trivial effective interactions between colloidal particles immersed in the bulk of an ionic complex fluid (Sec. 4.6) or trapped at the interface of two immiscible ionic complex fluids (Sec. 4.7).

Based on the systems discussed before, general conclusions on the general properties of ionic complex fluids are drawn in Ch. 5. It is argued there that the ionic complex

fluids discussed in Chs. 2–4 are not only interesting from the point of view of particular applications, but that they form a complete set of representatives of the different classes of general properties.

# Chapter 2

# Phase behaviour

As for any thermodynamic system, the phase behaviour of ionic complex fluids comprises information about the stable bulk phase as function of the relevant thermodynamic fields as well as the characteristics of phase transitions between the bulk phases. For dilute electrolyte solutions in complex solvents which exhibit liquid-liquid demixing transitions the fundamental question is discussed in Sec. 2.1 as to what extent is the presence of ions modifying the phase behaviour of the pure solvent. Since for dilute electrolyte solutions the Debye length is exceeding the size of the ions and solvent molecules the phenomenology is largely material-independent. An experimental finding common to all RTILs, which are ionic complex fluids that combine electrostatic interactions with highly asymmetric molecular shapes, is a tiny vapour pressure close to the triple point. The general character of this phenomenon and its relation to RTILs is explained in Sec. 2.2. Again, the molecular size and shape is expected to be irrelevant as the Debye length of a highly dilute plasma is exceedingly large. In contrast, in ionic liquid crystals, which are ionic complex fluids where electrostatic interactions are combined with anisotropically shaped molecules, the Debye length is smaller than the molecules. The mesogenic properties as function of the charge distribution and of the molecular geometry are discussed in Sec. 2.3. Finally, it is shown in Sec. 2.4 that charged spherical colloids, where the Debye length of the suspending medium is smaller than the colloids, exhibit an extremely rich phenomenology of crystalline phases which sensitively depends on the ratio of the Debye length and the colloidal size.

## 2.1 Electrolyte solutions

Within the early picture due to Arrhenius [8] more than a century ago ions were assumed to generate only colligative properties of electrolyte solutions, which depend exclusively on the particle number, e.g. osmotic pressure, freezing point depression and boiling point elevation [9]. This simple picture was questioned by Bjerrum, Debye and Hückel who pointed out that electrostatically induced ion-ion correlations are expected to influence the ion distribution and the equation of state of electrolyte solutions [91, 296]. Since then, the Debye-Hückel theory has been widely used, e.g. in plasma physics and as an ingredient of the DLVO theory of colloidal suspensions [385]. Within Debye-Hückel theory the solvent is considered to be a uniform dielectric continuum which influences the Coulomb interaction between the ions via a certain permittivity but which is otherwise inert. However, in recent years the mutual influence of ions and the solvent has been reconsidered by studying the solubility of ions and the double-layer structure in a near-critical complex solvents

[42, 43, 80, 327, 328, 334, 335], possible salt-induced changes of the structure of complex solvents [43, 44, 312–314, 388–392] and effects of the inhomogeneities of the permittivity close to interfaces [29, 329, 401, 436].

These investigations require a model for the solvent at least on the mesoscopic scale as well as a description of the ion-solvent interaction. To this end one can split the pair potential between the species into the long-ranged electrostatic monopole-monopole contribution and into the remaining contributions of shorter range due to the chemical interactions. In the vast majority of the theoretical studies of dilute electrolyte solutions, ions are described as point-like particles whose chemical contributions to the interactions with the solvent are modeled locally within the so-called bilinear coupling approximation (BCA). This amounts to a local density approximation for the chemical contribution to the excess free energy which is bilinear in the particle number densities [29, 312–314, 327, 328, 334, 335, 401, 436]. Within the approaches of Refs. [80] and [329] the ion size is accounted for by means of hard-core exclusion and solvation is modeled by non-local interactions within random-phase approximation (RPA). The BCA can be considered as the local version of the RPA, which is expected to be reliable only for interaction energies small compared with the thermal energy [176]. However, the ion-solvent interaction is typically of the order of some tens of the thermal energy [208, 286]. Therefore the application of the BCA or of the RPA to electrolyte solutions is questionable [43].

It has been shown in Ref. [43] that for realistic values of the parameters the BCA and the RPA indeed lead to unphysical results. Moreover, in order to demonstrate the importance of the ion-solvent coupling for the properties of an electrolyte solution, an alternative local density approximation (LDA) has been proposed in Ref. [43] the predictions of which are in qualitative agreement with experimental results and which does not lead to the artifacts introduced by the BCA.

The model considered in Ref. [43] is that of a three-dimensional ($d = 3$) container $\widetilde{\mathcal{V}} \subseteq \mathbb{R}^3$ filled with an incompressible binary liquid mixture acting as a (complex) solvent for cations (+) and anions (−). All solvent particles are assumed to be of equal size with non-vanishing volume $\widetilde{a}^3$ whereas the ions are considered to be point-like; hence ions do not contribute to the total packing fraction. The set of dimensionless positions $\mathbf{r} = (x, y, z) := \widetilde{\mathbf{r}}/\widetilde{a}$ for $\widetilde{\mathbf{r}} \in \widetilde{\mathcal{V}}$ is defined as $\mathcal{V}$. At $\mathbf{r} \in \mathcal{V}$ the number densities of the solvent components $A$ and $B$ are given by $\widetilde{\varrho}_A(\mathbf{r}) = \phi(\mathbf{r})\widetilde{a}^{-3}$ and $\widetilde{\varrho}_B(\mathbf{r}) = (1-\phi(\mathbf{r}))\widetilde{a}^{-3}$, respectively, with $0 \leq \phi \leq 1$, whereas the number densities of the cations and anions are given by $\widetilde{\varrho}_+(\mathbf{r}) = \varrho_+(\mathbf{r})\widetilde{a}^{-3}$ and $\widetilde{\varrho}_-(\mathbf{r}) = \varrho_-(\mathbf{r})\widetilde{a}^{-3}$, respectively. The walls $\partial\mathcal{V}$ of the container carry a surface charge density $\sigma(\mathbf{r})e\widetilde{a}^{-2}$ at $\mathbf{r} \in \partial\mathcal{V}$, where $e$ is the (positive) elementary charge. The influence of the walls onto the solvent due to short-ranged chemical effects is captured by surface fields localised at the walls. At $\mathbf{r} \in \partial\mathcal{V}$, the dimensionless volume fraction $\phi(\mathbf{r})$ of $A$ particles couples linearly to surface fields $h(\mathbf{r})$, where $h > 0$ ($< 0$) leads to a preferential adsorption of solvent component $A$ ($B$). The equilibrium profiles $\phi$, $\varrho_+$, and $\varrho_-$ minimise the approximate grand potential density functional $k_BT\Omega[\phi, \varrho_\pm]$,

$$\begin{aligned}\Omega[\phi, \varrho_\pm] &= \int_{\mathcal{V}} \mathrm{d}^3 r \left\{ \omega_{\mathrm{sol}}(\phi(\mathbf{r})) + \frac{\chi(T)}{6}(\nabla\phi(\mathbf{r}))^2 + \sum_{i=\pm} \left[ \omega_{\mathrm{ion}}^{(i)}(\varrho_i(\mathbf{r})) + \varrho_i(\mathbf{r}) V_i(\phi(\mathbf{r})) \right] \right. \\ &\quad \left. + \frac{2\pi\ell_B}{\varepsilon(\phi(\mathbf{r}))} \mathbf{D}(\mathbf{r}, [\varrho_\pm])^2 \right\} - \int_{\partial\mathcal{V}} \mathrm{d}^2 r \, h(\mathbf{r})\phi(\mathbf{r}), \end{aligned} \tag{2.1}$$

with $\omega_{\mathrm{sol}}(\phi) = \phi(\ln\phi - \mu_\phi) + (1-\phi)\ln(1-\phi) + \chi(T)\phi(1-\phi)$ and $\omega_{\mathrm{ion}}^{(\pm)}(\varrho_\pm) =$

$\varrho_\pm(\ln\varrho_\pm - 1 - \mu_\pm)$ as the bulk grand potential densities of the solvent and of the $\pm$-ions (in the low number density limit), respectively. Here $k_BT$ is the thermal energy, $\mu_\phi k_BT$ and $\mu_\pm k_BT$ are the chemical potential difference $(\mu_A - \mu_B)k_BT$ of the solvent particles and the chemical potentials of the $\pm$-ions, respectively, and $\ell_B\widetilde{a} = e^2/(4\pi\varepsilon_0 k_BT)$ is the Bjerrum length for the vacuum permittivity $\varepsilon_0$. The temperature-dependent Flory-Huggins parameter $\chi(T) > 0$ describes the effective interaction between solvent particles, where the temperature dependence is usually described by the empirical form $\chi(T) = \chi_S + \frac{\chi_H}{T}$ with the system specific entropic contribution $\chi_S$ and the enthalpic contribution $\chi_H$ [383]. For $\chi(T) \geq \chi(T_c)$ phase separation occurs in the pure, salt-free solvent within a certain range of $\phi$ whereas for $\chi(T) < \chi(T_c)$ the solvent components $A$ and $B$ are miscible in any proportion. A positive (negative) enthalpic contribution $\chi_H$ corresponds to an upper (lower) critical demixing point. The gradient term $\sim (\nabla\phi(z))^2$ with $\nabla = \widetilde{a}\widetilde{\nabla}$ penalises the spatial variation of the solvent composition [70]. The ion-solvent interaction is described within an LDA by the effective ion potential $k_BTV_\pm(\phi)$ generated by the solvent (see below). The relative permittivity $\varepsilon(\phi(\mathbf{r}))$ is assumed to depend locally on the composition of the solvent $\phi(\mathbf{r})$ but not on the ion densities $\varrho_\pm(\mathbf{r})$, which is justified for small ionic strengths, i.e. $\varrho_\pm(\mathbf{r}) \ll 1$. Here the mixing formula $\varepsilon(\phi) = \varepsilon_A\phi + \varepsilon_B(1-\phi)$ introduced by Böttcher [55] is used [29, 334, 401]. Using SI-units, the electric displacement $\widetilde{\mathbf{D}} = \mathbf{D}e\widetilde{a}^{-2}$ in Eq. (2.1) fulfills Gauss' law $\nabla\cdot\mathbf{D}(\mathbf{r},[\varrho_\pm]) = \varrho_+(\mathbf{r}) - \varrho_-(\mathbf{r}), \mathbf{r}\in\mathcal{V}$, with fixed surface charges $\mathbf{n}(\mathbf{r})\cdot\mathbf{D}(\mathbf{r},[\varrho_\pm]) = \sigma(\mathbf{r}), \mathbf{r}\in\partial\mathcal{V}$, where $\mathbf{n}$ is the unit vector perpendicular to $\partial\mathcal{V}$ pointing towards the exterior of $\mathcal{V}$ (see Ref. [385]). Note that $\mathbf{D}(\mathbf{r},[\varrho_\pm])$ is generated by the $\pm$-ions and the given surface charges $\sigma$; it does not depend explicitly on $\phi$. Within this model, besides being confined, ions interact with the walls only electrostatically.

Note that by using the square-gradient form of Eq. (2.1) the interactions are implicitly assumed to be short-ranged [131], i.e. van der Waals forces are not taken into account. Moreover, layering due to packing effects close to walls is also not accounted for by square-gradient theories. Nonetheless such a description provides reliable results at mesoscopic scales [131]. Finally, the ionic strength is assumed to be sufficiently low so that one can neglect short-ranged ion-ion interactions. Therefore the ions interact with each other only via the electrostatic field. Accordingly, the expression for $\omega_{\text{ion}}^{(\pm)}$ does not contain additional Flory-Huggins parameters and there are no square-gradient terms for $\varrho_\pm$.

In Eq. (2.1) the ion-solvent interaction is described, within an LDA, by a solvent-induced ion potential, $V_\pm(\phi)k_BT$. The BCA used in previous investigations (see, e.g., Refs. [29, 312–314, 327, 328, 334, 335, 338, 401]) corresponds to the choice $V_\pm^{(\text{BCA})}(\phi) := f_\pm\phi$, where $f_\pm k_BT = (f_{\pm A} - f_{\pm B})k_BT$ is the *difference* between the bulk solvation free energies of a $\pm$-ion in solvents consisting purely of component $A$, $f_{\pm A}k_BT$, and purely of component $B$, $f_{\pm B}k_BT$. The solubility contrasts $f_\pm k_BT$ are also known as Gibbs free energies of transfer. In this context the only relevant parameters are the two differences $f_\pm = f_{\pm A} - f_{\pm B}$ because the other two independent quantities $f_{\pm A} + f_{\pm B}$ can be absorbed as shifts in the definition of the chemical potentials $\mu_\pm k_BT$ of the ions. For bulk systems the BCA is identical to the RPA [176], which is expected to be reliable only if the coupling strengths are much smaller than the thermal energy, i.e. $|f_\pm| \ll 1$. However, for electrolyte solutions, this condition is in general not fulfilled. Instead, the Gibbs free energies of transfer between two liquids are usually of the order of some $10k_BT$ [208, 223, 286].

Figures 2.1(a) and 2.1(b) display the bulk phase diagram for a constant chemical potential (per $k_BT$) $\mu_I := \mu_+ + \mu_-$ of added salt obtained within BCA for the representative

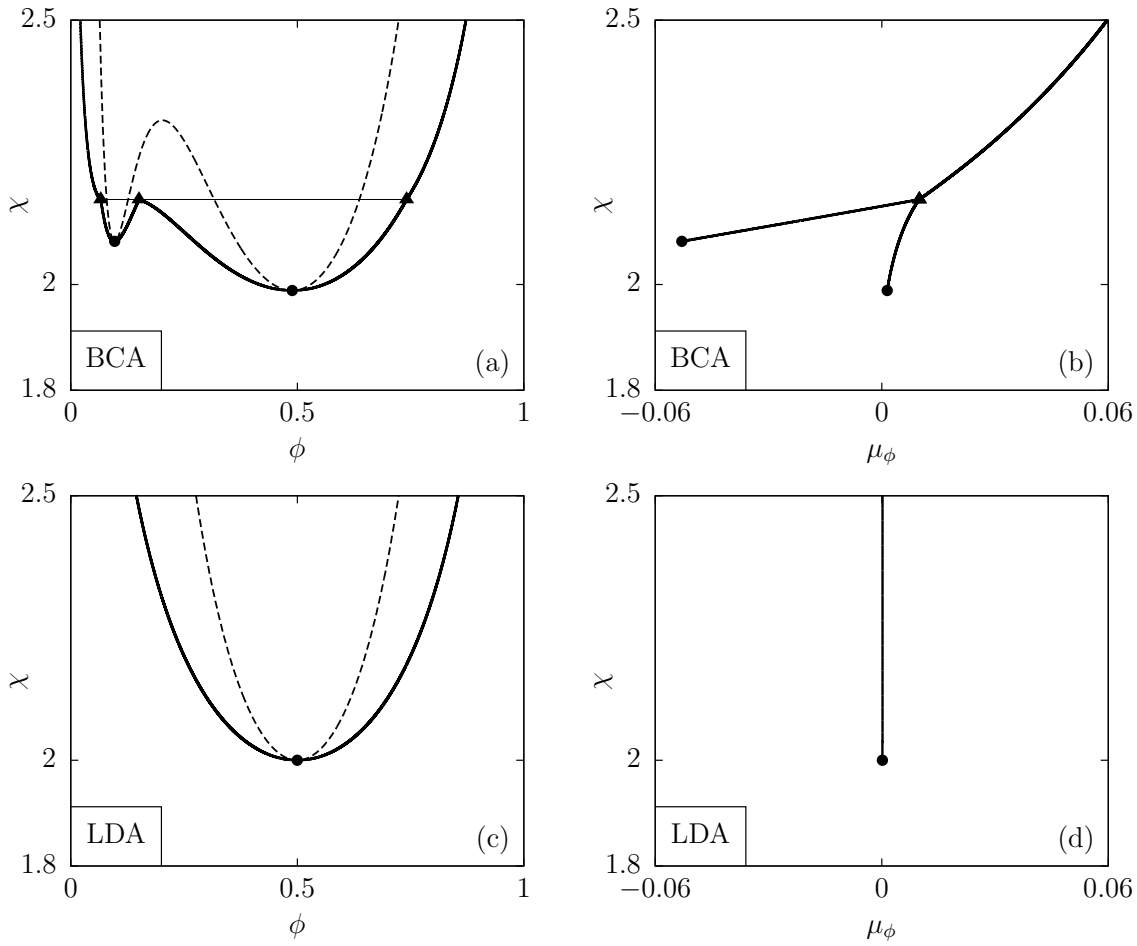


Figure 2.1: Bulk phase diagrams of a binary liquid mixture with added salt of constant chemical potential (per $k_BT$) $\mu_I = \mu_+ + \mu_-$ within the BCA $V_\pm^{(BCA)}(\phi) = f_\pm\phi$ [(a) and (b)] and within the LDA, see Eq. (2.3)) $V_\pm(\phi) = -\ln(1-\phi(1-\exp(-f_\pm)))$ [(c) and (d)] in terms of the Flory-Huggins parameter $\chi$ and the composition $\phi$ [(a) and (c)] or the chemical potential (per $k_BT$) $\mu_\phi = \mu_A - \mu_B$ conjugate to the composition $\phi$ of the binary solvent [(b) and (d)]. The thick solid lines correspond to the binodals, which delimit the two-phase coexistence regions in the $\phi$-$\chi$ diagrams [(a) and (c)] from below. The dashed lines are the spinodals and the thin horizontal line in panel (a) is the tie-line corresponding to the triple point (▲) found within BCA. Representative values for the solubility contrasts per $k_BT$, $(f_+, f_-) = (3, 26)$, have been chosen. The chemical potential $\mu_I k_BT$ of the salt corresponds to an ionic strength $\widetilde{I}_c = \widetilde{\varrho}_\pm = 10\,\mathrm{mM}$ at the critical point with composition $\phi = \phi_c \approx \frac{1}{2}$. The weak influence of the salt on the phase diagram within LDA leads to curves in panels (c) and (d) which are, on the present scale, almost (but not quite) symmetric with respect to $\phi = \frac{1}{2}$ and $\mu_\phi = 0$, respectively. Whereas the LDA [(c) and (d)], in agreement with the experimental evidence, exhibits a single critical point (•, $\phi_{c,1} \approx \frac{1}{2}, \chi_{c,1} \approx 2$), which slightly shifts upon changing the ionic strength (see Fig. 2.3), the standard BCA [(a) and (b)], in contrast to the available experimental observations, leads to a second critical point (•, $\phi_{c,2} \approx 0.1, \chi_{c,2} \approx 2.1$) as well as to a triple point (▲). (See Ref. [43])

values $f_+ = 3, f_- = 26$. This choice is similar to the Gibbs free energies of transfer for potassium chloride (KCl) from water to acetone: $f_+ = 2, f_- = 23$ [286]. The condition of local charge neutrality $\varrho_+ = \varrho_- =: I$ in the bulk implies that the ionic strength $I$ depends on the chemical potentials $\mu_\pm k_B T$ of the ions only via the sum $\mu_+ + \mu_- = \mu_I$. For given uniform composition $\phi$ and ionic chemical potential $\mu_I$ the Euler-Lagrange equation of $\Omega$ in Eq. (2.1) with respect to uniform ion densities $\varrho_\pm = I$ can be used to express the bulk ionic strength as [43]

$$I_{\text{bulk}}(\phi, \mu_I) = \exp\Big(\frac{1}{2}(\mu_I - V_+(\phi) - V_-(\phi))\Big). \tag{2.2}$$

Here $I_{\text{bulk}}$ is *independent* of the Flory-Huggins parameter $\chi$, i.e. it depends on the temperature $T$ only via the normalizations of $\mu_I$ and $V_\pm$, which are defined in units of $k_B T$. In Fig. 2.1 the chemical potential $\mu_I$ of the salt is fixed such that the solvent composition $\phi = \frac{1}{2}$ leads to an ionic strength $\widetilde{I} = I\widetilde{a}^{-3} = 10\,\text{mM} \approx 0.006\,\text{nm}^{-3}$, where the length scale $\widetilde{a} = 2\,\text{Å}$ has been chosen [43]. Due to the absence of gradients, electric fields and surfaces, the bulk phase diagram is determined by the first, third and fourth term on the right-hand side of Eq. (2.1). The occurrence of two critical points (•) as well as of a triple point (▲) predicted within BCA is not supported by experimental evidence, which signals the breakdown of BCA for such large parameters $f_\pm$. Whereas for most systems it is experimentally difficult to preclude the occurrence of such a second critical point or triple point, the experimental resolution is yet sufficiently high to exclude these features to occur visibly to the extent as predicted by the BCA (Figs. 2.1(a) and (b)).

A more appropriate approximation for the solvent-induced ion potential $V_\pm(\phi)k_B T$, which is derived in Ref. [43], is given by (see also Fig. 2.2(a))

$$V_\pm(\phi) = -\ln(1 - \phi(1 - \exp(-f_\pm))). \tag{2.3}$$

For $|f_\pm| \ll 1$ this expression reduces to the correct asymptotic expression $V_\pm(\phi) \simeq V_\pm^{(\text{BCA})}(\phi)$. In the limit $f_\pm \to \infty$, i.e. if ions are insoluble in component $A$, $V_\pm(\phi) \simeq -\ln(1-\phi)$, which corresponds to the free energy of the ions dissolving entirely in component $B$ only, which has the volume fraction $1 - \phi$. Similarly, in the limit $f_\pm \to -\infty$, i.e. if the ions are insoluble in component $B$, $V_\pm(\phi) \simeq f_\pm - \ln\phi$, which is the free energy of the ions dissolving entirely in component $A$ only, which has the volume fraction $\phi$ and for which the solvation free energy is $f_\pm$. For the same set of parameters as in Figs. 2.1(a) and (b), Figs. 2.1(c) and (d) display the phase diagram within LDA. In agreement with experimental observations, within LDA only a single critical point (•) occurs (see, e.g., the closed loop-binodals in Ref. [392] with only one lower critical demixing point in the presence of an antagonistic salt, i.e. with $f_+$ and $f_-$ having opposite signs). Hence one can conclude that the standard BCA, i.e. $V^{(\text{BCA})}(\phi) = f_\pm\phi$, introduces artifacts for too large ion-solvent couplings, $|f_\pm| \gg 1$, which are absent within the LDA proposed in Ref. [43] (see Eq. (2.3)).

If $\phi$ deviates slightly from a certain composition $\phi_0 \in [0, 1]$ one has $V_\pm(\phi) \simeq V_\pm(\phi_0) + \gamma_\pm(\phi - \phi_0)$ with the effective coupling strengths $\gamma_\pm := V_\pm'(\phi_0) = \dfrac{1 - \exp(-f_\pm)}{1 - \phi_0(1 - \exp(-f_\pm))} \in \Big[-\dfrac{1}{\phi_0}, \dfrac{1}{1-\phi_0}\Big]$ instead of $f_\pm$ as in BCA. For, e.g., $\phi_0 = 1/2$ one finds $\gamma_\pm = 2\tanh(f_\pm/2) \in [-2, 2]$, i.e. the use of BCA, which corresponds to $\gamma_\pm \approx f_\pm$, is justified only for Gibbs free

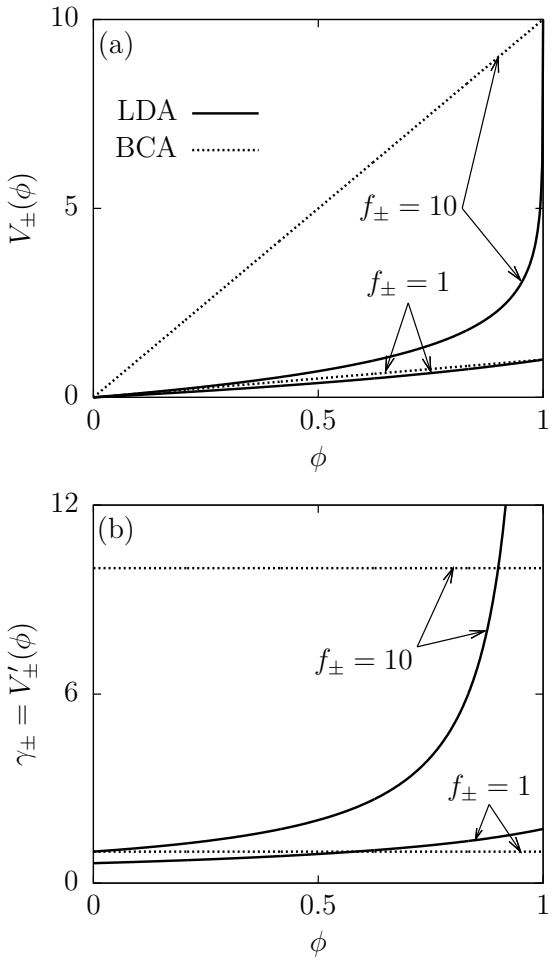


Figure 2.2: Comparison of the solvent-induced ion potential $V_\pm(\phi)$ [(a)] and its derivative $\gamma_\pm = V'_\pm(\phi)$ [(b)] within LDA and BCA for ion solubility contrast $f_\pm$ (see the main text). For small values of $f_\pm$ (see the case $f_\pm = 1$) the differences between LDA and BCA are small. For large values of $f_\pm$ (see the case $f_\pm = 10$) $V_\pm(\phi)$ and $\gamma_\pm = V'_\pm(\phi)$ become large at solvent compositions $\phi \approx 0.5$ within BCA whereas they remain small within LDA. Within LDA $V'_\pm(\phi = 0) = 1 - \exp(-f_\pm)$ and $V'_\pm(\phi = 1) = \exp(f_\pm) - 1$, while within BCA $V'_\pm(\phi) = f_\pm$. (See Ref. [43])

energies of transfer per $k_BT$, $f_\pm$, not larger than 2 (see Fig. 2.2(b)). However, in previous investigations BCA has been used even for large values of $|f_\pm|$ [29, 327, 328, 334, 335, 401].

There is experimental evidence [409] that in the phase diagram of a binary liquid mixture the critical point shifts upon adding salt. The direction as well as the magnitude of the shift depend on the materials properties of the binary liquid mixture and of the ions. Due to the relations $\varrho_A = \phi, \varrho_B = 1 - \phi, \varrho_+ = \varrho_- = I$ the bulk system, which comprises four particle species, is de facto a binary mixture, characterised by $\mu_\phi$, $\mu_I = \mu_+ + \mu_-$, and $\chi$ (i.e. $T$). Hence in this three-dimensional space of thermodynamic variables there is a sheet of first-order demixing phase transitions $(\mu_\phi^{(\mathrm{demix})}(\mu_I, \chi), \mu_I, \chi)$ bounded by a line of critical points $(\mu_\phi^{(\mathrm{crit})}(\mu_I), \mu_I, \chi^{(\mathrm{crit})}(\mu_I))$ which translates into $(\phi_c, I_c, \chi_c) \equiv (\phi^{(\mathrm{crit})}(\mu_I), I^{(\mathrm{crit})}(\mu_I), \chi^{(\mathrm{crit})}(\mu_I))$. For a given chemical potential $\mu_I k_B T$ the critical point $(\phi_c, I_c, \chi_c)$ is determined as the minimum of the Flory-Huggins parameter $\chi_s(\phi, I_{\mathrm{bulk}}(\phi, \mu_I))$ at the spinodal as a function of $\phi$ for constant $\mu_I$. The spin-

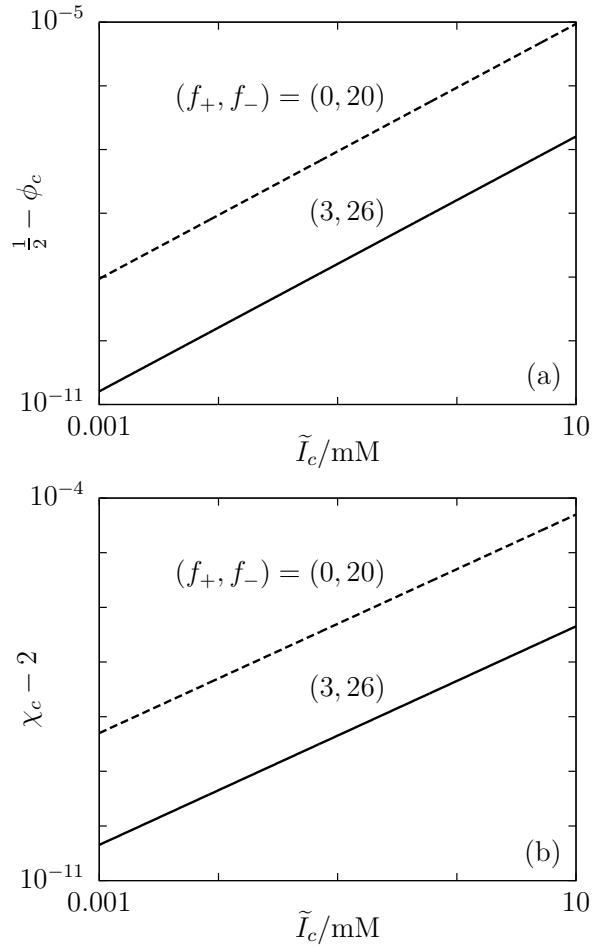


Figure 2.3: Variation of the critical volume fraction $\phi_c$ [(a)] and the critical Flory-Huggins parameter $\chi_c$ [(b)] as function of the ionic strength $\widetilde{I}_c = I_c \widetilde{a}^{-3}$ at the critical point for two representative sets of solubility contrasts: $(f_+, f_-) = (3, 26)$ and $(0, 20)$. These results show that both $\frac{1}{2} - \phi_c$ and $\chi_c - 2$ depend linearly on $I_c$ and that there are no quantitatively significant shifts of the critical point upon varying the ionic strength within experimentally reasonable ranges. On this scale, the phase diagrams for $(f_+, f_-) = (3, 26)$ (see Figs. 2.1(c) and (d)) and for $(f_+, f_-) = (0, 20)$ are almost indistinguishable. Note that $\phi_c(\widetilde{I}_c \to 0) = \frac{1}{2}$ and $\chi_c(\widetilde{I}_c \to 0) = 2$. (See Ref. [43])

odal is defined by the set of points $(\phi, I, \chi_s(\phi, I))$ in the bulk phase diagram for which points $(\phi, I, \chi)$ with $\chi > \chi_s(\phi, I)$ exhibit no longer at least a local minimum of the density functional Eq. (2.1) (see the dashed lines in Figs. 2.1(a) and (c)). Accordingly, at the spinodal the Hessian matrix of the bulk grand potential density $\Omega(\phi, I)/V$ corresponding to Eq. (2.1) has a zero eigenvalue. This condition leads to [43]

$$\chi_s(\phi, I) = \frac{1}{2}\left(\frac{1}{\phi} + \frac{1}{1-\phi} + \left(V_+''(\phi) + V_-''(\phi) - \frac{1}{2}(V_+'(\phi) + V_-'(\phi))^2\right) I\right). \tag{2.4}$$

By inverting the relation $I_c = I^{(\mathrm{crit})}(\mu_I)$ one obtains $\mu_I = \mu_I^{(\mathrm{crit})}(I_c)$. Figure 2.3 displays the variation of (a) the critical volume fraction $\phi_c = \phi^{(\mathrm{crit})}(\mu_I^{(\mathrm{crit})}(I_c))$ and (b) the critical Flory-Huggins parameter $\chi_c = \chi^{(\mathrm{crit})}(\mu_I^{(\mathrm{crit})}(I_c))$ as functions of the ionic strength $\widetilde{I}_c = I_c \widetilde{a}^{-3}$ at

the critical point within LDA. Without added salt ($I = 0$) one obtains the critical point $(\phi_c, \chi_c) = (\frac{1}{2}, 2)$ of the pure solvent. For the given choice of the parameters $(f_+, f_-)$ and for small $I_c$ the critical composition $\phi_c$ decreases and the critical Flory-Huggins parameter $\chi_c$ increases linearly upon increasing the ionic strength $I_c$. For small $I_c$ the asymptotically linear dependence of the critical point $(\phi_c, \chi_c)$ on the ionic strength $I_c$ is in agreement with experimental evidence [127, 409]. However, the magnitudes of these shifts are tiny, even for large differences in the solubility contrasts, e.g. $(f_+, f_-) = (0, 20)$, to the effect that the bulk phase diagrams are almost indistinguishable within experimentally relevant ranges of ionic strengths $\widetilde{I}_c \lesssim 10\,\mathrm{mM}$. Within the range of ionic strengths considered in Fig. 2.3 the experimentally observed critical point shifts are also small [409]. However, significant shifts of the critical temperature $T_c$ have been detected for large ionic strengths $\widetilde{I}_c \gg 100\,\mathrm{mM}$ [409].

Whether the description of a given electrolyte solution within a local model such as the LDA of Ref. [43] is justified or not does not depend on the salt alone but on the combination of salt and solvent. Experimentally observed effects in binary liquid mixtures due to adding salt, such as the shift of the critical point, depend sensitively on the type of mixture (compare Ref. [409] for water+2,6-dimethylpyridine and Ref. [389] for heavy water+3-methylpyridine). Moreover, the measured critical point shifts exhibit a strong dependence on the size of the ions (compare Ref. [389] for alkali halides and Ref. [390] for sodium tetraphenylborate). These evidences in combination with the analysis in Ref. [43], which implies a weak influence of the ionic *charge*, lead to the conclusion that steric effects might play an important role for the ion-solvent interaction. This interpretation is supported by reports of critical point shifts of similar magnitude in binary liquid mixtures due to adding non-ionic impurities [172]. Consequently it is mostly the property of an ion to be a structure maker or a structure breaker and only to a lesser extent its electric charge which determines the influence of a salt onto the phase behaviour of an electrolyte solution [43]. It will be shown in Sec. 3.2 that this conclusion on the *phase behaviour* is in stark contrast to the influence of charges on the *structure* of ionic complex fluids.

## 2.2 Vapour pressure of room temperature ionic liquids

One of the peculiar and probably most important properties of room temperature ionic liquids (RTILs) is a tiny vapour pressure at room temperature: $[C_4\mathrm{mim}][PF_6]$, e.g., has a vapour pressure of ca. 100 pPa at 298 K [346], whereas water has 3 kPa at the same temperature [258]. This offers the possibility to use RTILs as solvents under ultrahigh vacuum (UHV) conditions (i.e. for a pressure range 100 nPa ... 100 pPa [373]), where volatile organic solvents would evaporate immediately [277, 462]. Whereas RTILs are practically "non-volatile" at room temperature [462], they can be distilled at higher temperatures [123], where vapour pressures and enthalpies of vapourisation can be measured [347, 488].

In comparison with non-ionic liquids (NILs, such as benzene and water) with triple point pressures $p_3$ above 1 Pa (see Tab. 2.1(a)), RTILs exhibit ionic character due to the Coulomb interaction, which adds to the van der Waals interaction in NILs and which leads to a decrease of the vapour pressure at room temperature (see Tab. 2.1(b)). However, inorganic fused salts (IFSs, such as $CdCl_2$ and NaCl), also exhibit ionic character, which is even stronger than that of RTILs due to the smaller particle size, but the triple point

| (a) NIL | $T_3$/K | $p_3$/Pa | $T_b$/K | $T_c$/K | References |
|---|---|---|---|---|---|
| $C_6H_6$ | 278.7 | 4799 | 353.2 | 562.1 | [258] |
| $H_2O$ | 273.2 | 611.7 | 373.1 | 647.1 | [258] |

| (b) RTIL | $T_3$/K | $p_3$/Pa | $T_d$/K | $T_b^{\mathrm{extr}}$/K | References |
|---|---|---|---|---|---|
| $[C_4mim][dca]$ | 267 | $1.5 \times 10^{-13}$ | 695 | 719 | [129, 145] |
| $[C_2mim][NTf_2]$ | 271 | $8.9 \times 10^{-12}$ | 712 | 906 | [348, 432, 488] |
| $[C_8mim][NTf_2]$ | 264 | $7.8 \times 10^{-14}$ | 698 | 857 | [348, 432, 488] |

| (c) IFS | $T_3$/K | $p_3$/Pa | $T_b$/K | $T_c$/K | References |
|---|---|---|---|---|---|
| $CdCl_2$ | 837 | 214 | 1233 | ? | [23, 270] |
| NaCl | 1074 | 46 | 1738 | $> 3400$ | [23, 270, 293] |

Table 2.1: Experimental data for characteristic temperatures of (a) non-ionic liquids (NILs), (b) room temperature ionic liquids (RTILs) and (c) inorganic fused salts (IFSs) corresponding to the substances discussed in Figure 2.4. $T_3$ and $p_3$ denote the temperature and the pressure, respectively, at the triple point, $T_c$ is the critical temperature and $T_d$ denotes the temperature for the onset of decomposition of an RTIL [145, 432]. $T_b$ denotes the standard boiling temperature at ambient pressure $p_0 = 10^5\,\mathrm{Pa}$ for NILs and IFSs, whereas the standard boiling temperatures $T_b^{\mathrm{extr}}$ for RTILs are estimated by extrapolation [372] because boiling of RTILs is preempted by decomposition. (See Ref. [40])

pressures of IFSs are above 1 Pa (see Tab. 2.1(c)) — similar to those of NILs. Moreover, all these trends are not material specific, which points towards general properties of NILs, RTILs and IFSs.

From the different strengths of the interactions in NILs, RTILs and IFSs one can infer that the enthalpies of vaporisation $\Delta_{\mathrm{vap}}H(p) > 0$ at pressure $p$ are ordered as $\Delta_{\mathrm{vap}}H^{\mathrm{NIL}}(p) < \Delta_{\mathrm{vap}}H^{\mathrm{RTIL}}(p) < \Delta_{\mathrm{vap}}H^{\mathrm{IFS}}(p)$ for NISs, RTILs and IFSs, respectively [40]. Moreover, according to Trouton's rule [9], the molar entropy of vaporisation $\Delta_{\mathrm{vap}}S(p)$ at pressure $p$ is only weakly material dependent, since it is dominated by the translational and rotational degrees of freedom whereas vibrational and electronic modes and the structural arrangements contribute only as small corrections [450]. At ambient pressure $p_0 = 10^5\,\mathrm{Pa}$ the Trouton constant is approximately $\Delta_{\mathrm{vap}}S(p_0) \approx (95 \pm 15)\,\mathrm{J/mol}$ [212, 270]. Consequently, due to the Clausius-Clapeyron equation [9]

$$p_{\mathrm{sat}}(T) \approx p_0 \exp\Big( - \frac{\Delta_{\mathrm{vap}}H(p_0)}{RT} + \frac{\Delta_{\mathrm{vap}}S(p_0)}{R} \Big). \tag{2.5}$$

one obtains

$$p_{\mathrm{sat}}^{\mathrm{NIL}}(T) \gg p_{\mathrm{sat}}^{\mathrm{RTIL}}(T) \gg p_{\mathrm{sat}}^{\mathrm{IFS}}(T). \tag{2.6}$$

The rightmost inequality in Eq. (2.6) is apparently in contradiction with the experimental finding of triple point pressures $p_3$ for IFSs being much larger than for RTILs (see Tab. 2.1(b) and (c)). However, that this is indeed not the case can be inferred from Fig. 2.4, where the vapour pressure curves $p_{\mathrm{sat}}(T)$ for non-polar liquid benzene ($C_6H_6$, see Ref. [258]), hydrogen bond forming liquid water ($H_2O$, see Ref. [258]), the RTILs $[C_4mim][dca]$, $[C_2mim][NTf_2]$ and $[C_8mim][NTf_2]$ (see Refs. [129, 488]), as well as the IFSs cadmium chloride ($CdCl_2$) and sodium chloride (NaCl) (see Ref. [23]) are displayed.

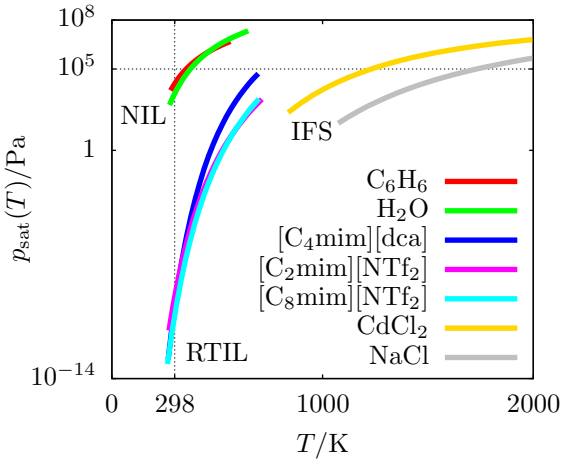


Figure 2.4: Experimental vapour pressures $p_{\mathrm{sat}}(T)$ at liquid-vapour coexistence of non-ionic liquids (NILs), room temperature ionic liquids (RTILs) and inorganic fused salts (IFSs) as a function of temperature $T$ for the non-polar liquid benzene ($C_6H_6$, see Ref. [258]), the hydrogen bond forming liquid water ($H_2O$, see Ref. [258]), the paradigmatic RTILs [$C_4$mim][dca], [$C_2$mim][$NTf_2$] and [$C_8$mim][$NTf_2$] (see Refs. [129, 488]), as well as fused cadmium chloride ($CdCl_2$) and sodium chloride (NaCl) as examples of IFSs (see Ref. [23]). At low temperatures all curves terminate at the corresponding triple point temperature $T_3$ (see Tab. 2.1), which is close to the standard melting temperature of that substance. At high temperatures the boiling curves for the RTILs terminate at the decomposition temperature $T_d$, whereas the boiling curves of the other liquids end at their critical points (see Tab. 2.1). Room temperature $T_0 = 298\,\mathrm{K}$ and ambient pressure $p_0 = 10^5\,\mathrm{Pa}$ are indicated. (See Ref. [40])

The key observation is, that IFSs crystallise before $p_{\mathrm{sat}}^{\mathrm{IFS}}(T)$ reaches small values, whereas RTILs stay liquid down to room temperature.

It is the unique *combination* of the melting point to occur around *room temperature* and of the *ionic* character which leads to the observed low triple point pressures of RTILs, and it is the class of RTILs, which, by definition, comprises systems with both these properties [40]. The feature of RTILs being liquids even at room temperature has been attributed to various mechanisms, e.g. frustrated crystallisation due to asymmetric ion shapes, charge delocalisation, packing inefficiency and conformational degeneracy [194, 250, 359, 410]. Hence, RTILs are necessarily complex fluids due to the additional conformation degrees of freedom. The combination with the ionic character results in the highly unique and material-indpendent general property of tiny triple point pressures of these ionic complex fluids.

## 2.3 Ionic liquid crystals

A very simple model to study the phase behaviour of ionic liquid crystals can be formulated in terms of a lattice model, where the ions occupy, according to their size and shape, one or more adjacent lattice sites; the correspondence to a real RTIL is sketched in Fig. 2.5.

A starting point for a description of the thermodynamic properties of the lattice model

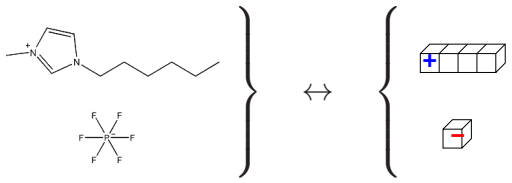

Figure 2.5: Correspondence of $[C_6mim][PF_6]$ and a possible representation within the lattice model.

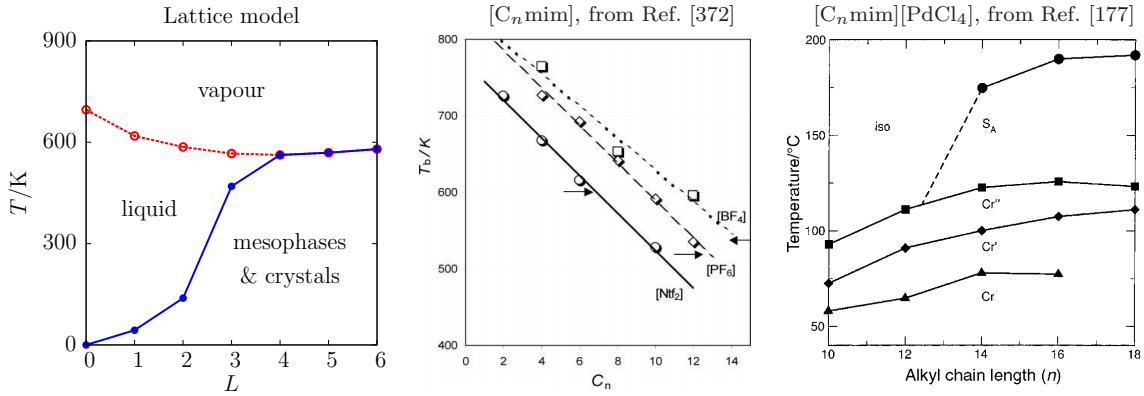


Figure 2.6: Comparison of the isobaric phase behaviour of ionic liquid crystals as function of the length of the chain attached to the charged group. The transitions between isotropic liquid and vapour phases as well as the transitions between isotopic and anisotropic phases within the simplistic lattice model of ionic liquid crystals ($L$ denotes the number of lattice sites repesenting the attached chain) is in qualitative agreement with the experimental results in Refs. [372] and [177], respectively. Here one lattice site within the lattice model corresponds approximetely to $3 \ldots 4$ C-atoms along an alkyl chain. Whereas the lattice model correctly accounts for the orientational phase transitions, the lattice model is not appropriate to distinguish the various anisotropic phases inside the regime "mesophases & crystals".

can be given by the approximative free energy density functional

$$F[\underline{\varrho}] = F^{\mathrm{h}}[\underline{\varrho}] + \frac{1}{2}\sum_{i,j}\int \mathrm{d}^3r \int \mathrm{d}^3s \; \varrho_i(\mathbf{r})\varrho_j(\mathbf{s})\Big(U_{ij}^{\mathrm{c}}(\mathbf{r},\mathbf{s}) + U_{ij}^{\mathrm{d}}(\mathbf{r},\mathbf{s})\Big) + \int \mathrm{d}^3r \; f_{\mathrm{MSA}}\Big(\sum_i \varrho_i(\mathbf{r})\Big), \tag{2.7}$$

where $F^{\mathrm{h}}$ denotes a hard-core fundamental measure reference functional for lattice particles derived along the lines of Ref. [245], long-ranged Coulomb interactions $U^{\mathrm{c}}$ and dispersion forces $U^{\mathrm{d}}$ are described within random phase approximation (RPA) and short-ranged Coulomb interactions contribute within local density approximation (LDA) in terms of the free energy density $f_{\mathrm{MSA}}$ of the mean spherical approximation (MSA) of charged hard spheres [454–456].

A comparison of the isobaric phase behaviour of ionic liquid crystals as function of the length of the chain attached to the charged group is displayed in Fig. 2.6. The

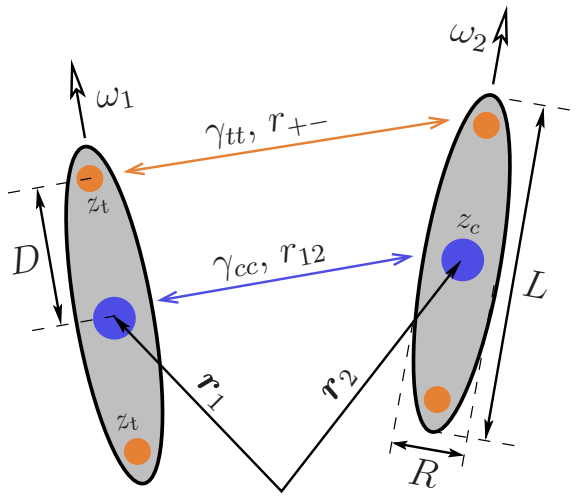


Figure 2.7: Schematic side view of two prolate ellipsoids with orientations $\boldsymbol{\omega}_1$ and $\boldsymbol{\omega}_2$. The centers of mass of the ellipsoids are located at $\mathbf{r}_1$ and $\mathbf{r}_2$, respectively, where $r_{12} = |\mathbf{r}_1 - \mathbf{r}_2|$. Only the projections of the ellipsoids on the plane of the figure are shown and the centers and main symmetry axes of the ellipsoids are chosen to lie within the plane of the figure. $R$ is the cross-sectional diameter of the ellipsoids and $L$ is the particle length. The full circles mark the location of possible charges with valencies $z_c$ and $z_t$ in the center of the ellipsoids and at the tails at a distance $D$ from the center, respectively. The energy scale of the Coulomb pair interaction acting between charged tails and between charged centers are denoted as $\gamma_{tt}$ and $\gamma_{cc}$ (see Eqs. (2.13) and (2.15)). In addition there is a corresponding Coulomb pair interaction acting between charged tails and centers. (See Ref. [236])

transitions between isotropic liquid and vapour phases as well as the transitions between isotopic and anisotropic phases within the lattice model is in qualitative agreement with the experimental results in Refs. [372] and [177], respectively. One can infer that one lattice site within the lattice model corresponds approximetely to 3 . . . 4 C-atoms of an alkyl chain. Whereas the lattice model correctly accounts for the orientational phase transitions, the lattice model is not appropriate to distinguish the various anisotropic phases inside the regime "mesophases & crystals" in Fig. 2.6. This can be traced back to the restriction of particles being located at discrete lattice sites, whereas the stability of smectic and crystalline phases hinges on packing effects on the scale of fractions of a lattice site.

A more refined model to study the properties of ionic liquid crystals has been proposed in Ref. [236]. The intermolecular pair potential is expressed as a sum of the contribution due to excluded-volume interactions and the contribution due to long-ranged interactions:

$$U(\mathbf{r}_{12}, \boldsymbol{\omega}_1, \boldsymbol{\omega}_2) = \begin{cases} \infty & , r_{12} < R\,\sigma(\hat{\mathbf{r}}_{12}, \boldsymbol{\omega}_1, \boldsymbol{\omega}_2) \\ U_{GB}(\mathbf{r}_{12}, \boldsymbol{\omega}_1, \boldsymbol{\omega}_2) + U_{CO}(\mathbf{r}_{12}, \boldsymbol{\omega}_1, \boldsymbol{\omega}_2) & , r_{12} \geq R\,\sigma(\hat{\mathbf{r}}_{12}, \boldsymbol{\omega}_1, \ \boldsymbol{\omega}_2) \end{cases} \quad .(2.8)$$

Here the pair potential $U(\mathbf{r}_{12}, \boldsymbol{\omega}_1, \boldsymbol{\omega}_2)$ between particles 1 and 2 is written as a function of the intermolecular vector $\mathbf{r}_{12}$ between the centers of mass of the two particles, and their orientations $\boldsymbol{\omega}_1$ and $\boldsymbol{\omega}_2$, where $r_{12} = |\mathbf{r}_{12}|$ is the magnitude of $\mathbf{r}_{12} = \mathbf{r}_2 - \mathbf{r}_1$ (see Fig. 2.7). The contact distance $R\,\sigma(\hat{\mathbf{r}}_{12}, \boldsymbol{\omega}_1, \boldsymbol{\omega}_2)$ depends on the orientations of both particles and on the unit vector $\hat{\mathbf{r}}_{12} = \mathbf{r}_{12}/r_{12}$ between their centers.

In Ref. [236] the well-known Gay-Berne pair potential is used as a generalization of the Lennard-Jones pair potential to fluids consisting of nonspherical particles (see e.g. Refs. [25, 66, 97–99, 153] and references therein):

$$\begin{aligned} U_{GB}(\mathbf{r}_{12},\boldsymbol{\omega}_1,\boldsymbol{\omega}_2) &= 4\varepsilon(\hat{\mathbf{r}}_{12},\boldsymbol{\omega}_1,\boldsymbol{\omega}_2) \qquad (2.9)\\ &\times \left[\left(\frac{r_{12}}{R_0}-\sigma(\hat{\mathbf{r}}_{12},\boldsymbol{\omega}_1,\boldsymbol{\omega}_2)+1\right)^{-12}-\left(\frac{r_{12}}{R_0}-\sigma(\hat{\mathbf{r}}_{12},\boldsymbol{\omega}_1,\boldsymbol{\omega}_2)+1\right)^{-6}\right], \\ \sigma(\hat{\mathbf{r}}_{12},\boldsymbol{\omega}_1,\boldsymbol{\omega}_2) &= \left[1-\frac{\chi}{2}\left(\frac{(\hat{\mathbf{r}}_{12}\cdot\boldsymbol{\omega}_1+\hat{\mathbf{r}}_{12}\cdot\boldsymbol{\omega}_2)^2}{1+\chi\boldsymbol{\omega}_1\cdot\boldsymbol{\omega}_2}+\frac{(\hat{\mathbf{r}}_{12}\cdot\boldsymbol{\omega}_1-\hat{\mathbf{r}}_{12}\cdot\boldsymbol{\omega}_2)^2}{1-\chi\boldsymbol{\omega}_1\cdot\boldsymbol{\omega}_2}\right)\right]^{-\frac{1}{2}}, \qquad (2.10)\\ \varepsilon(\hat{\mathbf{r}}_{12},\boldsymbol{\omega}_1,\ \boldsymbol{\omega}_2) &= \varepsilon_0\left(1-\chi^2(\boldsymbol{\omega}_1\cdot\boldsymbol{\omega}_2)^2\right)^{-\frac{1}{2}} \qquad (2.11)\\ &\times \left[1-\frac{\chi'}{2}\left(\frac{(\hat{\mathbf{r}}_{12}\cdot\boldsymbol{\omega}_1+\hat{\mathbf{r}}_{12}\cdot\boldsymbol{\omega}_2)^2}{1+\chi'\boldsymbol{\omega}_1\cdot\boldsymbol{\omega}_2}+\frac{(\hat{\mathbf{r}}_{12}\cdot\boldsymbol{\omega}_1-\hat{\mathbf{r}}_{12}\cdot\boldsymbol{\omega}_2)^2}{1-\chi'\boldsymbol{\omega}_1\cdot\boldsymbol{\omega}_2}\right)\right]^2. \end{aligned}$$

Here $\chi=(\kappa^2-1)/(\kappa^2+1)$ and $\kappa=L/R$, where $R$ is the cross-sectional diameter of the particle and $L$ is the particle length along the main symmetry axis (see Fig. 2.7). Accordingly, the parameter $\kappa$ is a measure of the length-to-breadth ratio of the particle. The interaction strength $\varepsilon(\hat{\mathbf{r}}_{12},\boldsymbol{\omega}_1,\boldsymbol{\omega}_2)$ depends on the relative orientations of the particles, $\varepsilon_0$ is a parameter setting the energy scale of the pair interaction, $\chi'=(\kappa'^{1/2}-1)/(\kappa'^{1/2}+1)$, and $\kappa'=\varepsilon_R/\varepsilon_L$. Here $\varepsilon_R$ is the minimum of the potential for a pair of parallel particles placed side-by-side ($\hat{\mathbf{r}}_{12}\cdot\boldsymbol{\omega}_1=\hat{\mathbf{r}}_{12}\cdot\boldsymbol{\omega}_2=0$) and $\varepsilon_L$ is the minimum for a pair of parallel particles placed end-to-end ($\hat{\mathbf{r}}_{12}\cdot\boldsymbol{\omega}_1=\hat{\mathbf{r}}_{12}\cdot\boldsymbol{\omega}_2=1$). The pair interaction potential due to the charges is decomposed into three terms [236]

$$U_{CO}(\mathbf{r}_{12},\boldsymbol{\omega}_1,\boldsymbol{\omega}_2) = U_{cc}(\mathbf{r}_{12})+U_{ct}(\mathbf{r}_{12},\boldsymbol{\omega}_1,\boldsymbol{\omega}_2)+U_{tt}(\mathbf{r}_{12},\boldsymbol{\omega}_1,\boldsymbol{\omega}_2), \qquad (2.12)$$

with

$$\begin{aligned} U_{cc}(\mathbf{r}_{12}) &= \gamma_{cc}\frac{e^{-r_{12}/\lambda_D}}{r_{12}}, \qquad (2.13)\\ U_{ct}(\mathbf{r}_{12},\boldsymbol{\omega}_1,\boldsymbol{\omega}_2) &= \gamma_{ct}\left[\frac{e^{-r_{c+}/\lambda_D}}{r_{c+}}+\frac{e^{-r_{+c}/\lambda_D}}{r_{+c}}+\frac{e^{-r_{c-}/\lambda_D}}{r_{c-}}+\frac{e^{-r_{-c}/\lambda_D}}{r_{-c}}\right], \qquad (2.14)\\ U_{tt}(\mathbf{r}_{12},\boldsymbol{\omega}_1,\boldsymbol{\omega}_2) &= \gamma_{tt}\left[\frac{e^{-r_{++}/\lambda_D}}{r_{++}}+\frac{e^{-r_{+-}/\lambda_D}}{r_{+-}}+\frac{e^{-r_{-+}/\lambda_D}}{r_{-+}}+\frac{e^{-r_{--}/\lambda_D}}{r_{--}}\right]. \qquad (2.15) \end{aligned}$$

Here the distances between the charges are given by

$$r_{c\pm} = |\mathbf{r}_{12}\mp\boldsymbol{\omega}_2 D|, \quad r_{\pm c}=|\mathbf{r}_{12}\pm\boldsymbol{\omega}_1 D|, \quad r_{\pm\pm}=|\mathbf{r}_{12}\pm\boldsymbol{\omega}_1 D\mp\boldsymbol{\omega}_2 D|, \qquad (2.16)$$

where $D$ is distance between the center of the particle and the charges at the tails of the particle (see Fig. 2.7). The Debye screening length is denoted as $\lambda_D$ and $\gamma_{cc}=z_c z_c e^2/\varepsilon$, $\gamma_{ct}=z_c z_t e^2/\varepsilon$, $\gamma_{tt}=z_t z_t e^2/\varepsilon$ characterise the energy scale. Here the sites at the center and the tails of the particle carry the charges $z_c e$ and $z_t e$, respectively. The permittivity is denoted as $\varepsilon$. Any counterions are considered at the linear response level, i.e. they screen the electrostatic potential on a scale given by the Debye screening length.

The number density of the center of mass of a particle at a point $\mathbf{r}$ with an orientation $\boldsymbol{\omega}$ is written as $\varrho(\mathbf{r},\boldsymbol{\omega})=\varrho\, f(\mathbf{r},\boldsymbol{\omega})$, where $f(\mathbf{r},\boldsymbol{\omega})$ represents a dimensionless distribution

function and $\varrho = N/V$ is the total number density. Here $N$ is the number of particles and $V$ is volume. The equilibrium density profile minimises the grand potential functional (see e.g. Refs.[133, 183–185, 479] and references therein):

$$\Omega[\{f(\mathbf{r},\boldsymbol{\omega})\},\varrho,T,\mu] = k_BT\varrho\left(\ln(4\pi\Lambda^3\varrho)-1\right)V + F[\{f(\mathbf{r},\boldsymbol{\omega})\},\varrho,T] - \mu\varrho V, \tag{2.17}$$

where $\mu$ is the chemical potential and $\Lambda$ is the thermal de Broglie wavelength. The excess (over the ideal gas) free energy functional $F[\{f(\mathbf{r},\ \boldsymbol{\omega})\},\varrho,T]$ is in general a very complicated, highly non-trivial object, because it is a characterising property of a many-body problem. $F[\{f(\mathbf{r},\boldsymbol{\omega})\},\varrho,T]$ is dealt with in various ways, which specify the explicit forms of the theory. The Parsons and Lee approach [253, 345] is used in Ref. [236] for the hard core interaction together with a perturbation expansion for the long-ranged interaction:

$$\begin{aligned} F[\{f(\mathbf{r},\boldsymbol{\omega})\},\varrho,T] &= k_BT\varrho\int d\mathbf{r}_1\,d\boldsymbol{\omega}_1\,f(\mathbf{r}_1,\boldsymbol{\omega}_1)\ln\left(f(\mathbf{r}_1,\boldsymbol{\omega}_1)\right) \\ &+ \frac{\varrho}{2}\int d\mathbf{r}_1\,d\boldsymbol{\omega}_1\,f(\mathbf{r}_1,\boldsymbol{\omega}_1)\left(U_{ref}[\{f(\mathbf{r},\boldsymbol{\omega})\},\varrho,T] + U_{exc}[\{f(\mathbf{r},\boldsymbol{\omega})\},\varrho,T]\right) \end{aligned} \tag{2.18}$$

with

$$U_{ref}[\{f(\mathbf{r},\boldsymbol{\omega})\},\varrho,T] = -k_BTJ(\varrho)\int d\mathbf{r}_2\,d\boldsymbol{\omega}_2\,f_M(\mathbf{r}_{12},\boldsymbol{\omega}_1,\boldsymbol{\omega}_2)f(\mathbf{r}_2,\boldsymbol{\omega}_2)\,, \tag{2.19}$$

$$U_{exc}[\{f(\mathbf{r},\boldsymbol{\omega})\},\varrho,T] = \varrho\int d\mathbf{r}_2\,d\boldsymbol{\omega}_2\,\left(1-f_M(\mathbf{r}_{12},\boldsymbol{\omega}_1,\boldsymbol{\omega}_2)\right)U(\mathbf{r}_{12},\boldsymbol{\omega}_1,\boldsymbol{\omega}_2)f(\mathbf{r}_2,\boldsymbol{\omega}_2)\,. \tag{2.20}$$

Here $f_M(\mathbf{r}_{12},\boldsymbol{\omega}_1,\boldsymbol{\omega}_2)$ is the Mayer function of the hard core pair interaction potential between two particles. The Mayer function equals -1 if the particles overlap, i.e. $r_{12} < R\,\sigma(\hat{\mathbf{r}}_{12},\boldsymbol{\omega}_1,\boldsymbol{\omega}_2)$, and is zero otherwise. Note that the range parameter $R\,\sigma(\hat{\mathbf{r}}_{12},\ \boldsymbol{\omega}_1,\boldsymbol{\omega}_2)$ given by Eq. (2.10) is, to a first approximation, the contact distance between two hard ellipsoids of elongation $\kappa$ with orientations $\boldsymbol{\omega}_1$ and $\boldsymbol{\omega}_2$ (see Ref. [81]). $U_{ref}[\{f(\mathbf{r},\boldsymbol{\omega})\},\varrho,T]$ and $U_{exc}[\{f(\mathbf{r},\boldsymbol{\omega})\},\varrho,T]$ are the effective reference and excess potential, respectively, acting on a particle due to the presence of the remaining particles. The Parsons-Lee modification amounts to scaling the reference Onsager free energy functional by the function (see Eq. (2.19))

$$J(\varrho) = \frac{1}{V_p}\frac{4\eta-3\eta^2}{4(1-\eta)^2}, \tag{2.21}$$

which incorporates the contributions of many-body hard core interactions in an approximate way. Here $\eta = \varrho V_p$ and $V_p = \pi LR^2/6$ are the volume fraction and the particle volume, respectively. In the case of $J(\varrho) = \varrho$ the effective reference potential $U_{ref}[\{f(\mathbf{r},\boldsymbol{\omega})\},\varrho,T]$ reduces to the original second-virial Onsager theory. The Parsons-Lee approach for thermodynamic properties of the isotropic and nematic phases of fluids consisting of hard ellipsoids or spherocylinders has been found to be in agreement with simulation data [71, 144, 294, 397].

The equilibrium distribution function $f(\mathbf{r},\boldsymbol{\omega})$ is obtained from minimising the excess free energy functional $F(\varrho,T,[f])$ with respect to $f(\mathbf{r},\boldsymbol{\omega})$. From $f(\mathbf{r},\omega)$ one obtains the

order parameters

$$\begin{aligned} S_2 &= \langle P_2(\cos\vartheta)\rangle\,, \\ W_0 &= \left\langle \cos\left(2\pi z d^{-1}\right)\right\rangle, \\ W_2 &= \left\langle P_2(\cos\vartheta)\cos\left(2\pi z d^{-1}\right)\right\rangle, \end{aligned} \tag{2.22}$$

where $P_2(x) = (3x^2 - 1)/2$ is the Legendre polynomial of degree 2 and $d$ is the layer spacing along the $z$ axis in the case of a smectic A phase. They serve to distinguish isotropic ($S_2 = W_0 = W_2 = 0$), nematic ($S_2 \neq 0$ and $W_0 = W_2 = 0$) and smectic A ($S_2, W_0, W_2 \neq 0$) structures. By introducing further order parameters it would in principle also be possible to describe other liquid crystalline and crystalline structures. However, these additional structures are strongly non-uniform and they occur at high densities, such that they are not expected to be well described by the approach in Ref. [236], i.e. one is actually restricted to the three order parameters given in Eq. (2.22).

At first fluid phase equilibria are discussed for non-spherical particles with the intermolecular pair potential given by Eq. (2.8). It is convenient to examine the phase behaviour in terms of the reduced temperature $T^* = k_B T/\varepsilon_0$, the packing fraction $\eta = \varrho V_p$, the dimensionless strengths of the Coulomb interactions $E_{cc} = \gamma_{cc}/(\varepsilon_0 R)$, $E_{ct} = \gamma_{ct}/(\varepsilon_0 R)$, $E_{tt} = \gamma_{tt}/(\varepsilon_0 R)$ and the reduced Debye screening length $\lambda_D^* = \lambda_D/R$.

The phase behaviour of uncharged particles with the length-to-breadth ratio $\kappa = L/R = 2$ and the anisotropy parameter $\kappa' = 2$ of the Gay-Berne potential (solid lines in Figs. 2.8 (a)–(c)) is discussed. The fluid is positionally and orientationally disordered ($S_2 = W_0 = W_2 = 0$) in the isotropic phase (I) at low packing fractions $\eta$ and high enough temperatures $T^*$. Upon increasing the packing fraction, a first-order phase transition to a smectic A phase ($S_A$) with $S_2, W_0, W_2 \neq 0$ occurs. The isotropic fluid undergoes a vapour-liquid separation below the critical temperature $T_c^*$ marked by the solid circles in Figs. 2.8 (a)–(c). Upon increasing the packing fraction, the phase sequence is vapour (V), isotropic liquid, and smectic A for temperatures $T_t^* < T^* < T_c^*$. Here $T_t^*$ is the triple point temperature (thin solid line in Figs. 2.8 (a)–(c)) at which the three phases V, I, and $S_A$ coexist. Increasing the anisotropy parameter $\kappa'$ of the Gay-Berne potential at fixed $\kappa$ leads to a shift of the vapour-liquid coexistence curve to lower temperatures as is apparent from Fig. 2.8 (a) where the phase diagram is shown for $\kappa' = 2$ (solid line) and $\kappa' = 5$ (dotted line). Moreover, the smectic region is pushed to lower packing fractions as $\kappa'$ increases. High values of $\kappa'$ favour the side-by-side configuration over the end-to-end configuration of two parallel particles. Therefore, the packing fractions of the coexisting isotropic and smectic A phases decrease upon increasing $\kappa'$. The relative stability of the side-by-side configuration decreases as $\kappa'$ is lowered and for $\kappa' = 1$ all configurations are equally stable for parallel particles, i.e. $\varepsilon(\mathbf{r}_{12}, \boldsymbol{\omega}_1, \boldsymbol{\omega}_2) = \varepsilon_0$ for $\kappa' = 1$ and $\boldsymbol{\omega}_1 \parallel \boldsymbol{\omega}_2$ in Eq. (2.11).

Figure 2.8 (b) demonstrates that the width of the I-$S_A$ phase transition broadens upon increasing the length-to-breadth ratio of the particles from $\kappa = L/R = 2$ (solid line) to $\kappa = 4$ (dash-dotted line). Furthermore, the vapour-liquid coexistence curve is metastable with respect to the I-$S_A$ coexistence for $\kappa = 4$. More details concerning the influence of the length-to-breadth ratio of the particles and the anisotropy parameter of the Gay-Berne potential on the fluid phase behaviour can be found in Refs. [66, 98].

Now the influence of two like charges ($E_{tt} = 45, \lambda_D^* = 50$) located at the tails ($D/R = 0.9$ for $\kappa = D/R = 2$ is examined, see Fig. 2.7) on the fluid phase behaviour (dashed line in Fig. 2.8(c)). The vapour-liquid critical temperature is seen to decrease with increasing the

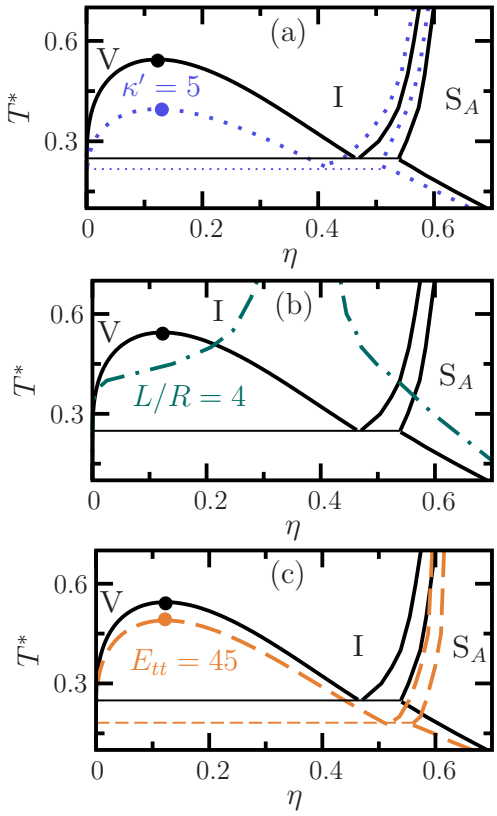


Figure 2.8: The influence of the anisotropy parameter of the Gay-Berne potential $\kappa'$ in panel (a), the length-to-breadth ratio of the particles $\kappa = L/R$ in panel (b) and like charges at the tails of the particles in panel (c) on the fluid phase behaviour of an ionic liquid crystal consisting of ellipsoidal particles (see Fig. 2.7). The phase diagrams are shown as functions of the packing fraction $\eta$ and the reduced temperature $T^*$. The solid lines in panels (a), (b), and (c) represent the phase diagram for uncharged particles with $\kappa = 2$ and $\kappa' = 2$, while the dotted and dash-dotted lines show the phase diagram for uncharged particles with $\kappa = 2$, $\kappa' = 5$ in panel (a) and $\kappa = 4$, $\kappa' = 2$ in panel (b). The dashed line in panel (c) represents the phase diagram for charged particles with $\kappa = 2$, $\kappa' = 2$, $D/R = 0.9$, $E_{tt} = 45$, and $\lambda_D^* = 50$. The solid horizontal lines in panels (a), (b) and (c) mark the coexistence of a vapour phase (V) with an isotropic liquid phase (I) and a smectic A phase ($S_A$) for the uncharged particles with $\kappa = 2$ and $\kappa' = 2$, while the solid circles mark the vapour-liquid critical point. The lower circles in panels (a) and (c) denote the vapour-liquid critical points corresponding to the phase diagrams represented by the dotted and dashed lines, respectively. Vapour-liquid coexistence is metastable for the length-to-breadth ratio $\kappa = 4$ in panel (b). The dashed horizontal line in panel (c) corresponds to V-I-$S_A$ three phase coexistence of the fluid consisting of charged particles. (See Ref. [236])

Coulomb interaction strength and the I-$S_A$ coexistence region is shifted to higher packing fractions. In the high-temperature limit the thermodynamic properties of the fluid are dominated by the repulsive steric interactions, and the I-$S_A$ phase transition tends to that of the corresponding hard core fluid, with packing fractions $\eta_I = 0.61$ and $\eta_{S_A} = 0.63$ at I-$S_A$ phase coexistence. The decrease of the vapour-liquid critical temperature is due to

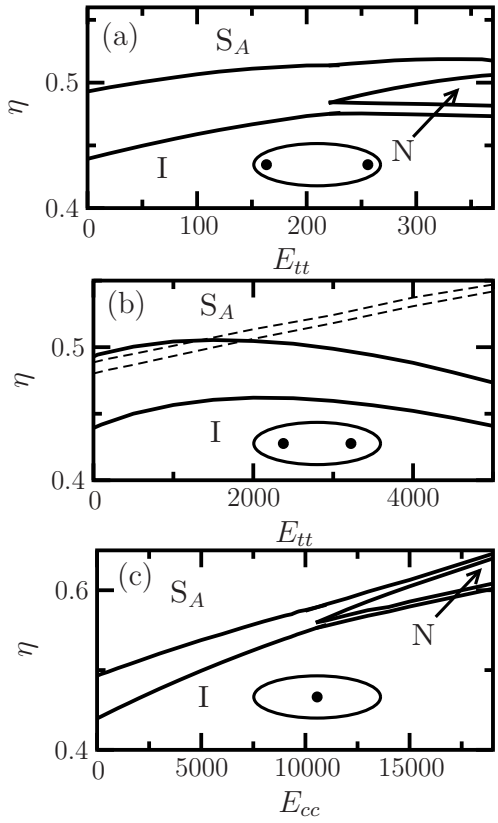


Figure 2.9: The influence of the location of two like charges on the fluid phase behaviour of an ionic liquid crystal consisting of charged ellipsoidal particles with length-to-breadth ratio $\kappa = L/R = 3$ at temperature $T^* = 1.5$. The anisotropy parameter of the Gay-Berne potential and the Debye screening length are fixed to $\kappa' = 8$ and $\lambda_D^* = 50$, respectively. Two like charges are located at the distance $D = 1.4R$ and $D = R$ from the center of the particles in panels (a) and (b), respectively, while a single charge is located at the center of the particles in panel (c). Schematic illustrations of the shape of the particles and the location of the charges (solid dots) are shown in the figures. The phase diagrams are plotted as functions of the Coulomb pair interaction strengths $E_{tt}$ or $E_{cc}$, and the packing fraction $\eta$. The solid lines denote the phase boundaries of thermal equilibrium of an isotropic (I), nematic (N), and smectic A ($S_A$) phase, while the dashed lines in panel (b) mark metastable isotropic-nematic phase coexistence. (See Ref. [236])

the repulsive Coulomb pair interaction between the like charged tails of the particles.

Next the effect of varying the location of charges on the particles with a fixed length-to-breadth ratio $L/R = 3$ and at a fixed temperature $T^* = 1.5$ is examined. Fluid phases are shown in Fig. 2.9 as functions of the strength of the Coulomb pair interactions $E_{tt}$ or $E_{cc}$, and the packing fraction $\eta$ for three different locations of the charges. Two like charges are located at the distance $D = 1.4R$ and $D = R$ from the center of the particles in Fig. 2.9(a) and (b), respectively, while a single charge is located at the center of the particles in Fig. 2.9(c). The length-to-breadth ratio and temperature have been chosen such that the fluids consisting of uncharged particles (i.e. $E_{tt} = E_{cc} = 0$) are isotropic at low packing fractions and a phase transition to the smectic A phase is observed at higher packing fractions. There is an important difference between the phase behaviour

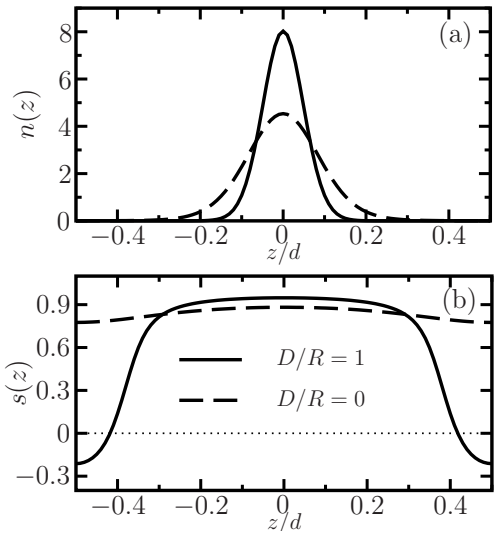


Figure 2.10: Normalised, orientationally averaged density profile $n(z)$ [Eq. (2.23)] in panel (a) and relative nematic order parameter $s(z)$ [Eq. (2.24)] in panel (b) of an ionic liquid crystal along the $z$-axis in the smectic A phase, where $d$ is the layer spacing. The solid lines represent the profiles for particles with two like charges located at the distance $D = R$ from the center of the particles (see Fig. 2.9(b)), while the dashed lines show the profiles for particles with a single charge located at the center of the particles (see Fig. 2.9(c)). The model parameters are fixed to $\kappa = L/R = 3$, $\kappa' = 8$, $T^* = 1.5$, $\eta = 0.67$, and $E_{tt} = E_{cc}/4 = 4000$. Therefore, the particles in panels (a) and (b) carry the same total charge. (See Ref. [236])

of fluids consisting of particles with charges located at $D = 1.4R$ and at $D = R$. While for $D = R$ the smectic A phase is the only stable phase at high packing fractions (see Fig. 2.9(b)), nematic phase ordering (N) with $S_2 \neq 0$ and $W_0 = W_2 = 0$ is found for $D = 1.4R$ (see Fig. 2.9(a)). In this case the nematic phase is stable for strong Coulomb pair interaction down to $E_{tt} = 215$ at the I-N-$S_A$ triple point. In the case of particles with two like charges located at the distance $D = R$ from the center, there is no stable nematic phase even at higher Coulomb interaction strengths. In this case the packing fractions of the coexisting isotropic and smectic A phases (solid lines in Fig. 2.9(b)) decrease with increasing Coulomb interaction strength $E_{tt}$, whereas the packing fractions of the metastable isotropic-nematic phase coexistence (dashed lines in Fig. 2.9 (b)) increase.

Surprisingly, the nematic phase is stable in the case of a fluid consisting of particles with a single charge located at the center as is shown in Fig. 2.9(c). The smectic A phase is preempted by the nematic phase which is stable above the Coulomb interaction strength $E_{cc} = 10465$ at the I-N-$S_A$ triple point.

In order to understand the influence of the location of two like charges on the fluid phase behaviour it is instructive to consider a set of position-dependent order parameters which quantifies the deviation of the number density from isotropy [179]. The normalised, orientationally averaged density profile

$$n(z) = 2\pi \int_0^\pi d\vartheta \, \sin\vartheta \, f(z, \vartheta) \tag{2.23}$$

and the position-dependent, relative nematic order parameter

$$s(z) = \frac{\pi}{n(z)} \int_0^\pi d\vartheta \, \sin\vartheta \, (3\cos^2\vartheta - 1) f(z, \vartheta) \tag{2.24}$$

are displayed in Fig. 2.10(a) and (b), respectively. The solid lines show the profiles for particles with two like charges located at the distance $D = R$ from the center of the particles (see Fig. 2.9(b)), while the dashed lines display the profiles for particles with a single charge located at the center of the particles (see Fig. 2.9(c)). The packing fraction is fixed to $\eta = 0.67$ and the Coulomb pair interaction strengths are given by $E_{tt} = E_{cc}/4 = 4000$. Hence the smectic A phase is stable and the particles in panels (a) and (b) carry the same total charge. The order parameter profiles are periodic functions with layer spacings $d \approx 3.8R$ and $d \approx 3.0R$ for the particles with two like charges at the tails (solid lines) and the particles with a single charge located at the center (dashed lines), respectively. The density profiles of the centers of the particles exhibit maxima in the center of the layers at $z = 0$ as is apparent from Fig. 2.10(a). Moreover, the density distribution along the layer axis is sharper for the particles with two like charges at the tails than that for the particles with a single charge located at the center.

Figure 2.10(b) demonstrates that there is a qualitative difference between the relative nematic order parameter profiles for particles with two like charges at the tails (solid lines) and the particles with a single charge located at the center (dashed lines). Whereas $s(z)$ is rather independent of $z$ in the latter case, the relative nematic order parameter profile exhibits pronounced oscillations along the $z$ axis in the former case, where particles located between the layers at $|z/d| \gtrsim 0.4$ are oriented with their main body mainly perpendicular to the $z$ axis, i.e. $s(z) < 0$. For comparison it is recalled that the value of the nematic order parameter is $s(z) = -0.5$ and $s(z) = 1.0$ for perfect perpendicular and parallel alignment to the $z$ axis, respecticely. The predominantly perpendicular orientation of particles with charges at the tails located in between the smectic layers can be understood in terms of a minimisation of the electrostatic repulsion due to a maximised distance from the particles in the smectic layers. For particles with the charge in the center the electrostatic energy is independent of the orientation; hence a parallel alignment of particles in between smectic layers is favourable, as non-parallel orientations would increase the free energy due to an increase in the layer spacing. The latter case is comparable with the results of Ref. [445] on spherocylinders (see Fig. 2 of Ref. [445]), where the majority of inter-layer particles is aligned parallel to the layer normal. The bimodal orientational distribution described in Ref. [445] is also expected to be found in the present situation.

Now the effect of varying the length-to-breadth ratio $\kappa = L/R$ is studied for charged particles with two like charges located at a fixed distance $L/2 - D = 0.1R$ from the end of the particles (see Fig. 2.7). Fluid phases are shown in Fig. 2.11 as functions of the strength of the Coulomb pair interaction$E_{tt}$ and the packing fraction $\eta$ for a fixed temperature $T^* = 2$. The length-to-breadth ratio is $\kappa = 3$ and $\kappa = 5$ in Fig. 2.11(a) and (b), respectively. Qualitatively similar types of phase behaviour are exhibited by both systems. The fluids consisting of uncharged particles, i.e. $E_{tt} = 0$, are isotropic at low packing fractions and a phase transition to the smectic A phase is observed at higher packing fractions. Upon increasing the Coulomb pair interaction strength $E_{tt}$ stable nematic islands in the phase diagrams are found. This nematic phase is bounded below and above by isotropic and smectic A phases, respectively. Moreover, the location

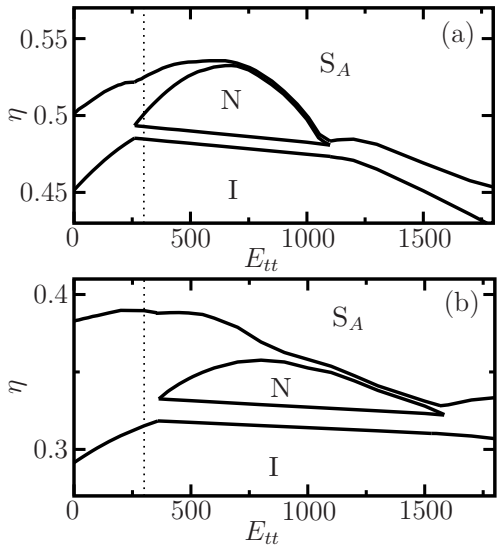


Figure 2.11: The influence of the length-to-breadth ratio $\kappa = L/R$ on the fluid phase behaviour of an ionic liquid crystal consisting of charged ellipsoidal particles with two like charges located at a fixed distance $L/2 - D = 0.1R$ from the end of the particles (see Fig. 2.7). The length-to-breadth ratio is $\kappa = 3$ in panel (a) and $\kappa = 5$ in panel (b). The anisotropy parameter of the Gay-Berne potential and the Debye screening length are fixed to $\kappa' = 8$ and $\lambda_D^* = 50$, respectively. The phase diagrams are plotted as functions of the Coulomb pair interaction strength $E_{tt}$ and the packing fraction $\eta$ for the fixed temperature $T^* = 2$. The solid lines denote the phase boundaries of thermal equilibrium of an isotropic (I), nematic (N), and smectic A ($S_A$) phase. In Fig. 2.12 phase diagrams are shown as functions of the packing fraction and the temperature for the Coulomb pair interaction strength indicated by the dotted lines. (See Ref. [236])

of the nematic region is seen to move to higher Coulomb pair interaction strength and lower volume fraction upon increasing the length-to-breadth ratio. The nematic phase disappears at high values of the Coulomb pair interaction strength when the repulsive steric interaction is less important. The competition of the steric interaction and the Coulomb pair interaction leads to the existence of a stable nematic phase for intermediate values of $E_{tt}$.

Packing fraction-temperature projections of the fluid phase diagrams for the systems with $E_{tt} = 300$ (see the dotted lines in Fig. 2.11) are shown in Fig. 2.12. The stable isotropic, nematic and smectic A regions are clearly visible for the fluid consisting of the smaller particles in Fig. 2.12 (a). For the larger particles the isotropic-nematic coexistence region is metastable with respect to the I-$S_A$ coexistence (dashed lines in Fig. 2.12(b)). For both systems, the low temperature part of the phase diagram is dominated by a wide two-phase region where the $S_A$ phase is in equilibrium with an isotropic phase. Note that the behaviour is reversed for $E_{tt}^{(l)} > E_{tt} > E_{tt}^{(s)}$, where $E_{tt}^{(s)} = 1099$ and $E_{tt}^{(l)} = 1570$ is the second triple point for the smaller and larger particles, respectively (see Fig. 2.11(a)). Increasing the length-to-breadth ratio induces the nematic phase in this case.

The model of ellipsoidal particles with point charges may be compared with models of spherocylinders with line charges [128, 163, 238]. The presence of a direct isotropic-smectic transition for small length-to-breadth ratios $\kappa = L/R$ and charges $E_{tt}$, the decrease of the

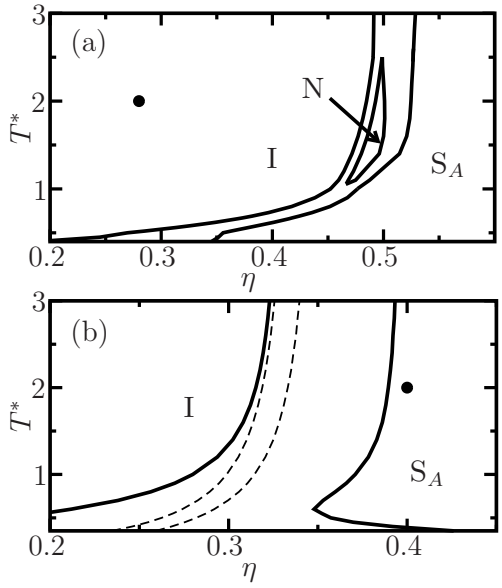


Figure 2.12: Phase diagrams of the same fluids as in Fig. 2.11 in the packing fraction ($\eta$)-temperature ($T^*$) plane. The Coulomb pair interaction strength is given by $E_{tt} = 300$ as indicated by the dotted lines in Fig. 2.11. The length-to-breadth ratio is $\kappa = 3$ in panel (a) and $\kappa = 5$ in panel (b). The solid lines denote the phase boundaries of thermal equilibrium of an isotropic (I), nematic (N), and smectic A ($S_A$) phase, while the dashed lines in panel (b) mark metastable isotropic-nematic phase coexistence. In panel (a) and (b) the solid circles denote two state points with equal temperature and pressure. (See Ref. [236])

packing fraction at the transition upon increasing $\kappa$, as well as the increase of the packing fraction at the transition upon increasing $E_{tt}$ (see Fig. 2.11) are in agreement with the trends for sphereocylinders as displayed in Figs. 2 and 3 of Ref. [238]. Hence there is qualitative similarity between the model of point charges at the particle tails and charged spherocylinders with line charges.

Next the influence of the Coulomb interaction strength on the phase behaviour is considered. The locations of the various ordering transitions in the case of a fluid consisting of ellipsoidal particles with a single charge located in the center of the particles and the length-to-breadth $\kappa = 3$ are summarised in Fig. 2.13 for three different Coulomb interaction strengths $E_{cc}$. From the phase behaviour of the systems shown in Fig. 2.13, it is apparent that the nematic phase becomes stable with increasing Coulomb interaction strength. There are I-N-$S_A$ triple points for the Coulomb interaction strengths $E_{cc} = 4500$ and $E_{cc} = 15000$ in Figs. 2.13(b) and (c), respectively, while the I-N coexistence region is metastable in the case of the weaker Coulomb interaction strength considered in Fig. 2.13(a). In the high-temperature limit the thermodynamic properties of the fluids are dominated by the repulsive steric interactions, and the I-$S_A$ phase transition tends to that of the corresponding hard core fluid. As expected the isotropic region becomes more extensive as the Coulomb interaction strength is increased. In the case of a large Coulomb interaction strength the long-ranged pair potential is rather independent of the orientations of the particles because the charges are located in the center of the ellipsoids. Therefore the locations of phase transitions from the isotropic phase to orientationally

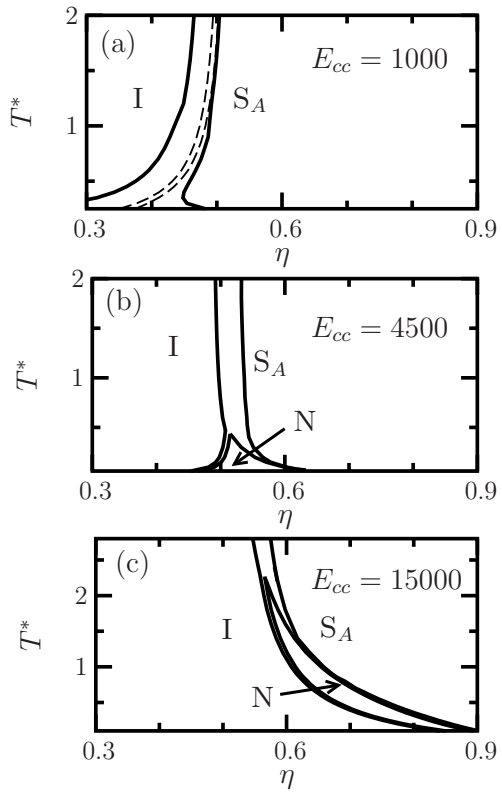


Figure 2.13: The influence of the Coulomb pair interaction strength $E_{cc}$ on the fluid phase behaviour of an ionic liquid crystal consisting of ellipsoidal particles ($\kappa = L/R = 3$) with a single charge located in the center of each particle. The phase diagrams are shown as functions of the packing fraction $\eta$ and the reduced temperature $T^*$. The solid lines denote the phase boundaries of thermal equilibrium of an isotropic (I), nematic (N) and smectic A ($S_A$) phase, while the dashed lines in panel (a) mark metastable isotropic-nematic phase coexistence. The anisotropy parameter of the Gay-Berne potential and the Debye screening length are given by $\kappa' = 8$ and $\lambda_D^* = 50$, respectively. (See Ref. [236])

ordered phases in the low temperature region are shifted to higher packing fractions upon increasing the Coulomb interaction strength.

In general the total number density of both thermotropic liquid crystals (see e.g. Ref. [295]) and colloidal suspensions consisting of charged nonspherical particles (see e.g. Ref. [114]) is smaller in the isotropic phase than in the coexisting nematic or smectic phase similar to our findings presented in Figs. 2.8, 2.9 and 2.11–2.13. Nevertheless, it is worthwhile to mention that the density of hard platelike particles in a binary mixture of thick and thin platelets can be larger in the isotropic phase than in the coexisting nematic phase depending on the chemical potentials [443]. This remarkable phenomenon of isotropic-nematic density inversion has been investigated using a two-component density functional theory for hard nonspherical particles [34].

In Ref. [190] isotropic and smectic phases of molecules consisting of two pyridinium head groups and a biphenylene core (see Fig. 2.14(a)) have been observed. Increasing the length of the alkyl chains, i.e. increasing $n$ in Fig. 2.14(a), stabilises the smectic phase. Both the transition temperature from the isotropic to the smectic phase and the layer spacing in the smectic phase increase with increasing length of the alkyl chains. These

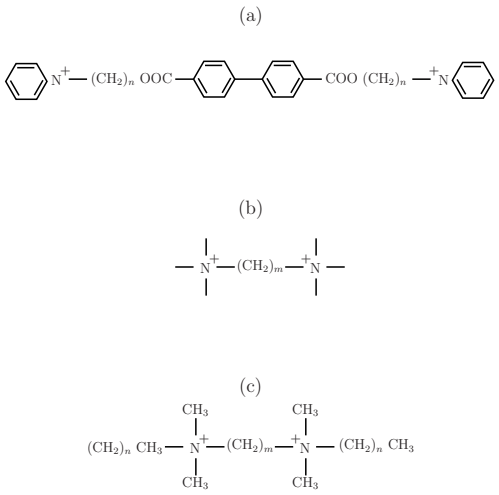


Figure 2.14: Chemical structure of dipolar amphiphiles with two pyridinium head groups and a biphenylene core in (a), diquaternary ammonium salts in (b) and diammonium salts in (c). These molecules exhibit liquid crystalline phases [147, 190, 235]. (See Ref. [236])

results agree with the theoretical results presented in Figs. 2.11 and 2.12. Increasing the length $L$ of particles with two like charges located at a fixed distance $L/2-D$ from the end of the particles (see Fig. 2.7) has a stabilising effect on the smectic phase. For example, the isotropic phase is stable for particles with $\kappa = 3$ at the state point denoted by the solid circle in Fig. 2.12(a), while the smectic A phase is s stable for larger particles with $\kappa = 5$ at the same temperature and pressure marked by the solid circle in Fig. 2.12(b). Moreover, the calculated layer spacing $d$ increases upon increasing $L$.

In Ref. [235] the phase behaviour of $\alpha-\omega$ diquaternary ammonium salts has been investigated (see Fig. 2.14(b)). By increasing the spacer length between the quaternary nitron atoms, more stable smectic phases were obtained in agreement with both the theoretical results shown in Figs. 2.11 and 2.12 as well as the aforementioned experimental study on dipolar amphiphiles with two pyridinium head groups and a biphenylene core [190].

It is known experimentally that slight changes of the molecular structure influence the occurrence of mesomorphism in ionic liquids [50]. Chemical details are in principle included in the parameters; however, relating the model parameters to the molecular structure is complicated. On the other hand, the experimentally found preference of ionic liquid crystals for the smectic A mesophase [50] is in agreement with the results displayed in Fig. 2.11 if one realizes that typical coupling strengths $E_{tt} = \ell_B/R$, where $\ell_B$ denotes the Bjerrum length, are not expected to exceed a value of 100.

Thermotropic and lyotropic mesomorphism has been observed for the diammonium salts shown in Fig. 2.14(c) [147]. Interestingly, a stable nematic phase has been found for small spacer length $(CH_2)_m$. This nematic phase disappeared upon increasing the spacer length similar to the theoretical findings shown in Figs. 2.12(a) and (b). Moreover, it is worthwhile to mention that a decrease of the layer spacing of the smectic phase with increasing temperature has been observed for various ionic liquid crystals [50] in agreement with the results of the present theoretical approach.

The main trends in the bulk phase behaviour of ionic liquid crystals obtained within the model above lead to the following general properties of this type of ionic complex fluids:

(1) The phase diagrams for representative examples of liquid crystals involve a vapour, an isotropic liquid and a smectic A phase (see Fig. 2.8). Increasing the anisotropy leads to a shift of the vapour-liquid coexistence curve to lower temperatures (see Fig. 2.8(a)). The width of the isotropic to smectic phase transition broadens upon increasing the length-to-breadth ratio of the particles (see Fig. 2.8(b)).

(2) There is a pronounced dependence of the phase behaviour on the location of two like charges on the ellipsoidal particles (see Fig. 2.9). While for small distances from the center the smectic A phase is the only stable phase at high packing fractions (see Fig. 2.9(b)), nematic phase ordering is found for large distances (see Fig. 2.9(a)). Moreover, the nematic phase is stable in the case of a fluid consisting of particles with a single charge located at the center (see Fig. 2.9(c)). Whereas the relative nematic order parameter profile $s(z)$ is rather independent of $z$ in the smectic A phase of particles with a single charge located at the center, it exhibits pronounced oscillations along the $z$ axis in the case of two like charges at the tails of the particles (see Fig. 2.10(b)).

(3) Increasing the length of the particles with two like charges located at a fixed distance from the center of the particles has a stabilising effect on the smectic A phase in agreement with earlier experimental findings (see Figs. 2.11 and 2.12). Moreover, the calculated layer spacing in the smectic A phase increases upon increasing the length. With increasing the Coulomb pair interaction strength stable nematic islands in the phase diagrams are found (see Fig. 2.11). This nematic phase is bounded by isotropic and smectic A phases. Moreover, the location of the nematic region moves to higher Coulomb pair interaction strength and lower volume fraction upon increasing the length of the particles.

(4) For particles with a single charge located in the center, the isotropic region in the phase diagram becomes more extensive as the Coulomb interaction strength is increased (see Fig. 2.13) similar to earlier theoretical findings for charged platelike particles [35] (see Sec. 4.5). Moreover, a nematic phase becomes stable with increasing the Coulomb interaction strength (see Figs. 2.13(b) and (c)). In the case of a large Coulomb interaction strength the long-ranged pair potential is rather independent of the orientations of the particles because the charges are located in the center of the ellipsoids.

## 2.4 Charged colloids

It is known from experiments [260] and computer simulations [28, 53, 200, 201, 289, 489] that under carefully chosen conditions mixtures of oppositely charged colloids exhibit a fluid phase and one or more crystalline phases, instead of random aggregation. However, the location of these phases as well as the types of crystalline phases present depend sensitively on the details of the interaction potentials, particularly on the range of the screened Coulomb interaction (Debye length).

Rather simple systems with a low dimension of the phase diagram are present for binary colloidal mixtures. In the following an example is discussed for the case of oppositely charged, equally-sized colloids, whose global phase diagrams in terms of the temperature, the pressure and the composition depends only on the Debye length as a single additional parameter [41]. The experiments in Ref. [260], e.g., have been performed with positively charged polymethylmethacrylate (PMMA) and negatively charged silica particles suspended in an indexed-matched mixture of cyclohexyl bromide (CHB) and cis-decalin, and the screening length has been adjusted by means of addition of tetrabutylammonium

| structure | c/d | $K_c$ | $\phi_{\rm cp}$ |
|---|---|---|---|
| $CaF_2$ | c | 3 | $3\pi\sqrt{3}/32$ |
| CsCl | c | 2 | $\pi\sqrt{3}/8$ |
| CuAu | c | 2 | $\pi(2+(c/a)^2)\sqrt{1+2(a/c)^2}/24$ |
| $Cu_3Au$ | c | 4 | $\pi\sqrt{2}/6$ |
| $LS_6^{\rm fcc}$ | c | 7 | $7\pi\sqrt{2}/48$ |
| NaCl | c | 2 | $\pi/6$ |
| NbP | c | 8 | $\pi\sqrt{2}/6$ |
| rbcc | d | 1 | $\pi\sqrt{3}/8$ |
| rfcc | d | 1 | $\pi\sqrt{2}/6$ |

Table 2.2: Candidate solid structures chosen on the basis of Refs. [200, 201, 260, 289]. The second column indicates a crystal ("c") or a substitutionally disordered solid ("d"). The third and the fourth columns give the numbers of particles per unit cell $K_c$ and the closed-packed packing fractions $\phi_{\rm cp}$, respectively. The CuAu structure with the aspect ratio $c/a \in [1, \sqrt{2}]$ of the underlying tetragonal lattice degenerates to the CsCl structure in the case $c/a = 1$. The $LS_6^{\rm fcc}$ structure has been introduced in Ref. [202]. The NbP structure was called "tetragonal" in Ref. [201]. (See Ref. [41])

bromide (TBAB). The approach of Ref. [41], which has been inspired by Ref. [448] on the restricted primitive model (RPM), is based on finding the phase with minimal Gibbs free energy within a set of candidate structures, where the Gibbs free energy is evaluated within a mean-field-like formalism which interpolates between the hard-sphere limit at high temperatures and a Madelung-type description at low temperatures.

Table 2.2 lists the candidate solid structures considered in Ref. [41]. This choice is based on the structures found in computer simulation studies of the cases $x = 0$ (see Ref. [200]) and $\kappa a = 3, x = 1/2$ (see Ref. [201]), as well as on Refs. [260, 289], where the limit $T^* \to 0$ is addressed by means of Madelung energy sums. Moreover, the CsCl (cesium chloride), CuAu (copper gold), NaCl (sodium chloride), and $Cu_3Au$ structures have been identified in experiments [260, 413]. Table 2.2 indicates whether the solid is crystalline ("c") or substitutionally disordered ("d") and it exhibits the numbers of particles per unit cell $K_c$ as well as the closed-packed packing fractions $\phi_{\rm cp}$. The CuAu structure, which is described by a tetragonal lattice of aspect ratio $c/a \in [1, \sqrt{2}]$ and a two-particle basis, degenerates to the CsCl structure in the case $c/a = 1$. The structure denoted by $LS_6^{\rm fcc}$ was introduced in Ref. [202] and the NbP (niobium phosphide) structure was called "tetragonal" in Ref. [201]. The former, $LS_6^{\rm fcc}$, is expected to occur in size-bidisperse mixtures [202], which was the motivation to include it in the list of candiate structures Tab. 2.2.

The phase diagrams for the case $\kappa a = 3$ in terms of $(T^*, p^*)$ and $(T^*, \phi)$ at compositions $x = 0$, $x = 1/4$, and $x = 1/2$ are displayed in Fig. 2.15. Thick solid lines represent phase boundaries whereas thin horizontal lines in $(T^*, \phi)$ diagrams (panels (b), (d), and (f)) are tie lines connecting coexisting states. At low temperatures two-phase coexistence $M_2 :=$ CsCl + rfcc is found (see Figs. 2.15(c) and (d)).

By construction a fluid-rfcc transition takes place for any $\kappa a$ and $x$ in the limit $T^* \to \infty$ at the coexistence pressure $p^*_{\rm coex}$ and volume fractions $\phi_{\rm f}$ and $\phi_{\rm rfcc}$. For $T^* \to 0$ and $x = 1/2$ a CsCl crystal coexists with a dilute gas, because the free energy of the

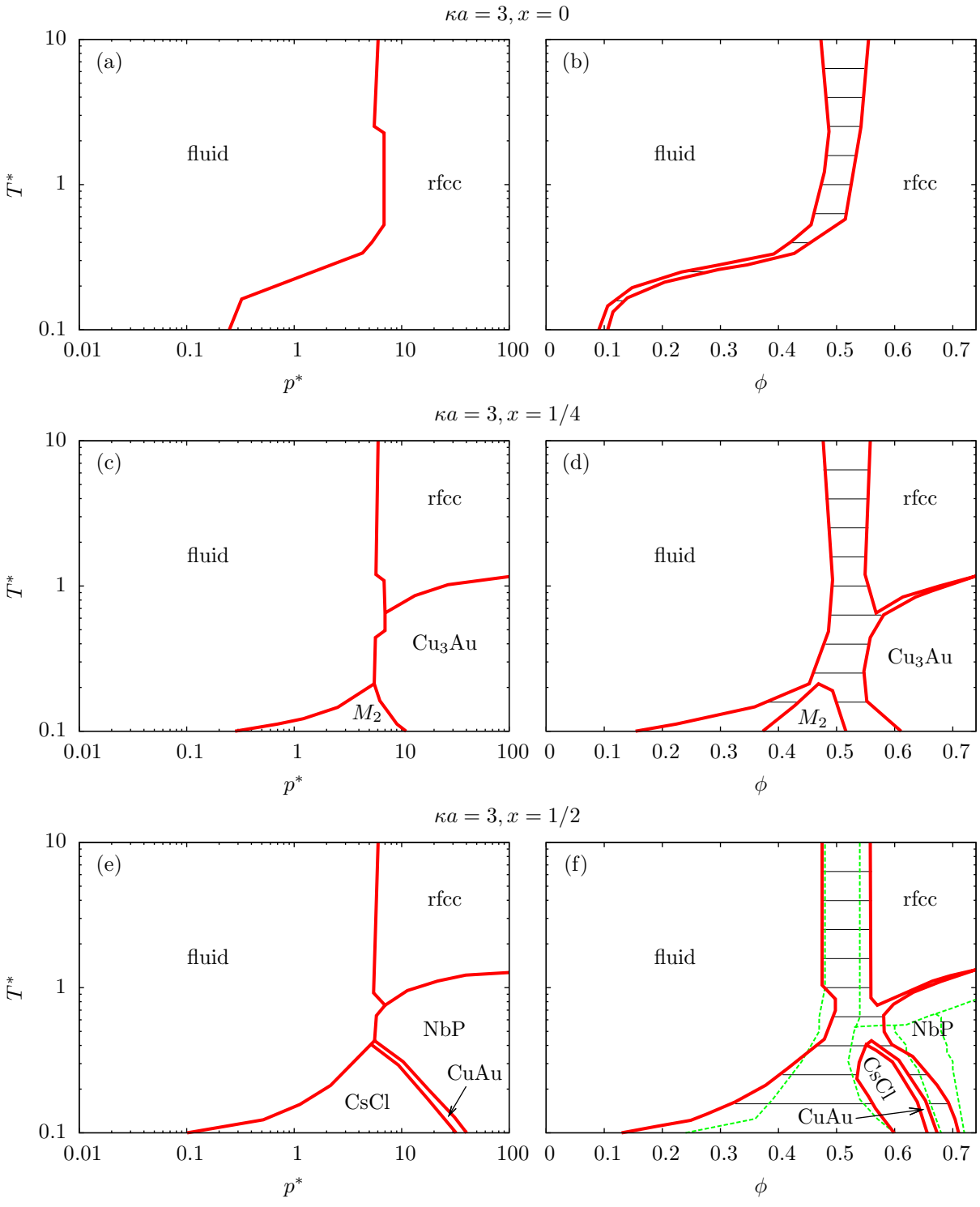


Figure 2.15: Phase diagrams for $\kappa a = 3$ at compositions $x$ in terms of $(T^*, p^*)$ and $(T^*, \phi)$. The green dashed lines in panel (f) reproduce the phase diagram of the computer simulation study of Ref. [201]. Labels of pure solid phases correspond to Tab. 2.2. Panels (c) and (d) exhibit a two-phase coexistence region $M_2 = \mathrm{CsCl} + \mathrm{rfcc}$. Horizontal thin lines in panels (b), (d), and (f) are tie lines. (See Ref. [41])

present formalism reduces to Madelung-like energy sums in this limit. A cut of the phase

diagrams at composition $x = 0$ is shown in Figs. 2.15(a) and (b), which involves merely the fluid and the rfcc structures, which is consistent with computer simulation results [200]. Figures 2.15(c) and (d) display a cut at $x = 1/4$, with an additional $Cu_3Au$ phase as well as the two-phase coexistence region $M_2$. The structures at composition $x = 1/4$ differ from those at composition $x = 3/4$ only by an exchange of the colloid species ($1 \leftrightarrow 2$).

In order to assess the reliability of the approach, Fig. 2.15(f) compares the calculated phase diagram (red solid lines) in terms of $(T^*, \phi)$ for $\kappa a = 3, x = 1/2$ with that obtained by means of free energy calculations using computer simulations in Ref. [201] (green dashed lines). Both studies agree in the predicted stable structures fluid, rfcc, CsCl, CuAu, and NbP. The overall topology is similar for both approaches; however, the formalism in Ref. [41] overestimates the stability of the NbP structure leading to a fluid-NbP transition (see Figs. 2.15(e) and (f)) which is not observed in the computer simulation. Moreover, it leads to a fluid-CuAu transition in a very narrow window around $T^* \approx 0.4$ but no rfcc-CuAu transition is found, whereas it is the opposite situation with the computer simulation results. Agreement between mean-field theory and computer simulation is observed with respect to the order of the phase transitions: The CsCl-CuAu transition is of second order because the CuAu structure transforms continuously into CsCl upon $c/a \to 1$, and the other phase transitions are of first order. Both the rfcc-NbP and the CuAu-NbP phase transitions are described as "weakly first-order" in Ref. [201], whereas within the approach of Ref. [41], only the rfcc-NbP transition exhibits a very narrow but non-vanishing $\phi$-gap and the CuAu-NbP transitions is strongly first-order (see Fig. 2.15(f)). The quantitative disagreement in the strength of the first-order CuAu-NbP transition can be understood on the basis of a smearing out of structural differences due to fluctuations, which are present in computer simulations but which are not fully accounted for by mean-field theories. This comparison between the formalism of Ref. [41] and the computer simulation study of Ref. [201] for the special case $\kappa a = 3, x = 1/2$ shows that, apart from well-known defects of mean-field theories, the theoretical approach is semi-quantitatively reliable. Moreover, its simplicity gives computational advantages over computer simulations such that now complete phase diagrams in terms of $(T^*, p^*, x)$ as a function of the parameter $\kappa a$ can be determined readily. Interestingly the preference of the CsCl structure over the NaCl structure in Fig. 2.15(f) is also found within the quantitatively more sophisticated approach of Vega, Bresme, and Abascal on the restricted primitive model (RPM) [448].

Figure 2.16 displays the phase diagram for $\kappa a = 3$ in terms of $(p^*, x)$ for temperatures (a) $T^* = 10$, (b) $T^* = 1$, and (c) $T^* = 0.1$. At high temperatures (see Fig. 2.16(a)) only fluid and rfcc structures are present and the fluid-rfcc transition line becomes independent of the composition $x$ in the limit $T^* \to \infty$. At lower temperatures (see Figs. 2.16(b) and (c)) CsCl, CuAu, $Cu_3Au$, and NbP crystal structures occur at fixed compositions. At low temperatures and pressures as well as strongly asymmetric mixtures (see Fig. 2.16(c) for $p^* < 1$ and $x < 1/4$ or $x > 3/4$) the MSA applied to model the fluid phase leads to an unphysical artifact which exhibits the apparent coexistence of an almost pure rfcc crystal with a less pure fluid. The reason for this unphysical phenomenon is that under these conditions the MSA pair distribution function becomes negative such that an increasing repulsive interaction potential leads to a more and more negative, i.e. attractive, contribution to the free energy. However, outside of this range of the phase diagram MSA leads to a physically reasonable description of the fluid phase. The full phase diagram for $\kappa a = 3$ in terms of $(T^*, p^*, x)$ can be inferred from the two-dimensional cuts in Figs. 2.15

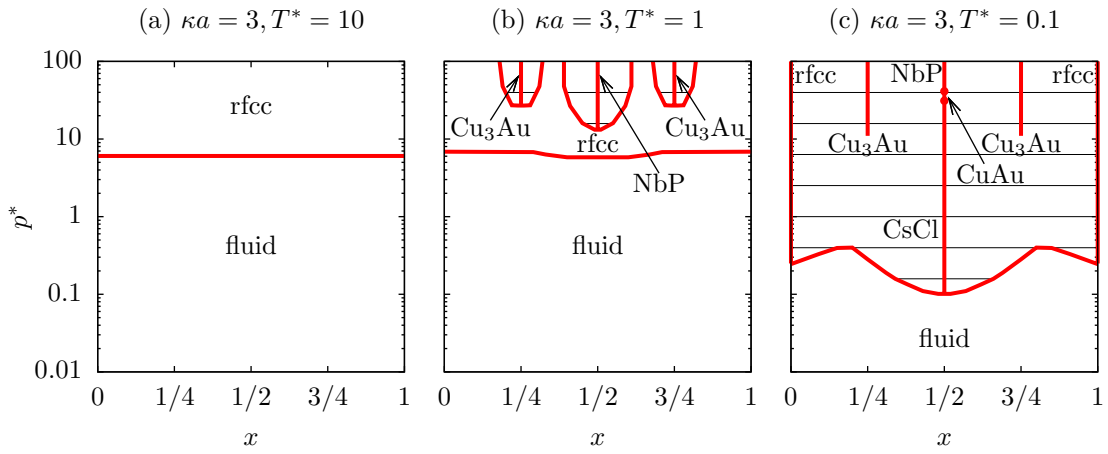


Figure 2.16: Phase diagrams for $\kappa a = 3$ in terms of $(p^*, x)$ at temperatures (a) $T^* = 10$, (b) $T^* = 1$, and (c) $T^* = 0.1$ (see also Fig. 2.15). Horizontal thin lines in panels (b) and (c) are tie lines. (See Ref. [41])

and 2.16.

In order to study the changes of the phase diagram upon changing the screening strength $\kappa a$, the phase diagrams for various screening strengths $\kappa a \in \{2, 3, 5, 10\}$ have been calculated in Ref. [41]. The trends in the variations of the phase diagrams upon changing $\kappa a$ are found to be monotonic such that it is sufficient to discuss the case $\kappa a = 10$.

Figures 2.17 displays the phase diagram for $\kappa a = 10$ in terms of $(T^*, p^*)$ and $(T^*, \phi)$ at compositions $x = 0$, $x = 1/4$, and $x = 1/2$. Two-phase coexistence regions $M_1 := \mathrm{CsCl} + \mathrm{fluid}$, $M_2 = \mathrm{CsCl} + \mathrm{rfcc}$, and $M_3 := \mathrm{CuAu} + \mathrm{rfcc}$ are present in Figs. 2.17(c) and (d). By comparison of Figs. 2.15 and 2.17 one infers a shift of the rfcc phase to lower temperatures upon increasing $\kappa a$. This observation can be understood by the fact that the interaction potential is approaching the hard-sphere potential in the limit $\kappa a \to \infty$. The $Cu_3Au$ phase in Figs. 2.15(c) and 2.17(c) or Figs. 2.15(d) and 2.17(d) shrinks upon increasing $\kappa a$, which is partly due to the growing rfcc phase. Figures 2.15(e) and 2.17(e) or Figs. 2.15(f) and 2.17(f) exhibit an increasing temperature range of stability of the CuAu structure upon increasing $\kappa a$. As a consequence the NbP phase, located in between the extending rfcc and CuAu phases, shrinks upon increasing $\kappa a$. Moreover, upon increasing $\kappa a$, the fluid-NbP transition disappears and an rfcc-CuAu coexistence is established. Finally, the $\phi$ range of the CsCl phase becomes smaller upon increasing $\kappa a$ as can be inferred from Figs. 2.15(f) and 2.17(f).

In order to make predictions on the conditions to synthesise certain crystal structures, it is expected within the formalism of Ref. [41] that colloids with strongly screened Coulomb interaction, i.e. large values of $\kappa a$, are preferable to prepare CuAu structures, whereas CsCl, $Cu_3Au$, and NbP crystals are expected to be found most easily in systems of weakly screened Coulomb interaction. Given a certain crystal structure has been prepared, the above reasoning leads to the following conclusions: CuAu structures become more whereas CsCl, $Cu_3Au$, and NbP structures become less stable against temperature variations upon increasing $\kappa a$. These considerations show that mixtures of charged colloids are ionic complex fluids whose rich self-assemblance phenomenology and structural stability can be tuned by varying the Debye length, i.e. the ionic strength.

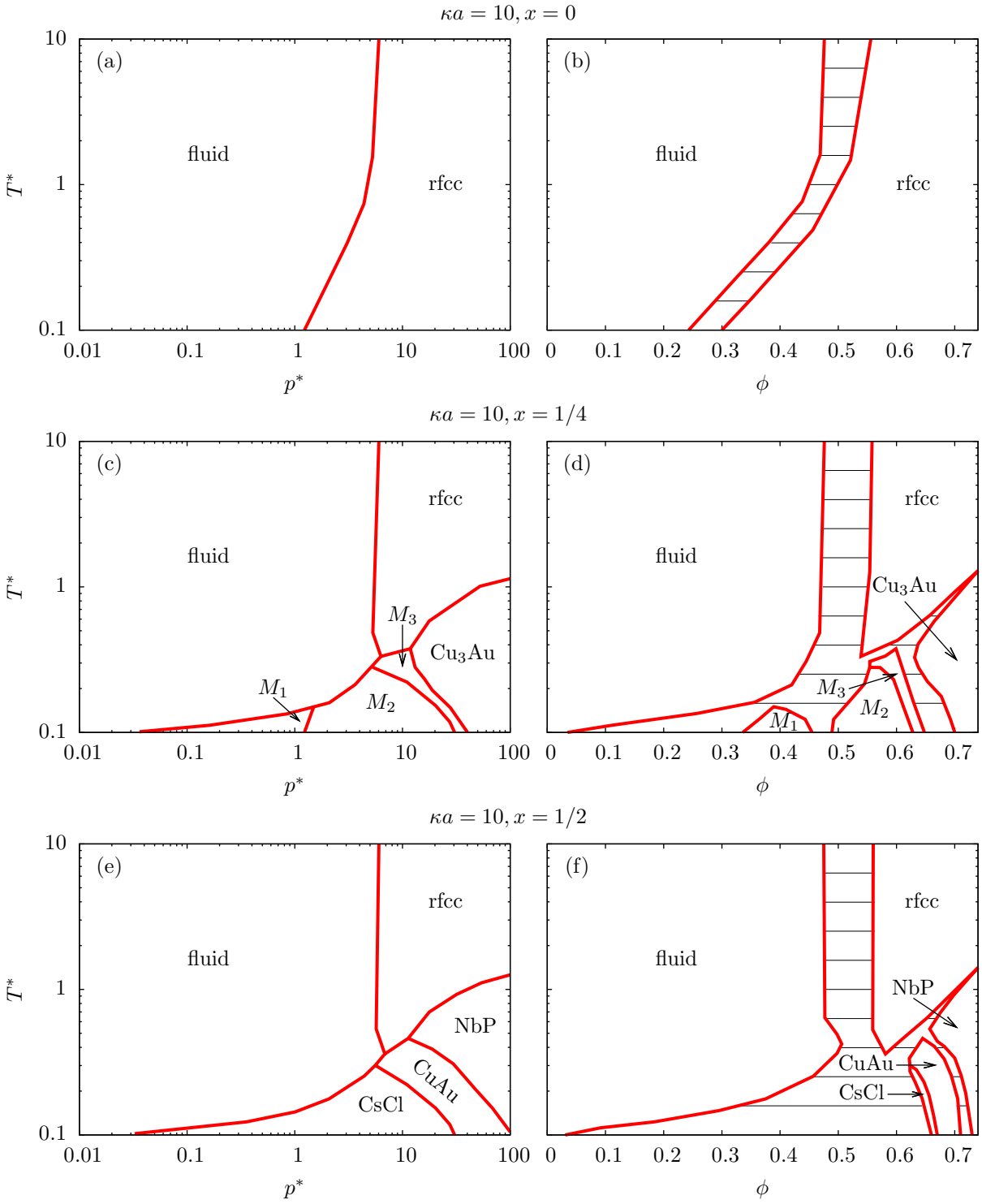


Figure 2.17: Phase diagrams for $\kappa a = 10$ at compositions $x$ in terms of $(T^*, p^*)$ and $(T^*, \phi)$. Labels of pure solid phases correspond to Tab. 2.2. Panels (c) and (d) exhibit two-phase coexistence regions $M_1$ = CsCl+fluid, $M_2$ = CsCl+rfcc, and $M_3$ = CuAu+rfcc. Horizontal thin lines in panels (b), (d), and (f) are tie lines. (See Ref. [41])

# Chapter 3

# Bulk structure

The influence of charges onto the structure of complex fluids is described in detail here. It is well-known that the spatial decay of electric fields in dilute electrolute solutions is characterised by the Debye length, which is the dominant length scale and which increases upon decreasing the ionic strength. However, the key observation is that the bulk structure of ionic complex fluids can be influenced by the competition of the Debye length with another material-independent length scale: the diverging correlation length close to a critical point of the solvent (Sec. 3.1). An interesting phenomenon to be discussed in Sec. 3.2 is that ionic impurities, in contrast to non-ionic ones, can alter the bulk structure of a solvent, which provides a qualitative difference between ionic and non-ionic complex fluids. By analysing the dielectric properties of a dense ionic fluid, where the Debye length is smaller than the particles, one observes a crossover between the well-known plasma-like behaviour at large length scales and a dipolar-fluid-like behaviour at small length scales (Sec. 3.3). Furthermore it is shown in Sec. 3.4 that the long-range of the bare Coulomb interaction is only sufficient but not necessary for the thermal and structural properties of dense ionic fluids. Rather, the impact of the Coulomb interaction on the properties of dense ionic complex fluids is due to its valency-dependence, i.e. it is attractive between equally charged and repulsive between oppositely charged ions.

## 3.1 Structure of electrolyte solutions close to critical points

The bulk structure of fluids, which is experimentally accessible by X-ray and neutron scattering, provides information complementary to those which follow from the bulk phase behaviour. Within the model of Ref. [43] described in Sec. 2.1, consider a spatially uniform equilibrium state $(\phi, I, \chi)$ in the one-phase region of the phase diagram (see Fig. 2.1(c)), which minimises the density functional $\Omega$ in the absence of surfaces, i.e. without the last term in Eq. (2.1). The corresponding two-point correlation functions $G_{ij}(r) = \varrho_i \varrho_j h_{ij}(r) = \varrho_i \varrho_j (g_{ij}(r) - 1), i, j \in \{\phi, +, -\}, \varrho_\phi := \phi, \varrho_\pm = I$, are obtained from $G_{ij}(r) = G_{ij}(\mathbf{r}, \mathbf{0}), r = |\mathbf{r}|$, with the inverse $G^{-1}_{ij}(\mathbf{r}, \mathbf{r}') = \dfrac{\delta^2 \Omega}{\delta \varrho_i(\mathbf{r}) \delta \varrho_j(\mathbf{r}')}$, where $\displaystyle\sum_j \int_{\mathcal{V}} \mathrm{d}^3 r' \, G^{-1}_{ij}(\mathbf{r}, \mathbf{r}') G_{jk}(\mathbf{r}', \mathbf{r}'') = \delta_{ik} \delta(\mathbf{r} - \mathbf{r}'')$. The three-dimensional Fourier transforms $\widehat{G}_{ij}(k) := \dfrac{4\pi}{k} \displaystyle\int_0^\infty \mathrm{d}r \, r G_{ij}(r) \sin(kr)$,

which are proportional to the partial structure factors [176], are given by [43]

$$\begin{aligned}
\widehat{G}_{\phi\phi}(k) &= \frac{1}{L(k)}\left(k^2+\kappa^2\right),\\
\widehat{G}_{\phi\pm}(k) &= -\frac{I}{L(k)}\left(V'_{\pm}(\phi)k^2+\frac{\kappa^2}{2}(V'_{+}(\phi)+V'_{-}(\phi))\right),\\
\widehat{G}_{\pm\pm}(k) &= \frac{I}{L(k)}\Bigg(\left(\frac{1}{\phi}+\frac{1}{1-\phi}-2\chi+I(V''_{+}(\phi)+V''_{-}(\phi))+\frac{\chi}{3}k^2\right)\left(k^2+\frac{\kappa^2}{2}\right)\\
&\qquad -V'_{\mp}(\phi)^2Ik^2\Bigg),\\
\widehat{G}_{\pm\mp}(k) &= \frac{I}{L(k)}\Bigg(\left(\frac{1}{\phi}+\frac{1}{1-\phi}-2\chi+I(V''_{+}(\phi)+V''_{-}(\phi))+\frac{\chi}{3}k^2\right)\frac{\kappa^2}{2}\\
&\qquad +V'_{+}(\phi)V'_{-}(\phi)^2Ik^2\Bigg)
\end{aligned} \tag{3.1}$$

with

$$\kappa^2 := \frac{8\pi\ell_B I}{\varepsilon(\phi)} \tag{3.2}$$

as the square of the inverse Debye length and the denominator (see Eq. (2.4))

$$L(k) := (k^2+\kappa^2)\left(\frac{\chi}{3}k^2+2(\chi_s(\phi;I)-\chi)\right)-\frac{I}{2}(V'_{+}(\phi)-V'_{-}(\phi))^2k^2. \tag{3.3}$$

Note that $V'_{\pm}(\phi)=0$ leads to $\widehat{G}_{\phi\pm}(k)=0$, i.e. as expected, the fluctuations of the solvent composition and of the ion densities are uncorrelated in the absence of ion-solvent interactions.

Due to the constraint $\varrho_A+\varrho_B=1$, the correlation functions $\widehat{G}_{AA}(k)$, $\widehat{G}_{AB}(k)$, and $\widehat{G}_{BB}(k)$ of the number density fluctuations of the $A$ and $B$ particles are related to the correlation function $\widehat{G}_{\phi\phi}(k)$ by $\widehat{G}_{AA}(k)=-\widehat{G}_{AB}(k)=\widehat{G}_{BB}(k)=\widehat{G}_{\phi\phi}(k)$. In this section $\widehat{G}_{\phi\phi}(k)$ is referred to as the solvent structure factor. It can be written in the form [43]

$$\widehat{G}_{\phi\phi}(k) = \frac{\widehat{G}_{\phi\phi}(0)}{1+(\lambda k)^2\left(1-\dfrac{g^2}{1+(k/\kappa)^2}\right)} \tag{3.4}$$

with

$$\lambda := \sqrt{\frac{\chi}{6(\chi_s(\phi,I)-\chi)}} \tag{3.5}$$

and

$$g^2 := \frac{3(\Delta\gamma)^2\varepsilon(\phi)}{16\pi\ell_B\chi}, \tag{3.6}$$

where $\Delta\gamma := \gamma_+-\gamma_- = V'_{+}(\phi)-V'_{-}(\phi)$. The isothermal compressibility, which is proportional to $\widehat{G}_{\phi\phi}(0)=(2(\chi_s(\phi,I)-\chi))^{-1}$, diverges $\sim|\chi-\chi_c|^{-\gamma}$ upon approaching the critical point $(\phi_c,I_c,\chi_c)$. As expected within the present mean-field theory, one finds the classical critical exponent $\gamma=1$ instead of $\gamma\approx 1.24$ for the Ising universality class [349]. For a state point $(\phi,I,\chi)$ in the bulk phase diagram (see Figs. 2.1(a) and (c)) the length $\lambda$ is

an (inverse) measure of the deviation of $\chi$ from its value $\chi_s(\phi, I)$ at the spinodal. Equation (3.4) has already been derived in Ref. [334] within BCA, which corresponds to the linear approximation $\Delta\gamma \approx f_+ - f_-$. For $|g| \leq 1$ in Eq. (3.4) the solvent structure factor $\widehat{G}_{\phi\phi}(k)$ is a monotonically decreasing function of the wave number $k$, whereas for $|g| > 1$ at $k_{\max} = \kappa\sqrt{|g| - 1}$ a maximum $\widehat{G}_{\phi\phi}(k_{\max}) = \dfrac{\widehat{G}_{\phi\phi}(0)}{1 - (\kappa\lambda)^2(|g| - 1)^2}$ occurs [44] (see Sec. 3.2). Hence, if $|g| > 1$, $\widehat{G}_{\phi\phi}(k_{\max})$ diverges as function of $\chi$ at $\lambda = \lambda_{\text{unstable}} = (\kappa(|g| - 1))^{-1}$, i.e. the spatially uniform bulk state becomes unstable upon approaching the critical point. Note that in the limits $|g| \to 0$ (no ion-solvent coupling) or $\kappa \to 0$ (no salt) Eq. (3.4) leads to the Ornstein-Zernike-like solvent structure factor $\widehat{G}_{\phi\phi}(k) = \widehat{G}_{\phi\phi}(0)/(1 + (\lambda k)^2)$. In this case $\lambda$ can be identified with the bulk correlation length.

Experimental reports of uniform bulk states close to the critical point of water+2,6-dimethylpyridine mixtures with KBr, KCl, and $Mg(NO_3)_2$ (see Ref. [317]) as well as distributions of neutron scattering intensities of water+3-methylpyridine with LiCl, NaCl, KCl, NaBr, and $MgSO_4$, which vary monotonically as function of $k$ (see Refs. [388, 389]), indicate that in these systems one has $|g| < 1$. Within the LDA in Sec. 2.1 this latter relation is expected to be fulfilled: Close to the critical point $(\phi_c, \chi_c) \approx (\frac{1}{2}, 2)$ (see Fig. 2.3) of, e.g., the widely studied binary liquid mixture of 3-methylpyridine (component $A$, $\varepsilon_A = 10$) and water (component $B$, $\varepsilon_B = 80$) with a lower critical demixing point at $T_c \approx 316\,\text{K}$, i.e. $\ell_B\widetilde{a} \approx 529\,\text{Å}$, one obtains $|g| < 0.3$ independent of the type of salt, because $|\Delta\gamma| \lesssim 4$. However, within BCA, i.e. for $\Delta\gamma \approx f_+ - f_-$ with typically $|f_+ - f_-| \gg 1$ [208, 286], one has to expect $|g| \gg 1$, which, according to the above reasoning, is in sharp contrast to the available experimental results. It has to be mentioned that experimental reports [390–392] of "periodic structures" in heavy water+3-methylpyridine mixtures with sodium tetraphenylborate ($NaBPh_4$) cannot, however, be expected to find a consistent interpretation in terms of a local ion solvation model, neither within BCA nor within the LDA, because the anions ($[BPh_4]^-$) are much larger than the solvent particles, such that in these systems the ion size is expected to be relevant.

The charge-charge structure factor $S_{ZZ}(k) = (\widehat{G}_{\pm\pm}(k) - \widehat{G}_{\pm\mp}(k))/I$ [176], which measures correlations of fluctuations $Z$ of the local charge density around $\varrho_+ - \varrho_- = 0$, is obtained by inserting the expressions for $\widehat{G}_{\pm\pm}(k)$ and $\widehat{G}_{\pm\mp}(k)$ from Eq. (3.1):

$$S_{ZZ}(k) = k^2 \frac{\frac{\chi}{3}k^2 + 2(\chi_s(\phi, I) - \chi)}{L(k)}. \tag{3.7}$$

The asymptotic behaviour $S_{ZZ}(k \to 0) \simeq (k/\kappa)^2$ is the signature for perfect screening [176]. Further, the case $\Delta\gamma = 0$ corresponds to the Debye-Hückel limit $S_{ZZ}(k) = k^2/(k^2 + \kappa^2)$.

The asymptotic behaviour of the correlation function $G_{ij}(r) = \dfrac{1}{2\pi^2 r}\displaystyle\int_0^\infty \mathrm{d}k \;\; k\widehat{G}_{ij}(k)\sin(kr)$ can be inferred from a pole analysis of $\widehat{G}_{ij}(k)$, which amounts to determine the roots of the denominator $L(k)$ defined in Eq. (3.3) [134, 135]. Since $L(k)$ is a polynomial in $k$ of degree four it has four and only four complex roots $k_\nu = k'_\nu + ik''_\nu, k'_\nu = \text{Re}(k_\nu), k''_\nu = \text{Im}(k_\nu), \nu \in \{1, \ldots, 4\}$. Due to the actual structure of $L(k)$ there are constraints on the locations of the four roots $k_\nu$ in the complex plane [43]. If $L(k = k_\nu)$ vanishes this holds also for $k = k^*_\nu$, because $L(k)$ has real coefficients.

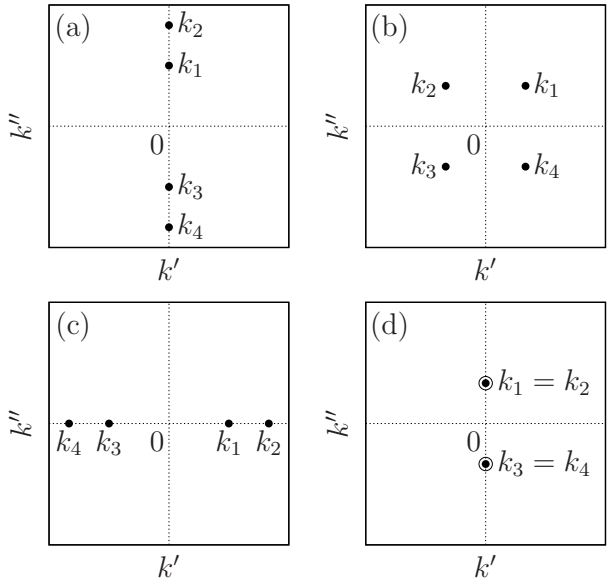


Figure 3.1: Poles $k_1, \ldots, k_4$ of the Fourier transform $\widehat{G}_{ij}(k)$ of the two-point correlation functions $G_{ij}(r)$ in the complex plane $k = k' + ik'' \in \mathbb{C}$, which correspond to the roots of the denominator $L(k)$ (see Eq. (3.3)). According to the analytic structure of $L(k)$ (see the main text) only the three distinct situations shown in panels (a)–(c) can occur. Purely imaginary poles [(a)] correspond to a monotonic decay of $G_{ij}(r \to \infty)$ whereas a pole structure as in panel (b) ($|k_\nu|$ all equal) corresponds to an oscillatory decay of $G_{ij}(r \to \infty)$. Purely real poles [(c)] indicate an unstable bulk state, which does not occur in the one-phase region of the phase diagram in Fig. 2.1(c). The merging of two poles on the imaginary axis [(d)] corresponds to a Kirkwood crossover point. (See Ref. [43])

Moreover, if $L(k = k_\nu)$ vanishes this also holds for $k = -k_\nu$, because $L(k)$ is a polynomial in $k^2$. Accordingly this is also true for $k = -k_\nu^*$. This implies the root structure shown in Fig. 3.1. Three distinct situations can occur. For purely imaginary roots given by $\{k_1 = ik_1'', k_2 = ik_2'', k_3 = -k_1, k_4 = -k_2\}$ with $0 < k_1'' < k_2''$ (see Fig. 3.1(a)) the asymptotic decay of the two-point correlation functions $G_{ij}(r \to \infty)$ is monotonic $\sim \exp(-k_1'' r)/r$. For complex roots $\{k_1 = k_1' + ik_1'', k_2 = -k_1^*, k_3 = -k_1, k_4 = k_1^*\}$ with $k_1', k_1'' > 0$ (see Fig. 3.1(b)) the two-point correlation functions $G_{ij}(r)$ vary asymptotically $\sim \sin(k_1' r + \text{const}) \exp(-k_1'' r)/r$ giving rise to a damped oscillatory decay. Finally, purely real roots $\{k_1 = k_1', k_2 = k_2', k_3 = -k_1, k_4 = -k_2\}$ with $0 < k_1' < k_2'$ (see Fig. 3.1(c)) indicate an unstable bulk state, i.e. the corresponding point in the phase diagram is located in between the spinodals. The exponential decay of the two-point correlation functions (whether monotonically or oscillatory) is consistent with the short range of the interactions implied by taking a gradient expansion.

Thermodynamic states in the bulk phase diagram with monotonically decaying $G_{ij}(r \to \infty)$ are separated from states with damped oscillatory decay of $G_{ij}(r \to \infty)$ by so-called Kirkwood crossover lines [259]. Crossing these lines is associated with the merging of two purely imaginary poles (see Figs. 3.1(a) and (d)) of $\widehat{G}_{ij}(k)$ in the upper (and similarly in the lower) half of the complex plane and with a subsequent emergence of a pair of two poles (see Fig. 3.1(b)) with equal imaginary parts and with real parts of equal absolute value but of opposite sign [230]. In the phase diagrams of Fig. 3.2 the Kirkwood crossover lines are

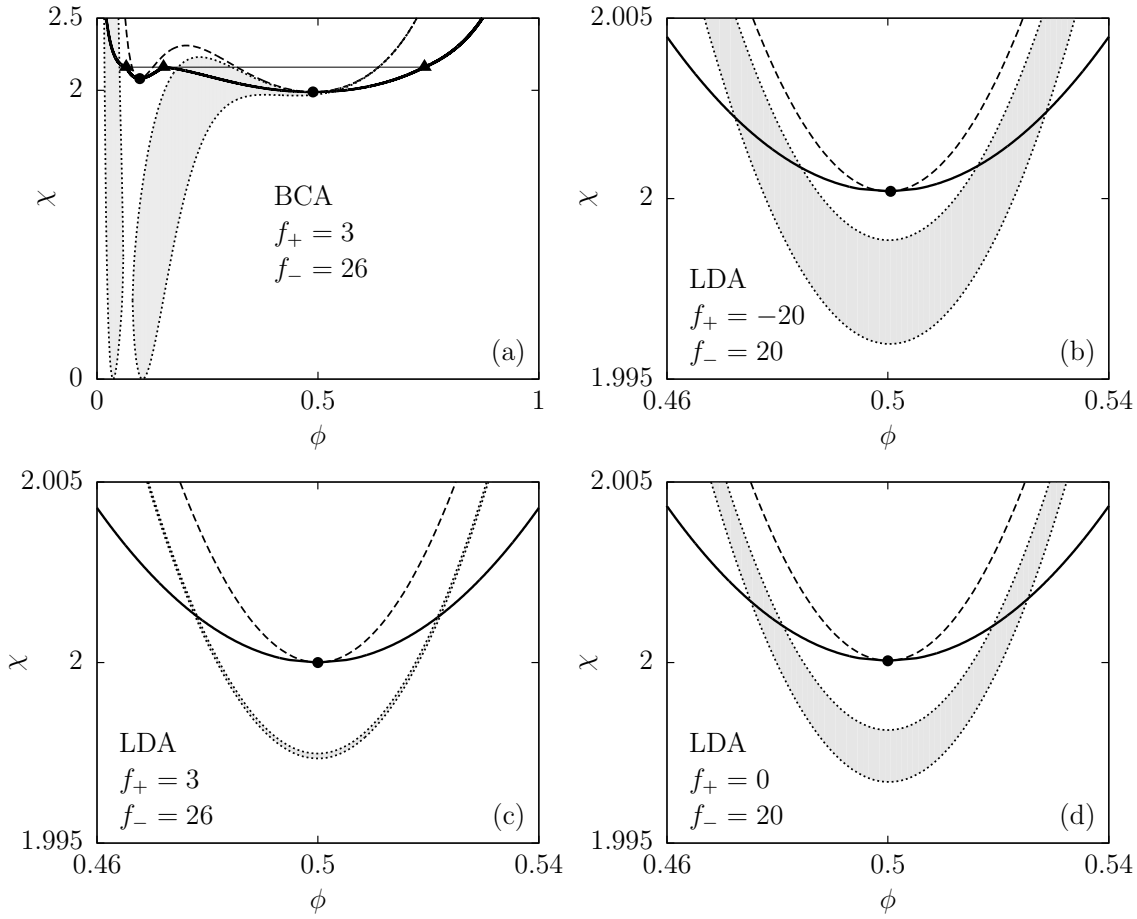


Figure 3.2: Phase diagrams as in Fig. 2.1 with Kirkwood crossover lines (dotted lines) within the bilinear coupling approximation (BCA) [(a)] and the local density approximation (LDA) described in Sec. 2.1 [(b)–(d)]. The parameters correspond to the binary liquid mixture water+3-methylpyridine ($\varepsilon_A = 10$, $\varepsilon_B = 80$, $\ell_B \widetilde{a} = 529\,\text{Å}$); for simplicity the temperature dependence of the Bjerrum length $\ell_B$ is ignored. The chemical potential $\mu_I k_B T$ of the salt is fixed such that at the (slightly shifted) critical point with composition $\phi = \phi_c \approx \frac{1}{2}$ there is an ionic strength $\widetilde{I}_c = 10\,\text{mM}$. Outside the grey regions bounded by the dotted lines the two-point correlation functions exhibit asymptotically a monotonic decay, whereas inside these regions damped oscillatory decays occur. Within BCA a large portion of the phase diagram corresponds to oscillatory decay, whereas within LDA this occurs only in a narrow band within which the value of the bulk correlation length is close to that of the Debye screening length. Note the differences in scales for the axes in (a) and in (b)–(d). (See Ref. [43])

denoted by dotted lines and damped oscillatory decay of $G_{ij}(r \to \infty)$ occurs at state points in the grey area enclosed by the Kirkwood crossover lines. The parameters correspond to the aforementioned binary liquid mixture water+3-methylpyridine ($\varepsilon_A = 10$, $\varepsilon_B = 80$, $\ell_B \widetilde{a} = 529\,\text{Å}$); for simplicity the temperature dependence of the Bjerrum length $\ell_B$ is ignored. The chemical potential $\mu_I$ of the salt is fixed such that there is an ionic strength $\widetilde{I}_c = 10\,\text{mM}$ at the (shifted) critical point. Figures 3.2(a) and (c) correspond to the parameters $(f_+, f_-) = (3, 26)$ used in Figs. 2.1(a) (BCA) and (c) (LDA), respectively. Figure 3.2(b) refers to the case of a strongly antagonistic salt, $(f_+, f_-) = (-20, 20)$,

whereas Fig. 3.2(d) relates to the intermediate case $(f_+, f_-) = (0, 20)$. Within BCA (see Fig. 3.2(a)), the damped oscillatory decay of $G_{ij}(r \to \infty)$ prevails in a large portion of the phase diagram, and wave lengths of the oscillations as small as the particle size $\widetilde{a}$ can occur at state points in the center of the grey area. However, within the LDA of Sec. 2.1, damped oscillatory decay of $G_{ij}(r \to \infty)$ is found only in a narrow range of $\mathcal{O}(\Delta\gamma I)$ for values of $\chi$ around $\chi = \dfrac{\chi_s(\phi, I)}{1 + \kappa^2/6} + \mathcal{O}((\Delta\gamma)^2 I)$, which extends into the one-phase region only in the vicinity of the critical point [43] (see Figs. 3.2(b)–(d)).

For small wave numbers $k$ the structure factor $\widehat{G}_{\phi\phi}(k \ll \kappa) \simeq \dfrac{\widehat{G}_{\phi\phi}(0)}{1 + (\lambda k)^2(1 - g^2)}$ (see Eq. (3.4)) takes the Ornstein-Zernike form $\dfrac{\widehat{G}_{\phi\phi}(0)}{1 + (\xi^{(\mathrm{OZ})} k)^2}$ with the length [43]

$$\xi^{(\mathrm{OZ})} = \lambda\sqrt{1 - g^2} = \sqrt{\frac{\chi(1 - g^2)}{6(\chi_s(\phi, I) - \chi)}} \tag{3.8}$$

which is referred to as the Ornstein-Zernike length. This length $\xi^{(\mathrm{OZ})}$ is determined routinely in scattering experiments by fitting an Ornstein-Zernike expression to scattered intensities at small momentum transfer [317]. For water+2,6-dimethylpyridine mixtures with KBr, KCl and $Mg(NO_3)_2$ (see Ref. [317]) it has been found experimentally that the amplitude $\xi_0^{(\mathrm{OZ})}$ of $\xi^{(\mathrm{OZ})} = \xi_0^{(\mathrm{OZ})} |(T - T_c)/T_c|^{-\nu}$ is to a large extent independent of the considered type of salt and ionic strength. Due to $\xi_0^{(\mathrm{OZ})} \sim \sqrt{1 - g^2}$ this observation indicates that one has $g^2 \ll 1$, which, according to the arguments given above, is expected within the LDA of Sec. 2.1 but is not compatible with predictions following from BCA.

The poles $\{k_1, \ldots, k_4\}$ of the solvent structure factor $\widehat{G}_{\phi\phi}(k)$ can be expressed in terms of the Ornstein-Zernike length $\xi^{(\mathrm{OZ})}$ and the inverse Debye length $\kappa$. For a monotonic decay of $G_{\phi\phi}(r \to \infty)$ one has purely imaginary poles $k_\nu = ik''_\nu$ with $k''_1 = -k''_3$ and $k''_2 = -k''_4$, whereas a damped oscillatory decay of $G_{\phi\phi}(r \to \infty)$ is characterised by the poles at $k_1 = k'_1 + ik''_1, k_2 = -k_1^*, k_3 = -k_1, k_4 = k_1^*$. Close to the critical point (i.e. for $\xi^{(\mathrm{OZ})} \to \infty$) one finds a monotonic decay of $G_{\phi\phi}(r \to \infty)$ with the decay length $1/k''_1 \simeq \xi^{(\mathrm{OZ})} \sim |\chi - \chi_c|^{-\nu}$ with the mean-field critical exponent $\nu = \frac{1}{2}$ instead of $\nu \approx 0.63$ for the Ising universality class [349]. Therefore the electrostatic interactions do not affect the universal critical exponent, but they can influence the non-universal critical amplitude $\xi_0^{(\mathrm{OZ})}$ [43].

Figure 3.3 displays the real and imaginary parts of the poles $k_\nu$ of $\widehat{G}_{ij}(k)$ in the ranges $k'_\nu = \mathrm{Re}(k_\nu), k''_\nu = \mathrm{Im}(k_\nu) \geq 0$ at the critical composition $\phi = \phi_c \approx \frac{1}{2}$ for the parameters corresponding to Fig. 3.2(b). The four poles $\{k_1, \ldots, k_4\}$ can be expressed in terms of $(k'_1, k''_1, k''_2)$. In Fig. 3.3 the two purely imaginary poles $k_1$ and $k_2$ with positive imaginary parts for monotonically decaying $G_{ij}(r \to \infty)$ occur as two branches, which merge at the Kirkwood crossover points (•). The Kirkwood crossover points (•) are characterised by $\kappa\xi^{(\mathrm{OZ})} = \sqrt{\dfrac{2}{1 \pm g} - 1} \approx 1$ (see Ref. [43]). Hence at the Kirkwood crossover points the inverse decay lengths of $G_{ij}(r \to \infty)$ correspond approximately to $\kappa$ (dashed line) and $1/\xi^{(\mathrm{OZ})}$ (dotted line). At the critical point ($\chi = \chi_c$, i.e. $k''_1 = 0$), $G_{ij}(r \to \infty)$ decays as $1/r$ with a subdominant contribution $\sim \exp(-\kappa r\sqrt{1 - g^2})/r$ (see Fig. 3.3), i.e. as anticipated above, the leading decay at large distances is governed by the vicinity to the

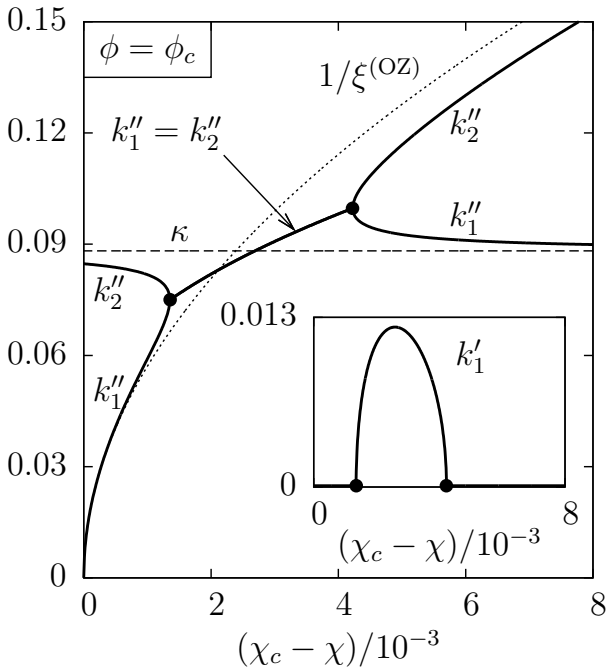


Figure 3.3: Real and imaginary parts of the poles $k_\nu = k_\nu' + ik_\nu'', k_\nu' = \mathrm{Re}(k_\nu), k_\nu'' = \mathrm{Im}(k_\nu), \nu \in \{1, \ldots, 4\}$, of the Fourier transform $\widehat{G}_{ij}(k)$ of the two-point correlation functions $G_{ij}(r)$ as functions of the deviation $\chi_c - \chi$ from the critical point at the critical composition $\phi = \phi_c \approx \frac{1}{2}$ for the parameters corresponding to Fig. 3.2(b). The four poles $k_1, \ldots, k_4$ can be expressed in terms of $(k_1', k_1'', k_2'')$ (see Fig. 3.1). If $G_{ij}(r \to \infty)$ decays monotonically, the poles of $\widehat{G}_{ij}(k)$ are purely imaginary ($k_1' = 0$), giving rise to two branches $k_1''$ and $k_2''$ of positive imaginary parts (see Fig. 3.1(a)). If $G_{ij}(r \to \infty)$ decays oscillatorily, there is only one pole of $\widehat{G}_{ij}(k)$ with positive real and imaginary parts ($k_2'' = k_1''$) (see Fig. 3.1(b)). The merging of the two branches $k_1''$ and $k_2''$ for monotonic asymptotic decay takes place at the Kirkwood crossover points (•) (see Fig. 3.1(d)). Upon varying $\phi$ these points form the Kirkwood crossover lines (dotted lines in Fig. 3.2). For comparison the inverse Debye length $\kappa$ (dashed line) as well as the inverse Ornstein-Zernike length $1/\xi^{(\mathrm{OZ})} \sim \sqrt{\chi_c - \chi}$ (dotted line, see Eq. (3.8)) are displayed. Within the range of values of $\chi$ leading to an oscillatory decay, depicted by the grey regions in Fig. 3.2, one has $\kappa \approx 1/\xi^{(\mathrm{OZ})}$. Within the range of monotonic decay the decay rate of the leading contribution to $G_{ij}(r \to \infty)$ is given by $k_1''$ whereas that of the subdominant contribution is $k_2''$. For $\chi_c - \chi \leq 1.3 \times 10^{-3}$ the decay rates are $k_1'' \approx 1/\xi^{(\mathrm{OZ})}$ and $k_2'' \approx \kappa$, whereas for $\chi_c - \chi \geq 4.3 \times 10^{-3}$ the decay rates are $k_1'' \approx \kappa$ and $k_2'' \approx 1/\xi^{(\mathrm{OZ})}$. (See Ref. [43])

critical point, whereas the ion-solvent coupling manifests itself in the corrections to the leading behaviour. Further away from the critical point the leading contribution decays $\sim \exp(-k_1'' r)/r$ with a subdominant contribution $\sim \exp(-k_2'' r)/r$ (see Fig. 3.3). The inset of Fig. 3.3 displays the absolute value of the real parts $|k_\nu'| = k_1'$ of the poles of $\widehat{G}_{ij}(k)$, which is identical to the wave number $k_1'$ of the oscillatory part of $G_{ij}(r)$ and which is non-zero within the grey region of Fig. 3.2(b). For the strongly antagonistic salt with $f_+ = -20$ and $f_- = 20$, in Fig. 3.2(b) the shortest wave length of the oscillations is given by $(2\pi/k_1')_{\min} \approx 513$ (see the inset in Fig. 3.3). The corresponding value of $k_1''$ is $\approx 0.0873$ so that $(2\pi/k_1')_{\min} \approx 45/k_1''$, i.e. $G_{ij}(r) \sim \sin(k_1' r + \mathrm{const}) \exp(-k_1'' r)/r$ decays

already within 1/45 of a period. In less extreme cases of solubility contrasts $f_\pm$, such as those in Figs. 3.2(c) and (d), the shortest wave lengths are even larger [43]. Therefore, within the LDA of Sec. 2.1, the oscillations in $G_{ij}(r)$, if they occur, are not expected to be experimentally detectable. In contrast, as already mentioned above, within BCA it is possible that the shortest wave lengths of the oscillations are of the order of the particle size; such an asymptotic oscillatory decay can be expected to be visible in the pair distribution function. However, there are no experimental reports of Kirkwood crossover lines, which is in line with the results obtained within the LDA.

In conclusion, the bulk structure of eletrolyte solutions is determined by the Debye length far away from the critical point of the solvent and by the bulk correlation length close to it. The two regimes are connected by a sequence of two Kirkwood crossovers, which, however, are not expected to be easily detectable in experiments. Whereas ion-solvent coupling does not modify the universal behaviour close to critical points, e.g. critical exponents, it can modify non-universal properties, e.g. critical amplitudes.

## 3.2 Structure of fluids with ionic impurities

The expression Eq. (3.4) of the solvent-solvent structure factor $\widehat{G}_{\phi\phi}(k)$ of an electrolyte solution has been derived within the particular model of Sec. 2.1 (see Refs. [43, 334]). A more general point of view is to consider the ions of an electrolyte solution as impurities in the solvent and to ask for the influence of impurities on the bulk structure of the solution. In order to address the problem whether and how impurities alter the form of the fluid structure factor one can derive asymptotic forms of the structure factor by means of general, model independent arguments [44].

A rather general setting is to consider a spatially uniform fluid mixture of three components of which component 1 is referred to as the "solvent" whereas components 2 and 3 are called "impurities". The interaction potentials $U_{ij}(r)$ between two particles of components $i$ and $j$ are assumed to be isotropic and vanishing at infinite particle separation ($r \to \infty$). Note that no particular asymptotic decay of $U_{ij}(r \to \infty)$ is assumed. The mole fraction $x_i$ of component $i \in \{1, 2, 3\}$ may be expressed in terms of the mole fraction $x = x_2 + x_3$ of impurities and the composition $\phi \in [0, 1]$ of the impurities such that $x_1 = 1-x$, $x_2 = \phi x$ and $x_3 = (1-\phi)x$. For *ionic* impurities with valencies $z_2, z_3 > 0$ of the respective components the constraint $z_2 x_2 = z_3 x_3$ of local charge neutrality of the bulk fluid leads to the composition $\phi = z_3/(z_2 + z_3)$, whereas the composition $\phi$ of *non-ionic* impurities is not restricted to a particular value.

For small mole fraction $x \ll 1$ of impurities and inverse wave numbers $1/q$ larger than the particle sizes, the direct correlation functions $\widehat{c}_{ij}(q)$ can be expanded in a Laurent series around $q = 0$ up to terms of $\mathcal{O}(q^2)$ [44]. In the case of non-ionic impurities, i.e. $z_2 = z_2 = 0$, no pole occurs at $q = 0$ [44].

In the absence of impurities, i.e. for $x = 0$, one obtains for the solvent partial structure factor the well-known Ornstein-Zernike structure factor $S_{11}(q) = (1 - \varrho(c_{11}^{(0)} + c_{11}^{(1)} q^2))^{-1}$, where where $c_{ij}^{(p)}$ is the coefficient of $q^{2p}$ in the expansion of $\widehat{c}_{ij}(q)$. From the relation $S_{11}(0) > 0$, which holds due to the fact that $S_{11}(0)$ is the ratio between the compressibility of the solvent and that of a gas of non-interacting particles of the same temperature and density [176], one infers $1 - \varrho c_{11}^{(0)} \geq 0$. Moreover, if the bulk phase diagram of the pure solvent exhibits critical points and if the pure solvent is uniform throughout the whole

one-phase region of the bulk phase diagram, i.e. $S_{11}(q)$ for $q > 0$ does not diverge even close to critical points, where $1 - \varrho c_{11}^{(0)}$ vanishes, $c_{11}^{(1)} < 0$ is required. Note that these conditions are not fulfilled by a fluid of hard spheres, because there is no critical point in the corresponding bulk phase diagram, which is independent of temperature and which exhibits only a first-order phase transition.

Considering only the dominant contributions in the mole fraction $x \ll 1$ of impurities leads to the asymptotic form [44, 334]

$$S_{11}(q) \simeq \frac{S_{11}(0)}{1 + (\xi q)^2 \left(1 - \dfrac{g^2}{1 + (q/\kappa)^2}\right)}, \tag{3.9}$$

of the solvent partial structure factor, where

$$S_{11}(0) = \frac{1}{1 - \varrho(1-x)c_{11}^{(0)} - \varrho^2 x(\phi c_{12}^{(0)} + (1-\phi)c_{13}^{(0)})^2} \tag{3.10}$$

is related to the compressibility of the solvent [176], $\xi = \sqrt{-\varrho c_{11}^{(1)} S_{11}(0)}$ is the bulk correlation length, $\kappa = \sqrt{8\pi\ell_B I}$ is the inverse Debye length with $I = \varrho x(z_2^2\phi + z_3^2(1-\phi))/2$ denoting the ionic strength and the quantity

$$g^2 := \frac{(c_{12}^{(0)} - c_{13}^{(0)})^2}{-4\pi\ell_B c_{11}^{(1)}(z_2 + z_3)^2} \tag{3.11}$$

measures the contrast of impurity-solvent interactions. Whereas expressions equivalent to Eq. (3.9) have first been derived in Refs. [43, 334] within specific models of electrolyte solutions, it has been shown that Eq. (3.9) is generally valid [44] (see e.g. Eq. (3.4)). However, it has to be noted that Eqs. (3.9)–(3.11) apply only in the limit of high dilution of impurities. Deviations beyond this limit have been recognised in Ref. [367].

Considering $S_{11}(q)$ in Eq. (3.9) one immediately recognises

$$S_{11}(q) \simeq \begin{cases} \dfrac{S_{11}(0)}{1 - g^2(\kappa\xi)^2 + (\xi q)^2} & , q \gg \kappa \\ \dfrac{S_{11}(0)}{1 + (1-g^2)(\xi q)^2} & , q \ll \kappa. \end{cases} \tag{3.12}$$

In particular, for non-ionic impurities, i.e. for $\kappa = 0$, the solvent structure factor $S_{11}(q) \simeq S_{11}(0)/(1+(\xi q)^2)$ is not altered to leading order in the mole fraction $x$. However, ionic impurities due to, e.g., alkali halides of ionic strength $I \approx 1\,\mathrm{mM}$ in water at room temperature, i.e. $x \approx 4 \cdot 10^{-5}$, lead to an inverse Debye length $\kappa \approx 0.1\,\mathrm{nm}^{-1}$, i.e. a Debye length $1/\kappa \approx 10\,\mathrm{nm}$, which is much larger than the particle size.

For ionic impurities it is readily seen that $S_{11}(q)$ is monotonically decreasing with $q$ if $|g| \leq 1$ (see Figs. 3.4(a) and (b)). If $|g| > 1$ a maximum of $S_{11}(q)$ occurs at $q = q_{\max} = \kappa\sqrt{|g| - 1}$. In this latter case $S_{11}(q_{\max}) = S_{11}(0)/(1 - (\kappa\xi(|g| - 1))^2)$ is finite for $\xi < (\kappa(|g| - 1))^{-1}$ (see Fig. 3.4(c)), whereas $S_{11}(q)$ has a pole for $\xi \geq (\kappa(|g| - 1))^{-1}$ (see Fig. 3.4(d)). Obviously, whenever $|g| > 1$, a divergence of $S_{11}(q)$ occurs upon approaching a critical point, where the bulk correlation length $\xi$ diverges. Hence, by adding ionic impurities the solvent remains uniform within the whole one-phase region of the bulk

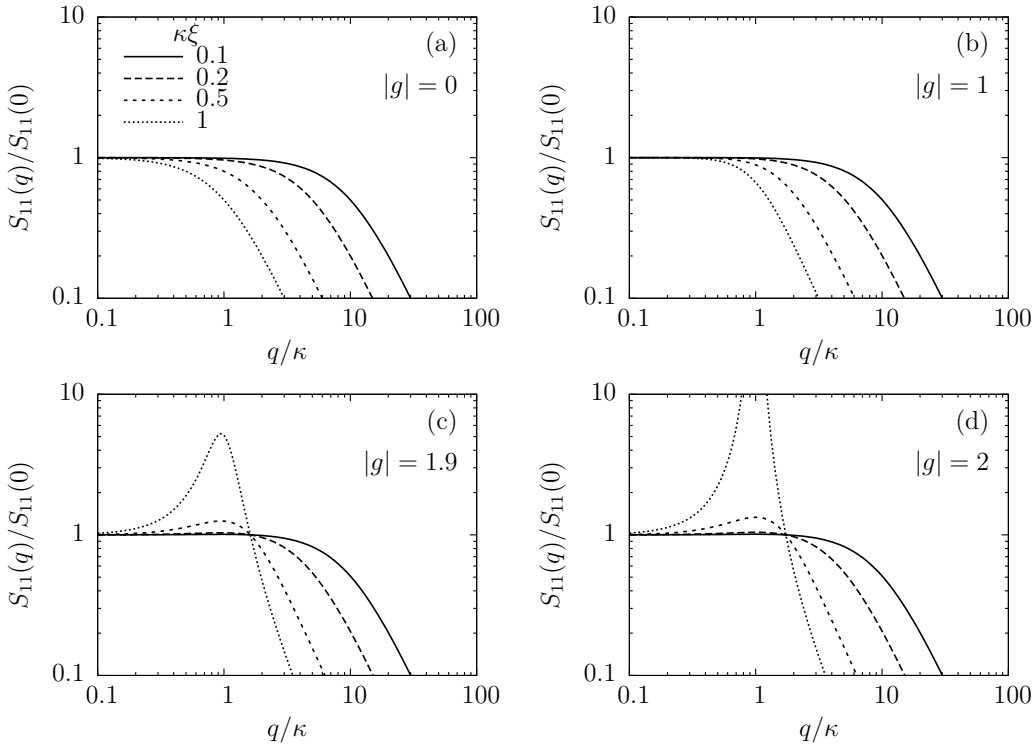


Figure 3.4: Influence of dilute ionic impurities on the solvent structure factor $S_{11}(q)$. The bulk correlation length is denoted by $\xi$, whereas the inverse Debye length is given by $\kappa$. The contrast of impurity-solvent interactions is measured by the parameter $|g|$ (see Eq. (3.11)). For $|g| \leq 1$ (see panels (a) and (b)) a monotonic structure factor is found, whereas a non-monotonic behaviour with a maximum close to the Debye length $1/\kappa$ occurs for $|g| > 1$ (see panels (c) and (d)). In the latter situation the maximum diverges at a sufficiently large but finite bulk correlation length (see panel (d)). (See Ref. [44])

phase diagram if and only if $|g| \leq 1$, i.e. if the contrast of impurity-solvent interactions is sufficiently small. This can be understood in such a way that a contrast of impurity-solvent interactions ($|g| > 0$) promotes density fluctuations of finite wave length of the solvent, which may be enhanced by the long-ranged density fluctuations occurring upon approaching a critical point.

Fundamental insight is gained by addressing the question on the origin of a sufficiently strong contrast of impurity-solvent interactions ($|g| > 1$). Non-monotonic solvent structure factors have indeed been found in heavy water+3-methylpyridine mixtures in the presence of sodium tetraphenylborate ($NaBPh_4$) by means of small-angle neutron scattering (SANS) [267, 390]. However, the same solvent under the same conditions with simple salt impurities (LiCl, NaCl, NaBr, KCl and $MgSO_4$) led to monotonic solvent structure factors [388, 389]. This experimental observation implies that the valency of impurity ions is *not* expected to be the origin for impurity-induced non-uniformities of the solvent. In agreement with this, it has been concluded within a theoretical model [43], which is not plagued by the artifacts present in the model of Ref. [334], that neither the valency nor differences in solubility give rise to a sufficiently large parameter $|g| > 1$. The experimental results of ions in water+3-methylpyridine mixtures can be explained by steric effects, i.e. due to the property of (ionic) impurities being structure-makers or structure-breakers.

For molecular-sized impurity particles $c_{12}^{(0)} \sim (R_1 + R_2)^3$ and $c_{13}^{(0)} \sim (R_1 + R_3)^3$ can be expected, where $R_i$ denotes the extension of a particle of component $i$. Hence, according to Eq. (3.11), $|g| > 1$ may be reached for impurities of significantly different particle sizes (e.g. $Na^+$ and $[BPh_4]^-$), whereas $|g| < 1$ for particles of similar size (e.g. simple salts).

It is important to understand that it is not the valency, i.e. the charge, but the long-ranged character ($\sim 1/r$) of electrostatic interactions of the impurities which gives rise to the relevance of the parameter $|g|$ for the formation of a non-uniform solvent structure. However, whether the solvent becomes non-uniform upon adding ionic impurities is mainly determined by the size-differences between the impurity particles [44].

While the systems considered so far were composed of molecular particles, it is interesting to consider the colloidal limit, where one of the impurity components (component 2, say) comprises charged colloids, whereas the solvent (component 1) and the second impurity component (component 3, playing the role of counterions) are of molecular size. Under these conditions one has to expect $c_{12} \sim R_2^2$ and $z_2 \sim R_2^2$, because the colloid-solvent interaction as well as the colloid charge will be proportional to the surface area of the colloids. One realises from Eq. (3.11) that $|g|$ remains finite for $R_2 \to \infty$. The magnitude of $|g|$ in the colloidal limit is determined by adsorption (i.e. solubility) properties, which, as mentioned above, usually lead to $|g| < 1$.

The formation of a non-uniform (microheterogeneous) bulk fluid due to ionic impurities with sufficiently large contrasts of impurity-solvent interactions is a general feature of ionic complex fluids. The typical fundamental length scale of such microheterogeneities is of the order of the Debye length, which depends only weakly on the specific material properties of the ionic components. The structures formed have been qualitatively described as "membranes" and "multilamellar vesicles" [393, 394], but a detailed classification is still an open question.

## 3.3 Dielectric properties of dense ionic fluids

As RTILs are used as solvents in chemical studies, their polarity is one of the most important characteristics because it describes the global solvation capability of the solvent. In this context an interesting surface force apparatus (SFA) study of the interaction between a mica and a gold surface in an environment of the pure RTIL $[C_4mim][NTf_2]$ is reported in Ref. [154], which, after subtracting the steric repulsion and the van der Waals attraction from the force data, led to the conclusion of a double layer attraction corresponding to a Debye length of more than 10 nm. In aqueous electrolyte solutions such large Debye lengths are brought about by an ionic strength of less than 1 mM, which is puzzeling in the light of the large ion number density of an RTIL. Hence it has been proposed in Ref. [154] to view pure RTILs as dilute electrolyte solutions with a few mobile ions in an effective solvent made of temporarily paired ions. Whereas these SFA data have been doubted [155, 352], the interpretation of RTILs as dilute electrolyte solutions has attracted some interest [257]. For non-conducting fluids the static dielectric constant $\varepsilon$ is well defined and precisely measurable (see, e.g., Ref. [32, 306]). However, conducting fluids, such as ionic fluids, are well-known to perfectly screen external charges at *long* ranges [175, 422] so that the corresponding static dielectric constant is infinitely large. On the other hand, it is also well-known that cations and anions form a characteristic alternating pair structure at *short* ranges [175, 422], which, when considering neighbouring cation-anion pairs, is

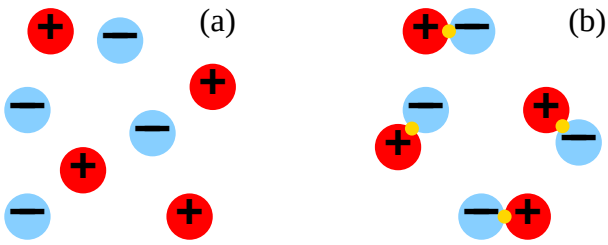


Figure 3.5: Sketch of (a) the restricted primitive model (RPM) and (b) the corresponding dumbbell model (DM) with particles being constructed by pairwise gluing together oppositely charged hard spheres of the RPM. (See Ref. [487])

analogous to the charge separation inside dipolar molecules. Therefore, it appears that the dielectric properties of dense ionic fluids depend on the length scale.

One possibility is to analyse the response of bulk ionic fluids to a static nonuniform electric field which spatially varies on a particular length scale [487]. It has to be stressed that this approach focusses on nonuniform static electric fields, the response onto which is described in terms of the wavenumber-dependent dielectric function $\varepsilon(k)$, whereas numerous experimental studies consider uniform time-dependent fields, which give rise to the frequency-dependent dielectric function $\varepsilon(\omega)$ (see, e.g., [86, 278, 465, 466]). Both quantities, $\varepsilon(k)$ and $\varepsilon(\omega)$, are not easily related because the former describes the equilibrium structure whereas the latter quantifies the dynamics in uniform electric fields.

The dielectric properties of a substance can be interpreted in terms of two well-known mechanisms [9]: Orientation polarisation refers to the rotation of dipolar moments upon keeping the magnitude constant, whereas distortion polarisation describes the change of magnitude of dipolar moments at constant orientations. The according orientation susceptibility $\chi_{\text{ori}}(k)$ and distortion susceptibility $\chi_{\text{dis}}(k)$ both contribute to the total electric susceptibility $\chi(k) = \varepsilon(k) - 1 = \chi_{\text{ori}}(k) + \chi_{\text{dis}}(k)$. However, in order to infer the dominant polarisation mechanism as a function of the wave number $k$, one has to somehow determine the decomposition of the observable $\chi(k) = \varepsilon(k) - 1$ into the orientation and the distortion contribution. Perfect screening in ionic fluids and the according divergence $\chi(k) \to \infty$ in the limit $k \to 0$ [175, 422] corresponds to a dominating distortion polarisation in the long-wavelength limit. This long-range behaviour of ionic fluids is in sharp contrast to that of dipolar fluids, whose electric susceptibility $\chi(k)$ attains a finite limit $\chi(0)$ as $k \to 0$.

A decomposition of the electric susceptibility $\chi(k)$ of an ionic fluid into the orientation and the distortion susceptibility $\chi_{\text{ori}}(k)$ and $\chi_{\text{dis}}(k)$, respectively, can be achieved as follows [487]: In addition to determine the electric susceptibility $\chi(k)$ of the ionic fluid composed of freely moving cations and anions, a corresponding dipolar fluid is considered whose particles are overall charge-neutral dumbbells formed by gluing together pairs of cations and anions of the ionic fluid. This dipolar fluid does not exhibit distortion polarisation, i.e. $\chi_{\text{dis}}(k) = 0$, but only pure orientation polarisation, i.e. $\chi(k) = \chi_{\text{ori}}(k)$, and the latter can be expected to be similar to $\chi_{\text{ori}}(k)$ of the corresponding ionic fluid at short ranges [487]. The applicability of this approach can be used for any ionic fluid model.

Whereas various models and force fields for realistic RTILs exist [119], the model used in Ref. [487] to represent the ionic fluid is the three-dimensional restricted primitive model (RPM), i.e. a collection of $N/2$ positively and $N/2$ negatively charged hard spheres of

equal diameter $\sigma$ and equal absolute valencies $|z_+| = |z_-|$ (see Fig. 3.5(a)). The interaction potential between two ions of species $i$ and $j$ with $i, j \in \{+, -\}$ at positions $\boldsymbol{r}_i$ and $\boldsymbol{r}_j$, respectively, can be described as

$$\beta U_{ij}(\boldsymbol{r}_i, \boldsymbol{r}_j) = \begin{cases} \dfrac{z_i z_j l_\mathrm{B}}{|\boldsymbol{r}_i - \boldsymbol{r}_j|} & , |\boldsymbol{r}_i - \boldsymbol{r}_j| \geq \sigma \\ \infty & , |\boldsymbol{r}_i - \boldsymbol{r}_j| < \sigma \end{cases} \tag{3.13}$$

with the vacuum Bjerrum length $l_\mathrm{B} = \beta e^2/(4\pi\varepsilon_0)$, where $e$ is the elemenatry charge, $\beta = 1/(k_\mathrm{B}T)$ denotes the inverse temperature and $\varepsilon_0$ is the vacuum permittivity.

In Ref. [487] the dielectric properties of the RPM (see Fig. 3.5(a)) are compared with those of a corresponding dipolar fluid model whose particles are composed of one cation and one anion of the RPM glued together (see Fig. 3.5(b)). The particles within this dumbbell model (DM) possess three positional and two orientational degrees of freedom, in contrast to six translational degrees of freedom of a pair of ions within the RPM. Obviously, all configurations of $N/2$ dumbbells correspond to possible configurations of the RPM with $N/2$ positive and $N/2$ negative hard spheres, but not all configurations of the RPM can be realised within the DM. The interaction energy between two dumbbell particles is given by the sum of contributions Eq. (3.13) of the constituent charged hard spheres.

The dielectric properties of ionic and dipolar fluids can be studied by analysing the linear response of the above models in the presence of a weak static nonuniform external electric field. Within the linear response regime the dielectric properties are given by the dielectric function tensor $\overleftrightarrow{\varepsilon}(\boldsymbol{k})$ or, equivalently, by the electric susceptibility tensor $\overleftrightarrow{\chi}(\boldsymbol{k}) = \overleftrightarrow{\varepsilon}(\boldsymbol{k}) - 1$. However, since electrostatic fields are purely longitudinal due to Faraday's law, the polarisation field is also purely longitudinal in isotropic fluids. Therefore, only the longitudinal components (parallel to the wave vector $\boldsymbol{k}$)

$$\begin{aligned} \varepsilon(\boldsymbol{k}) := \varepsilon_\parallel(\boldsymbol{k}) &= \frac{\boldsymbol{k} \cdot \overleftrightarrow{\varepsilon}(\boldsymbol{k}) \cdot \boldsymbol{k}}{\boldsymbol{k}^2} \quad \text{and} \\ \chi(\boldsymbol{k}) := \chi_\parallel(\boldsymbol{k}) &= \frac{\boldsymbol{k} \cdot \overleftrightarrow{\chi}(\boldsymbol{k}) \cdot \boldsymbol{k}}{\boldsymbol{k}^2} = \varepsilon(\boldsymbol{k}) - 1 \end{aligned} \tag{3.14}$$

are of relevance [487].

It can be shown [176] that the longitudinal dielectric function $\varepsilon(\boldsymbol{k})$ is related to the charge-charge structure factor

$$S_{zz}(\boldsymbol{k}) = \frac{1}{N} \left\langle \sum_m z_m \exp(-i\boldsymbol{k} \cdot \boldsymbol{r}_m) \sum_n z_n \exp(i\boldsymbol{k} \cdot \boldsymbol{r}_n) \right\rangle \tag{3.15}$$

via

$$\frac{1}{\varepsilon(\boldsymbol{k})} = 1 - \frac{4\pi l_\mathrm{B}}{\boldsymbol{k}^2} \frac{N}{V} S_{zz}(\boldsymbol{k}). \tag{3.16}$$

In Ref. [487] the averaging in Eq. (3.15) is obtained by means of grandcanonical Monte Carlo simulations of the RPM and of the DM in a cubic box of side length $V^{1/3} = 10\sigma$ with periodic boundary conditions using Metropolis sampling [5, 146, 297] and Ewald's method [5, 137, 146].

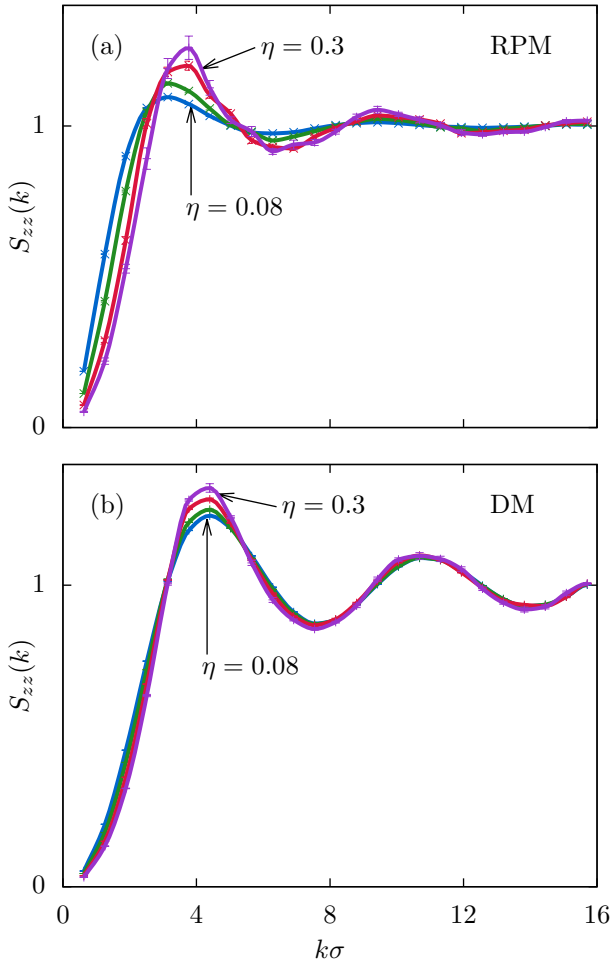


Figure 3.6: Charge-charge structure factor of (a) the RPM (Fig. 3.5(a)) and (b) the DM (Fig. 3.5(b)) for the temperature $T^* = 1$ and various values of the packing fraction $\eta \in \{0.08, 0.14, 0.23, 0.3\}$. (See Ref. [487])

The thermodynamic state of the RPM can be characterised by the packing fraction $\eta = \pi N\sigma^3/(6V)$ and the temperature $T^* = \sigma/l_\mathrm{B}$; the corresponding plasma parameter is given by $\Gamma = 2\eta^{1/3}/T^*$.

Figures 3.6(a) and (b) display the charge-charge structure factors $S_{zz}(\boldsymbol{k})$ of the RPM ionic fluid and of the DM, respectively. It is apparent that $S_{zz}(\boldsymbol{k})$ of the ionic fluid is sensitive to density changes only for very low packing fractions $\eta$. The slightly more pronounced oscillations of $S_{zz}(\boldsymbol{k})$ within the DM (Fig. 3.6(b)) as compared to those within the RPM (Fig. 3.6(a)) are perhaps an artifact of the DM, within which two charged hard spheres are kept exactly at a distance $\sigma$, whereas the principal peak of the cation-anion pair distribution function within the RPM has a finite width [487].

Using Eq. (3.16), Fig. 3.7 displays the inverse dielectric functions $1/\varepsilon(\boldsymbol{k})$ of the RPM and of the DM. The perfect screening condition [176, 422] implies $1/\varepsilon(\boldsymbol{k}) \to 0$ for $\boldsymbol{k} \to 0$ for an ionic fluid due to the asymptotic behaviour of the charge-charge structure factor [176]

$$S_{zz}(\boldsymbol{k}) \overset{\boldsymbol{k}\to 0}{\simeq} \frac{\boldsymbol{k}^2}{\kappa^2} \tag{3.17}$$

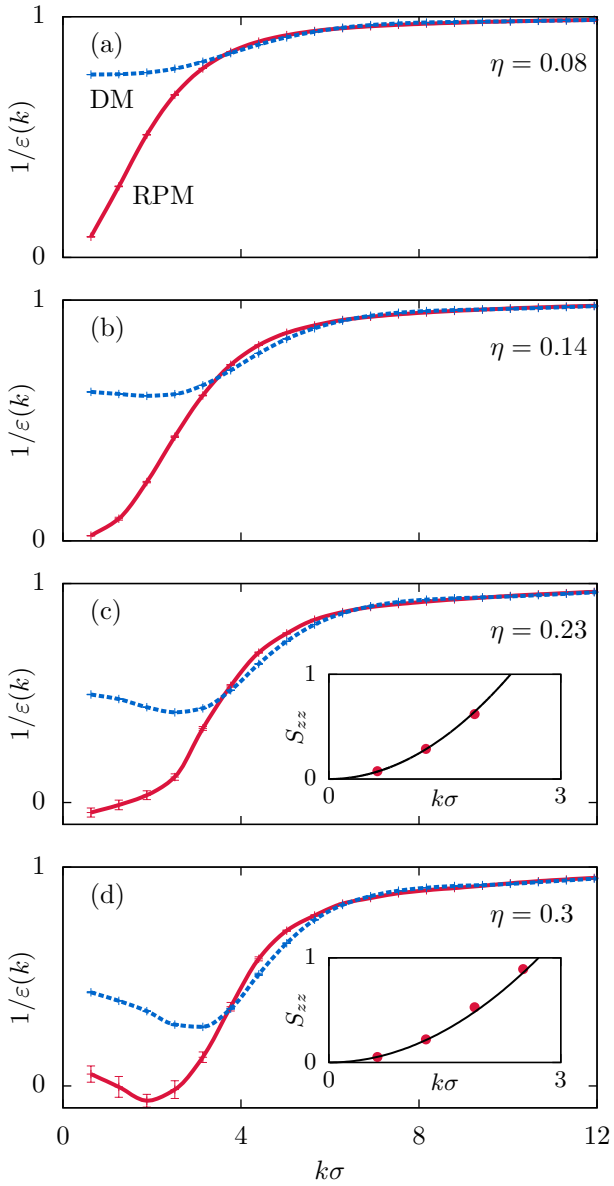


Figure 3.7: Inverse dielectric functions $1/\varepsilon(\boldsymbol{k})$ of the RPM ionic fluid (red solid lines, see Fig. 3.5(a)) and of the DM dipolar fluid (blue dashed lines, see Fig. 3.5(b)) at temperature $T^* = 1$ and packing fractions $\eta \in \{0.08, 0.14, 0.23, 0.3\}$. Whereas $1/\varepsilon(\boldsymbol{k} \to 0)$ becomes small (i.e. $\varepsilon(\boldsymbol{k} \to 0)$ becomes large) for the ionic fluid, the dielectric function of the dipolar fluid approaches a finite value $\varepsilon(0)$ for small wavenumbers. The inset in panels (c) and (d) compares the charge-charge structure factor $S_{zz}(\boldsymbol{k})$ obtained by means of Monte Carlo simulations (red circles) with the asymptotic behaviour Eq. (3.17) (black solid line). (See Ref. [487])

with the Debye length $1/\kappa$ being given by $\kappa^2 = 4\pi l_\mathrm{B} N/V$, which is shown in the insets of Figs. 3.7(c) and 3.7(d). Since the DM can exhibit only orientation polarisation, its dielectric function $\varepsilon(\boldsymbol{k} \to 0)$ approaches a finite value of the "dielectric constant" $\varepsilon(0)$, which increases upon increasing the packing fraction $\eta$ (see Fig. 3.7).

In order to determine the dominant polarisation mechanism in an ionic fluid the inverse

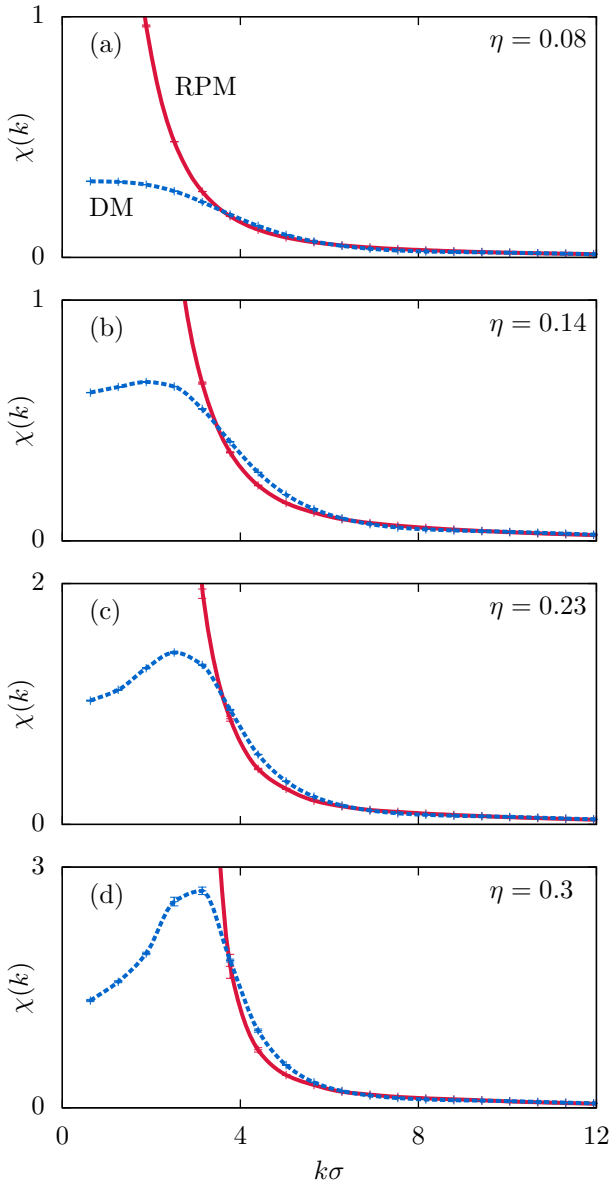


Figure 3.8: Electric susceptibility $\chi(\boldsymbol{k}) = \varepsilon(\boldsymbol{k}) - 1$ of the RPM ionic fluid (red solid lines, see Fig. 3.5(a)) and of the DM dipolar fluid (blue dashed lines, see Fig. 3.5(b)) at temperature $T^* = 1$ and packing fractions $\eta \in \{0.08, 0.14, 0.23, 0.3\}$. Whereas $\chi(\boldsymbol{k} \to 0)$ diverges for the ionic fluid due to the perfect screening of the external charges, the susceptibility of the dipolar fluid approaches a finite value $\chi(0)$ for small wavenumbers. At large wavenumbers $|\boldsymbol{k}|\sigma \gtrsim 2\pi$ the electric susceptibility $\chi(\boldsymbol{k}) = \chi_{\text{ori}}(\boldsymbol{k}) + \chi_{\text{dis}}(\boldsymbol{k})$ of the RPM almost coincides with that of the DM, which, by construction, possesses only orientation polarisation whose electric susceptibility can be expected to be close to $\chi_{\text{ori}}(\boldsymbol{k})$ of the RPM (see Fig. 3.5). (See Ref. [487])

dielectric functions $1/\varepsilon(\boldsymbol{k})$ of the RPM and of the DM in Fig. 3.7 are converted into the electric susceptibilities $\chi(\boldsymbol{k}) = \varepsilon(\boldsymbol{k}) - 1$. Figure 3.8 shows that the electric susceptibility $\chi^{\text{RPM}}(\boldsymbol{k}) = \chi^{\text{RPM}}_{\text{ori}}(\boldsymbol{k}) + \chi^{\text{RPM}}_{\text{dis}}(\boldsymbol{k})$ of the RPM, which comprises a contribution $\chi^{\text{RPM}}_{\text{ori}}(\boldsymbol{k})$ due to orientation polarisation and a contribution $\chi^{\text{RPM}}_{\text{dis}}(\boldsymbol{k})$ due to distortion polarisation,

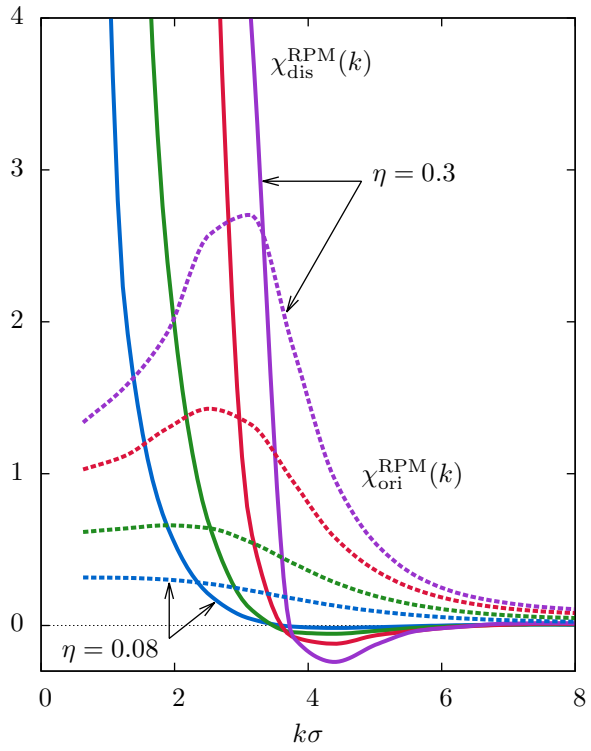


Figure 3.9: Distortion susceptibilities $\chi_{\rm dis}^{\rm RPM}(\boldsymbol{k})$ (solid lines) and orientation susceptibilities $\chi_{\rm ori}^{\rm RPM}(\boldsymbol{k})$ (dashed lines) of the RPM at temperature $T^* = 1$ for packing fractions $\eta \in \{0.08, 0.14, 0.23, 0.3\}$. Perfect screening corresponds to the divergence of $\chi_{\rm dis}^{\rm RPM}(\boldsymbol{k})$ in the long wavelength limit $|\boldsymbol{k}| \to 0$. The region of negative distortion susceptibility, $\chi_{\rm dis}^{\rm RPM}(\boldsymbol{k}) < 0$, can be interpreted as overscreening. At sufficiently large wave numbers orientation polarisation dominates over distortion polarisation with the crossover wave numbers increasing with the packing fraction $\eta$ (see Fig. 3.10). (See Ref. [487])

almost coincides in the range $|\boldsymbol{k}|\sigma \gtrsim 2\pi$ with the electric susceptibility $\chi^{\rm DM}(\boldsymbol{k}) = \chi_{\rm ori}^{\rm DM}(\boldsymbol{k})$ of the DM, which, by construction, exhibits only orientation polarisation with susceptibility $\chi_{\rm ori}^{\rm DM}(\boldsymbol{k})$. Since for sufficiently large packing fractions $\eta$ it can be expected that the orientation susceptibility $\chi_{\rm ori}^{\rm RPM}(\boldsymbol{k})$ of the RPM is identical to the electric susceptibility $\chi_{\rm ori}^{\rm DM}(\boldsymbol{k})$ of the DM, i.e. $\chi_{\rm ori}^{\rm RPM}(\boldsymbol{k}) = \chi_{\rm ori}^{\rm DM}(\boldsymbol{k})$ for all wavenumbers $\boldsymbol{k}$, one can infer the orientation and the distortion susceptibility of the RPM separately [487]:

$$\begin{aligned} \chi_{\rm ori}^{\rm RPM}(\boldsymbol{k}) &= \chi^{\rm DM}(\boldsymbol{k}), \\ \chi_{\rm dis}^{\rm RPM}(\boldsymbol{k}) &= \chi^{\rm RPM}(\boldsymbol{k}) - \chi^{\rm DM}(\boldsymbol{k}). \end{aligned} \tag{3.18}$$

Figure 3.9 clearly indicates that, at $T^* = 1$, orientation polarisation is the dominant mechanism of the RPM at sufficiently large wave numbers $\boldsymbol{k}$, whereas distortion polarisation is dominating at sufficiently small wave numbers $\boldsymbol{k}$. The weak distortion polarisation, i.e. $\chi_{\rm dis}^{\rm RPM}(\boldsymbol{k}) \approx 0$ at large wave numbers $\boldsymbol{k}$ (see Fig. 3.9) can be attributed to the impenetrable hard cores of the ions of the RPM. The crossover wavenumber between distortion-dominated and orientation-dominated polarisation increases with packing fraction $\eta$. There is a certain interval of wavenumbers $|\boldsymbol{k}|\sigma \approx 4 \ldots 5$ with $\chi_{\rm dis}^{\rm RPM}(\boldsymbol{k}) < 0$ (see Fig. 3.9), which indicates overscreening, which is caused by steric effects, i.e. by the

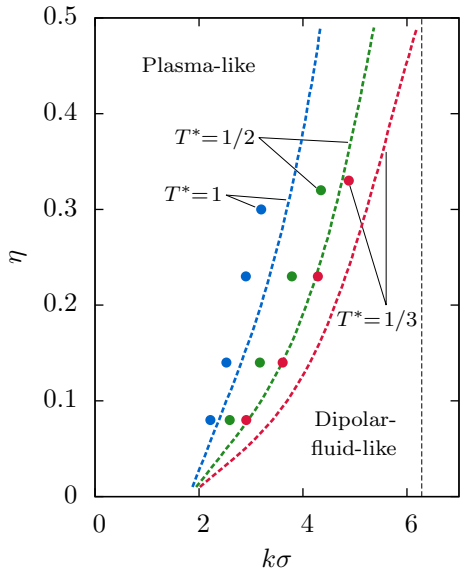


Figure 3.10: Crossover wave numbers $k^{\times}(\eta, T^*)\sigma$ of the RPM between plasma-like behaviour for $k < k^{\times}(\eta, T^*)$ and dipolar-fluid-like behaviour for $k > k^{\times}(\eta, T^*)$ as functions of the packing fraction $\eta$ and of the temperature $T^*$. The crossover wave number $k^{\times}(\eta, T^*)$ is defined by equal orientation and distortion susceptibilities, $\chi_{\text{ori}}^{\text{RPM}}(k^{\times}) = \chi_{\text{dis}}^{\text{RPM}}(k^{\times})$ (see Eq. (3.18)). The dots correspond to simulation data whereas the dashed lines are obtained by means of the simple approximative calculation described in the main text. The latter captures the correct trends of increasing values $k^{\times}(\eta, T^*)\sigma$ upon increasing the packing fraction $\eta$ or decreasing the temperature $T^*$. (See Ref. [487])

hard ion cores, too. The distortion susceptibility of the RPM diverges for $\boldsymbol{k} \to 0$ according to $\chi_{\text{dis}}^{\text{RPM}}(\boldsymbol{k}) \sim 1/\boldsymbol{k}^2$, which corresponds to the perfect screening property of plasmas [176, 422]. Hence, the RPM ionic fluid exhibits dielectric properties similar to a dipolar fluid at short range, whereas it behaves plasma-like at long range.

Figure 3.10 displays the crossover wave numbers $k^{\times}(\eta, T^*)\sigma$ (dots •), defined by equal orientation and distortion susceptibilities, $\chi_{\text{ori}}^{\text{RPM}}(k^{\times}) = \chi_{\text{dis}}^{\text{RPM}}(k^{\times})$, as functions of the packing fraction $\eta$ and of the temperature $T^*$. The RPM exhibits plasma-like behaviour for $k < k^{\times}(\eta, T^*)$ and dipolar-fluid-like behaviour for $k > k^{\times}(\eta, T^*)$. The general trend is that of increasing values of $k^{\times}(\eta, T^*)\sigma$ upon increasing the packing fraction $\eta$ or decreasing the temperature $T^*$. However, it can be expected that $k^{\times}(\eta, T^*) < 2\pi/\sigma$ for any set of parameters $(\eta, T^*)$ since an external electric field oscillating with a wave length of the ion diameter $\sigma$ cannot lead to distortion polarisation, i.e. the crossover $\chi_{\text{ori}}^{\text{RPM}}(k^{\times}) = \chi_{\text{dis}}^{\text{RPM}}(k^{\times})$ has to occur at some smaller wave number [487]. The dashed lines in Fig. 3.10 correspond to an approximation of $k^{\times}(\eta, T^*)\sigma$ with $\chi^{\text{RPM}}(\boldsymbol{k})$ in Eq. (3.18) being approximated within the mean spherical approximation (MSA) of the RPM [176] and with $\chi^{\text{DM}}(\boldsymbol{k})$ in Eq. (3.18) being approximated by the expression of a single dumbbell particle in an external electric field. Whereas this simple approximation slightly overestimates the value of $k^{\times}(\eta, T^*)\sigma$, the general trends of increasing values of $k^{\times}(\eta, T^*)\sigma$ upon increasing the packing fraction $\eta$ or decreasing the temperature $T^*$ are captured correctly. Hence for dense ionic fluids, e.g. inorganic fused salts ($\eta \approx 0.5, T^* \approx 1/30$) or RTILs ($\eta \approx 0.5, T^* \approx 1/50$), one can expect plasma-like behaviour in a very wide range of wave numbers $k < k^{\times}$ with $2\pi/k^{\times}$

corresponding almost to the size of the ions [487].

The main observation of Ref. [487], that the RPM ionic fluids exhibits dielectric properties similar to a dipolar fluid at short range whereas it behaves plasma-like at long range, does not hinge on any peculiar property of the RPM and can hence be expected to be made for other ionic fluids, too. Moreover, the approach to decompose the electric susceptibility $\chi(\boldsymbol{k}) = \chi_{\mathrm{ori}}(\boldsymbol{k}) + \chi_{\mathrm{dis}}(\boldsymbol{k})$ into a contribution $\chi_{\mathrm{ori}}(\boldsymbol{k})$ due to orientation polarisation and a contribution $\chi_{\mathrm{dis}}(\boldsymbol{k})$ due to distortion polarisation by introducing a corresponding dipolar fluid made of cation-anion compounds applies to the case of other ionic fluids, too. In general, the structure of the cation-anion compounds comprising the dipolar fluid corresponding to an ionic fluid can be conjectured on the basis of, e.g., the pair distribution function, which is routinely calculated for numerous ionic fluid models (see, e.g., Ref. [120, 339]).

However, these results are restricted to bulk ionic fluids and they cannot be directly applied quantitatively in the context of the discussion on the interpretation of the above-mentioned SFA measurements in an RTIL environment [154, 155, 352], which are related to confined ionic fluids. The reason for this restriction is that the static dielectric function for non-uniform systems is of the form $\varepsilon(\boldsymbol{k}, \boldsymbol{k}')$ due to the absence of translational symmetry. On the other hand, the qualitative picture above implies, that strongly confined ionic fluids tend to behave as dipolar fluids whereas they progressively exhibit plasma-like properties upon relaxing the confinement. This suggests that the recently debated interpretation of RTILs as dilute electrolyte solutions [154, 257] might not be simply a yes-no-question but it might depend on the considered length scale [487]. The general feature, that the static dielectric properties of ionic complex fluids depend on the length scale, may be considered complementary to the observation that the quantification of the polarity of RTILs depends on the intrinsic time scale of the measurement [278].

The conclusion one can draw from the study in Ref. [487] is that ionic complex fluids behave as a plasma on length scales larger than the molecular size, where steric interactions and chemical bonding dominate. However, if the ionic strength is sufficiently large such that the Debye length is not larger than the molecular size, e.g. for RTILs in the liquid phase, this large-scale plasma behaves as a uniform fluid of quasi-non-interacting particles, because all correlations decay on much smaller (molecular) lengths.

## 3.4 Effective interaction in dense ionic fluids

It is well-known that the Coulomb interaction acts repulsively for equally-charged and attractively for oppositely-charged ions and it decays $\sim 1/r$, i.e. it is long-ranged. On the other hand, the thermodynamic limit of globally charge-neutral Coulombic systems exists [252, 271] because the pair distribution functions of an ionic fluid decay exponentially, which is called the Stillinger-Lovett perfect screening property [176, 275, 421, 422] and which is a necessary consequence of the long range of the Coulomb potential [288, 304]. It is a challenge for more than a century now to develop quantitatively reliable theoretical descriptions of this peculiar combination of properties. For dilute electrolyte solutions Debye-Hückel theory [140, 233, 254] is typically a good starting point, whereas for dense ionic systems ion-pairing is relevant [275, 421]. From experimental work [33, 474–476] as well as continuum simulations [229, 279, 341, 482], there is evidence that in particular the critical behaviour of ionic systems is very similar to the Ising universality class, which

typically applies to systems with short-ranged interactions. This result suggests that the long-range character of the bare Coulomb potential might be of minor importance for the critical properties of ionic fluids.

The relevance of the long range of the Coulomb interaction for the whole phase diagram and the bulk structure has been investigated in Ref. [24], where the lattice restricted primitive model (LRPM) for the Coulomb potential being truncated smoothly on a length scale $1/\alpha$ and sharply at a cut-off radius $r_{\text{cut}}$ has been considered. The long-ranged LRPM is well-known to exhibit tricritical behaviour at the crossover from a first- to a second-order phase transition between a charge-ordered and a charge-disordered phase [105, 375]. The (L)RPM renders the ions as homogeneous charged hard spheres, which is of course not valid for ionic liquids in general, since they may exhibit charge as well as shape anisotropy. However, in order to investigate the relevance of the long range of the electrostatic interaction for the properties of ionic fluids simple models are sufficient, because the impact of the long range will not depend on rather short-range features like charge or shape anisotropy. Upon varying the smooth cut-off decay constant $\alpha$ and the sharp cut-off radius $r_{\text{cut}}$, the short-ranged LRPM can be tuned from a system void of a charged-ordered phase via one exhibiting charge-ordered and charge-disordered phases but differing quantitatively from the long-ranged LRPM to a model with short-ranged interactions whose phase behaviour and structure is quantitatively the same as for the long-ranged Coulomb interaction [24]. Moreover, even the Stillinger-Lovett perfect screening property can be fulfilled for suitable smooth cut-off potentials, an observation which is not trivial in the context of short-ranged interactions. Since the characteristic phase behaviour and structure of ionic fluids can also be found in systems with short-ranged potentials, it can be concluded that the decisive property of the electrostatic potential in ionic fluids is not the long range but rather the valency dependence.

Consider the lattice restricted primitive model (LRPM) of univalent cations (valency $z_{\oplus} = +1$) and anions (valency $z_{\ominus} = -1$) with hard cores of diameter $\sigma$ occupying but not necessarily exhausting the sites of a three-dimensional simple cubic lattice with lattice constant $\sigma$. Global charge neutrality is guaranteed by an equal number of cations and anions in the system, and the hard cores ensure that each site is either empty or singly occupied. Within the original LRPM two ions of species $i, j \in \{\oplus, \ominus\}$ at a distance $r$ interact, besides the hard core exclusion, via the infinitely-ranged Coulomb potential $\dfrac{l_b z_i z_j}{r}$, where $l_b = \dfrac{e^2}{4\pi\varepsilon kT}$ is the Bjerrum length with the electronic permittivity $\varepsilon$, the Boltzmann constant $k$, and the temperature $T$, and where $r$ is measured with the Euclidean metric.

One possibility to study the relevance of the long-range character of the Coulomb interaction for the properties of ionic systems is to consider the implications of replacing the infinitely-ranged Coulomb potential by the truncated Coulomb-like potential [24]

$$\beta\phi_{p,q}(\mathbf{r}, z_i, z_j) = \begin{cases} \dfrac{l_b z_i z_j}{\|\mathbf{r}\|_p} \operatorname{erfc}(\alpha\|\mathbf{r}\|_p) & , \|\mathbf{r}\|_q \leq r_{\text{cut}} \\ 0 & , \|\mathbf{r}\|_q > r_{\text{cut}} \end{cases} \tag{3.19}$$

with the inverse temperature $\beta = 1/(kT)$, the decay constant $\alpha \geq 0$, and the cut-off radius $r_{\text{cut}}$. By means of Eq. (3.19) two different methods of cutting off the Coulomb potential can be studied: On the one hand, the factor $\operatorname{erfc}(\alpha\|\mathbf{r}\|_p)$, leads to a smooth cutting off on the length scale $1/\alpha$, and, on the other hand, a sharp cutting off at ra-

dius $\|\mathbf{r}\|_q = r_{\text{cut}}$ can be considered. Analogous to the short-ranged potentials appearing within the Ewald method [137], the smoothening factors can be chosen as complementary error functions $\text{erfc}(x) = 2/\pi \int_x^\infty \mathrm{d}\tau \exp(-\tau^2)$. Obviously, the infinitely-ranged Coulomb potential corresponds to $\alpha = 0, r_{\text{cut}} = \infty$. Besides the Euclidean norm $\|\mathbf{r}\|_2 = \sqrt{x^2+y^2+z^2}$ to measure distances, the 1-norm $\|\mathbf{r}\|_1 = |x| + |y| + |z|$ and the supremum norm $\|\mathbf{r}\|_\infty = \max(|x|, |y|, |z|)$ are considered, which are more adapted to a lattice model since, for lattice vectors $\mathbf{r}$, they lead to values which are integer multiples of the lattice constant $\sigma$ [24]. Since all norms are equivalent in finite dimensions, the power law $\sim 1/r$ is asymptotically preserved irrespective of the choice of the norm. The parameters $p$ and $q$ in Eq. (3.19) describe the norms to be used for measuring the distance determining the interaction potential and the sharp cut-off, respectively.

In order to discuss the thermal and structural properties of the LRPM with the truncated Coulomb-like interaction Eq. (3.19), the packing fraction $\eta$ and the pair distribution functions $g_{ij}(r)$, $i, j \in \{\oplus, \ominus\}$, are determined in Ref. [24] for cubic boxes $\mathcal{V} := \{0, \sigma, \ldots, (L-1)\sigma\}^3, L \in \mathbb{N}$, with periodic boundary conditions using grandcanonical Monte Carlo simulations. The set of all configurations $\zeta$ of cations and anions occupying $\mathcal{V}$ can be expressed as the set of all maps $\zeta : \mathcal{V} \to \{0, z_\oplus, z_\ominus\}$, which result in the charge $\zeta(\mathbf{r}) \in \{0, z_\oplus, z_\ominus\}$ located at position $\mathbf{r} \in \mathcal{V}$, i.e. $\zeta(\mathbf{r}) = 0$ iff site $\mathbf{r}$ is empty, $\zeta(\mathbf{r}) = z_\oplus$ iff site $\mathbf{r}$ is occupied by a cation, and $\zeta(\mathbf{r}) = z_\ominus$ iff site $\mathbf{r}$ is occupied by an anion. Standard Metropolis importance sampling [297] of the grandcanonical Boltzmann distribution $P(\zeta) \sim \exp(\beta\mu N[\zeta] - \beta H[\zeta])$ with the chemical potential $\mu$, the total number of ions $N[\zeta] = N_\oplus[\zeta] + N_\ominus[\zeta]$ and the Hamiltonian

$$\beta H[\zeta] = \frac{1}{2} \sum_{\substack{\mathbf{r},\mathbf{r}' \in \mathcal{V} \\ \mathbf{r} \neq \mathbf{r}'}} \beta\phi_{p,q}\left(\mathbf{r} - \mathbf{r}', \zeta(\mathbf{r}), \zeta(\mathbf{r}')\right) \tag{3.20}$$

on the set of all charge-neutral configurations $\zeta$ is applied. Charge neutrality is preserved during the simulation runs due to insertions and removals of only neutral pairs of cations and anions, i.e. the number of cations $N_\oplus[\zeta]$ equals the number of anions $N_\ominus[\zeta]$.

The packing fraction is the average

$$\eta = \frac{\langle N[\zeta] \rangle}{L^3} \tag{3.21}$$

and the pair distribution functions are given by

$$g_{i,j}(r) = \frac{4\langle N_{i,j}(r, [\zeta]) \rangle}{V_{\text{shell}}(r) L^3 \eta^2} \tag{3.22}$$

with $i, j \in \{\oplus, \ominus\}$, $r$ being a distance measured in the 1-norm, $V_{\text{shell}}(r) = 4(r/\sigma)^2 + 2$ representing the number of all sites in the shell of 1-norm distance $r$ around a site, and $N_{i,j}(r, [\zeta])$ denoting the total number of all ordered pairs $(\mathbf{r}_i, \mathbf{r}_j)$ of positions $\mathbf{r}_i, \mathbf{r}_j \in \mathcal{V}$ being separated by a 1-norm distance $r = \|\mathbf{r}_i - \mathbf{r}_j\|_1$ and such that an ion of species $i$ is located at position $\mathbf{r}_i$ and an ion of species $j$ is located at position $\mathbf{r}_j$. The pair distribution functions $g_{i,j}(r)$ are defined in terms of 1-norm distances $r$ because, for the simple-cubic lattice geometry, this choice is most convenient in order to distinguish charge-ordered and charge-disordered phases [24].

The structure of the charge-ordered and charge-disordered phase in terms of the pair distribution functions $g_{i,j}(r)$ is displayed in Fig. 3.11 for the case $T^* = \sigma/l_b = 2, L =$

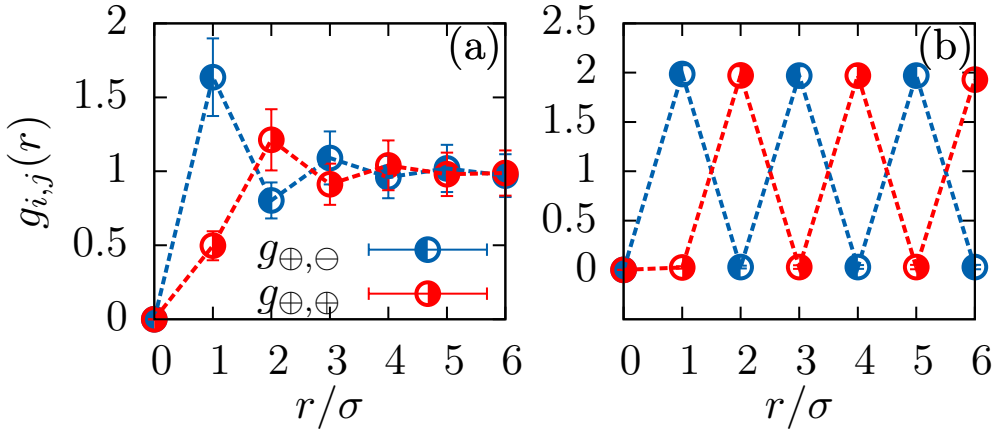


Figure 3.11: Pair distribution functions for $L = 12, \alpha = 0, r_{\text{cut}}/\sigma = 1$ using the 1-norm ($p = q = 1$) in Eq. (3.19) at temperature $T^* = 2$ and packing fraction $\eta = 0.37$ (a) and $\eta = 0.90$ (b). The red curves represent the pair distribution function for equally charged ions, while the blue curves represent those of oppositely charged ions. Panel (a) shows the structure of the charge-disordered phase, which is characterized by a rapid vanishing of the spatial correlations. Panel (b) displays the case of the charge-ordered phase, where correlations are long-ranged due to a shell-wise alternating distribution of cations and anions. (See Ref. [24])

$12, \alpha = 0, r_{\text{cut}}/\sigma = 1$ using the 1-norm ($p = q = 1$) in Eq. (3.19). For the charge-disordered phase, spatial correlations vanish rapidly, while for the charge-ordered phase one observes long-ranged correlations due to a shell-wise alternating assembly of cations and anions.

In order to locate the charge-ordered/charge-disordered phase transition, i.e. the $\lambda$-line, in the phase diagram, the staggered order parameter

$$\phi := \left\langle \frac{1}{L^3} \sum_{\mathbf{r} \in \mathcal{V}} (-1)^{||\mathbf{r}||_1} \zeta(\mathbf{r}) \right\rangle \tag{3.23}$$

is considered [24]. Figure 3.12 displays $|\phi|$ as a function of the chemical potential $\mu^* = \beta\mu$ for decay constant $\alpha = 0$, cut-off radius $r_{\text{cut}}/\sigma = 1$ and temperature $T^* = 1.67$ for box sizes $L \in \{12, 18\}$. For this example, the second-order phase transition, which is expected to belong to the Ising universality class [211], is located at $\mu^* \approx -1.65$.

For a sharp cutting off of the Coulomb potential, i.e. $\alpha = 0$ in Eq. (3.19), with cut-off radii $r_{\text{cut}}/\sigma \leq (L-1)/2$, the critical temperature $T_c^*$ using the 1-norm ($p = q = 1$) and the 2-norm ($p = q = 2$) in Eq. (3.19) is compared in Fig. 3.13 with the critical temperature $\Theta_c^* \in [0.14, 0.16]$ of the long-ranged Coulomb system, i.e. for $r_{\text{cut}} = \infty$ [105, 340, 375]. Distinct oscillations of $T_c^*$ for both 1-norm and 2-norm can be observed, where the amplitude of the latter is much smaller than that of the former. For both metrics, no sign of convergence of $T_c^*$ towards the value $\Theta_c^*$ of the long-ranged potential are observable within the considered range of cut-off radii $r_{\text{cut}}$. Moreover, the amplitude of the oscillations appears to even increase for the 1-norm. This odd-even-dependence likewise occurs within the structure for sufficiently large packing fractions: While for odd values of $r_{\text{cut}}/\sigma$ a charge-ordered phase is realised at large packing fractions, no

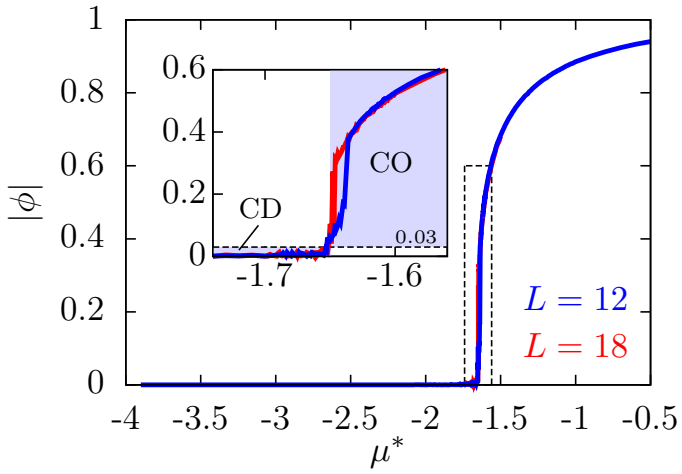


Figure 3.12: Staggered order parameter $|\phi|$ (see Eq. (3.23)) as a function of the chemical potential $\mu^*$ for decay constant $\alpha = 0$, cut-off radius $r_{\text{cut}}/\sigma = 1$ using the 1-norm ($p = q = 1$) in Eq. (3.19), and temperature $T^* = 1.67$ for box sizes $L \in \{12, 18\}$. It signals the second-order phase transition between the charge-disordered (CD) phase, where $|\phi| \approx 0$, and the charge-ordered (CO) phase, where $|\phi| \not\approx 0$. In order to account for finite-size effects, the convention is adopted that the phase transition occurs at $|\phi| = 0.03$, which is located at $\mu^* \approx -1.65$ here. (See Ref. [24])

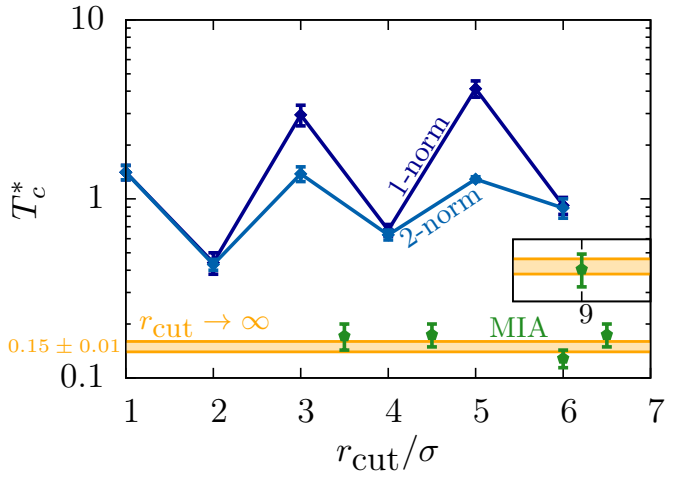


Figure 3.13: Critical temperature $T_c^*$ as a function of the cut-off radius $r_{\text{cut}}$ for sharp cut-off truncation schemes, where the decay constant $\alpha = 0$ is used in Eq. (3.19). Data points labeled by '1-norm' and '2-norm' are obtained by truncation of the Coulomb potential at distances $r_{\text{cut}}/\sigma \leq (L-1)/2$, where all distances are measured in the respective norms, i.e. $p = q$. Moreover, the values within the minimum image approximation ('MIA') are displayed, which corresponds to $p = 2, q = \infty, r_{\text{cut}}/\sigma = (L-1)/2$. By comparison with the critical temperature $\Theta_c^* \in [0.14, 0.16]$ for the long-ranged Coulomb potential ($r_{\text{cut}} = \infty$) one observes that the MIA results match the long-range value very well, whereas the 1-norm and the 2-norm results largely overestimate the critical temperature. (See Ref. [24])

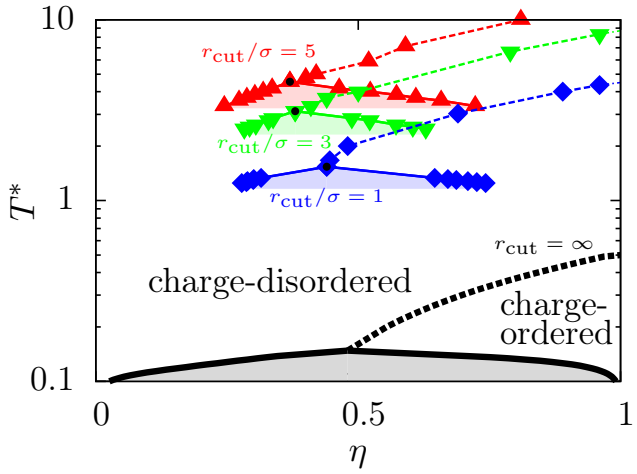


Figure 3.14: Phase diagrams for 1-norm metric ($p = q = 1$ in Eq. (3.19)), decay constant $\alpha = 0$, box size $L = 12$, and cut-off radii $r_{\rm cut}/\sigma \in \{1, 3, 5\}$ compared with that of the conventional long-ranged LRPM ($r_{\rm cut} = \infty$ [375]). All these phase diagrams exhibit the same topology of a charge-ordered and a charge-disordered phase separated by a first-order phase transition below and a continuous phase transition above a tricritical point (•). However, for the cases with finite values of the cut-off radius $r_{\rm cut}$, the tricritical temperature is about an order of magnitude too high and it *increases* upon increasing $r_{\rm cut}$. (See Ref. [24])

charge-ordering is observed for even values of $r_{\rm cut}/\sigma$. This feature can be understood in terms of simple energy considerations of perfectly charge-ordered configurations [24]. The absence of a charge-ordered phase in the case of even-valued cut-off radii and the increasing deviation of the critical temperature $T_c^*$ from that of the conventional LRPM with long-ranged Coulomb potential, $\Theta_c^* \in [0.14, 0.16]$ in the case of odd-valued cut-off radii leads to the conclusion of some major defect of the sharp cut-off scheme.

Figure 3.14 displays the phase diagrams for cut-off radii $r_{\rm cut}/\sigma \in \{1, 3, 5\}$ (1-norm, $p = q = 1$). Close to the critical point, the binodals follow a straight line, which corresponds to the critical exponent $\beta = 1$. Due to this observation and since the $\lambda$-line terminates at the critical point, this critical point actually is a *tricritical* point (tagged by a black dot). The long-ranged LRPM qualitatively shows the same phase diagram, including tricriticality. In accordance with the results of Fig. 3.13, the tricritical point moves upwards to higher temperatures for larger odd values of $r_{\rm cut}/\sigma$; however, the topology of the phase diagram is not affected. It has already been mentioned that for even values of the cut-off radius $r_{\rm cut}/\sigma$ no charge-ordered phase is present so that a phase separation occurs between a charge-disordered gas and a charge-disordered liquid, and the phase diagram exhibits an ordinary critical point and no $\lambda$-line.

The phase diagram for odd values of the cut-off radius $r_{\rm cut}/\sigma \leq (L-1)/2$ turned out to be qualitatively identical to the phase diagram of the conventional long-ranged LRPM, but the tricritical point is located at a too high temperature $T_c^*$, which even increases upon increasing $r_{\rm cut}$. Another sharp cut-off scheme is discussed in Ref. [24] which, in the notation of Eq. (3.19), can be specified by $\alpha = 0, q = \infty, r_{\rm cut}/\sigma = (L-1)/2$. This cut-off scheme is equivalent to the well-known minimum image approximation (MIA) [72, 297], which disregards all contributions to the interaction energy, which do not correspond to

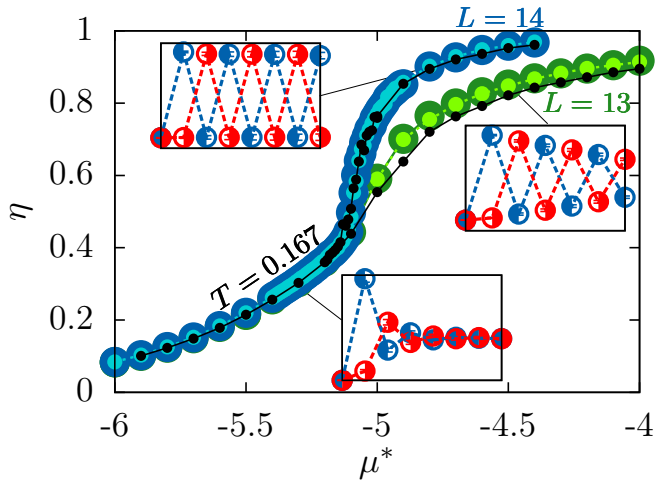


Figure 3.15: Comparison of the equations of state and of the pair distribution functions for odd and even box sizes $L$. The green and blue dots in the main plot correspond to results within MIA ($p = 2, q = \infty, \alpha = 0, r_{\text{cut}}/\sigma = (L-1)/2$ in Eq. (3.19)) and the black dots are obtained by means of the Ewald method. The same odd-even-effect of $L$ in the high-density regime is encountered within both methods. Furthermore, the high-density phase displays decorrelations in the case of odd values of $L$, whereas the charge ordering is long-ranged in the case of even values of $L$. The occurrence of decorrelations in the high-density phase for odd-valued $L$ can be understood in terms of equally charged ions at the rim of the simulation box, which interact with each other due to periodic boundary conditions. (See Ref. [24])

the minimum distance between two ions or their periodic images. For a cubic simulation box, it can be interpreted such that only those interactions within a cut-off distance $\|\mathbf{r}\|_\infty \leq r_{\text{cut}}$ are taken into account, where the cut-off radius $r_{\text{cut}}$ has to be chosen such that the interaction range equals a cube of volume $L^3$ with $L = 2r_{\text{cut}}/\sigma + 1$. Note, that the distances, which determine interaction potential, are measured in the $p$-norm (see Eq. (3.19)), which is chosen as $p \in \{1, 2\}$.

Figure 3.13 also displays the critical temperatures $T_c^*$ within MIA for $p = 2$, which are in excellent agreement with the critical temperature $\Theta_c^* \in [0.14, 0.16]$ of the long-ranged LRPM. Moreover, the MIA results in Fig. 3.13 can be subdivided into integer and half-integer values of $r_{\text{cut}}/\sigma$, which corresponds respectively to odd and even values of the box size $L = 2r_{\text{cut}}/\sigma + 1$. A close look at Fig. 3.13 reveals that the values of $T_c^*$ within MIA for odd values of $L$ are slightly below those for even values of $L$, which indicates a certain odd-even effect of $L$ on $T_c^*$. Whereas the odd-even effect of $L$ on $T_c^*$ is rather weak, Fig. 3.15 shows for the examples $L = 13$ and $L = 14$ that there is a significant odd-even effect of $L$ on the equation of state and on the structure at large packing fractions. The reason for mentioning the odd-even effects of $L$ within MIA here is that exactly the same odd-even effects of $L$ occur for the long-ranged LRPM using the full Ewald method, which are shown in Fig. 3.15, too. In other words, MIA is such a good approximation of the full Ewald method that it exhibits even the same odd-even effects [24].

The insets in Fig. 3.15, which show the pair distribution functions at the indicated thermodynamic states, reveal a distinct charge-ordering behaviour in the high-density regime for even box sizes $L$, whereas for odd $L$ a decaying oscillatory behaviour of the

pair distribution functions can be observed. Although the latter behaviour does not correspond to a genuine charge-ordered phase, it is clearly different from the structure in the dilute regime, where correlations decay rapidly. What is the reason for this qualitatively different high-density structure for even and odd box sizes $L$? In the limit of perfect charge-ordering at sufficiently high densities, the periodic boundary conditions lead to destabilizing contributions to the interaction energy for odd values of $L$, since in this case there are equally charged ions located at the rim of the simulation box which, due to the periodicity, are nearest neighbours. This effect does not occur for even box sizes $L$. Since this is obviously an effect related to the 'surface' of the simulation box, it decreases with increasing box size $L$. The same odd-even dependence of the equation of state and of the structure is observable within the long-ranged LRPM. As a consequence of the above argumentation, the results for even box sizes $L$, whether using MIA or the full Ewald method, can be expected to be more accurate, than for odd box sizes $L$ [24].

It is striking that isotherms within MIA sample the long-range limit $r_{\mathrm{cut}} \to \infty$ very well for dilute as well as for dense systems. This indicates that the Hamiltonian of an ionic fluid with long-ranged Coulomb interaction can be reliably approximated by Eq. (3.20) with $p = 2, q = \infty, \alpha = 0, r_{\mathrm{cut}}/\sigma = (L-1)/2$ in Eq. (3.19). In fact, for $L = 14$, there is almost no difference between MIA and the full Ewald method with respect to the equations of state (see Fig. 3.15).

This quantitative agreement can be understood as follows: The contribution to the energy due to the long-ranged Coulomb potential beyond MIA involves the electrostatic interaction of the simulation box with its images, which, due to the charge neutrality of the simulation box, decays at least as a dipole-dipole interaction, i.e. $\sim 1/r^3$. However, numerical calculations reveal that the dipole-dipole contribution vanishes and that the decay is actually $\sim 1/r^4$, which renders the long range contributions beyond MIA absolutely convergent and, for sufficiently large $L$, small. The same argument does not apply to the sharp cut-off potentials, since no charge neutrality inside spheres of radius $r_{\mathrm{cut}}$ within the underlying norm is guaranteed so that the long range contributions beyond those due to the sharp cut-off potential are due to an effective monopole-monopole interaction, i.e. $\sim 1/r$, and, hence, typically not small [24].

Figure 3.16 displays the phase diagram within MIA for $r_{\mathrm{cut}}/\sigma = 4.5$; those for $r_{\mathrm{cut}}/\sigma \in \{6, 6.5, 9\}$ obtained similarly are not shown here. For all considered cases of $r_{\mathrm{cut}}$, the phase diagrams are qualitatively and quantitatively in accordance with those obtained by means of the corresponding full Ewald method. The important point is that the MIA can be interpreted as a sharp cut-off truncation scheme of the Coulomb potential. The results discussed above indicate that the long-range character of the electrostatic interaction may not be necessary for the thermal and structural properties of ionic fluids, because there is the possibility that the same properties can be generated by suitable short-ranged interactions. A comparison of the MIA, where $r_{\mathrm{cut}}/\sigma = (L-1)/2$, with the sharp cut-off schemes, where $r_{\mathrm{cut}}/\sigma \leq (L-1)/2$, reveals that the ability of a sharp cut-off scheme to mimic the properties of the long-ranged LRPM depends delicately on the relation between the cut-off radius $r_{\mathrm{cut}}$ and the size of the simulation box $L$. However, the simulation box $L$ is not a physical but rather a technical parameter, and the properties of the LRPM within reasonable sharp cut-off schemes Eq. (3.19) with $\alpha = 0$ should be independent of (large values of) $L$. Consequently, there are no sharp cut-off schemes which quantitatively reproduce the thermal and structural properties of the long-ranged LRPM and which, at the same time, correspond to physically acceptable underlying short-ranged interactions.

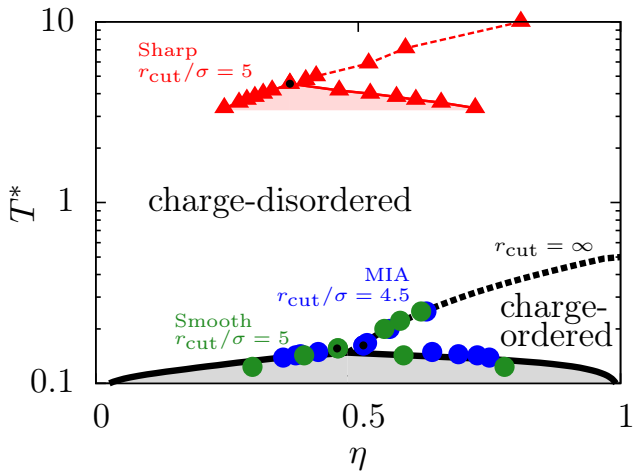


Figure 3.16: Comparison of the phase diagrams of the LRPM within the sharp cut-off scheme $p = q = 1, \alpha\sigma = 0, r_{\rm cut}/\sigma = 5 \leq (L-1)/2$ in Eq. (3.19), the MIA ($p = 2, q = \infty, \alpha\sigma = 0, r_{\rm cut}/\sigma = 4.5 = (L-1)/2$), the smooth cut-off scheme ($p = q = 2, \alpha\sigma = 0.8, r_{\rm cut}/\sigma = 5 \leq (L-1)/2$) and the long-ranged Coulombic interaction ($\alpha\sigma = 0, r_{\rm cut} = \infty$). The agreement of the MIA and the smooth cut-off scheme with the case of the long-ranged interaction is excellent, whereas there are large quantitative deviations of the sharp cut-off scheme with $r_{\rm cut}/\sigma \leq (L-1)/2$. (See Ref. [24])

In order to remedy this, potentials Eq. (3.19) with $\alpha > 0$ can be considered [24], which correspond to a smooth cutting off of the Coulomb potential on the length scale $1/\alpha$. Note, that this type of functions occurs within the Ewald method as a result of splitting the total electrostatic potential into a short-ranged contribution, which leads to a sum in real space, and a long-ranged contribution, which leads to a sum in reciprocal space. Within the Ewald method, $\alpha$ is adjusted such that, on the one hand, the error due to the unavoidable truncation of the sums in real and reciprocal space are sufficiently small and that, on the other hand, the computational effort is acceptable. However, here $\alpha$ controls the decay length of a genuine short-ranged interaction, which can take, in principle, any (positive) value. For $\alpha \to 0$ the sharp cut-off truncation are obtained.

Figure 3.17 displays the critical temperature $T_c^*$ and the critical packing fraction $\eta_c$ of the LRPM with smooth cut-off potentials Eq. (3.19) with $p = q = 2, r_{\rm cut}/\sigma \in \{1, 5\}$ as functions of the decay constant $\alpha\sigma$. For $r_{\rm cut}/\sigma = 5$ a plateau of $T_c^*$ is present in the range $\alpha\sigma \in [0.4, 1.0]$, where the critical temperature $T_c^*$ is quantitatively equivalent to the critical temperature $\Theta_c^*$ of the long-ranged LRPM (see Fig. 3.17(a)). For larger values of $\alpha\sigma$ the decay length of the interaction Eq. (3.19) becomes too short, so that even nearest neighbours barely interact with each other. Hence, for $\alpha\sigma \to \infty$, one obtains the ideal gas limit and consequently $T_c^* \to 0$. For $r_{\rm cut}/\sigma = 1$ all contributions beyond the nearest neighbours are neglected, and no plateau is observable at all. However, the critical packing fraction $\eta_c \approx 0.5$ appears to be independent of the decay constant $\alpha$ and the cut-off radius $r_{\rm cut}$. In addition to the coincidence of the critical points for the appropriate choice of $\alpha\sigma$, a charge-ordered phase at large packing fractions and a charge-disordered phase at small packing fractions can be found. Ultimately, the phase diagrams of the smooth cut-off scheme are in quantitative agreement with the long-ranged limit, too (see Fig. 3.16).

The long-range character of the Coulomb interaction is well-known to generate the so-

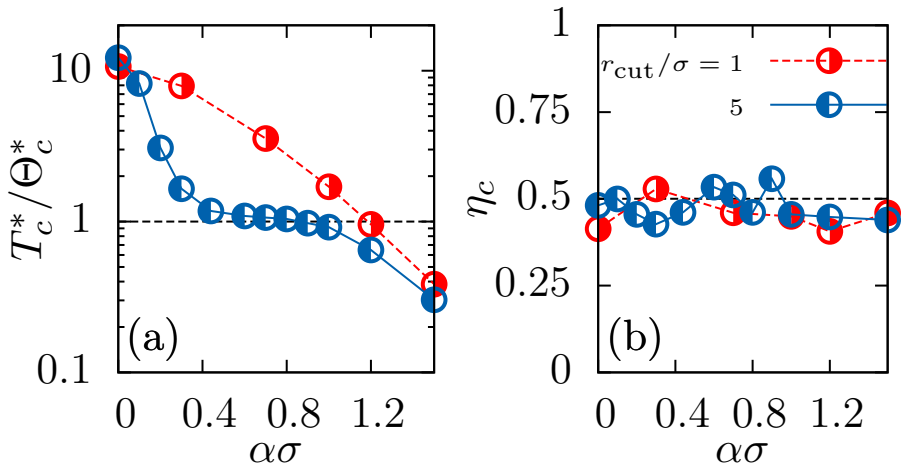


Figure 3.17: Critical temperature $T_c^*$ and critical packing fraction $\eta_c$ of the LRPM with smooth cut-off potentials Eq. (3.19) with $p = q = 2, L = 12, r_{\rm cut}/\sigma \in \{1, 5\}$ as functions of the decay constant $\alpha\sigma$. For $r_{\rm cut}/\sigma = 5$ the critical temperature $T_c^*$ exhibits a plateau around $\alpha\sigma \approx 0.8$ which is close to the critical temperature $\Theta_c^*$ of the long-ranged Coulombic system. As in Figs. 3.13, 3.14, and 3.16, the critical temperature $T_c^*$ within sharp cut-off schemes ($\alpha\sigma = 0$) is an order of magnitude to high. The critical packing fraction $\eta_c \approx 0.5$ is rather independent of the decay constant $\alpha$ and the cut-off radius $r_{\rm cut}$. (See Ref. [24])

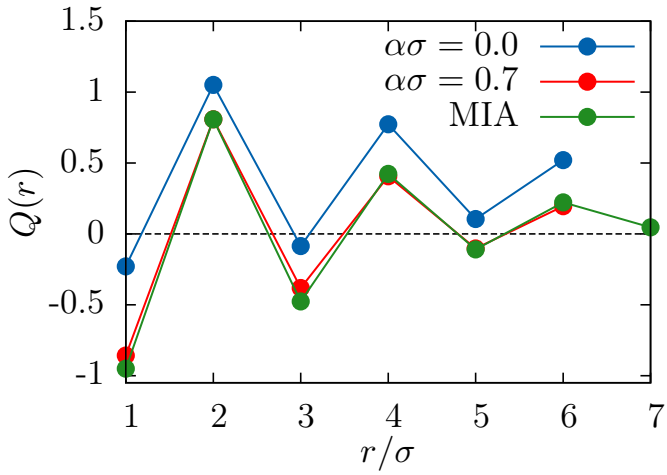


Figure 3.18: Accumulated charge $Q(r)$ (see Eq. (3.24)) up to a distance $r$ in 1-norm around a positively charged central ion. The Stillinger-Lovett sum rule [176, 275, 421, 422] requires $Q(r)$ to vanish in the limit of large distances $r \to \infty$. This condition appears to be fulfilled within the charge-disordered phase (here at packing fraction $\eta \approx 0.3$) for the case of the smooth cut-off potential $\alpha\sigma = 0.7$ ($p = q = 2, r_{\rm cut}/\sigma = 5, L = 12$) as well as for the MIA ($\alpha\sigma = 0, p = 2, q = \infty, r_{\rm cut}/\sigma = 6.5 = (L-1)/2, L = 14$), but not for the sharp cut-off potential $\alpha\sigma = 0$ ($p = q = 2, r_{\rm cut}/\sigma = 1, L = 12$). (See Ref. [24])

called Stillinger-Lovett perfect screening property of ionic fluids [176, 275, 288, 304, 421,

422]. In the present context of an LRPM it corresponds to the accumulated charge [24]

$$Q(r) := 1 + \frac{\eta}{2} \sum_{\substack{\mathbf{r}' \in \mathcal{V} \\ 1 \leq \|\mathbf{r}'\|_1 \leq r}} \left[ g_{\oplus,\oplus}(\mathbf{r}') - g_{\oplus,\ominus}(\mathbf{r}') \right] \tag{3.24}$$

up to a 1-norm distance $r$ around a positively charged central ion to vanish $Q(r) \to 0$ in the limit $r \to \infty$. Figure 3.18 compares the accumulated charge $Q(r)$ for the sharp cut-off potential with $\alpha\sigma = 0, r_{\text{cut}}/\sigma = 1, p = q = 2$, the MIA with $\alpha\sigma = 0, r_{\text{cut}}/\sigma = 6.5, p = 2, q = \infty$ and the smooth cut-off potential $\alpha\sigma = 0.7, r_{\text{cut}}/\sigma = 5, p = q = 2$ within the charge-disordered phase at packing fraction $\eta \approx 0.3$. For the sharp cut-off potential, $Q(r)$ appears to converge towards a non-vanishing (positive) value for large radii $r$, which corresponds to an imperfect screening of the positive central charge. However, perfect screening occurs within the MIA and the smooth cut-off potential. This is an interesting finding since, in contrast to the long-range Coulomb potential, the perfect screening property is not necessarily fulfilled in systems with short-ranged interactions [24].

It can be shown for smoothly cut off potentials Eq. (3.19) with $r_{\text{cut}}\alpha \gg 1$ that the charge-charge pair correlation function $h_{zz}(r) := 2\left(g_{\oplus,\oplus}(r) - g_{\oplus,\ominus}(r)\right)$, which is related to the accumulated charge $Q(r)$ in Eq. (3.24), decays asymptotically on the length scale of the Debye length $1/\kappa$ with $(\kappa\sigma)^2 = 4\pi\eta/T^*$ iff $\kappa \gg 2\alpha$. Since $\alpha > 0$ is a constant, which is chosen to match the phase diagram of the long-ranged Coulomb interaction (see Figs. 3.16 and 3.17) and which does not depend on the thermodynamic state $(\eta, T^*)$, the condition $\kappa \gg 2\alpha > 0$ will not be fulfilled at very low packing fractions $\eta$ and/or high temperatures $T^*$, i.e. the Debye-Hückel limit is not recovered within smooth cut-off schemes. However, this is not a major defect for two reasons [24]: On the one hand, the remaining parts of the phase diagram outside the region of the Debye-Hückel limit, particularly in the range of high densities, e.g. close to the critical point ($\eta_c \approx 0.5$), are reproduced quantitatively (see Figs. 3.16 and 3.17). On the other hand, the crossover, where the condition $\kappa \gg 2\alpha$ begins to be violated, can be shifted to arbitrarily small values of $\kappa$ by decreasing $\alpha$, which can be achieved by accordingly increasing $r_{\text{cut}}$ (see Fig. 3.17(a)).

The findings of Ref. [24] can be summarised as follows: Concerning the phase behaviour and the structure, the LRPM with the smooth cut-off potentials is qualitatively equivalent to that with long-ranged Coulomb interactions. Moreover, by choosing an appropriate decay constant $\alpha$, the short-ranged smooth cut-off potential LRPM becomes even quantitatively equivalent to the conventional long-ranged LRPM. The essential difference to the sharp cut-off schemes is that these statements are independent of the choice of the actual (large) value of the simulation box $L$, i.e. the smooth cut-off potentials based on Eq. (3.19) are candidates of physically meaningful short-ranged interactions. Consequently, the long-range character of the electrostatic potentials is of minor importance for the thermal and structural properties of dense ionic fluids, since short-ranged interaction potentials do exist, which lead to the same thermal and structural properties.

It has to be stressed, that the remarkable result of Ref. [24] on dense ionic fluids is not that the Coulomb potential is screened, i.e. the charge-charge correlation function is short-ranged [75, 91, 92, 161, 162], but that the long-range character of the bare Coulomb potential is irrelevant for the phase behaviour and the structure. Rather the relevant feature of the electrostatic interaction for the behaviour of dense ionic complex fluids is the valency-dependence, i.e. the property that ions with charges of equal sign repel and

those with charges of opposite sign attract each other. This property in combination with material-specific steric and chemical interactions leads to more or less perturbed alternating charge structures in the bulk [311], at charged walls [300–302] and in between two electrodes [62–64, 138].

# Chapter 4

# Interfacial properties

Besides the intrinsic length scales which determine the bulk structure of of ionic complex fluids (Ch. 3) additional length scales are present at interfaces which influence the structure formation. Such an additional length scale related to the adsorption properties of ions in electrolyte solutions leads to the Ray-Jones effect of the surface tension (Sec. 4.1). Another example is the thickness of an adsorption layer close to an electrode which enters into the phenomenon of electrowetting (Sec. 4.4). The non-trivial structure formation, e.g. the unequal partitioning of ions in a non-uniform solvent, can give rise to unexpected features of the effective interaction between colloidal particles dispersed in an ionic complex fluid (Sec. 4.6). When comparing the Debye length with the size of the particles two extreme cases occur: in a dilute electrolyte solution the Debye length is larger than the size of the ions, whereas in a colloidal dispersion the Debye length is smaller than the size of the colloids. The wetting properties of these types of ionic complex fluids are discussed in Sec. 4.2 and 4.5. The competition between the Debye length and the bulk correlation length close to a critical point of the solvent gives rise to the question on the influence of ions onto the phenomenon of critical adsorption. It is shown in Sec. 4.3 that electrostatics is modifying the subleading contributions. Finally the effective interaction between colloidal particles trapped at the interface of two immiscible electrolyte solutions is determined by the structures of the ionic complex fluids at the colloid-fluid and fluid-fluid interfaces (Sec. 4.7).

## 4.1 Interfacial tension of electrolyte solutions

### Planar electrolyte interfaces

The temporal stability of liquid-liquid emulsions, which is of enormous importance for applications in, e. g., chemical, pharmaceutical, food and cosmetic industries, largely hinges on the liquid-liquid interfacial tension [48] modified by surfactants, cosurfactants and even colloidal particles [13–15, 18, 290, 387]. In order to theoretically understand and predict the liquid-liquid interfacial tension as a function of additives a first step is modeling a liquid-liquid interface in the presence of electrolytes but in the absence of surfactants. Remarkably, the dependence of the liquid-liquid interfacial tension on the electrolyte concentration is, in contrast to the liquid-gas surface tension [167, 284, 431], not widely studied. This is quite astonishing because liquid-liquid interfaces have been investigated for a long time by means of electrocapillary measurements [452]. The few

reported measurements of the liquid-liquid interfacial tension as a function of the ionic strength [12, 159, 168] seem to confirm the linear relation at large ionic strengths well-known from liquid-gas surface tension measurements [292, 468]. At low ionic strengths the liquid-gas surface tension exhibits the Jones-Ray effect, i.e. a minimum of the surface tension as a function of the ionic strength [216–220, 353, 354], whose analog for liquid-liquid interfacial tensions has been addressed in the experimental literature only in Ref. [168]. Theoretical approaches to liquid-gas surfaces are very often based on the assumption that the gas phase is completely free of ions [284], which leads to a charge neutral liquid phase. Considering the image charge interaction as dominating the liquid-gas surface tension at low ionic strength the Onsager-Samaras limiting law can be derived [69, 116, 263–265, 333]. However, assuming a non-vanishing ionic strength in the gas phase, Nichols and Pratt found indications that the liquid-gas surface tension in some instances can also scale with the square root of the ionic strength in the low salt limit [322]. By means of an elaborate Ginzburg-Landau-like model for liquid-liquid interfaces, taking ion densities and solvent composition explicitely into account, Onuki observed such a square root behaviour for the liquid-liquid interfacial tension, too [335–337]. It has been argued in Ref. [37] in terms of a *minimal* model that unequal ion partitioning and charge separation are the key features of liquid-liquid interfaces of electrolyte solutions at low ionic strength. Onsager-Samaras-like behaviour can be found only in the absence of unequal ion partitioning and is therefore unexpected for liquid-liquid interfaces.

In Ref. [37] an infinite system is considered which is composed of two homogeneous solvents $A$ and $B$ located within the half spaces $z < 0$ and $z > 0$, respectively, of a Cartesian coordinate system. In the interior of the solvents the relative dielectric constant $\varepsilon(z)$ at position $z$ is given by $\varepsilon(z < 0) = \varepsilon_A$ and $\varepsilon(z > 0) = \varepsilon_B$. Monovalent ions are distributed in *both* solvents giving rise to local equilibrium number densities $\varrho_\alpha(z)$ at position $z$ with $\alpha = +$ and $\alpha = -$ denoting cations and anions, respectively. Deep in the solvent phases local charge neutrality holds, i.e. $\varrho_\alpha(-\infty) =: \varrho_A$ and $\varrho_\alpha(\infty) =: \varrho_B$, which define the *partition coefficient* $p := \sqrt{\varrho_A/\varrho_B}$. In general, the solubility of $\alpha$ ions differs in the two solvents. This effect can be described by solvent-induced potentials $V_\alpha(z)$ which take the limiting values $V_\alpha(-\infty) := 0$ and $V_\alpha(\infty) := f_\alpha$ where $f_\alpha$ is the solvation free energy difference of an $\alpha$ ion in solvent $B$ as compared to solvent $A$ (compare Sec. 2.1). Such a partitioning at liquid-liquid interfaces also finds practical applications, e.g. for size separation of DNA [170]. Verwey and Niessen [449] assumed the steplike form $V_\alpha^{\mathrm{VN}}(z) = f_\alpha \Theta(z)$, where $\Theta$ denotes the Heaviside function. Such a model ignores interfacial effects due to an actually smooth dielectric function $\varepsilon$, finite ion size, van der Waals forces, solvation (structure making and structure breaking) and image charges [284]. All these effects depend on material parameters of the system but they depend, with the exception of the image charge interaction, not directly on the ionic strength. Moreover, the image charge interaction decays as $\mathcal{O}(\exp(-2\kappa_{A,B}|z|)/|z|)$ with $\kappa_{A,B}^{-1}$ denoting the Debye screening length in phase $A$ for $z \to -\infty$ and in phase $B$ for $z \to \infty$ [69, 116, 263–265, 284, 333, 335–337], whereas the electrostatic potential is expected to decay much slower as $\mathcal{O}(\exp(-\kappa_{A,B}|z|))$. Hence the image charge interaction is expected to be negligible outside the interfacial region. A simple account of the mentioned interfacial effects is given by the *shifted* Verwey-Niessen potentials $V_\alpha(z) := f_\alpha \Theta(z - s)$ where the discontinuity is located at position $z = s$, similar to the interface model by Johansson and Eriksson [214]. Note that the electrostatic potential is the only interaction which is *not* described by the solvent-induced potentials $V_\alpha$ because it is the longest-ranged

ionic-strength-dependent interaction. Moreover, the shift of the ion densities with respect to the solvent composition profile in Onuki's work [335–337] are compatible with the introduction of external fields similar to the present solvent-induced potentials $V_\alpha$. The location of the discontinuity of the solvent-induced potentials with respect to the dielectric interface at $z = 0$ is a property of the solvents and the electrolyte. The analysis of Ref. [37] in fact revealed that only changing the anion type can shift the discontinuity of $V_\alpha$ to the opposite side of the interface. Without restriction $s \geq 0$ is assumed, i.e. solvent $B$ is *defined* as the one where the discontinuity of $V_\alpha$ is located.

In units of the thermal energy $k_BT$, the elementary charge $e$, and the vacuum Bjerrum length $\ell = \dfrac{e^2}{4\pi\varepsilon_{\text{vac}}k_BT}$ with the permittivity of the vacuum $\varepsilon_{\text{vac}}$, and within a mean-field theory ignoring ion-ion correlations, the density functional of the grand potential per unit surface area

$$\Omega[\varrho_\pm] = \sum_{\alpha=\pm} \int \mathrm{d}z \varrho_\alpha(z) \Big( \ln(\varrho_\alpha(z)) - 1 - \mu_\alpha + V_\alpha(z) + \alpha \frac{1}{2} \phi(z, [\varrho_\pm]) \Big) \tag{4.1}$$

is to be minimised with respect to the ion density profiles $\varrho_\pm$. Here $\mu_\alpha$ is the chemical potential of species $\alpha$ and $\phi(z, [\varrho_\pm])$ is the electrostatic potential at position $z$, which is a functional of the ion density profiles $\varrho_\pm$.

The interfacial tension is known to be highly sensitive to details of the interfacial structure. In terms of the density functional $\Omega$ (see Eq. (4.1)) the interfacial tension in excess of the pure, salt-free liquid-liquid interface is given by $\Delta\gamma = \Omega[\varrho_+, \varrho_-] - \Omega[\varrho_{\text{ref}}, \varrho_{\text{ref}}]$, where $\varrho_{\text{ref}}$ is the steplike reference ion number density profile. For the excess interfacial tension with respect to the dielectric interface at $z = 0$ the reference density is defined by $\varrho_{\text{ref}}(z < 0) := \varrho_A$ and $\varrho_{\text{ref}}(z > 0) := \varrho_B$ which leads to [37]

$$\Delta\gamma = 2(1 - p^2)s\varrho_B - \frac{\phi_D^2\sqrt{\varepsilon_B}p}{2\sqrt{2\pi}D}(n\cosh(\kappa_i s) + \sinh(\kappa_i s))\sqrt{\varrho_B} \tag{4.2}$$

with $\kappa_i^2 := 8\pi\varrho_A/\varepsilon_B$. As the second term on the right-hand side of Eq. (4.2) is of the order $\mathcal{O}(-\sqrt{\varrho_B})$ for both $\varrho_B \to 0$ and $\varrho_B \to \infty$ one finds the following asymptotic behaviour of the excess interfacial tension [37]:

$$\Delta\gamma \simeq \begin{cases} -\dfrac{\phi_D^2\sqrt{\varepsilon_B}}{2\sqrt{2\pi}} \dfrac{np}{1+np}\sqrt{\varrho_B} & , \varrho_B \to 0 \\ 2(1-p^2)s\varrho_B & , \varrho_B \to \infty. \end{cases} \tag{4.3}$$

As $n$ and $p$ are experimentally accessible, one can use Eq. (4.3) to determine $\phi_D$ or $s$. The crossover, where the low-density asymptotics $\Delta\gamma = \mathcal{O}(-\sqrt{\varrho_B})$ and the high-density asymptotics $\Delta\gamma = \mathcal{O}(\pm\varrho_B)$ are of the same magnitude, takes place at the ionic strength [37]

$$\varrho_B^\times := \frac{\phi_D^4\varepsilon_A p^2}{32\pi s^2(1+np)^2(1-p^2)^2}. \tag{4.4}$$

For $\varrho_B > \varrho_A$ one finds $\Delta\gamma(\varrho_B \ll \varrho_B^\times) < 0$ and $\Delta\gamma(\varrho_B \gg \varrho_B^\times) > 0$, i. e., the excess interfacial tension vanishes near the crossover. For $\varrho_B < \varrho_A$, on the other hand, $\Delta\gamma(\varrho_B) < 0$ for all $\varrho_B$. As the two bulk ion concentrations $\varrho_A$ and $\varrho_B$ are proportional to each other within the present model, one can choose either one calling it the *ionic strength* $I$. Equation (4.4) leads to a corresponding crossover ionic strength $I^\times$.

These results have been derived from the *linear* Poisson-Boltzmann equation, which is expected to be reliable for small Donnan potential $|\phi_D| = |f_- - f_+|/2 \ll 1$. However, upon solving the *non-linear* Poisson-Boltzmann equation numerically, one finds the *same* asymptotic dependence on the ionic strength $I$, $\Delta\gamma(I \ll \widetilde{I}^{\times}) = \mathcal{O}(-\sqrt{I})$ and $\Delta\gamma(I \gg \widetilde{I}^{\times}) = \mathcal{O}(\pm I)$, as in Eq. (4.3) with a crossover at $\widetilde{I}^{\times} \geq I^{\times}$ where the difference $\widetilde{I}^{\times} - I^{\times}$ increases with $|\phi_D|$. Hence the asymptotic scaling of the interfacial tension difference $\Delta\gamma$ with the ionic strength $I$ and the existence of a crossover $I^{\times}$ are robust qualitative features of the linear theory when compared to the non-linear Poisson-Boltzmann theory. Moreover, by numerical fitting one obtains renormalised parameters $\phi_D^*$ and $s^*$ in Eq. (4.2) such that $\Delta\gamma$ calculated within non-linear Poisson-Boltzmann theory is reproduced even *quantitatively* [37].

As the asymptotic behaviour of the excess interfacial tension $\Delta\gamma = \mathcal{O}(\pm I)$ for $I \gg I^{\times}$ in Eq. (4.3) involves the parameter $s$ one concludes that the finite size of the interfacial region is responsible for this asymptotics. This finding is confirmed by published measurements of liquid-liquid interfacial tensions [12] and is in fact well-known from liquid-gas surface tensions [284, 292, 468]. In contrast, the behaviour $\Delta\gamma = \mathcal{O}(-\sqrt{I})$ for $I \ll I^{\times}$ in Eq. (4.3) can be attributed to the unequal ion partitioning because the prefactor of the asymptotics contains a term of electrostatic origin which vanishes if $\phi_D = 0$. The latter regime, which gives rise to a *negative* contribution to the interfacial tension, is in contradiction to the Onsager-Samaras limiting law $\mathcal{O}(-I\ln(I))$ [69, 116, 263–265, 333], which contributes *positively* [322]. However, according to the model in Ref. [37], the image charge interaction is neglected in comparision to the electrostatic potential due to the unequal ion partitioning, whereas it is the dominating interaction within the Onsager-Samaras model [69, 116, 263–265, 333]. Therefore it can be concluded that unequal ion partitioning, which is expected to be a general phenomenon for liquid-liquid interfaces [335–337], leads to $\Delta\gamma = \mathcal{O}(-\sqrt{I})$ for small $I$, whereas the absence of unequal ion partitioning gives rise to $\Delta\gamma = \mathcal{O}(-I\ln(I))$ [69, 116, 263–265, 333]. The situation of a liquid-gas surface with non-vanishing ionic strength in the gas phase investigated by Nichols and Pratt [322] can be considered as the borderline between both scenarios such that features of both, the square root and the Onsager-Samaras limiting law, can be visible.

From Eq. (4.4) one infers a high sensitivity of the crossover ionic strength $I^{\times}$ from the low ionic strength regime $\gamma(I \ll I^{\times}) = \mathcal{O}(-\sqrt{I})$ to the high ionic strength regime $\gamma(I \gg I^{\times}) = \mathcal{O}(\pm I)$ upon the model parameters $\phi_D$, $s$ and $p$, i.e. upon the material parameters of the system. This obervation is also borne out by the results of Onuki [335–337]. Hence, depending on the actual system under investigation, $I^{\times}$ can be larger or smaller than the experimentally available range of ionic strength as will be shown in the following [37].

Figure 4.1 displays the magnitude of the excess interfacial tension $|\Delta\gamma|$ of a water-decaline interface as a function of the ionic strength $I$ in *water* for three different salts, KSCN (△), KCl (◯), and KI (■), as published in Ref. [168]. The interfacial tension of a salt-free water-decaline interface is 50.94 $\mathrm{mNm}^{-1}$. The dashed lines are power laws $\sim I$ passing through the largest data points for KSCN and KCl, whereas the solid line is a power law $\sim I^{1/2}$ passing through the smallest data point for KI. Within the present model one concludes from Fig. 4.1 that the crossover ionic strength $I^{\times}$ for KSCN and KCl is smaller than 0.01M whereas for KI it is larger than 0.5M. The prediction $\Delta\gamma(I \ll I^{\times}) < 0$ from Eq. (4.3) is in agreement with the data for KI in Ref. [168]. Finally, the excess interfacial tension measured in Ref. [168] is *negative* for KSCN and *positive* for KCl.

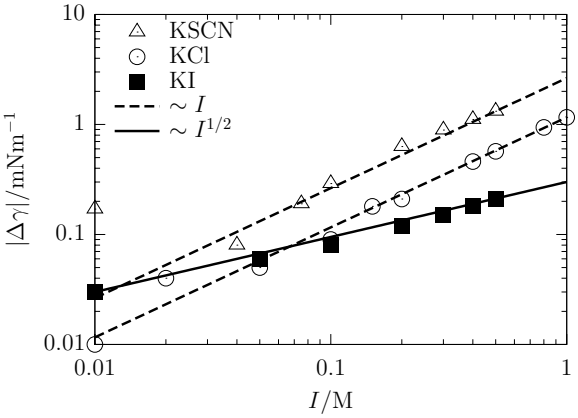


Figure 4.1: Magnitude of the excess interfacial tension $|\Delta\gamma|$ as a function of the ionic strength $I$ in water of a water-decaline interface for the three salts KSCN (△), KCl (◯), and KI (■) according to Ref. [168]. The interfacial tension of a salt-free water-decaline interface is 50.94 $\mathrm{mNm}^{-1}$. The dashed lines are power laws $\sim I$ whereas the solid line is a power law $\sim I^{1/2}$ both derived from the model (see Eq. (4.3)). (See Ref. [37])

Within the model this observation is to be interpreted as follows [37]: For the case of KSCN ($\Delta\gamma(I \gg I^{\times}) < 0$) one infers $p > 1$ from Eq. (4.3), and consequently in this case solvent $A$ is water and solvent $B$ is decaline, because the ionic strength in water is larger than in decaline. Assuming $p \gg 1$ Eq. (4.3) leads to $\Delta\gamma(I \gg I^{\times}) \simeq -2sI$ with $I = \varrho_A$ which, for KSCN, yields $s \approx 0.53$ nm. Hence the discontinuity of the solvent-induced potentials $V_\alpha$ for KSCN is located at a distance 0.53 nm on the *decaline*-side of a water-decaline interface. Here KSCN acts like a surfactant, which accumulates at the liquid-liquid interface and which reduces the interfacial tension [303]. For KCl ($\Delta\gamma(I \gg I^{\times}) > 0$), on the other hand, $p < 1$ due to Eq. (4.3), i.e. solvent $A$ is decaline and solvent $B$ is water. Assuming $p \ll 1$ gives rise to $\Delta\gamma(I \gg I^{\times}) \simeq 2sI$ with $I = \varrho_B$ which, for KCl, leads to $s \approx 0.23$ nm. Thus the discontinuity of $V_\alpha$ for KCl is located at a distance 0.23 nm on the *water*-side of the water-decaline interface. These findings suggest a weaker affinity of $\mathrm{Cl}^-$ for the organic decaline phase than $[\mathrm{SCN}]^-$, which agrees with the structure of these anions. Hence the excess interfacial tension data in Ref. [168] can be consistently described in terms of Eq. (4.3) with respect to the sign and the power law in the ionic strength. Moreover, $s$ is, as expected, comparable to the size of the ions [37].

It can be concluded that at small ionic strength $I$ the excess liquid-liquid interfacial tension of electrolyte solutions behaves as $\mathcal{O}(-\sqrt{I})$ due to an unequal partitioning of ions, whereas at large ionic strength it behaves as $\mathcal{O}(\pm I)$ due to a finite interfacial thickness. The occurrence of the asymptotic regimes at low ionic strengths, which is related to solvation properties and the interfacial structure, is a general property ionic complex fluids formed by electrolyte solutions, whose solvents cannot be considered as structureless.

## Curved electrolyte interfaces

Common wisdom in emulsion science tells that, in order to kinetically stabilise an emulsion of water and oil, say, surfactants are needed in order to decrease the interfacial tension thereby decreasing the thermodynamic force causing droplet coalescence [395]. This pic-

ture has been upset in Refs. [261, 262], where it has been shown experimentally that in certain additive-free water-oil mixtures micron-sized water droplets in oil may be stabilised electrostatically by absorbing ions present in the system. Several aspects of these experiments such as the proposed charging of the water droplets due to an unequal partitioning [37, 490, 491] and the formation of a colloidal crystal of water droplets [96] can be understood theoretically within a simple Poisson-Boltzmann model. However, to understand the rather unimodal size distribution of the water droplets in the above-mentioned experiments as well as the observation of experimental indications of the existence of thermodynamically favoured droplet radii in certain emulsions stabilised by nano-sized colloids [387] requires a radius dependent water-oil interfacial tension because otherwise the global minimum of the free energy would be attained for one single macroscopic drop [39]. One is thereby led to the problem of analysing the liquid-liquid interfacial tension as a function of the droplet radius.

The study of the curvature dependence of liquid-vapour surface tensions has been pioneered by Gibbs [158], Tolman [433] and Kirkwood and Buff [231]. Tolman introduced a low-curvature expansion of the form $\gamma(a)/\gamma(\infty) \simeq 1/(1+2\delta/a) \simeq 1-2\delta/a$ where $a$ denotes the radius of curvature, $\gamma(a)$ is the surface tension of the curved surface, and $\gamma(\infty)$ is its planar value. The parameter $\delta$, which has the dimension of length, is called the *Tolman length* and it can be identified with the spatial distance between the Gibbs dividing surface and the surface of tension. In the last decades the concept of a curvature dependent liquid-vapour surface tension has been taken up within various studies on critical phenomena [139], interface elasticity [52] and nucleation [22, 426].

However, whereas in all these investigations the droplet and the surrounding bulk were composed of the same substance, albeit in different phases, here a mixture of two different liquids and ions is studied. Moreover, only the excess interfacial tension due to the electrolyte is of interest here while the two liquids forming droplet and bulk merely act as external fields onto the ions.

The investigation in Ref. [39] is carried out within the spherical version of the model studied in Ref. [37] (see Subsec. 4.1). As in Ref. [37] linearisation of the Poisson-Boltzmann equation offers the possibility of closed analytical expressions for the interfacial tension. The approximative analytical expressions for the interfacial tension can be shown to at least qualitatively, in many realistic cases even quantitatively, agree with the numerical results obtained within the full, non-linear theory.

In the following dimensionless quantities are expessed in units of the thermal energy $k_{\mathrm{B}}T$, the elementary charge $e$, and the vacuum Bjerrum length $\ell = \dfrac{e^2}{4\pi\varepsilon_{\mathrm{vac}}k_{\mathrm{B}}T}$ with the permittivity of the vacuum $\varepsilon_{\mathrm{vac}}$. Dimensional quantities are denoted by the same symbol as the corresponding dimensionless quantities.

Consider a liquid spherical droplet of radius $a$ and relative dielectric constant $\varepsilon_{\mathrm{d}}$ surrounded by bulk liquid of relative dielectric constant $\varepsilon_{\mathrm{b}}$. Due to the spherical symmetry of the setting the only relevant positional variable is the distance $r \in [0,\infty)$ from the droplet center. Monovalent cations (+ ions) and anions (− ions) are distributed in both liquids. The difference in solvation free energy of a ± ion in the droplet with respect to the bulk liquid is denoted by $f_{\pm}$, which, within the Born approximation [60], can be estimated by $f_{\pm} = \dfrac{1}{2a_{\pm}}\Big(\dfrac{1}{\varepsilon_{\mathrm{d}}} - \dfrac{1}{\varepsilon_{\mathrm{b}}}\Big)$ with the ion radius $a_{\pm}$. As derived in detail in Ref. [37] all interfacial effects due to, e.g., smooth interfaces, finite ion size, van der Waals forces

and image charges, which are short ranged as compared to the electrostatic potential, are accounted for by introducing solvent-induced ion potentials $V_\pm(r) = f_\pm\Theta(a+s-r)$ with $\Theta$ the Heaviside function. Note that the parameter $s$, which describes the radial offset of the discontinuity of the solvent induced ion potentials $V_\pm$ with respect to the dielectric interface at $r = a$ and which is expected to be of the order of the size of a molecule or ion [37], can be positive or negative, depending on whether the net effect of the above-mentioned interfacial effects gives rise to a preference of the fluid structure in the droplet or in the bulk, respectively. More detailed representations of the interfacial effects are possible at the expense of more phenomenological parameters [335–337], but for the sake of convenience and because handy analytical expressions are desired a simple choice is made in Ref. [39].

A convenient approach to calculate the interfacial tension of the system under consideration is to first determine the equilibrium ion number density profiles $\varrho_\pm$ by means of density functional theory [131–133] and then to infer the interfacial tension from inserting these equilibrium profiles into the grand potential density functional. Poisson-Boltzmann theory corresponds to the mean-field grand potential density functional (compare Eq. (4.1))

$$\Omega[\varrho_\pm] = 4\pi \sum_{\alpha=\pm} \int_0^\infty \mathrm{d}r\, r^2 \varrho_\alpha(r) \Big( \ln(\varrho_\alpha(r)) - 1 - \mu_\alpha + V_\alpha(r) + \frac{\alpha}{2}\phi(r,[\varrho_\pm]) \Big) \tag{4.5}$$

with $\mu_\alpha$ the chemical potential of $\alpha$ ions and $\phi(r,[\varrho_\pm])$ the electrostatic potential functional at radius $r$. The interfacial tension with respect to the dielectric interface at $r = a$ in excess to the pure, salt-free liquid-liquid interfacial tension between the droplet and the bulk liquid is determined by

$$\begin{aligned} \gamma^{\mathrm{ex}} &= \frac{\Omega[\varrho_\pm] - \Omega[\varrho^{\mathrm{ref}}(\cdot,a)]}{4\pi a^2} \\ &= -\frac{1}{a^2} \sum_{\alpha=\pm} \int_0^\infty \mathrm{d}^\infty r\, r^2 \Big( \varrho_\alpha(r) - \varrho^{\mathrm{ref}}(r,a) + \frac{\alpha}{2}\varrho_\alpha(r)\phi(r,[\varrho_\pm]) \Big). \end{aligned} \tag{4.6}$$

As solutions of the non-linear Poisson-Boltzmann equation in the spherical geometry can be obtained only numerically, the same holds for the excess interfacial tension $\gamma^{\mathrm{ex}}$ in Eq. (4.6). However, upon linearising the Euler-Lagrange equation and the Poisson-Boltzmann equation one obtains analytical expressions which give rise to an expression of the droplet charge per surface area of the form

$$\sigma(a+s) = \frac{\phi_D}{\Big(1+\frac{s}{a}\Big)^2} \sqrt{\frac{\varepsilon_{\mathrm{b}}\varrho_{\mathrm{b}}^{\mathrm{ref}}}{2\pi}} F(s/a, \kappa_{\mathrm{b}}a, n, p), \tag{4.7}$$

with $\kappa_{\mathrm{b}} := \sqrt{8\pi\varrho_{\mathrm{b}}^{\mathrm{ref}}/\varepsilon_{\mathrm{b}}}$, $n := \sqrt{\varepsilon_{\mathrm{d}}/\varepsilon_{\mathrm{b}}}$, $p := \sqrt{\varrho_{\mathrm{d}}^{\mathrm{ref}}/\varrho_{\mathrm{b}}^{\mathrm{ref}}}$ and the Donnan potential $\phi_D$ [2, 20, 121, 122]. The full scaling function $F$, which is recorded in Ref. [39], appears somewhat lengthy but is straightforward to obtain in principle.

However, since the effective interfacial width parameter $s$ is usually very much smaller than the droplet radius and the local Debye lengths, $|s| \ll a, \kappa(r)^{-1}$, the first argument

of the scaling function $F$ can, within an excellent approximation, be set to zero [39]:

$$F(0,y,n,p) = \frac{np + \dfrac{n(p-n)}{y} - \left(\dfrac{n}{y}\right)^2 + \exp\Big(-2y\dfrac{p}{n}\Big)\Big(np + \dfrac{n(p+n)}{y} + \left(\dfrac{n}{y}\right)^2\Big)}{1 + np + \dfrac{1-n^2}{y} + \exp\Big(-2y\dfrac{p}{n}\Big)\Big(-1 + np - \dfrac{1-n^2}{y}\Big)}. \quad (4.8)$$

At this level of approximation Eqs. (4.6) and (4.7) reduce to [39]

$$\gamma^{\mathrm{ex}} = 2s\varrho_{\mathrm{b}}^{\mathrm{ref}}(1-p^2) - \frac{\phi_D}{2}\sigma(a) \quad (4.9)$$

and

$$\sigma(a) = \phi_D\sqrt{\frac{\varepsilon_b\varrho_{\mathrm{b}}^{\mathrm{ref}}}{2\pi}}F(0,\kappa_{\mathrm{b}}a,n,p), \quad (4.10)$$

respectively. According to Eq. (4.10), the droplet charge per droplet surface area $\sigma(a)$ is (almost) independent of the interfacial width $s$. On the other hand, the excess interfacial tension $\gamma^{\mathrm{ex}}$ in Eq. (4.9) comprises a contribution describing the ion exclusion due to the short-ranged *interfacial effects*

$$\gamma_{\mathrm{ie}}^{\mathrm{ex}} := 2s\varrho_{\mathrm{b}}^{\mathrm{ref}}(1-p^2), \quad (4.11)$$

which is (essentially) linear in $s$ and (almost) independent of the droplet radius $a$, as well as an *electrostatic* contribution

$$\gamma_{\mathrm{es}}^{\mathrm{ex}} := -\frac{\phi_D}{2}\sigma(a), \quad (4.12)$$

which is (almost) independent of the effective interfacial width $s$.

In order to understand the involved dependence of the scaling function $F(0,y,n,p)$ on $y$ it is useful to investigate the asymptotic behaviour for large and small values of $y$. If $y \gg y_1^\times := n/p$ and with $y_2^\times := \dfrac{|1-n^2|}{1+np}$ and $y_3^\times := 1$ one infers the leading order asymptotic behaviour [39]

$$F(0, y \gg y_1^\times, n, p) \simeq \begin{cases} \dfrac{np}{1+np} & (\mathrm{I})\, y \gg y_3^\times \\ \dfrac{np}{1+np}y^{-1} & (\mathrm{II})\, y_2^\times \ll y \ll y_3^\times \\ \dfrac{np}{1-n^2} & (\mathrm{III})\, y \ll y_2^\times. \end{cases} \quad (4.13)$$

The three cases considered in Eq. (4.13) are exhaustive and mutually exclusive for $y \gg y_1^\times$ because $y_2^\times \le \max(y_1^\times, y_3^\times)$. If $y \ll y_1^\times$, Eq. (4.8) leads to

$$F(0, y \ll y_1^\times, n, p) \simeq \frac{p^2}{3}y. \quad (4.14)$$

Figure 4.2 displays $F(0,y,n,p)$ for the case $y_1^\times \ll y_2^\times \ll y_3^\times$, where all four asymptotic regimes I–IV of Eqs. (4.13) and (4.14) are apparent. If $y_2^\times \ll y_1^\times \ll y_3^\times$, however, regime III in Fig. 4.2 is absent, and a crossover between regimes II and IV takes place at $y = y_1^\times$. Moreover, if $y_1^\times \gg y_3^\times$ regime II is also absent, and $F(0,y,n,p)$ exhibits a single crossover at $y = y_1^\times$ between regimes I and IV [39].

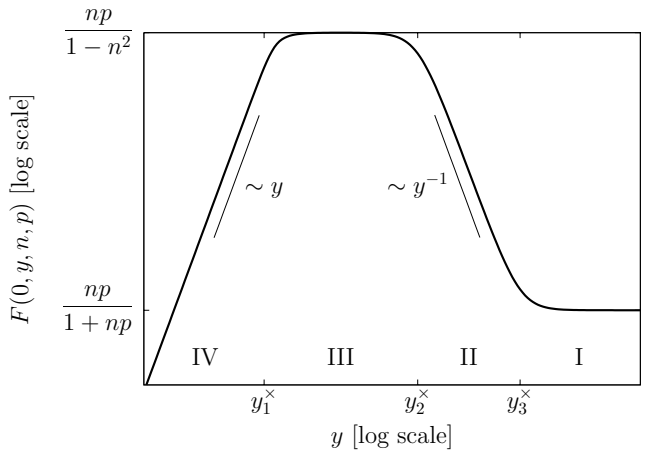


Figure 4.2: Scaling function $F(0, y, n, p)$ as a function of $y$ for the relation $y_1^\times \ll y_2^\times \ll y_3^\times$ of the crossover positions (see main text) in a log-log plot. The asymptotic regimes I–IV corresponding to Eqs. (4.13) and (4.14) are visible. For $y_1^\times \gg y_2^\times$ regime III is absent, and for $y_1^\times \gg y_3^\times$ also regime II. (See Ref. [39])

(a) O/W

| $\varepsilon_\mathrm{o}$ | $n$ | $p$ | $\phi_D$ | $y_1^\times$ | $y_2^\times$ |
|---|---|---|---|---|---|
| 5 | 0.25 | 0.000285 | 1.48 | 876 | 0.937 |
| 7.5 | 0.306 | 0.00520 | 0.956 | 58.9 | 0.905 |
| 10 | 0.354 | 0.0222 | 0.692 | 15.9 | 0.868 |

(b) W/O

| $\varepsilon_\mathrm{o}$ | $n$ | $p$ | $\phi_D$ | $y_1^\times$ | $y_2^\times$ |
|---|---|---|---|---|---|
| 5 | 4 | 3500 | −1.48 | 0.00114 | 0.00107 |
| 7.5 | 3.27 | 192 | −0.956 | 0.0170 | 0.0154 |
| 10 | 2.83 | 45.1 | −0.692 | 0.0627 | 0.0545 |

Table 4.1: Quantities $n$, $p$ and $\phi_D$ as well as the crossover values $y_1^\times$ and $y_2^\times$ within the Born approximaion for (a) O/W and (b) W/O systems with the oil dielectric constant $\varepsilon_\mathrm{o} \in \{5, 7.5, 10\}$ and ion radii $a_+ = 0.36\,\mathrm{nm}$ and $a_- = 0.30\,\mathrm{nm}$. (See Ref. [39])

According to $y = \kappa_\mathrm{b} a$ (see Eqs. (4.7) and (4.10)) the crossover values $y_i^\times, i \in \{1, 2, 3\}$ correspond to crossover droplet radii $a_i^\times, i \in \{1, 2, 3\}$, i.e. regimes I–IV can be understood in terms of length scales of the system. Obviously $a_3^\times = \kappa_\mathrm{b}^{-1}$ and $a_1^\times = \kappa_\mathrm{d}^{-1} := \kappa_\mathrm{b}^{-1} n/p$ equal the Debye lengths in the bulk and in the droplet, respectively. Finally $a_2^\times = |\varepsilon_\mathrm{b} - \varepsilon_\mathrm{d}|/(\varepsilon_\mathrm{b}\kappa_\mathrm{b} + \varepsilon_\mathrm{d}\kappa_\mathrm{d})$ is a length scale which accounts for the dielectric contrast between bulk and droplet.

As an example systems are considered with one of the liquids being water with dielectric constant $\varepsilon_\mathrm{w} = 80$. Moreover, the largely arbitrary but representative choice of ion radii $a_+ = 0.36\,\mathrm{nm}$ and $a_- = 0.30\,\mathrm{nm}$ is made. Given the dielectric constant of the second liquid, called "oil", the parameters $n$, $p$ and $\phi_D$ are known within the Born approximation. The cases of an oil droplet in water (O/W) and of a water droplet in oil (W/O) will be distinguished.

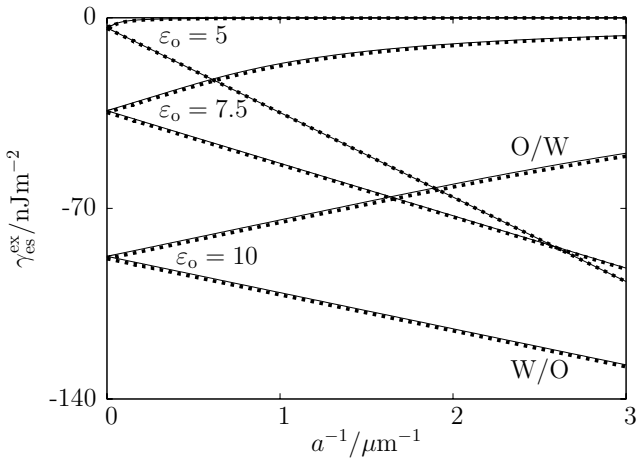


Figure 4.3: Electrostatic contribution to the excess interfacial tension $\gamma_{es}^{ex}$ in mixtures of oil ($\varepsilon_o \in \{5, 7.5, 10\}$) and water ($\varepsilon_w = 80$) as a function of the radius $a$ of an oil droplet in water (O/W, ascending curves) and a water droplet in oil (W/O, descending curves) with ion radii $a_+ = 0.36\,\mathrm{nm}$ and $a_- = 0.30\,\mathrm{nm}$ as well as an ionic strength in water $I_w = 1\,\mathrm{mM}$. The thin solid curves are calculated by means of the analytical expressions within the linear theory whereas the thick dotted curves are obtained by numerically solving the non-linear Poisson-Boltzmann equation (see Ref. [96]). Upon swapping oil and water (O/W $\leftrightarrow$ W/O) the slope of the curves at $a^{-1} = 0$ (planar system) changes its sign. (See Ref. [39])

Figure 4.3 displays the electrostatic contribution to the excess interfacial tension $\gamma_{es}^{ex}$ (see Eq. (4.12)) of oil droplets in water (O/W, ascending curves) and water droplets in oil (W/O, descending curves) for an ionic strength in water $I_w = 1\,\mathrm{mM}$, where $I_w := \varrho_b^{ref}$ for O/W and $I_w := \varrho_d^{ref}$ for W/O, as a function of the droplet radius $a$. The analytical expression Eq. (4.12) within linearised Poisson-Boltzmann theory (thin solid curves) is compared with numerical results of the non-linear Poisson-Boltzmann theory (thick dotted curves, see Ref. [96]). The slight quantitative differences are due to the linearisation approximation and they are already present in the planar system ($a^{-1} = 0$). The quantities $n$, $p$ and $\phi_D$ as well as the crossover values $y_1^\times$ and $y_2^\times$ correponding to the curves in Fig. 4.3 are displayed in Tab. 4.1. Regime III is expected to be absent for the W/O systems because $y_3^\times > y_1^\times > y_2^\times$, whereas regimes II and III are absent for the O/W systems because $y_1^\times > y_3^\times > y_2^\times$.

Due to Eq. (4.12) the relative change of the electrostatic excess interfacial tension $\gamma_{es}^{ex}(a)$ and the droplet charge per droplet surface area $\sigma(a)$ with respect to their planar values $\gamma_{es}^{ex}(\infty)$ and $\sigma(\infty)$, respectively, are equal, and they exhibit the low-curvature asymptotic behaviour

$$\frac{\gamma_{es}^{ex}(a)}{\gamma_{es}^{ex}(\infty)} = \frac{\sigma(a)}{\sigma(\infty)} \simeq G(\kappa_b a, n, p) \qquad , \kappa_b a \gg y_1^\times , \tag{4.15}$$

where

$$G(y \gg y_2^\times, n, p) = 1 - \frac{n(1-p^2)}{p(1+np)} y^{-1} - \frac{\frac{n(p+n)^2}{p(1+np)^2} y^{-2}}{1 + \mathrm{sign}(1-n)\frac{y_2^\times}{y}}$$
$$\simeq 1 - \frac{n(1-p^2)}{p(1+np)} y^{-1} - \frac{n(p+n)^2}{p(1+np)^2} y^{-2}, \tag{4.16}$$

which equals an expansion in $y^{-1}$ up to second order. Hence, the low-curvature expansion up to second order in $a^{-1}$ obtained by combining Eqs. (4.15) and (4.16) is expected to be acurate if $\kappa_\mathrm{b} a \gg y_1^\times, y_2^\times$. Traditionally, empirically motivated expansions in $a^{-1}$ have been used to represent the curvature dependence of the interfacial tension without knowing their applicability a priori. However, it has been argued by König, Roth, and Mecke on the basis of a morphometrical approach that the deviation of intensive thermodynamic quantities from their planar values are linear combinations of the mean and the Gaussian curvature *provided* the geometrical length scales are much larger than any correlation length [234], i.e. $a \gg \kappa_\mathrm{d}^{-1}, \kappa_\mathrm{b}^{-1}$ or equivalently $\kappa_\mathrm{b} a \gg y_1^\times, y_3^\times$. This condition is only sufficient but not necessary for the validity of the above low-curvature expansion because it already implies $\kappa_\mathrm{b} a \gg y_2^\times$ due to $y_2^\times \leq \max(y_1^\times, y_3^\times)$. For $n, p \gg 1$, the low-curvature expansion is valid if $\kappa_\mathrm{d} a \gg 1$, *independent* of the bulk Debye length $\kappa_\mathrm{b}^{-1}$, because in this case $y_2^\times \approx y_1^\times$. This is the case, e.g., for the W/O systems considered in Tab. 4.1.

For the scaling function $G(y, n, p)$ in Eq. (4.15) one straightforwardly recognises the symmetry $G(py/n, 1/n, 1/p) = G(-y, n, p)$ (see Ref. [39]) which means that swapping droplet and bulk liquid, i.e. $p \mapsto 1/p$, $n \mapsto 1/n$ and $\kappa_\mathrm{b} \mapsto \kappa_\mathrm{d}$, while keeping the droplet radius $a$ fixed has numerically the same effect on function $G$ as inverting the sign of the droplet radius. Due to this symmetry one concludes for the coefficients of an expansion in inverse powers of $a$ as in Eq. (4.16) for $y = \kappa_\mathrm{b} a$ that upon swapping droplet and bulk liquid the odd-order coefficients merely invert their sign, whereas the even-order coefficients do not change. This phenomenon can be observed in Fig. 4.3, where the slope close to the planar limit ($a^{-1} = 0$), which is proportional to the excess Tolman length due to the presence of ions, simply changes its sign upon swapping oil and water (O/W $\leftrightarrow$ W/O).

Figure 4.4 exhibits the electrostatic contribution to the excess interfacial tension $\gamma_\mathrm{es}^\mathrm{ex}$ as a function of the dielectric constant $\varepsilon_\mathrm{o}$ of the oil for the ionic strength in water $I_\mathrm{w} = 1\,\mathrm{mM}$ and for various droplet radii $a \in \{50\,\mathrm{nm}, 100\,\mathrm{nm}, 250\,\mathrm{nm}, 500\,\mathrm{nm}, 1000\,\mathrm{nm}, \infty\}$. As in Fig. 4.3, the thin solid curves correspond to the analytic linear theory whereas the thick dotted curves are the numerical results of the non-linear scheme (see Ref. [96]). Quantitative agreement is observed, even in the low-$\varepsilon_\mathrm{o}$ range where the Donnan potential $\phi_D$ is *not* small and the linearisation approximation is *not a priori* justified. From the linearised theory one can derive [39] the asymptotic behaviour $\gamma_\mathrm{es}^\mathrm{ex} = \mathcal{O}(-(\varepsilon_\mathrm{o} - \varepsilon_\mathrm{w})^2)$ for $\varepsilon_\mathrm{o} \to \varepsilon_\mathrm{w}$ as well as $\gamma_\mathrm{es}^\mathrm{ex} = \mathcal{O}(-\exp(-\mathrm{const}/\varepsilon_\mathrm{o}))$ for an O/W system and $\gamma_\mathrm{es}^\mathrm{ex} = \mathcal{O}(-1/\varepsilon_\mathrm{o})$ for a W/O system as $\varepsilon_\mathrm{o} \to 0$. This behaviour is apparent in Fig. 4.4, too.

The total excess interfacial tension $\gamma^\mathrm{ex}$ comprises not only the electrostatic part $\gamma_\mathrm{es}^\mathrm{ex}$ but also the contribution $\gamma_\mathrm{ie}^\mathrm{ex}$ due to the interfacial effects (see Eq. (4.11)). It is readily seen that $\gamma_\mathrm{ie}^\mathrm{ex} = \pm\mathcal{O}(s(\varepsilon_\mathrm{w} - \varepsilon_\mathrm{o}))$ for $\varepsilon_\mathrm{o} \to \varepsilon_\mathrm{w}$ and $\gamma_\mathrm{ie}^\mathrm{ex} = \pm\mathcal{O}(s)$ for $\varepsilon_\mathrm{o} \to 0$ where the upper (+) and the lower (−) sign correspond to an O/W and a W/O system, respectively. Hence, if $s \neq 0$, the interfacial effects will dominate over the electrostatic effects in the limits

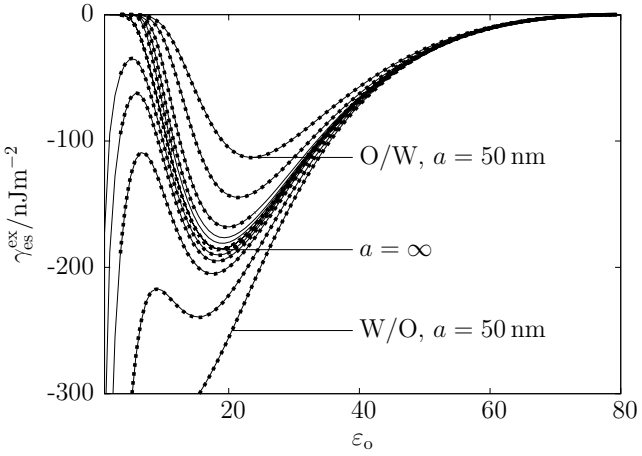


Figure 4.4: Electrostatic contribution to the excess interfacial tension in mixtures of oil and water ($\varepsilon_{\rm w} = 80$) as a function of the dielectric constant $\varepsilon_{\rm o}$ of the oil for droplet radii $a \in \{50\,{\rm nm}, 100\,{\rm nm}, 250\,{\rm nm}, 500\,{\rm nm}, 1000\,{\rm nm}, \infty\}$ of an oil droplet in water (O/W) and a water droplet in oil (W/O) with ion radii $a_+ = 0.36\,{\rm nm}$ and $a_- = 0.30\,{\rm nm}$ as well as the ionic strength in water $I_{\rm w} = 1\,{\rm mM}$. The thin solid curves are calculated by means of the analytical expressions within the linear theory whereas the thick dotted curves are obtained by numerically solving the non-linear Poisson-Boltzmann equation (see Ref. [96]). There is quantitative agreement between the linear and the non-linear theory for the ranges of $a$ and $\varepsilon_{\rm o}$ considered here. (See Ref. [39])

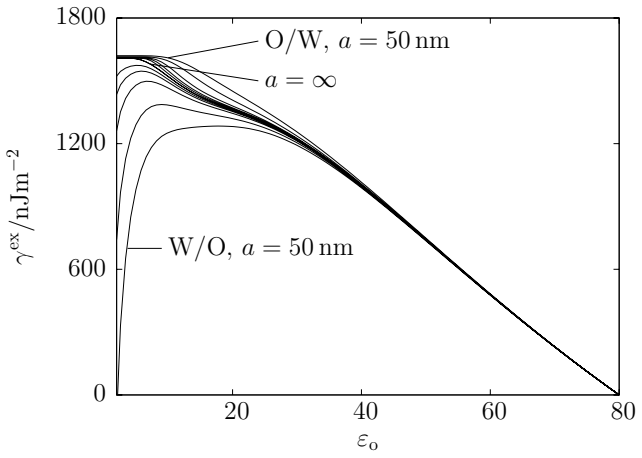


Figure 4.5: Total excess interfacial tension in mixtures of oil and water ($\varepsilon_{\rm w} = 80$) as a function of the dielectric constant $\varepsilon_{\rm o}$ of the oil for droplet radii $a \in \{50\,{\rm nm}, 100\,{\rm nm}, 250\,{\rm nm}, 500\,{\rm nm}, 1000\,{\rm nm}, \infty\}$ of an oil droplet in water (O/W) and a water droplet in oil (W/O) with ion radii $a_+ = 0.36\,{\rm nm}$ and $a_- = 0.30\,{\rm nm}$, interfacial width parameter $|s| = 0.33\,{\rm nm}$, as well as the ionic strength in water $I_{\rm w} = 1\,{\rm mM}$. (See Ref. [39])

$\varepsilon_{\rm o} \to 0$ for O/W systems and $\varepsilon_{\rm o} \to \varepsilon_{\rm w}$ for arbitrary systems. Figure 4.5 displays the total excess interfacial tension corresponding to the parameters used in Fig. 4.4 and an interfacial width parameter $s$ with $|s| = 0.33\,{\rm nm}$ on the water side of the interface, i.e. $s > 0$ for O/W and $s < 0$ for W/O.

The electrostatic excess interfacial tension $\gamma_{\rm es}^{\rm ex}$ as a function of the bulk ionic strength

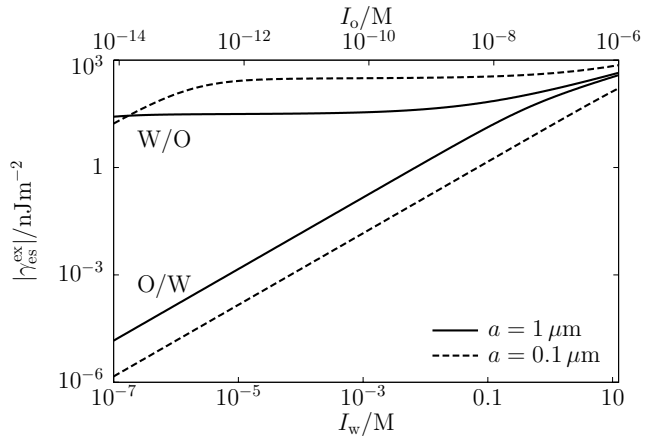


Figure 4.6: Electrostatic excess interfacial tension in mixtures of oil ($\varepsilon_o = 5$) and water ($\varepsilon_w = 80$) as a function of the ionic strength in oil ($I_o$) or water ($I_w$) for droplet radii $a \in \{0.1\,\mu\text{m}, 1\,\mu\text{m}\}$ of an oil droplet in water (O/W) and a water droplet in oil (W/O) with ion radii $a_+ = 0.36\,\text{nm}$ and $a_- = 0.30\,\text{nm}$. The O/W system exhibits only the regimes I and IV (see main text and Fig. 4.2), whereas for the W/O system the regimes I, II, and IV are present. Upon changing the droplet size $a$ the crossover ionic strengths shift by a factor $a^{-2}$. (See Ref. [39])

$I_b := \varrho_b^{\text{ref}}$ can be asymptotically described by

$$\gamma_{es}^{ex} \simeq \begin{cases} -\phi_D^2 \sqrt{\frac{\varepsilon_b}{8\pi}} \frac{np}{1+np} I_b^{1/2} & \text{(I) } I_b \gg I_{b1}^\times, I_{b3}^\times \\ -\phi_D^2 \frac{\varepsilon_b}{8\pi} \frac{np}{(1+np)a} & \text{(II) } I_{b1}^\times, I_{b2}^\times \ll I_b \ll I_{b3}^\times \\ -\phi_D^2 \sqrt{\frac{\varepsilon_b}{8\pi}} \frac{np}{1-n^2} I_b^{1/2} & \text{(III) } I_{b1}^\times \ll I_b \ll I_{b2}^\times \\ -\phi_D^2 \frac{p^2}{3} a I_b & \text{(IV) } I_b \ll I_{b1}^\times \end{cases} \tag{4.17}$$

with the crossover bulk ionic strengths $I_{bk}^\times := \frac{\varepsilon_b (y_k^\times)^2}{8\pi a^2}, k \in \{1,2,3\}$. For a planar system ($a = \infty$) the crossovers are at zero ionic strength, hence only the high-ionic strength regime I in Fig. 4.2 ($I_b \gg I_{b1}^\times, I_{b3}^\times$) is present, which coincides exactly with the electrostatic contribution to the excess interfacial tension in Ref. [37].

For an oil dielectric constant $\varepsilon_o = 5$ and a droplet radius $a = 1\,\mu\text{m}$ the crossover bulk ionic strengths are $I_{b1}^\times \approx 71\,\text{mM}, I_{b2}^\times \approx 82\,\text{nM}, I_{b3}^\times \approx 93\,\text{nM}$ for an O/W system, where $I_b = I_w$ is the ionic strength in water, and $I_{b1}^\times \approx 7.6\,\text{fM}, I_{b2}^\times \approx 6.6\,\text{fM}, I_{b3}^\times \approx 5.8\,\text{nM}$ for a W/O system, where $I_b = I_o$ is the ionic strength in oil (see Tab. 4.1). Here, ionic strengths in oil, $I_o$, and in water, $I_w$, are related to each other by $I_o/I_w \approx 8.1 \cdot 10^{-8}$. Figure 4.6 displays $\gamma_{es}^{ex}$ as a function of the ionic strength in the physical range $I_w \in [10^{-7}\,\text{M}, 10\,\text{M}]$ for the droplet radii $a = 1\,\mu\text{m}$ and $a = 0.1\,\mu\text{m}$. The crossover ionic strengths of the latter droplet size are larger by a factor 100 as compared to the former because $I_{bk}^\times \sim a^{-2}$. By inspection of the values of the crossover bulk ionic strengths one expects only the regimes I and IV of Fig. 4.2 to be present for the O/W system whereas the regimes I, II, and IV are expected for the W/O system. The occurrence of the regimes I and IV for the O/W

system and I, II, and IV for the W/O system can be inferred from Fig. 4.6 in conjunction with Eq. (4.17).

Hence the analytical theory based on a linearised Poisson-Boltzmann theory is in good (at least) qualitative agreement with the results from the full non-linear theory. It can therefore be expected that the general conclusions drawn from that linear theory apply to more elaborate models [335–337], too.

According to Eqs (4.9), (4.11), and (4.12) the excess liquid-liquid interfacial tension is $\gamma^{\rm ex} = \gamma^{\rm ex}_{\rm ie} + \gamma^{\rm ex}_{\rm es}$ where the curvature dependence is essentially only due to the electrostatic part $\gamma^{\rm ex}_{\rm es}$ and not due to the contribution of the short-ranged interfacial effects $\gamma^{\rm ex}_{\rm ie}$. While $\gamma^{\rm ex}$ can indeed be negative, thereby decreasing the total interfacial tension, the largest magnitude $|\gamma^{\rm ex}|$ is attained at high ionic strengths where $\gamma^{\rm ex} \approx \gamma^{\rm ex}_{\rm ie}$, i.e. where $\gamma^{\rm ex}$ is essentially curvature-independent. One has to conclude that the unimodal droplet size distribution of W/O emulsions observed in Refs. [261, 262] *cannot* be explained by the curvature dependence of the interfacial tension due to electrostatic effects alone. However, this conclusion does not apply to the experiments in Ref. [387], where highly charged colloids instead of monovalent ions are present, as the linearised theory is not a priori justified for multivalent ions or highly charged colloids. In particular, it has been found that in systems where the ionic strength and the dielectric constant in the droplet are much larger than in the bulk the range of validity of low-curvature expansions up to second order in the inverse radius of curvature is independent of the bulk Debye length.

## Crystallisation of water droplets

The making and breaking of oil-water emulsions is not only a problem of extreme importance in chemical, oil, pharmaceutical, food, and cosmetics industries, but is also a scientifically fascinating topic. It is well-known that the intrinsic tendency of oil and water to demix can be slowed-down or delayed by adding surfactants or colloidal particles to the mixture. These additives strongly adsorb to the oil-water interface, which lowers the interfacial tension (the main driving force for demixing) and/or provides a kinetic barrier that prevents droplet coalescence [49, 387]. However, it was observed that emulsions of water droplets dispersed in somewhat polar oils can be stable for a long time (so far for more than 18 months), *without any additives* [261]. Moreover, the water droplets, which are of micrometer dimensions in these experiments, spontaneously form crystalline structures with lattice spacings of the order of $5 - 15$ $\mu$m. These observations suggest long-ranged electrostatic droplet-droplet repulsions due to a net water droplet charge stemming from a preferential uptake of ions from the oil [261, 262, 490]. Theoretical calculations based on Poisson-Boltzmann theory for monovalent ions in the geometry of a planar water-oil interface showed that the order of magnitude of the charge separation process, caused by the different cationic and anionic Born self-energies in oil and water, is indeed sufficiently strong to explain the observed stability and crystallisation [262, 490], at least qualitatively. These predictions are based on the assumption of a pairwise screened-Coulomb potential of the charged water droplets through the oil and an explicit empirical crystallisation condition based on simulations [174, 446].

The ionic charge separation at the planar oil-water interface and the resulting crystallisation regime of water droplets dispersed in oil in the high-dimensional parameter space of salt concentration, dielectric constant of the oil, ionic sizes and self-energies, droplet size and droplet concentration have been studied in Ref [491]. The analytic solution admitted

by the nonlinear Poisson-Boltzmann equation in the planar geometry [242, 449] allows for such a detailed exploration efficiently; the effects of droplet curvature were studied numerically [96] and analytically [39] (see Subsec. 4.1). Crystallisation of water droplets is only possible for sufficiently large droplet radii ($\gtrsim$ 100 nm), sufficiently large water content (volume fraction $\gtrsim 10^{-3}$) and sufficiently (but not too) polar oils with dielectric constants between 4 and 10.

The liquids are considered as structureless homogeneous linear dielectric media, filling the two half spaces $z < 0$ (water) and $z > 0$ (oil), forming a flat interface at $z = 0$. The relative dielectric constant is a step function, $\varepsilon(z) = \varepsilon_\mathrm{w}$ ($z < 0$) and $\varepsilon(z) = \varepsilon_\mathrm{o}$ ($z > 0$). The grand potential functional per unit area of the variational density profiles $\varrho_\pm(z)$ of the cations (+) and anions (−) in units of $k_\mathrm{B}T \equiv 1/\beta$ is given by [37, 96, 131, 490]

$$\beta\Omega[\varrho_\pm] = \sum_{\alpha=\pm} \int_{-\infty}^{\infty} \mathrm{d}z \; \varrho_\alpha(z) \Big( \ln \frac{\varrho_\alpha(z)}{\varrho_\mathrm{w}} - 1 + \beta V_\alpha(z) + \frac{\alpha}{2}\phi(z,[\varrho_\pm]) \Big), \tag{4.18}$$

with the self-consistent dimensionless electrostatic potential $\phi(z,[\varrho_\pm])$, and with the external potential acting on the ions

$$\beta V_\pm(z) = \begin{cases} 0 & , z < 0; \\ \dfrac{e^2}{2a_\pm k_\mathrm{B}T}\Big(\dfrac{1}{\varepsilon_\mathrm{o}} - \dfrac{1}{\varepsilon_\mathrm{w}}\Big) + g_\pm \equiv f_\pm & , z > 0, \end{cases}$$

representing the Born self-energy and an additional specific solvation energy $g_\pm$ (e.g. due to hydration, hydrogen bonding, local modification of dielectric constant [280, 335, 336]), which is set either to 0 or to 4 here in order to study specific effects. The salt concentration in bulk water is denoted by $\varrho_\mathrm{w}$, $e$ is the elementary charge, and $a_\pm$ is the ionic radius. Both $\phi(z)$ and $V_\pm(z)$ are gauged to zero in the bulk water phase ($z \to -\infty$). Figure 4.7 shows $f_\pm$ as a function of the oil dielectric constant $\varepsilon_\mathrm{o}$, and ionic radius $a_\pm$ (inset), for $g_\pm = 0$. Typical values for the self-energies are $5 - 20\ k_\mathrm{B}T$, and self-energy differences are of the order of $1 - 10\ k_\mathrm{B}T$ for ionic radii differing by, say, 1 Å.

The general solution of the Euler-Lagrange equation is [491]

$$\phi(z) = \begin{cases} 4\ \mathrm{arctanh}(C_\mathrm{w} e^{\kappa_\mathrm{w} z}) & , z < 0; \\ 4\ \mathrm{arctanh}(C_\mathrm{o} e^{-\kappa_\mathrm{o} z}) + \phi_\mathrm{D} & , z > 0, \end{cases} \tag{4.19}$$

with integration constants that follow from the boundary conditions as

$$\begin{aligned} C_\mathrm{w} &= \frac{n + \cosh\frac{\phi_\mathrm{D}}{2} - D}{\sinh\frac{\phi_\mathrm{D}}{2}}, \\ C_\mathrm{o} &= -\frac{1 + n\cosh\frac{\phi_\mathrm{D}}{2} - D}{n\sinh\frac{\phi_\mathrm{D}}{2}}, \end{aligned} \tag{4.20}$$

where $n \equiv \varepsilon_\mathrm{w}\kappa_\mathrm{w}/\varepsilon_\mathrm{o}\kappa_\mathrm{o}$, and $D \equiv \sqrt{n^2 + 2n\cosh\frac{\phi_\mathrm{D}}{2} + 1}$. An experimental determination of the ion distributions $\varrho_\pm(z)$ at liquid-liquid interfaces has been reported in Refs. [196, 244]. The derivation so far is equivalently presented in [242, 449]. A separation of charge is found near the interface for unequal self-energies, comprising a cloud of net charge in the

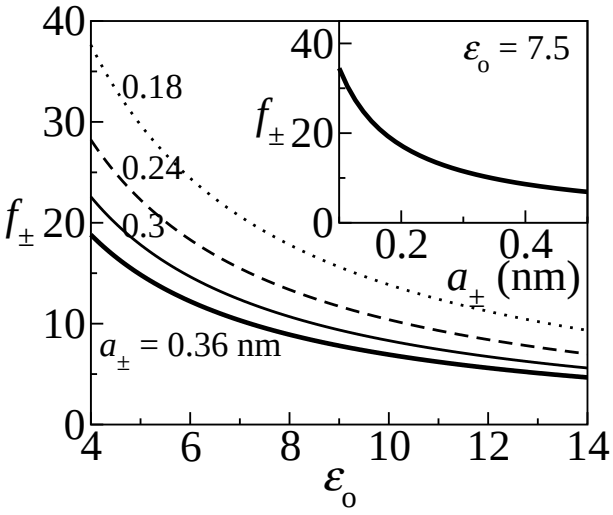


Figure 4.7: The Born self-energy $f_\pm$ in units of $k_\mathrm{B}T$ as a function of dielectric constant $\varepsilon_\mathrm{o}$, for several ionic radii $a_\pm$, and as a function of the ionic radius at $\varepsilon_\mathrm{o} = 7.5$ (inset). (See Ref. [491] © IOP Publishing. Reproduced with permission. All rights reserved)

water phase of typical width $\kappa_\mathrm{w}^{-1}$ and one in the oil phase of typical width $\kappa_\mathrm{o}^{-1}$, with a charge per area at the water side given in units of $e$ by [491]

$$\sigma_\mathrm{w} = \int_{-\infty}^{0} \mathrm{d}z(\varrho_+(z) - \varrho_-(z)) = -\frac{8\varrho_\mathrm{w}}{\kappa_\mathrm{w}} \frac{C_\mathrm{w}}{1 - C_\mathrm{w}^2}; \tag{4.21}$$

the compensating charge resides at the oil side as the system is globally neutral.

Consider $N$ oil-dispersed water droplets of radius $a$ in a volume $V$, such that the typical droplet-droplet separation is $R = (V/N)^{\frac{1}{3}}$ and the water volume fraction is $x = \frac{4}{3}\pi a^3 N/V = \frac{4}{3}\pi(a/R)^3$. It is assumed that each water droplet has a charge $Z = 4\pi a^2 \sigma_\mathrm{w}$, where $\sigma_\mathrm{w}$ follows from the nonlinear PB theory (4.21), and that a screened Coulomb (Yukawa) potential acts between two droplets [491]

$$V_\mathrm{Yuk}(r) = \frac{(Ze)^2}{\varepsilon_\mathrm{o}} \Big( \frac{e^{\kappa_\mathrm{o} a}}{1 + \kappa_\mathrm{o} a} \Big)^2 \frac{e^{-\kappa_\mathrm{o} r}}{r}, \tag{4.22}$$

with $r$ the center-to-center separation between the droplets. According to simulation results, crystallisation of such a Yukawa system occurs if $\Gamma \gtrsim 106$ [174, 446], with the coupling parameter $\Gamma$ defined by

$$\Gamma \equiv \beta V_\mathrm{Yuk}(R)(1 + \kappa_\mathrm{o} R + \frac{(\kappa_\mathrm{o} R)^2}{2}). \tag{4.23}$$

Although this condition has been confirmed only for point-Yukawa systems, it is expected to hold also for finite droplets as long as $V_\mathrm{Yuk}(2a) \gtrsim 10\ k_\mathrm{B}T$ and $\kappa_\mathrm{o} a \lesssim 1$, conditions that are easily met for micron-sized droplets, provided $4 < \varepsilon_\mathrm{o} < 10$ as can be seen in Fig. 4.9.

The electrostatic contribution $\gamma$ to the interfacial tension can be calculated analytically by evaluating the functional (4.18) with the equilibrium profiles, minus the functional evaluated with the step profile $\varrho_\pm(z < 0) = \varrho_\mathrm{w}$, $\varrho_\pm(z > 0) = \varrho_\mathrm{o}$ [37, 96, 336]. After a

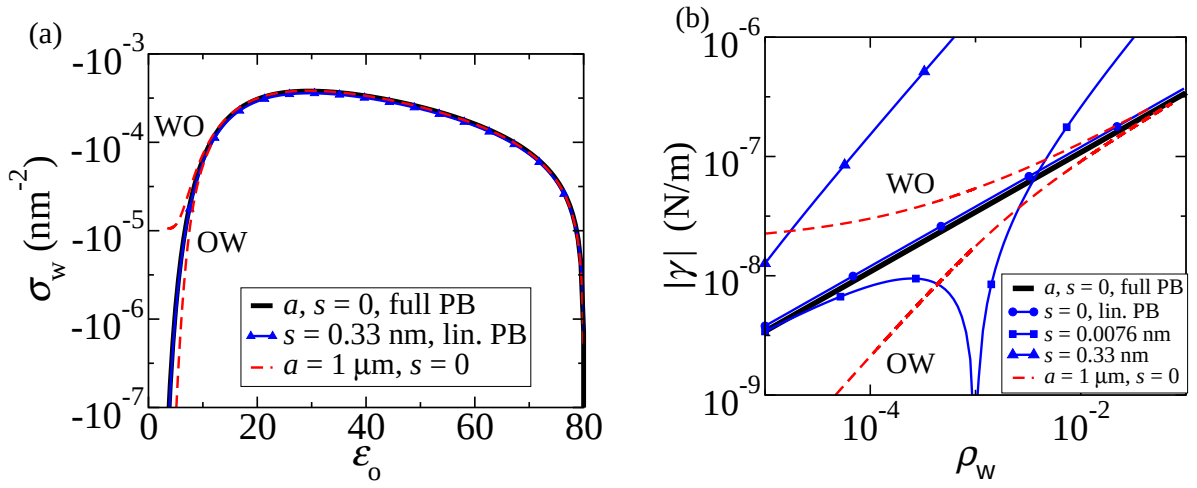


Figure 4.8: (a) Interfacial charge density as a function of the oil dielectric constant. (b) Excess interfacial tension as a function of ionic strength, at $\varepsilon_o = 7.5$. If the interfacial width $s = 0$, the planar calculations clearly show a square root behaviour. The sign of $\gamma$ is negative. The dashed lines show the numerical results from the PB-theory in spherical geometry, for water droplets of radius $a = 1$ $\mu$m (WO), and equal sized oil droplets in water (OW) [96]. The thin lines show the result of the planar linearised PB-theory with interfacial width $s$, for which $\gamma$ has a linear asymptote and positive sign in the high-$\varrho_w$ limit [37], if $s \neq 0$. (See Ref. [491] © IOP Publishing. Reproduced with permission. All rights reserved)

tedious but straightforward calculation one finds [491]

$$\beta\gamma = -\frac{16\varrho_w}{\kappa_w}\frac{C_w}{1-C_w^2}(C_w - C_o) \sim -\sqrt{\varrho_w}, \tag{4.24}$$

which is symmetric under exchanging w $\leftrightarrow$ o and where the proportionality to $\sqrt{\varrho_w}$ follows from $\kappa_w \sim \sqrt{\varrho_w}$ and the fact that $C_w$ and $C_o$ are independent of $\varrho_w$. Typical values of the excess interfacial tension are at most $\mathcal{O}(\mu\text{N/m})$, and are therefore vanishingly small compared to the value of the bare oil-water interfacial tension ($\mathcal{O}(10$ mN/m)).

As standard parameters $\varepsilon_o = 7.5$, $\varrho_w = 10^{-3}$ M, which are close to the experimental values of [261, 262], $g_\pm = 0$ and $(a_+, a_-) = (0.36, 0.3)$ nm are used. The surface charge density $\sigma_w$ of the interface appears to be strongly dependent on the oil dielectric constant, keeping the ionic radii fixed. Typically it is of the order of $\mathcal{O}(10^{-4})$ elementary charges per nm$^2$ in the range $10 < \varepsilon_o < 70$, and decays rapidly to $10^{-7}$ nm$^{-2}$ for $\varepsilon_o = 4$, see Fig. 4.8(a). Numerical calculations in the spherical geometry [96] predict a smaller $\sigma_w$ for oil-in-water droplets, and a larger one for water-in-oil droplets in the regime $4 < \varepsilon_o < 10$, as shown in Fig. 4.8(a) for a radius $a = 1$ $\mu$m. The excess interfacial tension $\gamma$ differs correspondingly for finite droplets, Fig. 4.8(b). The linearised PB theory that takes into account a finite interfacial width $s \neq 0$ [37] between oil and water agrees quantitatively with the present results for $\sigma_w$, indicating that the charge separation is hardly dependent on $s = \mathcal{O}(10^{-1}$ nm), even if the ions are effectively excluded in a band of several tenths of nanometers. On the other hand, above a certain crossover ionic strength, the same theory predicts a qualitatively different asymptotic behaviour of the excess interfacial tension, being positive and proportional to the ionic strength $\varrho_w$, Fig. 4.8(b). One can understand

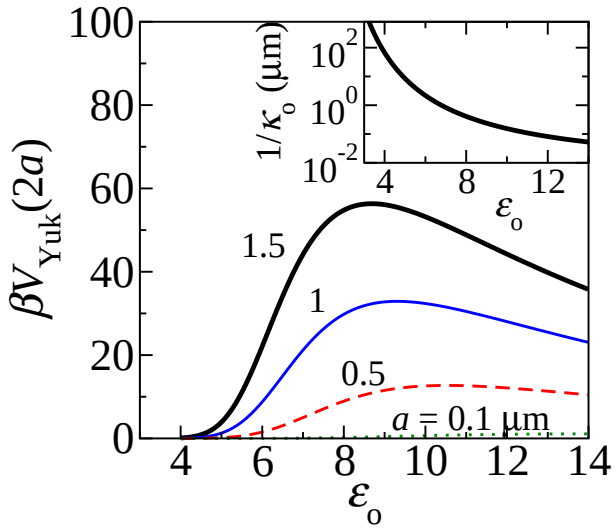


Figure 4.9: The Yukawa potential at contact and the Debye screening length in oil (inset) as a function of the oil dielectric constant $\varepsilon_o$, at $\varrho_w = 10^{-3}$ M, $(a_+, a_-) = (0.36, 0, 3)$. The contact value $V_{Yuk}(2a) > 1\ k_BT$ only for $\varepsilon_o > 4$ and droplet radii $a > 100$ nm. On the other hand, the range of the Yukawa potential decays rapidly for $\varepsilon_o > 10$ (inset); for droplets with a radius $a > 100$ nm, the value of $\kappa_o a \gg 1$ above $\varepsilon_o \gtrsim 12$. Therefore, significant long range Coulomb interactions are only expected between $4 \lesssim \varepsilon_o \lesssim 10$. (See Ref. [491] © IOP Publishing. Reproduced with permission. All rights reserved)

that as follows: whereas the charge separation is hardly affected by the interfacial width $s$, the adsorption of particles, and hence the interfacial tension, is sensitive to the effective exclusion in a region of width $s$. As the absolute value of the excess interfacial tension is vanishingly small compared to the bare oil-water interface, $\gamma_{ow} = \mathcal{O}(10\ \text{mN/m})$, $\gamma$ will be considered not to contribute to the stability of the system of interest here.

It can be expected that water droplets in oil can only form crystalline structures if long range interactions are present ($\kappa_o a \lesssim 10$), and if the repulsion is sufficiently strong. Figure 4.9 shows the Yukawa potential (4.22) at contact, $V_{Yuk}(2a)$, for several droplet sizes as a function of $\varepsilon_o$, revealing that these two conditions already impose strong restrictions on the dielectric constant and size of the particles. The inset of Fig. 4.9 shows for instance that the screening length in oil decays from $10-100$ $\mu$m at $\varepsilon_o = 4$ to 100 nm at $\varepsilon_o = 12$, for $\varrho_w = 1$ mM, while the main part of Fig. 4.9 shows contact potentials that exceed 10 $k_BT$ for $\varepsilon_o \simeq 6 - 12$ provided the droplet size is in the micron regime. Thus one only expects crystallisation to be possible for micron-sized water droplet in oils that are sufficiently polar ($\varepsilon_o \gtrsim 4$) to have enough charge (see also Fig. 4.8(a)), but not too polar ($\varepsilon_o \lesssim 12$) to have a long enough range $\kappa_o^{-1}$ of the repulsions. This regime of $\varepsilon_o$ is in remarkably good agreement with the range found experimentally [261, 262].

The actual parameter regime where droplets are expected to form crystalline structures, on the basis of $\Gamma > 106$, is depicted in Fig. 4.10, where the varied parameters are the ionic radii $a_+, a_-$ (Fig. 4.10(a)) and the volume fraction and droplet radius $x, a$ (Fig. 4.10(b)). The lines show the envelopes of the regimes $\Gamma > 106$ for all physically achievable ionic strengths $\varrho_w$. Variations of the external potential $\beta V_\pm(z)$ by taking a non-zero $g_\pm$ are seen to result into a significantly modified crystallisation regime. Other solvation effects, e.g. hydration, hydrogen bonding, local alignment of dipolar fluid molecules, are therefore

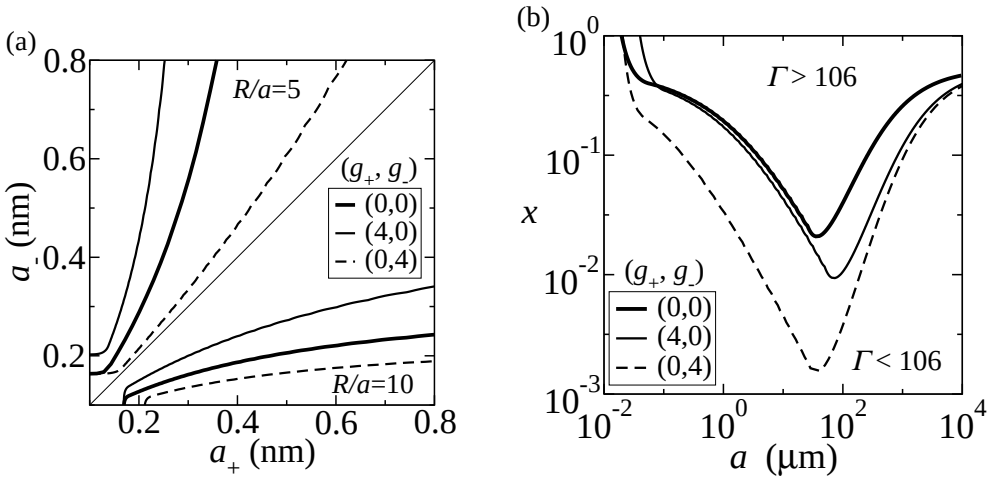


Figure 4.10: (a) The ionic radii $(a_+, a_-)$ for which $\Gamma > 106$ for some physically achievable ionic strength $\varrho_w$. The droplets crystallise in the area between the curves and the horizontal axis $(R/a = 10)$, and between the curves and the vertical axis $(R/a = 5)$, respectively. The lines can be mirrored in the diagonal since there is a symmetry under $a_+ \leftrightarrow a_-$, together with $g_+ \leftrightarrow g_-$. The thin and dashed lines show the results if one of the ionic species has an additional solvation energy (independent of $\varrho_w$ and $\varepsilon_o$) of $g_\pm = 4$. The dielectric constant of the oil is $\varepsilon_o = 7.5$ and droplet radius $a = 1.5$ $\mu$m. (b) The volume fractions of water $x$ and droplet radii $a$ for which $\Gamma > 106$ for some physically achievable ionic strength $\varrho_w$, for several combinations for $g_\pm$. (See Ref. [491] © IOP Publishing. Reproduced with permission. All rights reserved)

expected to be important for a proper quantitative picture. This has been examined in Ref. [491] for $g_\pm = 4$ (Fig. 4.10), which is considerable compared to $|f_+ - f_-| \simeq 2$ for the present parameters but small compared to $f_\pm \simeq 12$. Figure 4.10(b) shows that micron-sized droplets, for the standard parameter set, tend to crystallise at $x \simeq 10^{-2} - 10^{-1}$, which is somewhat higher than the experimentally observed regime $x \simeq 10^{-3} - 10^{-2}$ [261, 262]. A similarly relatively high theoretical value for the crystallisation volume fraction was found in [96], where curvature effects were studied, with $g_\pm \equiv 0$. Combining these results with those of Fig. 4.10(b) suggests that the experimental results may only be quantitatively explained by taking both curvature and specific solvation effects $(g_\pm \neq 0)$ into account (see Subsec. 4.1).

The spontaneous charging of the water droplets might play an important role in the production and stabilisation of emulsions with rather polar oils, since by a judicious choice of the type of oil and salt ions, water droplets can be stabilised by these, sometimes surprisingly strong, electrostatic effects alone [396]. This property is generated by the combination of electrostatic interactions between the ions and material-specific solvation properties of the ions which leads to a structuring, i.e. formation of non-uniformities, of the considered ionic complex fluids.

## 4.2 Wetting properties of electrolyte solutions

Wetting transitions are surface phase transitions which occur whenever a phase C intrudes at the interface between two phases A and B, with either A, B and C in thermodynamic

coexistence or with A as a spectator phase and B and C in thermodynamic coexistence. As an example, A is an inert substrate and B and C are the gas and the liquid phase, respectively, of a simple fluid. The thickness of the intruding liquid film can be either finite (incomplete wetting) or macroscopically large (complete wetting) upon approaching gas-liquid coexistence along an isotherm. The transition at two-phase coexistence from incomplete to complete wetting occurs at the wetting transition temperature $T = T_{\rm w}$. It can be either continuous (second-order), in which case the film thickness diverges smoothly as $T \to T_{\rm w}$ along two-phase coexistence, or discontinuous (first-order), implying a macroscopically large jump of the film thickness from a finite value below $T_{\rm w}$ to a macroscopically large one above $T_{\rm w}$. In the surface phase diagram a first-order wetting transition has a prewetting line associated with it which is connected tangentially to the gas-liquid coexistence line at $T_{\rm w}$, extends into the gas phase region, and ends at a critical point. The richness of wetting phenomena has been covered by various reviews [57, 58, 94, 107, 407].

So far, to a large extent, wetting studies have been devoted to fluids composed of electrically neutral molecules. However, for numerous real systems the presence of ions is either of crucial importance for wetting phenomena, such as electrowetting [309], or unavoidable because many substrates release ions once they are brought into contact with polar solvents [136]. For example, electrowetting refers to the change of the contact angle between a fluid-fluid interface and a substrate as a response to an applied electrostatic potential difference between the substrate and the fluid bulk (see Sec. 4.4). This effect offers numerous applications in devices based on the manipulation of tiny amounts of liquids, such as microfluidic devices [361, 437]. Theoretical studies of those systems started back in 1938 when Langmuir developed a model to determine the equilibrium thickness of water layers on planar surfaces in contact with undersaturated water vapour, based on the calculation of the repulsive force between two plates immersed in electrolyte solutions [248]. The typical values for the equilibrium layer thickness as predicted by Langmuir's formula were confirmed experimentally [173] and the experimental data were used to analyze the effect of various contributions to the disjoining pressure onto the stability of the wetting films [102]. Some years later Kayser generalised Langmuir's model for the equilibrium thickness of wetting layers to liquid mixtures of polar and non-polar components in contact with ionisables substrates [226]; in contact with the wetting liquid these substrates donate ions to the liquid which act as counterions to the emerging opposite charge left on the substrate with overall charge neutrality. This analysis was followed up by including the effect of added salt the ions of which do not stem from the substrate [227]. These papers did not address the issue of wetting transitions at coexistence but rather focused on the thickness of the wetting layer and the behaviour of the disjoining pressure. For wetting films of solvents without added salt, i.e. with counterions only, Langmuir [248] and Kayser [226] found that the film thickness $l$ increases as $l \sim (\Delta\mu)^{-1/2}$, with $\Delta\mu = \mu_{co} - \mu$, as the chemical potential $\mu$ approaches its value $\mu_{co}$ at coexistence from the vapour side ($\mu < \mu_{co}$). In contrast, wetting films without ions and at neutral substrates but with van der Waals interactions lead to $l \sim (\Delta\mu)^{-1/4}$ or $l \sim (\Delta\mu)^{-1/3}$, depending on whether retardation effects are taken into account or not, respectively [107]. In the case that the effect of added salt dominates van der Waals interactions Kayser [227] found $l \sim \ln(\Delta\mu)$ as it holds for short-ranged interactions.

Only recently theoretical investigations concerning wetting transitions of electrolyte solutions at charged solid substrates have emerged [101, 203, 204, 329, 330]. In Ref. [101] the effect of adding ions onto the wetting behaviour of the pure solvent was studied by

using Cahn's phenomenological theory [57, 94, 107, 407] for the solvent combined with the Poisson-Boltzmann theory for the ions. This model does not take into account the solvent particles explicitly, neglecting the coupling between solvent particles and ions. On the other hand, the model in Ref. [329] takes all three types of particles (solvent, cations, and anions) explicitly into account in terms of hard spheres of different diameters with a Yukawa attraction between all pairs and the Coulomb interaction between ions. The model was studied by using Rosenfeld's density functional theory [378, 379] combined with a mean-field approximation for the Yukawa and the electrostatic interactions. Within this model, the polar nature of the solvent molecules was ignored; it was included in a subsequent article by the same authors in which the solvent particles were represented by dipolar hard spheres [330]. However, for technical reasons, the numerical analyses of these continuum models in which all three types of particles are treated explicitly on a microscopic level were limited to small system sizes. Therefore Refs. [329, 330] focused on the case of strong screening of the Coulomb interactions which is provided by large ionic strengths, i.e. large ion concentrations. However, the approaches used in Refs. [101, 329, 330] are not reliable for large ionic strengths due to the use of Poisson-Boltzmann theory for the electrostatic interactions which has been proved to be valid only for low ionic concentrations [434].

In order to overcome these problems a lattice model for an electrolyte solution exposed to a charged substrate has been introduced which takes into account all three components via density functional theory and offers the possibility to study significantly broader interfacial regions [203].

The solution consists of three components: solvent (0), anions ($-$), and cations ($+$). The coordinate perpendicular to the wall is $z$. The region above the wall, accessible to the electrolyte components, is divided into a set of cells the centers of which form a simple cubic lattice $\{\mathbf{r}\}$ with lattice constant $a$. The volume $a^3$ of a cell corresponds roughly to the volumes of the particles, which are assumed to be of similar size. The centers of the molecules in the top layer of the substrate form the plane $z = 0$. At closest approach the centers of the solvent molecules and ions are at $z = a$. The plane $z = a/2$ is taken to be the surface of the planar wall. Each cell is either empty or occupied by a single particle. This mimics the steric hard core repulsion between all particles. Particles at different sites interact among each other via an attractive nearest-neighbour interaction of strength $u$ which is taken to be the same for all pairs of particles. In addition, ion pairs interact via the Coulomb potential. The solvent particles are taken to carry a dipole moment.

The wall attracts particles only in the first adjacent layer via an interaction potential of strength $u_{\mathrm{w}}$ which is the same for all species. In addition it can carry a homogeneous surface charge density $\tilde{\sigma} = \sigma e a^{-2}$ which is taken to be localised in the plane $z = a/2$ and which interacts electrostatically with the ions; $e > 0$ is the elementary charge. Since the focus is on the influence of the ions onto wetting phenomena the more realistic, long-ranged van der Waals forces which are known to be relevant for wetting transitions [107] are disregarded first. Within the mean-field theory, the choice of nearest-neighbour interactions provides a significant computational bonus.

The Bragg-Williams approximation [27, 73, 360, 395] leads to the grand canonical den-

sity functional

$$\beta\Omega\left[\{\varrho_i(\bar{\mathbf{r}})\}\right] = \sum_{\bar{\mathbf{r}}}\left[\sum_i \varrho_i(\bar{\mathbf{r}})\ln\varrho_i(\bar{\mathbf{r}}) + \left(1-\sum_i\varrho_i(\bar{\mathbf{r}})\right)\ln\left(1-\sum_j\varrho_j(\bar{\mathbf{r}})\right)\right] + \frac{1}{2}\beta\sum_{\substack{\bar{\mathbf{r}},\bar{\mathbf{r}}'\\ \bar{\mathbf{r}}\neq\bar{\mathbf{r}}'}}\sum_{i,j}\varrho_i(\bar{\mathbf{r}})\varrho_j(\bar{\mathbf{r}}')w\left(|\bar{\mathbf{r}}-\bar{\mathbf{r}}'|\right) - \beta\sum_{\bar{\mathbf{r}}}\sum_i u_{\mathrm{w}}\delta_{\bar{z},1}\varrho_i(\bar{\mathbf{r}}) - \beta\sum_{\bar{\mathbf{r}}}\sum_i\mu_i\varrho_i(\bar{\mathbf{r}}) + 2\pi l_B\int_V d^3\bar{r}^*\frac{\left(\mathbf{D}\left(\bar{\mathbf{r}}^*,[\varrho^*_\pm]\right)\right)^2}{\varepsilon(\varrho_0^*(\bar{\mathbf{r}}^*))}. \tag{4.25}$$

The first term of Eq. (4.25) represents the ideal gas (entropic) contribution to the Helmholtz free energy, the second term accounts for the hard core interaction and the third term represents the non-electrostatic nearest-neighbour interaction $w\left(|\bar{\mathbf{r}}-\bar{\mathbf{r}}'|=1\right)=u$ within the random phase approximation (RPA) [131]. This approximation is justified because RPA is reliable in the present situation of vanishing contrast between the non-electrostatic interactions of the three species [43] (see Sec. 2.1). The strength $u$ of the nearest-neighbour interaction is expressed in terms of the reduced temperature $T^*=1/(3\beta u)$. The last term is the electrostatic energy. The density profiles $\varrho_\pm(\bar{z})$ have to fulfill global charge neutrality, i.e.

$$\sum_{\bar{z}=1}^{\bar{L}}\left[\varrho_+(\bar{z})-\varrho_-(\bar{z})\right]+\sigma=0, \tag{4.26}$$

where $\sigma$ is the surface charge density.

The relative permittivity $\varepsilon(\bar{z}^*)$ is taken to depend locally on the solvent density $\varrho_0^*(\bar{z}^*)$ through the Clausius-Mossotti expression [210]

$$\varepsilon(\varrho_0^*(\bar{z}^*)) = \frac{1+\frac{2\alpha}{3\varepsilon_0}\varrho_0(\bar{z}^*)}{1-\frac{\alpha}{3\varepsilon_0}\varrho_0^*(\bar{z}^*)}, \tag{4.27}$$

where $\alpha$ is an effective polarisability of the solvent molecules. In the following its value is chosen such that $\varepsilon=60$ for $\varrho_0=1$; this choice corresponds to a mean value for liquid water along the liquid-vapour coexistence curve.

For bulk ionic strength $\varrho_+=\varrho_-=I=0$ the resulting phase diagram can be determined analytically and is plotted in Fig. 4.11. The reduced critical temperature is $T_c^*(I=0)=0.5$ and the critical number density is $\varrho_{0,c}(I=0)=0.5$. For $I\neq 0$ the binodal curves are determined numerically and the critical points are obtained by determining the maximum of the corresponding spinodal curves. Within the model the reduced critical temperature $T_c^*$ is independent of $I$ whereas $\varrho_{0,c}(I)=0.5-2I$. In agreement with experimental evidence [409] the shift of the binodal curves is negligibly small for ionic strengths up to 10 mM, i.e. $I\leq 3.9\times 10^{-4}$.

First the case $I=0$ is considered, in which the model reduces to the lattice-gas model studied by Pandit et al. [342, 343]. In that case, the Euler-Lagrange equation reduces to

$$\ln\varrho_0(\bar{z})-\ln\left[1-\varrho_0(\bar{z})\right]-\mu_0^*-\beta u_{\mathrm{w}}\delta_{1,\bar{z}}-\frac{1}{3T^*}\left[4\varrho(\bar{z})+\varrho(\bar{z}+1)+\varrho(\bar{z}-1)\right]=0, \tag{4.28}$$

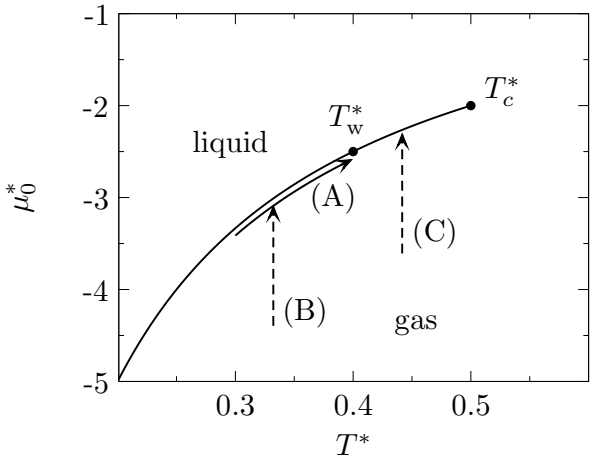


Figure 4.11: Bulk phase diagram $\mu_{0,co}(T)$ of liquid-gas *co*existence in the $\mu_0^* - T^*$ plane for the salt-free ($I = 0$) case of a pure solvent. If the wetting transition temperature $T_w^*$ is above the triple point $T_t^* \simeq 0.21$ (for water), three types of paths (A), (B), and (C) are used to study the wetting behaviour of the model. (A) is a path along gas-liquid coexistence on the gas side whereas along the paths (B) and (C) two-phase coexistence is approached along isotherms leading to incomplete (B) and complete (C) wetting, respectively. (See Ref. [203])

and the ratio $u_w/u = 3T^*\beta u_w$ controls the wetting and drying transitions. For $u_w/u > 1$ the substrate is so strong that it is already wet at $T^* = 0$; in the range $0.5 < u_w/u < 1$ there is a wetting transition at $T_w^* > 0$; and in the parameter range $0 \leq u_w/u < 0.5$ a drying transition occurs. Depending on the value of the ratio $u_w/u$ one observes layering transitions, i.e. one can distinguish the number of discrete layers which are forming upon reaching thick films. The transition from $n$ to $n+1$ layers is first order and shows up as a jump in the film thickness $l$. The loci of these discontinuities are layering transition lines, each ending at a critical point $T_{c,n}^*$. For large $n$, $T_{c,n}^*$ approaches the roughening transition. However, within the present mean-field theory $T_{c,n}^*$ approaches $T_c^*$. Since layering transitions should only occur along or near the melting curve or the sublimation line, these layering transitions are a special feature of the lattice-gas model used to describe the liquid and gas phases [107].

In Ref. [203] calculations have been carried out in the parameter range $0.5 < u_w/u < 1$. A wider range of the parameter $u_w/u$ was studied thoroughly by Pandit et al. [342, 343]. Figure 4.12 shows the effective interface potential $\omega(l) = \Omega_s(l) - \gamma_{g,l} - \gamma_{l,s}$ for three different temperatures along a path at coexistence [path (A) in Fig. 4.11] for the rather arbitrarily chosen values $u_w/u = 0.81$ and $u_w/u = 0.69$. Here $\gamma_{g,l}$ and $\gamma_{l,s}$ are the gas-liquid and liquid-substrate interfacial tensions, respectively, such that by construction at two-phase coexistence $\omega(l \to \infty) = 0$. The equilibrium thickness of the liquid film is given by the position of the global minimum of $\omega(l)$. If $l = \infty$ is the global minimum of $\Omega_s(l)$ the system is wet. In this case, the gas-substrate surface tension is given by $\gamma_{g,s} = \Omega_s(l = \infty) = \gamma_{g,l} + \gamma_{l,s}$ [107].

In the two cases which have been considered in Fig. 4.12, $\omega(l)$ exhibits only a single minimum, the position of which diverges continuously or via steps of finite size as $T^* \to T_w^*$. For $T^* > T_w^*$ the position of the minimum is $l = \infty$ and the system is wet. The wetting

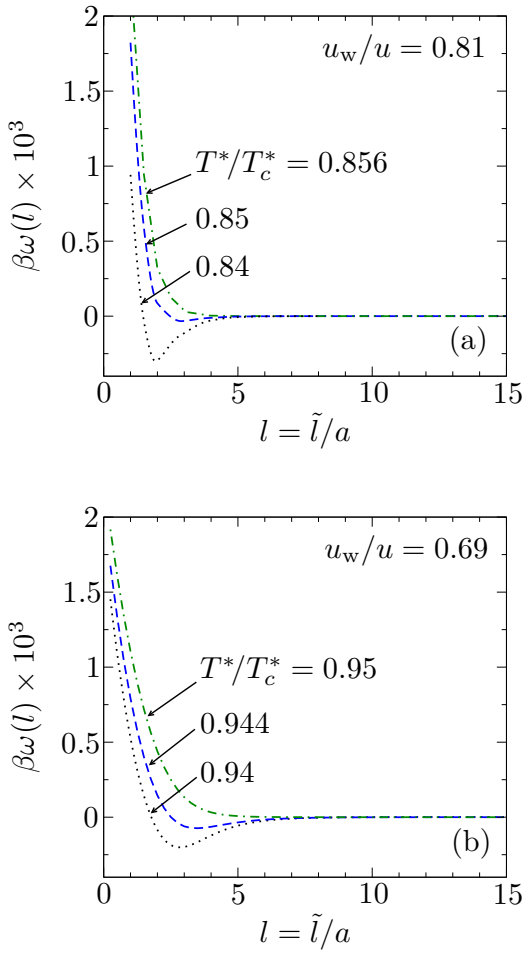


Figure 4.12: Effective interface potential $\omega(l) = \Omega_s(l) - \gamma_{g,l} - \gamma_{l,s}$ at two-phase coexistence as a function of the thickness $\tilde{l} = la$ of the adsorbed liquid film for three temperatures in the salt-free case ($I = 0$) for $u_w/u = 0.81$ (a) and $u_w/u = 0.69$ (b) . In both cases $\omega(l)$ exhibits only a single minimum, the position of which diverges continuously as $T^* \to T_w^*$. Accordingly, the system undergoes critical wetting at $T_w^* \simeq 0.856 T_c^*$ for $u_w/u = 0.81$ and at $T_w^* \simeq 0.95 T_c^*$ for $u_w/u = 0.69$. (See Ref. [203])

transition is second order and occurs at the temperature $T_w^* \simeq 0.856 T_c^*$ for $u_w/u = 0.81$ and at $T_w^* \simeq 0.95 T_c^*$ for $u_w/u = 0.69$. Within the present model, in which all interactions are of the nearest-neighbour type only for the pure solvent, the system exhibits a second-order wetting transition in the entire parameter range $0.5 < u_w/u < 1$. This observation is compatible with corresponding Monte Carlo simulations of the Ising model on a cubic lattice [46, 47]. However, the order of wetting transitions depends sensitively on the range of interactions as well as on whether a continuous or a lattice model is considered. For a continuous analogue of the present model, Pandit et al. [343] found a second-order wetting transition only for $0.5 < u_w/u \lesssim 0.7$ but a first-order one for $u_w/u \gtrsim 0.7$.

Moreover, lattice-gas models with short-ranged particle-particle interactions and long-ranged substrate potentials were studied by de Oliveira and Griffiths [331] and Ebner [124, 125]. In Ref. [331] complete wetting in a system with $T_w = 0$ was studied within mean field theory. Ebner reported $T_w = 0$ or a first-order wetting transition depending on the strength of the substrate potential [124] and studied the same interaction potentials

as the ones used in Refs. [124, 331] applying Monte Carlo simulations [125]. Finally, in systems in which both the particle-particle interactions and the substrate potentials are long-ranged, critical (i.e. second-order) and first-order wetting can occur for suitable choices of the interaction potentials [106, 126].

The film thickness $l = \tilde{l}/a$ as function of $\mu^*_{0,co}(T^*) - \mu^*_0$, when bulk coexistence $\mu_{0,co}(T^*)$ (see Fig. 4.11) is approached along four isotherms from the gas phase [paths of type (B) and (C) in Fig. 4.11], is plotted in Fig. 4.13. In the case $u_w/u = 0.81$ (Fig. 3(a)) the isotherms exhibit vertical steps at the aforementioned layering transitions. Above $T^*_w$, i.e. when the substrate is completely wet at coexistence, the isotherms exhibit an unlimited number of such steps as $\mu^*_{0,co}(T^*) - \mu^*_0$ approaches zero, while for $T^* < T^*_w$ there is only a finite number of steps. For $u_w/u = 0.69$ (Fig. 3(b)) layering transitions do not occur and the film thickness diverges logarithmically for $T^* > T^*_w$, while for $T^* < T^*_w$ it reaches a finite value at coexistence.

Within the above concepts the influence of the ionic strength $\tilde{I} = Ia^{-3}$ and of the surface charge density $\tilde{\sigma} = \sigma e a^{-2}$ on the wetting behaviour of systems with $u_w/u = 0.81$ or $u_w/u = 0.69$ is studied. If the substrate is neutral ($\sigma = 0$), the addition of salt changes neither the order nor the transition temperature of the wetting transition, i.e. there is a second-order wetting transition at the wetting temperature $T^*_w$. This is expected because within the model all particles have the same size, the ions have the same absolute charge, and the strength of the particle-particle and of the substrate-particle nearest-neighbour interactions are the same for all three species. Hence local charge neutrality ($\varrho_+(\bar{z}) = \varrho_-(\bar{z})$) holds due to the exchange symmetry with respect to the ionic components. This implies that there is no electric field ($D(\bar{z}) = 0$). If the surface charge becomes non-zero, the order of the wetting transition changes from second order ($\sigma = 0$) to first order ($\sigma \neq 0$) for all values of the charge density $\sigma$ and ionic strength $I$ studied here, with $\sigma = 2 \times 10^{-5}$ (i.e. $\tilde{\sigma} \approx 0.002\ \mu\mathrm{C/cm^2}$) as the smallest non-zero value considered. This result is in agreement with previous studies. The influence of ionic solutes on the order of the wetting transition was studied in Ref. [101] by using Cahn's phenomenological theory and in Ref. [329] by using density functional theory for an explicit solvent model for an ionic solution. Both studies suggest that electrostatic interactions favour first-order wetting. An explanation for this general property of ionic complex fluids is given below (see also Ref. [204]).

Figure 4.14 shows examples of the effective interface potential $\omega(l)$ in the case of non-zero surface charge densities, $\sigma = 2 \times 10^{-3}$ and $\sigma = 2 \times 10^{-4}$, for two temperatures and at bulk coexistence [see path (A) in Fig. 4.11]. In both cases, $\omega(l)$ has two local minima. For $T^* < T^*_w$ the global minimum corresponds to a thin film whereas for $T^* > T^*_w$ the film is macroscopically thick. At the wetting transition temperature $T^*_w$ the two minima correspond to the same value of the effectiveinterface potential $\omega(l)$. Accordingly, at $T^*_w$ the film thickness jumps discontinuously from a finite value below $T^*_w$ to a macroscopic one above $T^*_w$ so that the system undergoes a first-order wetting transition. If $\sigma$ is decreased the height of the barrier in $\omega(l)$ at the wetting temperature $T^*_w$ decreases and the minimum close to the wall is shifted to larger thicknesses (Fig. 4.14(b)). In the case $\sigma = 0$, $\omega(l)$ has only a single minimum, like in the salt-free case (see Fig. 4.12), corresponding to a second-order wetting transition.

In Fig. 4.15 the wetting transition temperature is plotted as function of the surface charge density for two values of the ionic strength and for $u_w/u = 0.81$. As $\sigma = \tilde{\sigma} a^2/e$ is increased, the wetting transition temperature $T^*_w$ decreases due to the strengthening

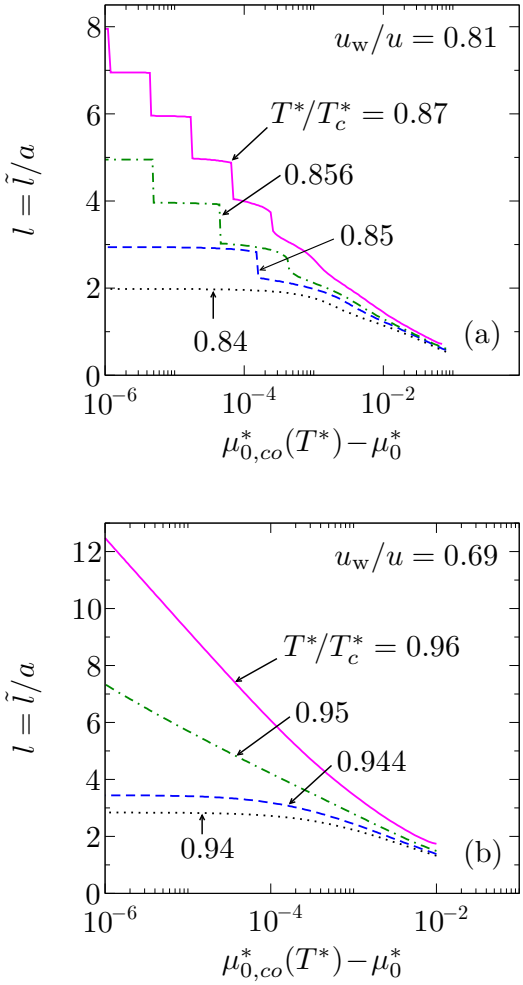


Figure 4.13: Film thickness $l = \tilde{l}/a$ in units of the lattice constant $a$ as a function of undersaturation $\mu^*_{0,co}(T^*) - \mu^*_0$ for the salt-free case ($I = 0$). Gas-liquid coexistence $\mu^*_{0,co}(T^*)$ is approached from the gas phase. (a) $u_w/u = 0.81$: for $T^* < T^*_w = 0.856 T^*_c$ the system is partially wet and, if at all, there is a finite number of layering transitions; for $T^* > T^*_w$ the isotherms exhibit an unlimited number of layering transitions as $\mu^*_{0,co}(T^*) - \mu^*_0 \to 0$ and the first few layering transitions are rounded because for this temperature $T^* > T^*_{c,n}$. (b) $u_w/u = 0.69$: the film thickness diverges logarithmically for $T^* > T^*_w = 0.95 T^*_c$, while it reaches a finite value at coexistence for $T^* < T^*_w$. In (b) there are no layering transitions. Note that with $T^*_c(I) = \frac{1}{2}$ one has $\mu^*_{0,co}(T^*) - \mu^*_0 = \frac{2/3}{T^*/T^*_c} \left[\frac{\mu_{0,co}(T^*) - \mu_0}{u}\right]$. (See Ref. [203])

of the substrate-fluid attraction as the substrate is charged up. This effect is similar to electrowetting (see Sec.4.4) and it has been observed experimentally with the surface charge being modified by ion adsorption [310]. For $\sigma \neq 0$ the system with a smaller ionic strength $I$ has always the lower wetting transition temperature $T^*_w$ because in this case the screening of the electrostatic forces of the substrate is reduced making them effectively stronger which favours wetting. As already mentioned above, within the model for $\sigma = 0$ the wetting transition temperature is independent of the ionic strength $\tilde{I} = Ia^{-3}$. The trend is the same for $u_w/u = 0.69$. In the case of first-order wetting transitions these

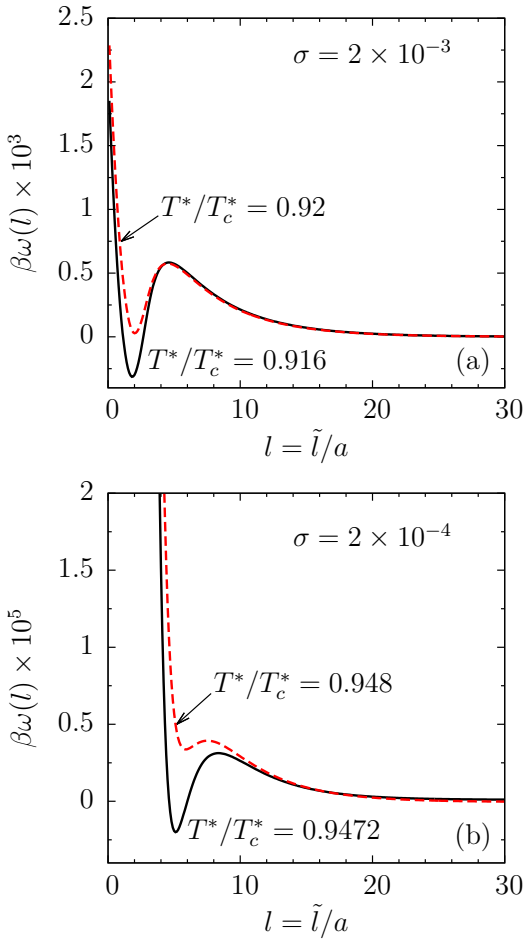


Figure 4.14: Effective interface potential $\omega(l)$ at gas-liquid coexistence as function of the thickness $l = \tilde{l}/a$ of the liquid film for $u_w/u = 0.69$, $I = 3.9 \times 10^{-5}$ ($\tilde{I} = 1$mM), and $\sigma = 2 \times 10^{-3}$ ($\tilde{\sigma} = 0.2\mu$C/cm$^2$) in (a) and $\sigma = 2 \times 10^{-4}$ ($\tilde{\sigma} = 0.02\mu$C/cm$^2$) in (b) for two temperatures in each case. The effective interface potential $\omega(l)$ has two local minima (one at $l < \infty$ and one at $l = \infty$) which have the same depth at $T_w^*$. Accordingly, for both surface charge densities $\sigma$ the system undergoes a first-order wetting transition. (See Ref. [203])

results are in qualitative agreement with Ref. [329]. However, the off-lattice model used therein exhibits also second-order wetting transitions, for which $T_w^*$ is a non-monotonic function of $\sigma$.

Since the wetting transitions for $\sigma \neq 0$ are first order [204] (see below), there is a prewetting line associated with them. The prewetting line is attached tangentially to the gas-liquid coexistence line at the wetting temperature $T_w^*$ and bends away from coexistence, marking the loci of a finite discontinuity in film thickness $l = \tilde{l}/a$. The discontinuity upon crossing the prewetting line gets smaller as one moves further away from coexistence and it vanishes at the prewetting critical point. Figure 4.16 shows the film thickness $l = \tilde{l}/a$ for four different isotherms as a function of undersaturation $\mu_{0,co}^*(T^*) - \mu_0^*$ for $u_w/u = 0.81$ and $\sigma = 2 \times 10^{-3}$ ($\tilde{\sigma} = 0.2\mu$C/cm$^2$). The film thickness increases for small undersaturation as $l \sim \ln(\mu_{0,co}^*(T^*) - \mu_0^*)$. Accordingly, $\omega(l) \sim \exp(-2\kappa l)$, where $\kappa = \sqrt{8\pi l_B I/\varepsilon(\varrho_0^l)}$ is the inverse Debye length (see inset of Fig. 4.16). This is in agreement with Refs.

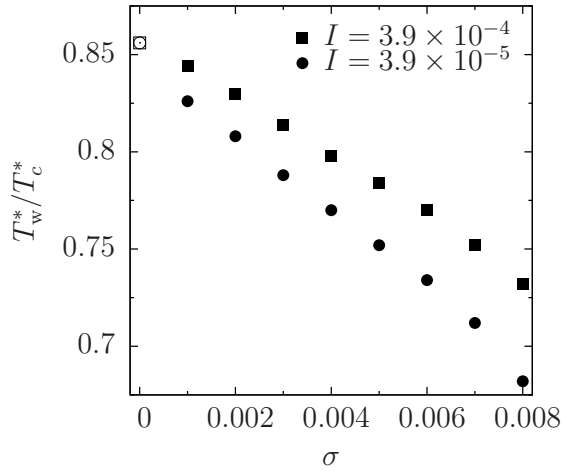


Figure 4.15: Wetting transition temperature $T_w^*$ as a function of the substrate surface charge density $\sigma = \tilde{\sigma}a^2/e$ for $u_w/u = 0.81$. The two types of symbols correspond to distinct values of the ionic strength $I = \tilde{I}a^3$ in the bulk liquid phase (• for $I = 3.9 \times 10^{-5}$ ($\tilde{I} = 1$mM) and ■ for $I = 3.9 \times 10^{-4}$ ($\tilde{I} = 10$mM)). Filled symbols correspond to first-order wetting transitions, while the empty one at $\sigma = 0$ corresponds to a second-order wetting transition, with the corresponding wetting transition temperature being independent of $I$. (See Ref. [203])

[227] and [101] for wetting of solvents with added salt. In contrast, for wetting films of solvents without addition of salt, i.e. with counterions only, one has $l \sim (\mu_{co} - \mu)^{-1/2}$ and $\omega(l) \sim l^{-1}$ [101, 102, 226, 248]. In order to obtain this result, Eq. (4.25) has to be modified to consider only solvent particles and counterions but leaving out coions. In addition to the finite thin-thick jumps in film thickness $l$ when crossing the prewetting line one observes first-order layering transitions similar to those found in the salt-free case for $u_w/u = 0.81$ (see Fig. 4.13). The addition of the electrostatic interaction leads to a series of triple points where the layering transition lines meet the prewetting line, as shown in the surface phase diagram in Fig. 4.17. A similar phase diagram was found by Ebner [124] using a lattice-gas model for a one-component fluid in which the fluid particles interact among each other via a Lennard-Jones (6-12) potential and a fluid particle interacts with the substrate via a (9-3) potential. This is also in line with the prediction by Pandit et al. [342] for a substrate of intermediate strength, i.e. for $0.5 < u_w/u < 1$, with interactions ranging beyond nearest neighbours.

In the case $u_w/u = 0.81$ and for fixed ionic strength $I$ the prewetting lines for various values of the surface charge density $\sigma$ have been studied in Ref. [203]. Figure 4.18 shows the prewetting lines for ionic strength $I = 3.9 \times 10^{-5}$ ($\tilde{I} = 1$mM) and for four values of $\sigma$. One can see clearly that as $\sigma$ decreases, the wetting temperature $T_w^*$ rises and the prewetting line becomes shorter. This is in agreement with the fact that in the limit $\sigma \to 0$ the wetting transition turns second order. The values of the prewetting critical points for the lines shown in Fig. 4.18 are given in Tab. 4.2.

Although the lattice model of Ref. [203] differs significantly from the continuum models used in Refs. [101, 329], it leads to similar conclusions concerning the trend that adding ions promotes *first*-order wetting transitions. Accordingly, this result can be considered

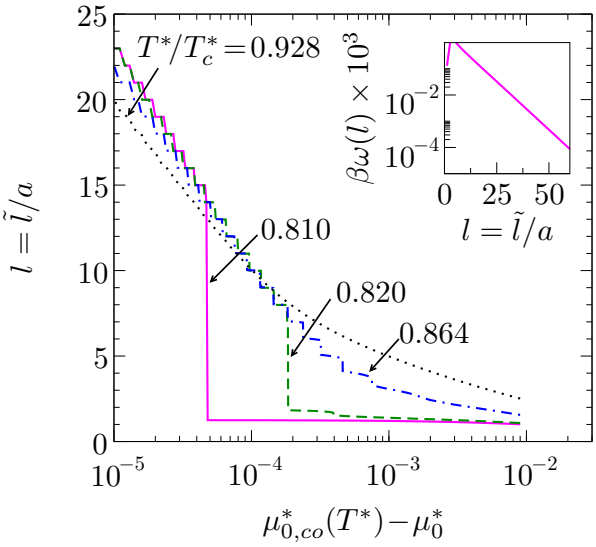


Figure 4.16: The film thickness $l = \tilde{l}a$ as a function of undersaturation $\mu^*_{0,co}(T^*)-\mu^*_0$ along four different isotherms for $u_w/u = 0.81$, $I = 3.9\times10^{-5}$ ($\tilde{I}$ = 1mM), and $\sigma = 2\times10^{-3}$ ($\tilde{\sigma} = 0.2\mu\mathrm{C/cm}^2$) exhibits a large but finite jump (corresponding to more than one monolayer) when the prewetting line is crossed and small jumps when the various layering transition lines are crossed. The film thickness increases for small undersaturation as $l \sim \ln(\mu^*_{0,co}(T^*)-\mu^*_0)$ where $\mu^*_{0,co}(T^*)-\mu^*_0 = \frac{2/3}{T^*/T_c^*}\left[\frac{\mu_{0,co}(T^*)-\mu_0}{u}\right]$. The inset displays the corresponding asymptotic behaviour of the effective interface potential $\omega(l) \sim \exp(-2\kappa l)$ where $\kappa = \sqrt{8\pi l_B I/(\varepsilon(\varrho_0^{(1)})}$ is the inverse Debye length. (See Ref. [203])

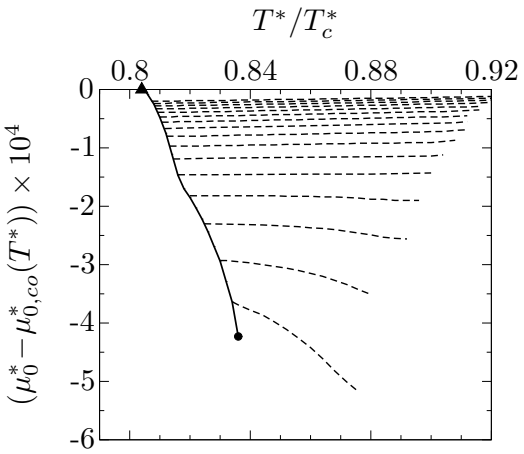


Figure 4.17: Surface phase diagram for $u_w/u = 0.81$ and $\sigma = 2\times10^{-3}$ ($\tilde{\sigma} = 0.2\mu\mathrm{C/cm}^2$). The full line is the prewetting line attached to $T^*_w = 0.864\,T^*_c$ (▲) and ending at the prewetting critical point (•). The dashed lines correspond to layering transition lines. They end at layering critical points $T^*_{c,n}$ (located at the end of the dashed lines without being indicated separately), which within the present mean-field theory accumulate for $n \to \infty$ at $T^*_c$ instead of at the roughening transition temperature of the gas-liquid interface on the lattice. (See Ref. [203])

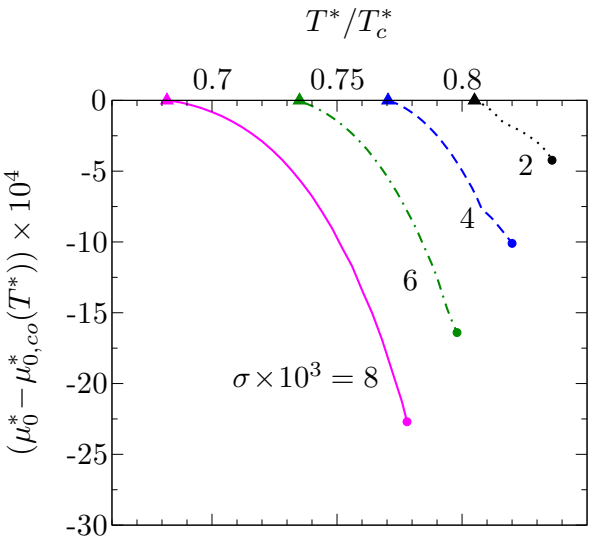


Figure 4.18: Prewetting lines for four values of the surface charge density $\sigma = \tilde{\sigma}a^2/e$ with ionic strength $I = 3.9 \times 10^{-5}$ ($\tilde{I} = 1$mM) in the bulk liquid phase and for $u_w/u = 0.81$. The locations of the wetting transitions (▲) and of the prewetting critical points (●) are given in Tab. 4.2. (See Ref. [203])

| $\sigma = \tilde{\sigma}a^2/e$ | $T_w^*/T_c^*$ | $T_{pw,c}^*/T_c^*$ | $\mu_{0,co}^*(T_{pw,c}^*) - \mu_{0,pw,c}^*$ |
|---|---|---|---|
| $2 \times 10^{-3}$ | 0.804 | 0.836 | $4.23 \times 10^{-4}$ |
| $4 \times 10^{-3}$ | 0.77 | 0.82 | $1.01 \times 10^{-3}$ |
| $6 \times 10^{-3}$ | 0.734 | 0.798 | $1.60 \times 10^{-3}$ |
| $8 \times 10^{-3}$ | 0.682 | 0.778 | $2.27 \times 10^{-3}$ |

Table 4.2: Prewetting critical points $(T_{pw,c}^*, \mu_{0,pw,c}^*)$ for the prewetting lines shown in Fig. 4.18. The ionic strength in the liquid phase is $I = 3.9 \times 10^{-5}$ ($\tilde{I} = 1$mM). $T_w^*$ is the transition temperature for first-order wetting. Note that $\mu_{0,co}^*(T_{pw,c}^*) - \mu_{0,pw,c}^* = \frac{2/3}{T_{pw,c}^*/T_c^*}\left[\frac{\mu_{0,co}(T_{pw,c}^*) - \mu_{0,pw,c}}{u}\right]$. (See Ref. [203])

to be robust. In addition within the lattice approach one is able to study, on the one hand, *wide* interfacial regions and therefore small ionic strengths which was not possible within the model studied in Ref. [329], and, on the other hand, prewetting, providing a more complete description of the wetting properties of electrolytes. In agreement with Refs. [101, 227] the growth law of the film thickness for complete wetting along an isotherm is not changed by adding ions to the solvent, in spite of their long-ranged Coulombic interaction (Figs. 4.13 and 4.16) . However, if only counterions are considered, which are donated by the substrate and the charge of which is opposite to that of the wall, the film thickness varies as $l \sim (\mu_{co} - \mu)^{-1/2}$ [101, 226, 248]. Hence, the ionic complex fluid nature of electrolyte solutions appears clearly in the context of wetting phenomena, but the features are, to a large extent, of general, i.e. material independent, character, because they are determined by the Debye length.

As mentioned above electrolyte solutions appear to exhibit in general first-order wetting transitions, independent of the model. In order to explain this general property one can resort to the model for an electrolyte solution near a charged wall which has been

introduced and studied in Ref. [43] (see Sec. 2.1). Hence the starting point in Ref. [204] is the following grand canonical functional, which is a modification of Eq. (2.1) applied to the case of a three-dimensional semi-infinte system at $z > 0$:

$$\begin{aligned}\beta\Omega_0[\phi(\mathbf{r}), \varrho_\pm(\mathbf{r})] = \int d^3r \Big\{ & \phi(\mathbf{r})(\ln(\phi(\mathbf{r})) - \beta\mu_\phi) + (1-\phi(\mathbf{r}))\ln(1-\phi(\mathbf{r})) \\ & + \chi(T)\phi(\mathbf{r})(1-\phi(\mathbf{r})) + \frac{\chi(T)}{6}(\nabla\phi(\mathbf{r}))^2 \Big\} \\ & - \beta h_1 \int d^2r_{||}\phi(\mathbf{r}_{||}, z=0) + \beta\frac{g}{2}\int d^2r_{||}\phi(\mathbf{r}_{||}, z=0)^2 \\ & + \int d^3r \Big\{ \sum_{i=\pm} \varrho_i(\mathbf{r}) \left(\ln \varrho_i(\mathbf{r}) - 1 - \beta\mu_i + V_i(\phi(\mathbf{r}))\right) \\ & + \frac{2\pi l_B}{\varepsilon(\phi(\mathbf{r}))} \left(\mathbf{D}(\mathbf{r}, [\varrho_\pm])\right)^2 \Big\}. \end{aligned} \tag{4.29}$$

In the following the fluid solvent at position $\mathbf{r}$ with $\phi(\mathbf{r}) < 1/2$ is referred to as a "gas", whereas for $\phi(\mathbf{r}) > 1/2$ it is called a "liquid". The first and the last integral are taken over the half-space $\mathbf{r} = (x, y, z \geq 0)$ whereas the second and the third integral run over the surface $z = 0$; $\varrho_\pm (\ln \varrho_\pm - 1 - \beta\mu_\pm)$ is the bulk grand potential density of the $\pm$-ions in the low number density limit. Within this model the interaction of the solvent with the wall is captured by the parameters $h_1$ and $g$. This implicitly assumes that the fluid-wall interactions are sufficiently short ranged so that their contributions to $\Omega_0$ depend only on the solvent density $\phi(\mathbf{r}_{||}, z=0)$ in the vicinity of the wall. This parametrisation has been used by Nakanishi and Fisher [315] in order to analyze the global surface phase diagram of the Landau-Ginzburg theory for wetting. $V_\pm(\phi)$ is the solvation free energy per $k_BT$ of a $\pm$-ion in the solvent of number density $\phi$. Whereas more realistic expressions of $V_\pm(\phi)$ are discussed in the literature [43] (see Eq. (2.3)), a simple piece-wise constant expression $V_\pm(\phi < 1/2) = V_g$ and $V_\pm(\phi > 1/2) = V_l$ with $V_g - V_l \gg 1$ is used in Ref. [204]. This choice guarantees a vanishingly small ionic strength in the gas ($\phi < 1/2$) as compared to the ionic strength in the liquid ($\phi > 1/2$). Without restriction of generality we choose $V_l := 0$, which can be achieved by a redefinition of the ionic chemical potentials ($\beta\mu_\pm - V_l \mapsto \beta =: \hat{\mu}_\pm$; in the following the hat $\hat{}$ is dropped). The discontinuity of $V_\pm(\phi)$ at $\phi = 1/2$ is expected to not affect the results significantly because only thermodynamic states of liquid-gas coexistence well below the critical point are considered, for which $\phi = 1/2$ is deep inside the unstable region of the bulk phase diagram. Note that here no unequal partitioning of ions in a non-uniform solvent occurs due to $V_+(\phi) - V_-(\phi) = 0$, i.e. due to a vanishing difference of solubility contrasts of anions and cations between the two phases in the sense of Ref. [43] (see Secs. 2.1 and 4.6). Moreover, no specific adsorption of ions at interfaces is considered, i.e. there are no surface fields acting on $\varrho_\pm$. Various empirical expressions for $\varepsilon(\phi)$ are in use [55]. However, for the sake of simplicity here a simple piece-wise constant expression $\varepsilon(\phi < 1/2) = 1$ and $\varepsilon(\phi > 1/2) = \varepsilon_l$ with the relative permittivity $\varepsilon_l$ of the liquid solvent is adopted. For the same reasons as for the case of the piece-wise constant expressions $V_\pm(\phi)$ (see above), the discontinuity of $\varepsilon(\phi)$ at $\phi = 1/2$ is expected to be irrelevant for the present purposes.

In the presence of walls, $\phi$ and $\varrho_\pm$ vary spatially in normal direction $z$. Their equilibrium profiles minimise the full functional $\Omega_0[\phi(\mathbf{r}), \varrho_\pm(\mathbf{r})]$ in Eq. (4.29) and thus render the equilibrium state. This procedure can be performed numerically. However, for the present

purpose, analytic expressions are sought. In order to achieve this goal a Taylor expansion of the local part in Eq. (4.29) is performed around the *s*harp-*k*ink reference density profiles [107]

$$\bar{\phi}(z) = \phi_{sk}(z) = \begin{cases} \phi_l, & 0 \leq z \leq \ell \\ \phi_g, & z > \ell \end{cases} \tag{4.30}$$

and

$$\bar{\varrho}_{\pm}(z) = \varrho_{sk,\pm}(z) = \begin{cases} I, & 0 \leq z \leq \ell \\ 0, & z > \ell \end{cases} \tag{4.31}$$

where $\ell$ is the position of the discontinuity of the sharp-kink profile $\phi_{sk}(z)$, and $\phi_l$ and $\phi_g$ are, respectively, the equilibrium bulk densities of the solvent in the liquid and gas phase for a bulk ionic strength $I$ in the liquid phase.

*At* two-phase coexistence and in the limit $\ell \gg 1/\kappa$ the effective interface potential $\omega(\ell) = \Omega_s(\ell) - \Omega_s(\infty)$ at two-phase coexistence is given by [204]

$$\begin{aligned} \beta\omega(\ell \gg 1/\kappa) \simeq\ & (\phi_l - \phi_g)\frac{\chi(T)}{3\xi}\frac{\beta(h_1 - g\phi_l)}{\beta g + \frac{\chi(T)}{3\xi}}\exp(-\ell/\xi) \\ & - (\phi_l - \phi_g)^2\frac{\chi(T)}{12\xi}\frac{\frac{\chi(T)}{3\xi} - \beta g}{\beta g + \frac{\chi(T)}{3\xi}}\exp(-2\ell/\xi) \\ & + \frac{4\pi l_B \sigma^2}{\varepsilon_l \kappa}\exp(-2\kappa\ell). \end{aligned} \tag{4.32}$$

The property $\xi_l = \xi_g$ at coexistence is a special feature of the present model. In general $\xi_l \neq \xi_g$ so that in this case an expansion of the effective interface potential $\omega(\ell)$ similar to Eq. (4.32) contains products of powers of $\exp(-\ell/\xi_l)$ and $\exp(-\ell/\xi_g)$.

First the case of a pure solvent (i.e. $I = 0$) near a neutral wall (i.e. $\sigma = 0$) and at gas-liquid coexistence is considered. For such a system the effective interface potential in Eq. (4.32) reduces to [204]

$$\beta\omega(\ell) = a_0(T)\exp(-\ell/\xi) + b_0(T)\exp(-2\ell/\xi) \tag{4.33}$$

with

$$a_0(T) = (\phi_l - \phi_g)\frac{\chi(T)}{3\xi}\frac{\beta(h_1 - g\phi_l)}{\beta g + \frac{\chi(T),}{3\xi}} \tag{4.34}$$

and

$$b_0(T) = -(\phi_l - \phi_g)^2\frac{\chi(T)}{12\xi}\frac{\frac{\chi(T)}{3\xi} - \beta g}{\beta g + \frac{\chi(T)}{3\xi}}. \tag{4.35}$$

For second-order wetting to occur at $T = T_{\mathrm{w}}$, the coefficient $a_0(T)$ must be negative for $T < T_{\mathrm{w}}$, vanish at $T = T_{\mathrm{w}}$ and be positive for $T > T_{\mathrm{w}}$. As $\phi_l > \phi_g$, and because $\phi_l$ can vary only between its value at the triple point $\phi_l(T_t)$ and the critical density $\phi_c = \phi_l(T_c)$, $a_0(T)$ fulfills the above mentioned conditions if [204]

$$\phi_c < \frac{h_1}{g} < \phi_l(T_t). \tag{4.36}$$

Here and in the following $h_1 > 0$ and $g > 0$ are considered. The order of the transition is determined by the higher-order coefficients in the expansion of $\omega(\ell)$ [107]. If $b_0(T_\mathrm{w}) < 0$, the transition is of first order while second-order wetting can occur if $b_0(T_\mathrm{w}) > 0$. Only in the latter case $a_0(T_\mathrm{w}) = 0$ determines the wetting transition temperature, so that

$$\phi_l(T_\mathrm{w}) = \frac{h_1}{g}. \tag{4.37}$$

Within the present approach, the wetting transition can be of second order if

$$\beta g > \frac{\chi(T_\mathrm{w})}{3\xi}, \tag{4.38}$$

and of first order if the inequality is reversed. The separatrix between first- and second-order wetting (i.e. the loci of tricritical wetting [315]) is given by [204]

$$\beta g = \frac{\chi(T_\mathrm{w})}{3\xi(T_\mathrm{w})}, \tag{4.39}$$

where

$$\chi(T_\mathrm{w}) = \frac{\ln(h_1/g) - \ln(1 - h_1/g)}{2h_1/g - 1}. \tag{4.40}$$

In the case of an electrolyte solution close to a charged wall the effective interface potential given by Eq. (4.32) has the generic form studied by Aukrust and Hauge [11] for a model in which both the wall-fluid and the fluid-fluid interaction potentials decay exponentially but on distinct scales. The electrostatic term $a_I(T)\exp(-2\kappa\ell)$ with

$$a_I(T) = \frac{4\pi l_B \sigma^2}{\varepsilon_l \kappa} \tag{4.41}$$

has a coefficient which is always positive; Eq. (4.32) shows that the coefficients $a_0(T)$ (Eq. (4.34)) and $b_0(T)$ (Eq. (4.35)) do not change upon adding ions. Accordingly, the wetting behaviour will depend on the competition between the Debye length $1/\kappa$ and the correlation length $\xi$ [204]:

(i) $1/\kappa < \xi$: In this case the electrostatic term decays faster than the remaining two terms in Eq. (4.32). Therefore one obtains the same wetting behaviour as for the pure solvent.

(ii) $\xi < 1/\kappa < 2\xi$: In this case the electrostatic term is the dominant subleading contribution in the expansion. Moreover, because $a_I(T) > 0$ for all temperatures, the transition can be second order if $a_0(T)$ satisfies the conditions given by Eq. (4.36).

(iii) $1/\kappa > 2\xi$: In this case, the electrostatic term is the leading contribution. As a result, if in the pure solvent the wetting transition is of second order, due to adding ions and due to a nonzero surface charge density at the wall it turns first order or the wall becomes wet at all temperatures $T > T_t$.

For the pure solvent it is possible to determine the separatrix between first- and second-order wetting in terms of the surface parameters $h_1$ and $g$ only. Accordingly, the phase diagram is of the type shown in Fig. 2(a) of Ref. [315] for $g > 0$ and of the type shown

there in Fig. 2(b) for $g = 0$. On the other hand, for electrolyte solutions this separatrix depends also on the surface charge density, the ionic strength and the competition between the Debye and the correlation lengths. As mentioned before the approach neglects the interaction between ions so that it can be used only for low ion concentrations, e.g. $I \lesssim$ 10mM, which corresponds to a Debye length $1/\kappa \gtrsim$ 3nm in water at room temperature. Thus one typically ends up with case (iii) ($1/\kappa > 2\xi$) except in close proximity to the critical point, where one can reach case (ii) ($\xi < 1/\kappa < 2\xi$) and ultimately case (i) ($1/\kappa < \xi$). Therefore, for $g > 0$ the phase diagram for $\sigma \neq 0$ is of the type shown in Fig. 2(a) of Ref. [315], as for the pure solvent case with $g > 0$, but the separatrix between first- and second-order wetting is shifted closer to the critical point upon increasing the Debye length, i.e. upon decreasing the ionic strength.

The wetting behaviour will be richer if $\xi_l \neq \xi_g$ (see the discussion below Eq. (4.32)). In this case, the possible wetting scenarios will depend on the competition between the Debye length $1/\kappa$, the correlation length $\xi_g$ of the gas, and the correlation length $\xi_l$ of the liquid. This creates additional cases compared to the ones discussed above (see (i)-(iii)). Nevertheless, in the present context, far from the critical point case (iii) is still the typical one with the distinction that here $1/(2\kappa)$ competes with the maximum of $\xi_l$ and $\xi_g$.

In the limit $\sigma \to 0$ one has $a_I(T) \to 0$ so that in this case there is no contribution to the effective interface potential due to the ions. This is due to the fact that within the present theory there are no surface fields acting on $\varrho_\pm$ if $\sigma = 0$. For considering instead the limit $I \to 0$, i.e. $\kappa \to 0$, in the expression for $a_I(T)$ one has to use the saturation value $|\sigma| = \sigma_{sat}(\kappa\ell)$ (see Ref. [204]), which implies $a_I(T) \sim \kappa^3 \to 0$ in the limit $I \to 0$ as for the pure solvent.

In order to understand the influence of the range of interactions in the solvent, systems are considered in Ref. [204] in which the solvent exhibits attractive long-ranged interaction potentials among the solvent particles as well as between the wall and the solvent particles. As before, one is interested in an analytic expression for the effective interface potential $\omega(\ell)$. Following Ref. [157] the attractive part of the pair potential between the solvent particles, as it enters the density functional, is modelled as

$$\bar{w}(r) = \frac{A_f}{(1+r^2)^3} \tag{4.42}$$

with $A_f < 0$ and the substrate potential as

$$V(z > 0) = -\sum_{i \geq 3} \frac{u_i}{z^i} \tag{4.43}$$

with $u_3 > 0$ corresponding to an asymptotically attractive interaction. The contribution $\sim u_4$ is generated, inter alia, by the discrete lattice structure of the substrate or by a thin overlayer [107] and thus it can be tuned. In Eq. (4.43) $V(z)$ describes properly both the short- and the long-ranged behaviour of the substrate potential. This can be inferred from the fact that, with $u_9 < 0$, Eq. (4.43) contains the commonly used 9-3 Lennard-Jones potential which comprises a short-ranged repulsive part together with a long-ranged attractive one. Therefore $V(z)$ diverges to $+\infty$ for $z \to 0$ and the corresponding asymptotic behaviour, in this limit, depends on the substrate properties, e.g. $V(z \to 0) \sim z^{-9}$ for a 9-3 Lennard-Jones substrate potential. Due to this divergence the solvent density $\phi(z)$ must vanish for $z \to 0$. In Ref. [204] this effect is taken into account approximately by

replacing the short-ranged part of $V(z)$ in Eq. (4.43) by a hard-wall potential positioned at $z = d_w$; the distances $z$ are still measured from $z = 0$ [108]. On the other hand, in order to account for the long-ranged attractive part of $V(z)$ (i.e. for $z \gg d_w$), only the first two terms of the sum in Eq. (4.43) are considered [204]. The functional form in Eq. (4.42) facilitates to carry out subsequent integrals analytically. These long-ranged interactions are treated as a perturbation of the grand canonical functional in Eq. (4.29):

$$\Omega[\phi(\mathbf{r}), \varrho_\pm(\mathbf{r})] = \Omega_0[\phi(\mathbf{r}), \varrho_\pm(\mathbf{r})] + \Delta\Omega[\phi(\mathbf{r})] \tag{4.44}$$

where $\Omega_0[\phi(\mathbf{r}), \varrho_\pm(\mathbf{r})]$ is given by Eq. (4.29) and

$$\Delta\Omega[\phi(\mathbf{r})] = \frac{1}{2}\int d^3r \int d^3r' \bar{w}(|\mathbf{r}-\mathbf{r}'|)\phi(\mathbf{r})\phi(\mathbf{r}) + \int d^3r \varrho_w V(\mathbf{r})\phi(\mathbf{r}). \tag{4.45}$$

The integrations run over the half space $\{\mathbf{r} = (x, y, z \geq d_w)\}$, $\bar{w}(r)$ is given by Eq. (4.42), and $V(\mathbf{r})$ is given by Eq. (4.43); $\varrho_w$ is the particle number density of the substrate. Concerning the interaction between the solvent particles, it turns out that it is most suitable captured by the quantity [107],

$$t(z) := \int_z^\infty dz' \int d^2r'_{||} \bar{w}\left(\left(r'^2_{||} + z'^2\right)^{1/2}\right). \tag{4.46}$$

For large distances and non-retarded van der Waals forces one has

$$t(z \to \infty) = -\left(\frac{t_3}{z^3} + \frac{t_4}{z^4} + \cdots\right), \tag{4.47}$$

which defines the coefficients $t_3 > 0$ and $t_4$. For the present model this implies [204]

$$t_3 = -\frac{\pi A_f}{6}, \tag{4.48}$$

$$t_4 = 0. \tag{4.49}$$

In a first-order perturbative theory approach the influence of $\Delta\Omega[\phi(\mathbf{r})]$ on the wetting behaviour of the electrolyte solution can be determined by inserting into Eq. (4.44) the solutions $\phi^{(0)}(\mathbf{r})$ and $\varrho_\pm^{(0)}(\mathbf{r})$ as obtained from $\Omega_0[\phi(\mathbf{r}), \varrho_\pm(\mathbf{r})]$. The superscript (0) denotes these solutions as the ones obtained from the unperturbed functional $\Omega_0$.

Expanding the local part of the grand canonical functional in Eq. (4.44) around the sharp-kink density profiles in Eqs. (4.30) and (4.31), for $\ell \to \infty$ one obtains the following form for the effective interface potential [204]:

$$\begin{aligned}\beta\omega(\ell \to \infty) \simeq\ & \frac{a_1(T)}{\ell^2} + \frac{b_1(T)}{\ell^3} + \cdots \\ & + a_0(T)\exp(-\ell/\xi) + b_0(T)\exp(-2\ell/\xi) \\ & + a_I(T)\exp(-2\kappa\ell),\end{aligned} \tag{4.50}$$

where ellipses stand for further subdominant terms as powers of $1/\ell$. As in the absence of long-ranged interactions, the ions enter into $\omega(\ell)$ only via the last term. The analytic expressions for the coefficients $a_1(T)$ and $b_1(T)$ are given in Ref. [204], $a_0(T)$ and $b_0(T)$ are

given by Eqs. (4.34) and (4.35), respectively, and $a_I(T)$ is given by Eq. (4.41). Corrections to the coefficients $a_0(T)$ and $b_0(T)$ due to the long-ranged interactions (Eqs. (4.42) and (4.43)) are neglected because these long-ranged interactions are treated as a small perturbation to the model with short-ranged interactions only. The sign of the coefficients $a_1(T)$, $b_1(T)$, $a_0(T)$, and $b_0(T)$ can change with $T$ while $a_I(T)$ is always positive.

In the case of a pure solvent, i.e. $a_I = 0$, the necessary conditions for the occurrence of critical wetting are (see Eq. (4.50) and Ref. [107])

$$a_1(T_{\rm w}) = 0, \quad a_1(T < T_{\rm w}) < 0, \text{ and } b_1(T_w) > 0, \tag{4.51}$$

i.e. $T^{(a_1)} = T_w$ with $T^{(a_1)}$ being defined by $a_1(T^{(a_1)}) := 0$, and, as before, one obtains conditions for the parameters of the pair potentials [204].

Although necessary, these conditions are not sufficient for critical wetting to occur. Large negative values of the coefficient $a_0(T)$ of the exponentially decaying contribution can still lead to a first-order wetting transition even if $b_1(T^{(a_1)}) > 0$. Within the present model one has $a_0(T) > 0$ for $h_1/g > \phi_l(T)$ (see Eq. (4.34)). If $b_1(T^{(a_1)}) < 0$ the wetting transition is always first order. However, in the case of a first-order wetting transition all details of $\omega(l)$, and not only its leading contributions, matter for a reliable description of the character of the transition and for determining the corresponding wetting transition temperature. Hence, an asymptotic expansion of $\omega(\ell)$ as in Eq. (4.50) is not conclusive in the case of first-order wetting.

For wetting of a wall by a one-component fluid with short- and long-ranged interactions and based on a Cahn type theory, in Refs. [206, 207] a wetting scenario has been predicted which involves a succession of two interfacial phase transitions upon increasing $T$. The first of these two transitions is a discontinuous jump between two finite values $\ell_1$ and $\ell_2 > \ell_1$ of the film thickness $\ell$ at two-phase coexistence and is referred to as a "thin-thick transition". The second one is the standard second-order wetting transition at $T = T_w$; in Refs. [206, 207] the possibility of a thin-thick transition preceding a first-order wetting transition has not been discussed. This wetting scenario can be explained in terms of the competition between the short- and long-ranged interactions. Such a thin-thick transition precedes the critical wetting transition only if the short-ranged interactions would give rise to a first-order wetting transition in the case that the long-ranged interactions were negligible. Because the present theory involves both short- and long-ranged interactions, the occurrence of this wetting scenario can be checked for the pure solvent case. In this case, the separatrix between first- and second-order wetting is given by Eq. (4.39) for the model with short-ranged interactions only (e.g. for $g = 1$ the transition will be first order in the pure solvent case without long-ranged interaction if $h_1 > 0.49$). By choosing a proper set of parameters one is able to observe the occurrence of this two-stage transition for the pure solvent for $\pi^2 A_f \lesssim 0.55 \times 10^{-19}$ J, $\phi_l(T_w) = u_3\varrho_w/t_3 = 0.7$, $u_4 = 2.3 \times t_3$, $g = 1$, and $h_1 = 0.76$, such that the condition for second-order wetting is satisfied [204].

This thin-thick transition has also been observed for wetting of a wall by a one-component fluid in models with short-ranged interactions only [205, 247, 356] and with long-ranged interactions only [106]. Furthermore it has been observed experimentally for wetting of hexane on water [412]. In Ref. [356] this thin-thick transition has been observed for a generalisation of the Sullivan model [423], in which in addition to the exponentially decaying wall-fluid potential a square-well attraction has been included. A thin-thick transition was also analyzed in Ref. [205] for a Landau theory of wetting which includes an extra surface term $h_3\,(\phi(0))^3$ linked to the substrate potential (see Ref. [315] and

Eq. (4.29)). In Ref. [247] it has been shown that the behaviour of the model in Ref. [356] can be mapped onto that used in Ref. [205]. With that it turns out that the thin-thick transition predicted in Refs. [356] and [205] involves short-ranged forces only and is due to the competition between two opposing (effective) surface fields at the same surface, one favouring wetting and the other favouring drying. Such a competition between surface fields is not considered in Ref. [204]. Therefore a thin-thick transition does not occur in the pure solvent case with short-ranged interactions only.

The influence of ions and of surface charges on the wetting behaviour of electrolytes with solvents governed by short- and long-ranged forces differs qualitatively from the one discussed above, because in this case the leading contributions to $\omega(\ell \to \infty)$ decay algebraically as function of the film thickness $\ell$. Accordingly, the contribution due to the ions and the charged wall can enter at most as the leading non-algebraic term in the expansion for $\ell \to \infty$; this is the case if the Debye length $1/\kappa$ is larger than (twice) the bulk correlation length $\xi$ [204].

One can choose parameter sets $(h_1, g, u_4, T^{(a_1)})$ such that the pure solvent with short- and long-ranged interactions near a charge neutral wall (i.e. for $a_I(T) = 0$) exhibits a second-order wetting transition at $T_w(I = 0, \sigma = 0)$ *without* being preceded by a thin-thick transition (i.e. different from the above scenario) [204]. For fixed ionic strength $I \neq 0$ and upon increasing the surface charge density $\sigma$, due to $a_I(T) \sim \sigma^2/\sqrt{I}$ (Eq. (4.41)) $\omega(\ell)$ rises at finite film thickness $\ell$ to the effect that the wetting transition temperature $T_w(I, \sigma)$ decreases for increasing surface charge density $\sigma$ [203] (see Fig. 4.15). Moreover, for fixed surface charge density $\sigma$ the wetting transition temperature $T_w(I, \sigma)$ decreases upon decreasing the ionic strength $I$ (i.e. increasing the amplitude $\sigma^2/\sqrt{I}$ and the Debye length $1/\kappa \sim 1/\sqrt{I}$) [203] (see Fig. 4.15). In addition, the positive and monotonically decreasing (as a function of increasing $\ell$) contribution $a_I(T)\exp(-2\kappa\ell)$ to $\omega(\ell)$ does lead to a thin-thick transition preceding the critical wetting transition which is absent without ions. Figure 4.19 shows the curves for $\omega(\ell)$ corresponding to the temperatures $T_1 = 0.918 \times T_c$, $T_2 = 0.919 \times T_c$, $T_3 = 0.92 \times T_c$, $T_4 = 0.932 \times T_c$, and $T_w = 0.944 \times T_c$ with $T_1 < T_2 \lesssim T_{t-t,w} < T_3 < T_4 < T_w$, i.e. the *t*hin-*t*hick transition occurs in between the temperatures $T_2$ and $T_3$, whereas the critical wetting transition takes place at the wetting temperature $T_w$.

However, in the case that the pure solvent exhibits a second-order wetting transition, which is preceded by a thin-thick wetting transition, the effect of the term due to the ions and to the surface charge density ($a_I(T) \neq 0$), in the case $1/\kappa > 2\xi$, is to decrease the thin-thick wetting transition temperature $T_{t-t,w}$ and to increase the value of the jump in film thickness [204].

The case of $a_I(T) \neq 0$ for a system in which a pure solvent with short- and long-ranged interactions near a charge neutral wall exhibits a first-order wetting transition is not discussed here, because within the present approach only the leading contributions of the effective interface potential for $\ell \to \infty$ are analytically accessible (see Eq. (4.50)) and reliable knowledge of the behaviour of $\omega(\ell)$ for small $\ell$, which is particularly important for first-order wetting transitions, is lacking. Therefore, in order to be able to analyse the effect of the ions and of the surface charge density on solvents which without ions exhibit first-order wetting transitions, more details of the effective interface potential are needed.

The thin-thick wetting transition at two-phase coexistence, which precedes a standard second-order wetting scenario, has been discussed in the context of wetting in electrolytes in Ref. [101] for a model of an ionic solution close to a charged wall in which the solvent-

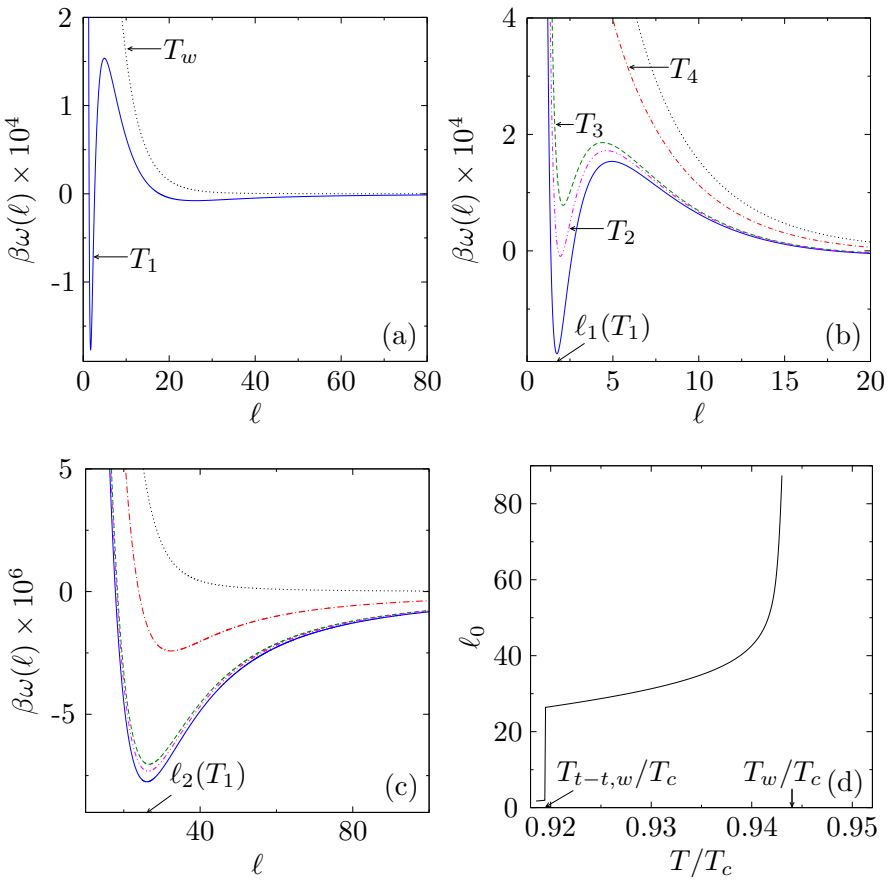


Figure 4.19: Effective interface potential $\omega(\ell)$ for systems governed by short- and long-ranged interactions as function of the thickness $\ell$ of the liquid film at gas-liquid coexistence in the presence of ions for the case that the pure, i.e. salt-free, solvent exhibits a critical wetting transition (without being preceded by a thin-thick transition). The parameters used are $A_f/k_B = -1013\text{K}$, $u_3 = 0.7 \times t_3$ (i.e. $\phi_l(T^{(a_1)} = T_w) = 0.7$), $u_4 = 2.28 \times t_3$, $g = 1$, $h_1 = 0.76 \times g$, $I = 1mM$, and $\sigma = 0.1\mu\text{C/cm}^2$ (see main text). The effective interface potential $\omega(\ell)$ has two local minima (at $\ell_1(T)$ (see (a) and (b)) and $\ell_2(T)$ (see (c)) with $\ell_1 < \ell_2 < \infty$), one of the two being the global one at a given temperature (see (a)). They have the same depth at $T = T_{t-t,w} \approx 0.919 \times T_c$ (not apparently visible). For $T > T_{t-t,w}$ the film thickness $\ell_2(T)$ is the global minimum and diverges continuously $1/(T_w - T)$ as $T \to T_w \approx 0.944 \times T_c$ (see (c)). The global minimum $l_0(T)$ as a function of temperature is plotted in (d). At $T_{t-t,w}$ the film thickness exhibits a finite jump and subsequently diverges smoothly for $T \nearrow T_w$. Accordingly, the system undergoes a thin-thick wetting transition at $T_{t-t,w}$, followed by a continuous one at $T_w$. Five different temperatures, $T_1 \approx 0.918 \times T_c$, $T_2 \approx 0.919 \times T_c$, $T_3 \approx 0.92 \times T_c$, $T_4 = 0.932 \times T_c$ and $T_w$ are displayed in (a), (b), and (c) (using a common color code) with $T_1 < T_2 \lesssim T_{t-t,w} < T_3 < T_4 < T_w$. (Note the different scales of the axes.) The film thickness $\ell$ is measured in units of $a$ such that $a^3$ is the volume of a solvent particle. Densities are measured in units of $a^3$. (See Ref. [204])

solvent and solvent-wall interactions are short-ranged only and the contribution of the ions to the effective interface potential is calculated by solving the full Poisson-Boltzmann

equation instead of the linearised one as in Ref. [204]. The thin-thick transition in Ref. [101] occurs in a restricted region of the parameter space, provided that the transition in the pure solvent is first order and that $1/\kappa < 2\xi$, i.e. for large ionic strength.

In contrast, in Ref. [204], the *combined* presence of short- *and* long-ranged interactions is taken into account. As discussed above for the case of a pure solvent with short- *and* long-ranged interactions, a thin-thick transition will precede a long-ranged critical wetting transition only if the short-ranged interactions alone would give rise to a first-order wetting transition in the case that the long-ranged interactions were negligible [206, 207]. This is precisely the case encountered in the context of the electrolyte solution when solvent-solvent and solvent-wall long-ranged interactions are taken into account: In the absence of these long-ranged interactions the transition is first-order if $1/\kappa > 2\xi$, such that $\ell$ jumps from $\ell_1$ to $\ell_2 = \infty$ (see Fig. 4.19). Once the long-ranged interactions are taken into account they block the jump of $\ell$ to $\ell_2 = \infty$ and limit this jump to one with a finite value $\ell_2 < \infty$. Once $\ell$ has reached the value $\ell_2$ a further increase in temperature leads to the unfolding of the standard wetting scenario under the aegis of long-ranged interactions at $T_w > T_{t-t,w}$. Therefore, the thin-thick wetting transition is the remnant of the first-order wetting transition that would occur in the electrolyte solution if the long-ranged solvent-solvent and solvent-wall interactions were negligible [204].

The situation can be summarised as follows:

(i) If in the pure solvent short-ranged interactions favour first-order wetting but additional long-ranged interactions produce second-order wetting, one finds a thin-thick transition followed by the continuous wetting transition [204, 206, 207].

(ii) A thin-thick transition can be observed in the pure solvent even if there are only short-ranged [205, 247, 356] or only long-ranged [106] interactions.

(iii) A solvent with short- *and* long-ranged interactions which exhibits a second-order wetting transition without being preceded by a thin-thick transition is considered in Ref. [204]. Adding ions renders such a short-ranged contribution to the effective interface potential that the resulting effective short-ranged interactions favour first-order wetting. This leads to a thin-thick transition preceding the continuous long-range type wetting transition. This mechanism is analogous to the one in (i).

(iv) If the solvent with short- and long-ranged interactions undergoes a continuous wetting transition, which *is* preceded by a thin-thick transition, adding ions decreases the transition temperature of the latter and increases the jump in film thickness.

(v) If the pure solvent is governed by short-ranged interactions only and exhibits a first-order wetting transition, adding ions can lead to a continuous wetting transition preceded by a thin-thick transition, provided that $1/\kappa < 2\xi$.

(vi) If the solvent is governed by short-ranged interactions only, adding ions renders a first-order wetting transition for $1/\kappa > 2\xi$. Adding further long-ranged interactions, which favour continuous wetting, renders a second-order wetting transition of the long-range type, preceded by a thin-thick transition.

The analysis in Ref. [204], which is valid in the case of low ion density $I$, shows that in the case of short-ranged solvent-solvent and solvent-wall interactions wetting transitions in the

presence of electrostatic interactions are typically first order [100, 101, 203, 204, 329, 330]. This result can be explained in terms of the competition between the two characteristic length scales in the ionic complex fluid, i.e. the bulk correlation length $\xi$ in the wetting liquid phase and the Debye length $1/\kappa$. If $1/\kappa > 2\xi$, which is typically the case for dilute electrolyte solutions away from (bulk) critical points, a wetting transition at two-phase coexistence will be always first order irrespective of its order in the pure, i.e. salt-free, solvent. It is the merit of the analysis of the effective interface potential to provide a transparent rationale for the pre-eminence of first-order wetting in electrolyte solutions in terms of competing length scales [204]. Moreover, if in those systems in addition long-ranged solvent-solvent and solvent-wall interactions, which favour a critical wetting transition, are present, the analysis reveals the possibility of a wetting scenario which actually corresponds to a sequence of two wetting transitions: first an electrostatically induced (i.e. $1/\kappa > 2\xi$) discontinuous jump between two finite wetting film thicknesses which upon raising the temperature is followed by a continuous divergence of the wetting film thickness $\ell$ (see Fig. 4.19).

## 4.3 Critical adsorption in electrolyte solutions

According to the fluctuation-dissipation theorem the linear density response of a fluid to a weak external field is determined by the two-point correlation functions of the unperturbed system [176]. Therefore, the number density profiles far from a wall exhibit asymptotically the same type of decay towards their bulk values, i.e. either monotonically or damped oscillatorily, with the same decay length and periodicity as the two-point bulk correlation functions $G_{ij}(r)$. (Note that this correspondence does no longer hold in the presence of algebraically decaying interaction potentials [108], which are not considerd here.) However, from this argument one cannot draw reliable conclusions concerning their structure close to the wall. Therefore in this latter range the structure is determined numerically in Ref. [43] (see Sec. 2.1) for particular sets of parameters. Moreover, close to the wall packing effects due to the finite size of the fluid particles lead to layering which extends a few particle diameters into the system. However, this kind of structure is not captured by the square-gradient model in Eq. (2.1).

The solid lines in Fig. 4.20 correspond to the composition $\phi(z)$ [(a)], the electrostatic potential $\widetilde{\psi}(z) = \psi(z)k_BT/e$ with $\varepsilon(\phi)\psi'(z) = -4\pi\ell_B D(z)$ and $\psi(z \to \infty) \to 0$ [(b)], the cation number density $\varrho_+(z)$ [(c)] and the anion number density $\varrho_-(z)$ [(d)] in a semi-infinite dilute electrolyte solution bounded by a wall positioned at $z = 0$ with surface charge density $\sigma$ and surface field strength $h$, as obtained from numerically minimising the density functional. The solvent permittivity is chosen to resemble that of a mixture of 3-methylpyridine (component $A$, $\varepsilon_A = 10$) and water (component $B$, $\varepsilon_B = 80$). The composition profiles $\phi(z)$ in Fig. 4.20(a) turn out to be monotonic for weak ($h = \pm 0.01$) as well as for strong surface fields ($h = \pm 1$). Due to the negative surface charge density $\sigma$, the monotonic electrostatic potential profile $\psi(z)$ in Fig. 4.20(b) is negative with surface potentials $\widetilde{\psi}(0)$ of some tens of mV, which is a common order of magnitude [90]. Within the range $0 \le z \le 2$ close to the wall the electrostatic potential $\psi$ becomes less negative upon changing the surface field strength from $h = 1$ to $h = -1$ due to the increase of the permittivity as a result of the increase of the volume fraction $1 - \phi$ of component $B$ close to the wall. Similarly, due to the negative surface charge, close to the wall the number

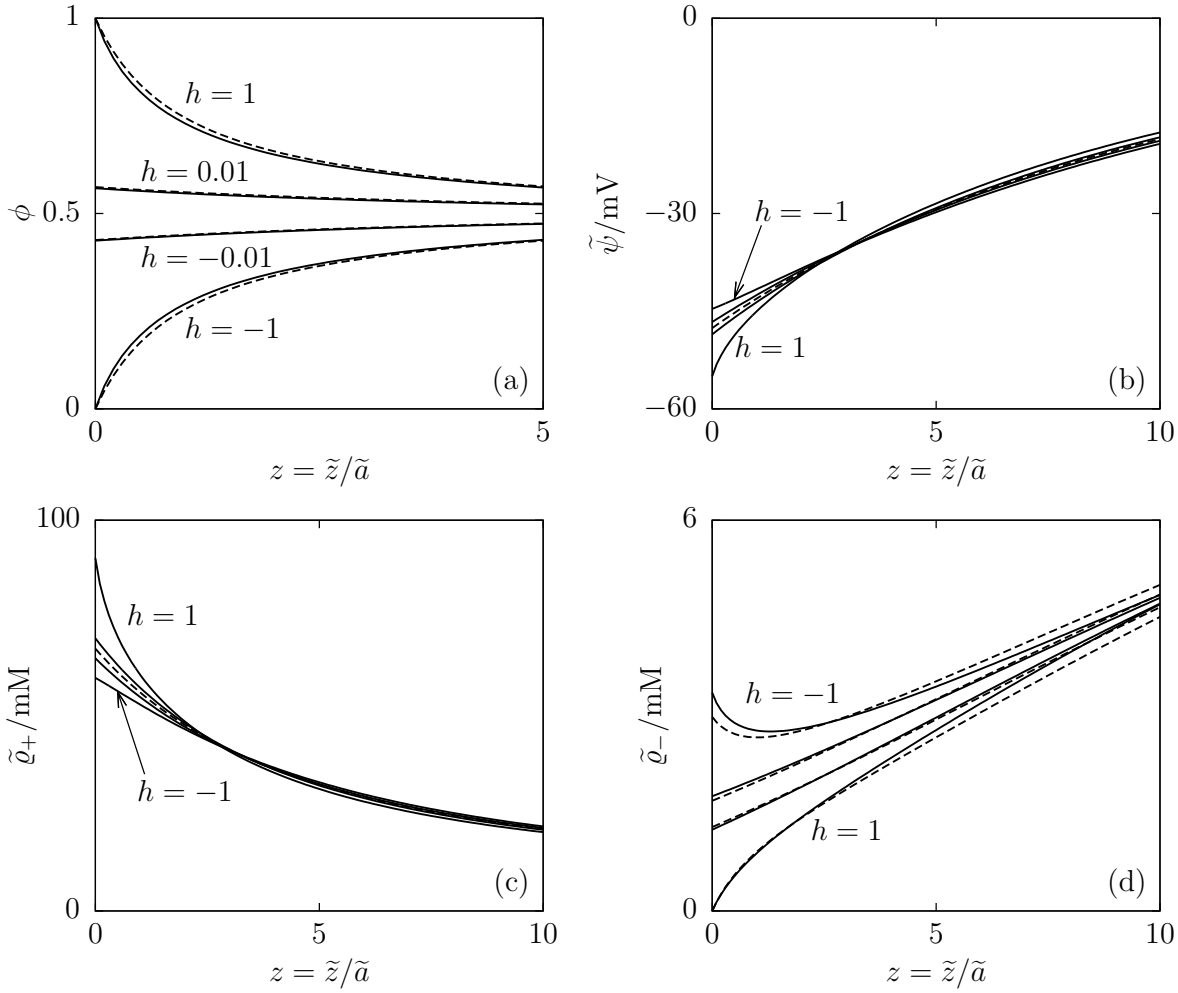


Figure 4.20: Profiles of the volume fraction $\phi$ of solvent component $A$ [(a)], the electrostatic potential $\widetilde{\psi}$ (with $\widetilde{\psi}(z \to \infty) \to 0$) [(b)], the cation number density $\widetilde{\varrho}_+$ [(c)], and the anion number density $\widetilde{\varrho}_-$ [(d)] in a semi-infinite system bounded by a wall at $z = \widetilde{z}/\widetilde{a} = 0$ with surface charge density $\widetilde{\sigma} = -1\,\mu\mathrm{C/cm^2}$ and surface field strength $h$. These results correspond to Gibbs free energies of transfer $f_+ = 0, f_- = 20$, the bulk volume fraction $\phi_b = 0.5$ of solvent component $A$, and the bulk ionic strength $\widetilde{I} = \widetilde{\varrho}_{\pm b} = 10\,\mathrm{mM}$. The Flory-Huggins parameter $\chi(T)$ is chosen to correspond to that temperature, for which the bulk correlation length $\xi$ is half of the Debye length $1/\kappa$, which is taken to be temperature independent (see Fig. 3.3). For the specified surface fields $h$ the solid lines are the numeric solutions obtained from the density functional model within LDA (see Sec. 2.1). For reasons of clarity in (b) and (c) the full lines for $h = \pm 0.01$ are not designated; they can be nonetheless identified in an obvious way. The dashed lines correspond to the approximate profiles $\overline{\phi}(z)$, $\overline{\psi}(z)$, and $\overline{\varrho}_\pm(z)$ introduced in Eqs. (4.52), (4.53), and (4.54), respectively. Note that $\overline{\psi}(z)$ and, due to the choice $f_+ = 0$, $\overline{\varrho}_+(z)$ are independent of the magnitude $|h|$; therefore both in (b) and (c) there is only one dashed line. For $z > 2$ the approximate profiles differ only slightly from the ones obtained by a full numerical minimisation. Density oscillations close to the wall, which are expected in actual fluids, do not occur, because packing effects are not captured by the present square-gradient approach. (See Ref. [43])

density $\varrho_+$ of the cations in Fig. 4.20(c) is larger and the number density $\varrho_-$ of the anions in Fig. 4.20(d) is smaller than in the bulk. Upon changing the surface field strength from $h = 1$ to $h = -1$, close to the wall the number density $\varrho_+$ of the cations decreases and that of the anions, $\varrho_-$, increases. This feature follows partly from the variation of the electrostatic potential $\psi$. In addition, for the current choice of parameters the anions dissolve better in component $B$ than in component $A$ of the solvent ($f_- > 0$), such that the component $B$ enriched near the surface (see Fig. 4.20(a)) mediates a certain preference of the anions for the wall.

The dashed lines in Fig. 4.20(a) correspond to the approximate profile [43]

$$\overline{\phi}(z) = \phi_b + \frac{C_{GL}}{\sinh((z+z_0)/\xi)}, \quad C_{GL} := \mathrm{sign}(h)\sqrt{\frac{\chi}{8\xi^2}} \tag{4.52}$$

with the extrapolation length $z_0$. Here and in the following $\xi \equiv \xi^{(\mathrm{OZ})}$ (see Eq. (3.8) is called the bulk correlation length [43]. Close to the critical point $1/\xi$ corresponds to the asymptotic decay rate $k_1''$ of the solvent structure factor $G_{\phi\phi}(r \to \infty) \sim \exp(-r/\xi)/r$ [43] (see Sec. 3.1). The profile $\overline{\phi}(z)$ is the analytic solution of the semi-infinite Ginzburg-Landau equation [276] obtained from minimising $\Omega[\phi, \varrho_\pm]$ after expanding up to fourth order in $\phi - \phi_b$ and neglecting the ion-solvent coupling, i.e. assuming $f_\pm = 0$, which implies $V_\pm(\phi) = 0$. Within Ginzburg-Landau theory the extrapolation length $z_0$ is fixed by the boundary condition on $\overline{\phi}'(0)$ set by the surface field strength $h$ (see Ref. [43]).

The dashed line in Fig. 4.20(b) is the approximate electrostatic potential [43]

$$\overline{\psi}(z) = 4\,\mathrm{artanh}(C_{PB}\exp(-\kappa z)), \quad C_{PB} := \tanh\Big(\frac{1}{2}\,\mathrm{arsinh}\Big(\frac{2\pi\ell_B\sigma}{\varepsilon(\phi_b)\kappa}\Big)\Big), \tag{4.53}$$

which is the analytic solution of the semi-infinite Poisson-Boltzmann equation [162] for a uniform permittivity $\varepsilon(\phi_b)$ and for neglecting the ion-solvent coupling (i.e. for $f_\pm = 0$).

Finally, the dashed lines in Figs. 4.20(c) and (d) are the approximate number density profiles of the $\pm$-ions [43]

$$\overline{\varrho}_\pm(z) = I_b \exp(-(\pm\overline{\psi}(z) + V_\pm(\overline{\phi}(z))) + V_\pm(\phi_b)), \tag{4.54}$$

which correspond to the Boltzmann distributions of non-interacting particles in the external fields due to the approximate electrostatic potential $\overline{\psi}(z)$ and the approximate composition $\overline{\phi}(z)$; $I_b = \varrho_\pm(z \to \infty)$. Whereas the composition profile $\overline{\phi}(z)$ (Eq. (4.52)) and the electrostatic potential profile $\overline{\psi}(z)$ (Eq. (4.53)) are independent of the ion-solvent coupling $V_\pm$, the ion number density profiles $\overline{\varrho}_\pm(z)$ (Eq. (4.54)) are not.

At distances from the wall of more than a few particle diameter ($z > 2$) the approximate profiles $\overline{\phi}(z)$, $\overline{\psi}(z)$ and $\overline{\varrho}_\pm(z)$ differ only slightly from the ones obtained by the full numerical minimisation of Eq. (2.1). Closer to the wall the deviations between the numerical and the approximate profiles are more pronounced, but in this spatial range the present local model is not conclusive because it neglects the surface layering of actual fluids. A similar situation occurs within BCA [29] (see Fig. 3(a) therein) shown in Fig. 4.21. There, at distances $\widetilde{z} < 2$Å, the solvent composition profile $\phi(\widetilde{z})$ for strong ion-solvent coupling ($f_+ = 30, f_- = 0$, solid line) differs strongly from that in the absence of ion-solvent coupling ($f_+ = f_- = 0$, dashed line). At large distances the deviations are small. A closer comparison between Fig. 4.21 and Fig. 4.20(a) would require the knowledge of the particle size, which is however not specified in Ref. [29]. A description of the

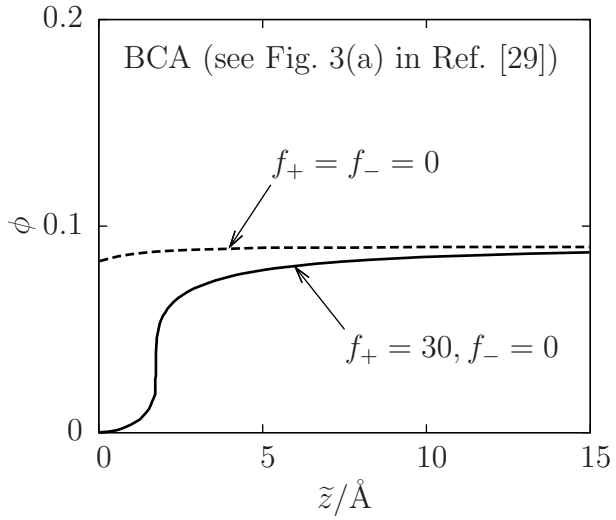


Figure 4.21: Composition profiles $\phi(\widetilde{z})$ within BCA for strong ion-solvent coupling ($f_+ = 30, f_- = 0$, solid line) and in the absence of ion-solvent coupling ($f_+ = f_- = 0$, dashed line) taken from Fig. 3(a) in Ref. [29]. Here a solvent with $\varepsilon_A = 80$ and $\varepsilon_B = 20$ at bulk composition $\phi_b = 0.09$ is considered. The bulk ionic strength is $\widetilde{I} = 0.1\,\mathrm{mM}$ and the surface charge density is $\widetilde{\sigma} = -16\,\mu\mathrm{C/cm^2}$. At distances $\widetilde{z} < 2\,\text{Å}$ from the wall the two curves differ strongly from each other, whereas the differences are small at large distances. (See Ref. [43])

presently considered semi-infinite planar system within RPA has been given in Ref. [80]. There the ion-solvent coupling has been treated perturbatively, but the full, numerically determined profiles $\phi(z)$, $\psi(z)$, and $\varrho_\pm(z)$ within RPA have not been discussed. However, by comparing these profiles, as obtained within RPA, with those obtained within BCA or LDA one could assess the influence of non-locality on the interfacial structure in the complex fluids studied here.

The approximate ion density profiles in Eq. (4.54) have been used in a grazing-incidence X-ray fluorescence (GIXF) study of KCl in a mixture of water and 2,6-dimethylpyridine at critical composition far away from the critical point inside the one-phase region of the phase diagram [478]. Whereas the experimental results and the theoretically predicted ion density profiles in Eq. (4.54) exhibit quantitative differences, the causes of which are probably due to the fact that the theoretical model is not reproducing the phase diagram quantitatively, there is good qualitative agreement of the interfacial structure of the ionic complex fluid.

In Ref. [43] critical adsorption at a wall with a strong surface field $h$ and with surface charge density $\sigma$ is investigated. The case is considered that in the bulk the binary liquid mixture is at the critical bulk composition $\phi_b = \phi_c$ in the presence of salt with bulk ionic strength $\varrho_{\pm b} \equiv I = I_c$. A surface field $h > 0$ ($h < 0$) favours the adsorption of $A$ ($B$) particles and leads to a local segregation. In order to obtain an analytical expression for the excess adsorption $\Gamma(\xi)$, which captures the full mean-field behaviour to leading order close to the critical point ($\xi \to \infty$), the density functional Eq. (2.1) is expanded in two steps in order to derive a Ginzburg-Landau-type description. In the first step the density functional $\Omega[\phi, \varrho_\pm]$ is expanded up to second order in the deviations $\Delta\varrho_\pm(z) := \varrho_\pm(z) - I$ of the ion densities from their bulk equilibrium values $I = I_c$. This leads to a

density functional $\Omega_1[\phi, \Delta\varrho_\pm]$. Minimising $\Omega_1[\phi, \Delta\varrho_\pm]$ with respect to $\Delta\varrho_\pm$ renders Euler-Lagrange equations linear in $\Delta\varrho_\pm(z)$, the solutions of which are functionals $\Delta\varrho_\pm^*(z, [\phi])$ of the (up to here unknown) solvent composition profile $\phi$. Inserting the solutions $\Delta\varrho_\pm^*(z, [\phi])$ into the density functional $\Omega_1[\phi, \Delta\varrho_\pm]$ and, as the second step, expanding $\Omega_1[\phi, \Delta\varrho_\pm^*[\phi]]$ up to fourth order in the order parameter deviations $\varphi(z) := \phi(z) - \phi_c$ leads to the Ginzburg-Landau-type functional (compare Eq. (4.105)) [43]

$$\frac{\mathcal{H}[\varphi]}{A} = \int_0^\infty \mathrm{d}z \left( a\big(\varphi(z)\big)^2 + b\big(\varphi(z)\big)^4 + c\big(\varphi'(z)\big)^2 + U(z)\varphi(z) \right) - h\varphi(0) + \mathcal{O}((\Delta\gamma)^2), \tag{4.55}$$

where the effective "external" field

$$U(z) = -\frac{\kappa\sigma\Delta\gamma}{2}\exp(-\kappa z) - \frac{2\pi\ell_B\sigma^2\varepsilon'(\phi_c)}{(\varepsilon(\phi_c))^2}\exp(-2\kappa z) \tag{4.56}$$

describes the influence of surface charges $\sigma$ on the order parameter $\varphi$. The first term on the right-hand side of Eq. (4.56) is due to the ion solubility whereas the second term is due to the dielectric properties of the solvent. Solving perturbatively to first order in $U$ the Euler-Lagrange equation, obtained from $\mathcal{H}/A$ in Eq. (4.55), leads to the equilibrium order parameter profile $\varphi_{\mathrm{eq}}(z; \xi)$.

At the critical point ($\xi = \infty$) and far away from the substrate the equilibrium order parameter profile $\varphi_{\mathrm{eq}}(z; \xi = \infty)$ decays as [43]

$$\varphi_{\mathrm{eq}}(z \to \infty; \xi = \infty) = \frac{\mathrm{sign}(h)}{2z} + \Big( -\frac{\mathrm{sign}(h)}{2} + \frac{9\sigma\Delta\gamma}{10\kappa^3} + \frac{9\pi\ell_B\sigma^2\varepsilon'(\phi_c)}{40\kappa^4(\varepsilon(\phi_c))^2} \Big)\frac{1}{z^2} + \mathcal{O}(z^{-3}). \tag{4.57}$$

The leading contribution $\mathrm{sign}(h)\dfrac{\sqrt{c/b}}{z}$ can be written in the scaling form $\mathrm{sign}(h) m_0 c_+ (z/\xi_0^+)^{-\beta/\nu}$ with the universal amplitude $c_+ = \sqrt{2}$ [141], where the critical exponents take their mean-field values $\beta = \nu = \frac{1}{2}$ [349]. Accordingly, the leading term in Eq. (4.57) is not affected by the surface charge, the presence of ions or the dielectric properties of the solvent. However, these materials properties do modify the amplitude of the subleading contribution ($\sim 1/z^2$).

Close to the critical point ($\xi \to \infty$) the excess adsorption $\Gamma(\xi) = \int_0^\infty \mathrm{d}z\, \varphi_{\mathrm{eq}}(z; \xi)$ with the perturbatively obtained profile $\varphi_{\mathrm{eq}}(z; \xi)$ (see above) is given by [43]

$$\Gamma(\xi) = \Gamma_0(\xi) + \Gamma_1(\xi) + \mathcal{O}(1/\xi) \tag{4.58}$$

with

$$\Gamma_0(\xi) := \frac{\mathrm{sign}(h)}{2}\ln(2\xi) \tag{4.59}$$

and

$$\Gamma_1(\xi) := \frac{3\sigma\Delta\gamma}{8\kappa^2} + \frac{3\pi\ell_B\sigma^2\varepsilon'(\phi_c)}{16\kappa^3(\varepsilon(\phi_c))^2}. \tag{4.60}$$

The leading contribution $\mathrm{sign}(h)\sqrt{\dfrac{c}{b}}\ln(\xi)$ can be written in the scaling form $\simeq \mathrm{sign}(h) m_0 \xi_0^+ g_+(-\ln(|t|))$ with the universal amplitude $g_+ = \sqrt{2}\nu = 1/\sqrt{2}$ within mean-field theory [141]. $\Gamma_0(\xi)$ diverges for $\xi \to \infty$ whereas $\Gamma_1(\xi)$ remains finite and thus repre-

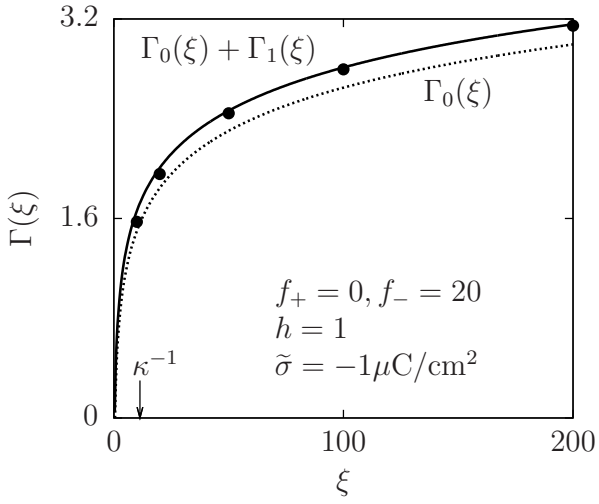


Figure 4.22: Comparison of the numerically calculated excess adsorption $\Gamma(\xi)$ obtained within the full model (•) (see Sec. 2.1) with the predictions of Eq. (4.58) for the parameters used in Fig. 4.20 with $h = 1$. The Debye length $\kappa^{-1}$ (marked by an arrow) corresponds to a bulk ionic strength $\widetilde{I} = 10\,\mathrm{mM}$. The term $\Gamma_0(\xi)$ (dotted line, see Eq. (4.59)), which contains the leading contribution to the excess adsorption and which corresponds to a vanishing surface charge density ($\sigma = 0$), exhibits visible deviations from the numerical results (•); nonetheless $\Gamma_1(\xi)/\Gamma_0(\xi) \to 0$ for $\xi \to \infty$. Taking into account in addition the term $\Gamma_1(\xi)$ (see Eq. (4.60)), which exhibits a dependence on the surface charge $\sigma$, quantitative agreement is found between $\Gamma_0(\xi) + \Gamma_1(\xi)$ (solid line) and the numerical results (•) in the limit $\xi \to \infty$. This finding also implies that those terms which have been left out upon deriving Eq. (4.55) do not contribute detectably. (See Ref. [43])

sents the first subdominant correction. Figure 4.22 compares the predictions of Eq. (4.58) with the results obtained by numerically calculating the excess adsorption within the *full* model (•) for the parameters used in Fig. 4.20 with $h = 1$, in particular for large $\xi$. Whereas the leading contribution $\Gamma_0(\xi)$ in Eq. (4.59) itself (dotted line) deviates visibly from the full numerical results (•), there is quantitative agreement between the latter and $\Gamma_0(\xi) + \Gamma_1(\xi)$ (solid line) in the limit $\xi \to \infty$. Since $\Gamma_0(\xi)$ corresponds to a vanishing surface charge ($\sigma = 0$), the difference between the dotted and the full line in Fig. 4.22 demonstrates the influence of electrostatic interactions on the excess adsorption. The quantitative agreement of $\Gamma_0(\xi) + \Gamma_1(\xi)$ (solid line) with the numerical results (•) indicates that the terms neglected upon deriving Eq. (4.55) do not contribute detectably to the leading and the first subleading behaviour of $\Gamma(\xi \to \infty)$. Moreover, for the given choice of parameters the magnitude of the correction $|\mathcal{O}(1/\xi)|$ in Eq. (4.58) turns out to be smaller than $|\Gamma_1(\xi)|$, which in turn vanishes relative to $\Gamma(\xi \to \infty)$.

Critical adsorption occurs upon approaching the critical point ($\xi \to \infty$), where the excess adsorption diverges as $\Gamma \sim \ln \xi$, which is in agreement with the expected universal scaling behaviour $\Gamma \sim \xi^{1-\beta/\nu}$ [107, 141] for the classical exponents $\beta = \nu = 1/2$ corresponding to the present mean-field theory. It is apparent from Eq. (4.58) that the leading contribution $\Gamma_0$ is not altered by the surface charge, the presence of ions or the dielectric properties of the solvent. However, these non-universal properties do influence the subleading contribution $\Gamma_1$.

The adsorption of critical water+2,6-dimethylpyridine mixtures with KBr of various

ionic strengths $I$ has been investigated by means of surface plasmon resonance [317]. For the case of a hydrophobic wall the excess adsorption turned out to be practically independent of the ionic strength. This is in agreement with Eq. (4.58) because a hydrophobic wall is only weakly charged [384] such that the second and third terms on the right-hand side of Eq. (4.58) are negligibly small.

For the case of a hydrophilic, negatively charged ($\sigma < 0$) wall a decrease of the adsorption of water has been measured upon adding salt [317]. Hydrophilic walls can be expected to be strongly charged [26] such that $\sigma = \mathrm{sign}(\sigma)\sigma_{\mathrm{sat}}$ with the saturation surface charge density $\sigma_{\mathrm{sat}} = \kappa\varepsilon(\phi_c)/(\pi\ell_B)$ [54]. In this case from Eq. (4.58) one obtains [43]

$$\frac{\partial\Gamma}{\partial I} = -\frac{3}{4\kappa^3}\Big(2\,\mathrm{sign}(\sigma)\Delta\gamma + \frac{\varepsilon'(\phi_c)}{\varepsilon(\phi_c)}\Big). \tag{4.61}$$

Equation (4.61) assumes only a weak dependence of $\phi_c$ (and thus of $\Delta\gamma$ and of $\varepsilon(\phi_c)$) on the ionic strength $I$ so that the derivative $\dfrac{\mathrm{d}\phi_c}{\mathrm{d}I}$ does not appear (see Fig. 2.3(a)).

If 2,6-dimethylpyridine is denoted as the $A$ component and water as the $B$ component of the binary liquid mixture (i.e. $\Gamma$ measures the excess of 2,6-dimethylpyridine), at the lower critical demixing point an experimental value of $\varepsilon'/\varepsilon \approx -1.2$ is found [222, 270]. For this mixture the solubility contrasts for KBr are $f_+ \approx 2.5$ and $f_- \approx 8.4$ [208] which leads to $f_+ - f_- \approx -5.9$ and $\Delta\gamma \approx -0.30$. Within LDA Eq. (2.3), from these numbers one finds $\partial\Gamma/\partial I > 0$ (i.e. decreasing water adsorption upon adding salt), and the second (dielectric) contribution on the right-hand side of Eq. (4.61) dominates. In contrast, within BCA one has $\partial\Gamma^{(\mathrm{BCA})}/\partial I < 0$ (i.e. increasing water adsorption upon adding salt), because $\Delta\gamma \approx f_+ - f_-$ leads to a dominance of the first (ion solubility) contribution on the right-hand side of Eq. (4.61). Hence the overestimation of the ion-solvent coupling within BCA leads to a sign of $\partial\Gamma^{(\mathrm{BCA})}/\partial I$ which is not compatible with the aforementioned experimental findings in Ref. [317], whereas the sign of $\partial\Gamma/\partial I$ within the present LDA is in agreement with these findings [43]. Since the dielectric properties are experimentally accessible one could use Eq. (4.61) to determine $\Delta\gamma$ from measurements of the excess adsorption $\Gamma$, e.g. by means of ellipsometry, second harmonic generation (SHG), sum frequency generation (SFG) or the small angle scattering scattering of X-rays (SAXS) or neutrons (SANS) [21, 109], as a function of the ionic strength $I$. A comparison of this resulting value for $\Delta\gamma$ with the difference $f_+ - f_-$ of the Gibbs free energies of transfer (inferred, e.g. from electrochemical methods) would be a direct way to probe quantitatively the difference between the LDA and the BCA.

In order to further assess the influence of solvation properties by testing the different predictions following from BCA and LDA additional adsorption measurements for hydrophilic walls have been suggested in Ref. [43]. For KBr as salt the arguments above lead to the assertions that, within LDA, one has $\partial\Gamma/\partial I > 0$ (i.e. decreasing water adsorption upon adding salt) independently of the sign of the surface charge $\sigma$ (because the last term on the right-hand side of Eq. (4.61) dominates), whereas within BCA $\partial\Gamma^{(\mathrm{BCA})}/\partial I$ is expected to change sign upon changing the sign of $\sigma$ (because the first term on the right-hand side of Eq. (4.61) dominates). More interestingly, using an antagonistic electrolyte (i.e. with $f_+$ and $f_-$ having opposite signs) such as HBr ($f_+ \approx -11.2, f_- \approx 8.4$ [208], i.e. $\Delta\gamma \approx -4$) the first (ion solubility) contribution on the right-hand side of Eq. (4.61) is dominating such that $\partial\Gamma/\partial I$ and $\sigma$ are expected to have the same sign [43]. In this case, upon adding salt, the amount of adsorbed water either decreases or increases depending

on the sign of the surface charge. This is in contrast to electrowetting where the water adsorption increases with the magnitude but independent of the sign of the surface charge [309] (see Sec. 4.4). Within the BCA approach of Ref. [401] the difference for cations and anions with respect to their solubility contrasts in the two pure solvent components is neglected (i.e. $f_+ = f_- \gg 1$ so that $\Delta\gamma = 0$) to the effect that the reported capillary condensation-like adsorption of water between two equally charged walls at variable distance should be independent of the sign of the surface charge. The analysis above implies that the same property is expected to occur for sufficiently small values of $|\Delta\gamma|$, but the adsorption may depend on the sign of the surface charge if $|\Delta\gamma|$ becomes of the order unity. These differences between BCA- and LDA-based approaches highlight the importance of solubility for numerous quantitative and sometimes even qualitative properties of ionic complex fluids.

## 4.4 Electrowetting

Since the pioneering work of Lippmann [272] and Pellat [350, 351] on the influence of electrostatic potentials on the wetting of substrates by fluids, electrowetting has been simultaneously studied to address fundamental issues of surface science, e.g. electrocapillarity [164], the structure of solid-fluid interfaces [417] or the characterisation of surface states [195], as well as to develop novel applications, e.g. driving, mixing or shaping of droplets in lab-on-a-chip devices, optical applications or microelectromechanical systems [309]. In the past electrowetting at low voltages was commonly interpreted as an electrocapillarity effect, i.e. it is assumed to hinge on the voltage-dependence of the substrate-fluid interfacial tension [30, 51, 88, 93, 221, 232, 309, 350, 351, 370, 371, 411, 416, 417, 438, 469]. A justification for this approach is frequently given in terms of the vast experimental evidence for systems of uncoated and hydrophobically coated electrodes.

An alternative approach to understand electrowetting in terms of general wetting phenomena [107] described by classical microscopic density functional theory, within which one has access to the interfacial structure of fluids in terms of non-uniform number density profiles, has been proposed in Ref. [45]. For example, the contact angle between a fluid-fluid interface and a substrate surface can be calculated from the number density profiles in the *two* coexisting fluid phases which form the fluid-fluid interface. Hence electrowetting, i.e. the dependence of the contact angle on the electrostatic substrate potential, monitors the voltage-dependence of the number density profiles, i.e. of the interfacial structure, in *both* fluid phases. However, it turned out that the commonly given derivations of the electrowetting equation [309] are incorrect in that they express the contact angle in terms of fluid-substrate interfacial tensions, which are descriptors of the interfacial structure of a *single* fluid phase in thermodynamic contact with a substrate. In the past it has been overlooked that the interfacial structure, and thus interfacial quantities, of a fluid can change upon bringing it into contact with another fluid. Although the interfacial structure of fluids close to substrates has been deeply examined in the surface science literature [3, 78, 79, 197, 198, 281, 282], its properties seem to be largely ignored in the context of electrowetting until recently. By ignoring structural differences which occur at substrate-fluid interfaces upon bringing two fluids in simultaneous contact with a substrate, one can interpret electrowetting as a consequence of voltage-dependent interfacial tensions, which is referred to as the electrocapillarity approach to electrowetting in the follow-

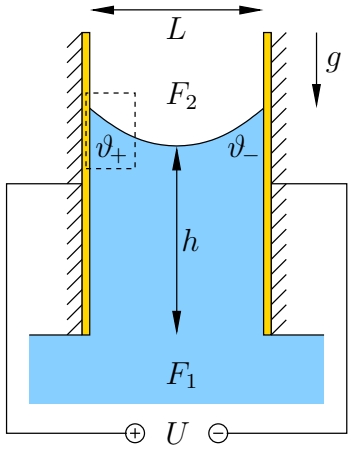


Figure 4.23: Pellat's setup [350, 351] of electrocapillary rise of a fluid $F_1$ in a vertical parallel plate capacitor of width $L$ initially filled with a fluid $F_2$. The meniscus height $h$ is related to the contact angles $\vartheta_+$ and $\vartheta_-$ by Eq. (4.63). Electrowetting corresponds to a dependence of $\vartheta_+$ and $\vartheta_-$, and hence of $h$, on the voltage $U$ between the plate electrodes. A closeup of the three-phase contact region marked by the dashed box is depicted in Fig. 4.24. (See Ref. [45])

ing. However, it turned out that electrowetting *cannot* be consistently understood as an electrocapillarity effect [45]. Alternative approaches to interpret electrowetting as a line tension effect have been proposed [110] but some of the predictions were in disagreement with experimental data [369].

The approach used in Ref. [45] is to study electrowetting in terms of the the effective interface potential, which is related to the macroscopic contact angle [107]. Whereas wetting transitions are concerned with the *thickness* of wetting films (see Sec. 4.2), the contact angle is related to the *depth* of the effective interface potential, which always vanishes continuously at wetting transitions [107]. It is convenient to consider Pellat's classical setup of a vertical parallel plate capacitor [350, 351] because its geometry is precisely defined, an issue which has been recently raised in a critical discussion of the more common setup of a droplet on a substrate with the counter electrode being a thin wire [232]. Although being based on a misconception, the classical derivation of the electrowetting equation within the electrocapillarity approach seems to be a good approximation for systems investigated up to now, i.e. uncoated or hydrophobically coated electrodes. However, setups have been proposed for which this is not the case [45].

Consider Pellat's classical setup [350, 351] depicted in Fig. 4.23. A vertical parallel plate capacitor of width $L$ is in contact with two immiscible fluids $F_1$ and $F_2$ of mass densities $\varrho_{\mathrm{m}1}$ and $\varrho_{\mathrm{m}2}$, respectively. At least one of the fluids $F_1$ and $F_2$ is assumed to be an electrolyte solution. It is further assumed that $\varrho_{\mathrm{m}1} > \varrho_{\mathrm{m}2}$ so that both fluids are separated in the gravitational field with $F_1$ being the lower and $F_2$ being the upper phase (see Fig. 4.23). Provided the capacitor width $L$ is smaller than the capillary length [95, 246, 382]

$$\lambda = \sqrt{\frac{\gamma_{12}}{(\varrho_{\mathrm{m}1} - \varrho_{\mathrm{m}2})g}} \tag{4.62}$$

with the $F_1$-$F_2$ interfacial tension $\gamma_{12}$ and the acceleration due to gravity $g$, the contact

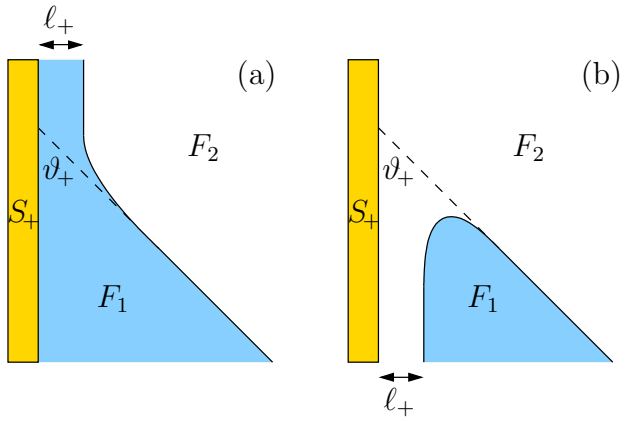


Figure 4.24: Closeup of the possible geometries of the three-phase contact region formed by the anodic substrate $S_+$ (and similarly for the the cathodic substrate $S_-$) and two immiscible fluids $F_1$ and $F_2$ marked by the dashed box in Fig. 4.23. The fluid which is preferred by the substrates $S_\pm$ is denoted by $A$, whereas the other, less preferred fluid is called $B$. Panel (a) corresponds to the case of an $F_1$-adsorbing ($A = F_1$) substrate $S_+$, while panel (b) displays the case of an $F_2$-adsorbing ($A = F_2$) substrate $S_+$. Here it is assumed that both substrates $S_+$ and $S_-$ prefer the same fluid. The macroscopic contact angle $\vartheta_+$ ($\vartheta_-$) shown in Fig. 4.23 describes the asymptotic inclination of the $F_1$-$F_2$ interface far away from the substrate $S_+$ ($S_-$), whereas close to the substrate $S_+$ ($S_-$) a film of microscopic thickness $\ell_+$ ($\ell_-$) of the preferred fluid $A$ is formed. (See Ref. [45])

angles $\vartheta_+$ and $\vartheta_-$ of phase $F_1$ are related to the meniscus height $h$ by [95, 246, 382]

$$\cos\vartheta_+ + \cos\vartheta_- \simeq \frac{hL}{\lambda^2} \quad \text{for } L \ll \lambda. \tag{4.63}$$

Depending on the interactions of the fluids $F_1, F_2$ and the substrates $S_+, S_-$, which are metal electrodes (represented by the hatched parts in Fig. 4.23) possibly coated with some dielectric (represented by yellow layers on top of the electrodes in Fig. 4.23), the respective contact angles $\vartheta_+$ and $\vartheta_-$ can be smaller or larger than $\pi/2$, which corresponds to positive or negative contributions to the meniscus height $h$. Electrowetting can be detected as the dependence of the contact angles $\vartheta_+(U)$ and $\vartheta_-(U)$, and in turn, via Eq. (4.63), of the meniscus height $h(U)$, on the electrostatic potential difference $U = \Psi_+ - \Psi_-$ applied between the electrodes.

The contact angles $\vartheta_+$ and $\vartheta_-$ in Fig. 4.23 provide a macroscopic description of the fluid-fluid-substrate three-phase contact region (highlighted by the dashed box in Fig. 4.23 for the anodic substrate $S_+$). According to the chemical properties of the fluids and the substrates, the contact of substrate $S_\pm$ with one fluid, henceforth denoted by fluid $A$, is more preferable than with the other fluid, henceforth denoted by fluid $B$. Here it is assumed that both substrates are chemically equal such that either fluid $F_1$ or fluid $F_2$ is preferred by both substrates $S_+$ and $S_-$. Consequently, if substrate $S_\pm$ is macroscopically in contact with the bulk of the less preferred fluid $B$ and if the thermodynamic state is away from wetting transitions such that the substrate is only partially wet by phase $A$, a film of microscopic extension $\ell_\pm > \xi$ composed of the preferred fluid $A$ forms in between substrate $S_\pm$ and the bulk of fluid $B$ [107], where $\xi$ denotes the bulk correlation length, which is of the order of the particle size if the thermodynamic state is away from critical

points. The microscopic film thickness is experimentally accessible via measurements of the excess adsorption $\Gamma_\pm$ by means of optical [21] or scattering [109] techniques. Then the fluid structure is similar to that of a composition of an $S_\pm$-$A$ interface at the substrate surface and a free $A$-$B$ interface at a distance $\ell_\pm$ away from the substrate, both being of typical extension $\xi$ [107]. This structure leads to a surface contribution $\Omega_{s,\pm B}(\ell_\pm) = \gamma_{\pm A} + \gamma_{12} + \omega_\pm(\ell_\pm)$ to the grand potential of the system, where $\gamma_{\pm A}$ and $\gamma_{12}$ denote the $S_\pm$-$A$ and $F_1$-$F_2$ interfacial tensions, respectively, and where $\omega_\pm(\ell_\pm)$ is the effective interface potential [107]. It is important to distinguish $\Omega_{s,\pm B}$ from the interfacial tension $\gamma_{\pm B}$ of an $S_\pm$-$B$ interface in the *absence* of phase $A$ [45]. Here $\Omega_{s,\pm B} \neq \gamma_{\pm B}$ because the presence of the preferred phase $A$ leads to a structural change, i.e. the formation of $A$-films, as compared to the situation in the absence of phase $A$. Ignoring the difference between $\Omega_{s,\pm B}$ and $\gamma_{\pm B}$ is equivalent to ignoring the formation of $A$-films and it is this crucial misconception which underlies the electrocapillarity approach to electrowetting [45]. In contrast, if substrate $S_\pm$ is in contact with the bulk of the preferred fluid $A$, the fluid is non-uniform only close to the substrate surfaces up to distances $\xi$, and this interfacial structure is not modified by the presence of fluid $B$, hence $\Omega_{s,\pm A} = \gamma_{\pm A}$. Depending on whether the preferred fluid $A$ is fluid $F_1$ or fluid $F_2$ the substrates $S_\pm$ are referred to as $F_1$-adsorbing or $F_2$-adsorbing, respectively. A closeup of the fluid-fluid-substrate three-phase contact region close to substrate $S_+$ marked by the dashed box in Fig. 4.23 is sketched respectively in Figs. 4.24(a) and (b) for an $F_1$-adsorbing ($A = F_1$) and an $F_2$-adsorbing ($A = F_2$) substrate.

The macroscopic contact angle $\vartheta_\pm$ (see Fig. 4.24) is related to the surface contributions $\Omega_{s,\pm 1}$, $\Omega_{s,\pm 2}$ and the interfacial tension $\gamma_{12}$ of the $S_\pm$-$F_1$, $S_\pm$-$F_2$, and $F_1$-$F_2$ interface, respectively, by Young's equation [95, 246, 382]

$$\Omega_{s,\pm 2} = \Omega_{s,\pm 1} + \gamma_{12} \cos\vartheta_\pm. \tag{4.64}$$

It is common to assume $\Omega_{s,\pm\alpha} = \gamma_{s,\pm\alpha}, \alpha \in \{F_1, F_2\}$, but this misconception to ignore the structural differences of a macroscopic $S_\pm$-$\alpha$ contact in the presence and in the absence of additional phases can have significant consequences [45]. The surface contributions $\Omega_{s,\pm 1}$ and $\Omega_{s,\pm 2}$ are related to the depth of the effective interface potential $\omega_+(\ell)$ evaluated at the equilibrium film thickness $\ell = \ell_\pm$ by [107]

$$\Omega_{s,\pm 1} = \gamma_{\pm 1}, \qquad \Omega_{s,\pm 2} = \gamma_{\pm 1} + \gamma_{12} + \omega_\pm(\ell_\pm) \tag{4.65}$$

for $F_1$-adsorbing substrates $S_\pm$ (see above the three-phase contact region in Fig. 4.24(a)) and by

$$\Omega_{s,\pm 1} = \gamma_{s,\pm 2} + \gamma_{12} + \omega_\pm(\ell_\pm), \qquad \Omega_{s,\pm 2} = \gamma_{s,\pm 2} \tag{4.66}$$

for $F_2$-adsorbing substrates $S_\pm$ (see below the three-phase contact region in Fig. 4.24(b)). Hence, one obtains [107]

$$\cos\vartheta_\pm = \frac{\Omega_{s,\pm 2} - \Omega_{s,\pm 1}}{\gamma_{12}} = p\left(1 + \frac{\omega_\pm(\ell_\pm)}{\gamma_{12}}\right), \tag{4.67}$$

where $p = +1$ for $F_1$-adsorbing and $p = -1$ for $F_2$-adsorbing substrates $S_\pm$. This equation connects the macroscopic contact angle $\vartheta_\pm$ with the microscopic structure represented by the effective interface potential $\omega_\pm(\ell)$ of $A$-films at substrate $S_\pm$ in macroscopic contact with bulk fluid $B$ [45].

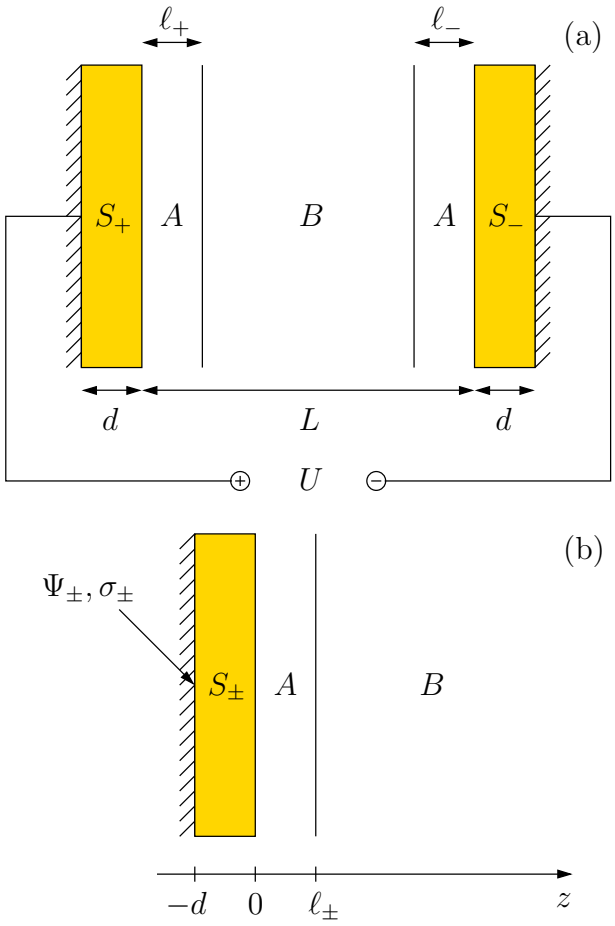


Figure 4.25: (a) Far above (Fig. 4.24(a)) or below (Fig. 4.24(b)) the three-phase contact regions (see Fig. 4.23) the dielectric substrates $S_+$ and $S_-$ of thickness $d$ and distance $L$ are covered by films of the preferred fluid $A$ of microscopic thicknesses $\ell_\pm$, which separate the substrates from the bulk of the less preferred fluid $B$. (b) Since the separation $L$ between the substrates $S_+$ and $S_-$ is typically the largest length scale, one can consider the limit $L \to \infty$, which renders the effective interface potential $\omega_\pm(\ell)$ at substrate $S_\pm$ that of a semi-infinite system. A coordinate axis normal to each substrate is introduced with the origin $z = 0$ at the surface and the fluids in the range $z > 0$. The interface between the $A$-film and the bulk fluid $B$ is located at $z = \ell_\pm$ and the electrode is at position $z = -d$, where the electrostatic potential is $\Psi_\pm$ and the surface charge density is $\sigma_\pm$. (See Ref. [45])

The dependence of the effective interface potentials $\omega_\pm(\ell_\pm; U)$ on the electrostatic potential difference $U$ between the electrodes in the setting of Fig. 4.23, together with Eq. (4.67), leads to the electrowetting equations. However, already without explicit expressions for the effective interface potentials, one can draw an important conceptual conclusion from Eq. (4.67): Electrowetting is *not* an electrocapillarity effect, since *no* $U$-dependent substrate-fluid interfacial tensions, which describe the contact of the substrate with *one* fluid, occur on the right-hand side. Instead, electrowetting is related to the depth of the effective interface potential $\omega_\pm(\ell; U)$, which describes the $U$-dependence of the microscopic fluid structure close to the substrate in the presence of *two* fluids [45].

In order to obtain the effective interface potential $\omega_\pm(\ell)$ of an $A$-film of thickness $\ell$

at substrate $S_\pm$ in Fig. 4.23, whose value for the equilibrium film thicknesses $\ell = \ell_\pm$ is related to the contact angle $\vartheta_\pm$ via Eq. (4.67), one may represent the structure in Fig. 4.23 far above (for an $F_1$-adsorbing substrate $S_\pm$, see Fig. 4.24(a)) or below (for an $F_2$-adsorbing substrate $S_\pm$, see Fig. 4.24(b)) the three-phase contact region by the quasi-one-dimensional slab depicted in Fig. 4.25(a). The chemically identical substrates $S_+$ and $S_-$, which comprise metal electrodes coated with dielectric layers of thickness $d$, are separated by a distance $L$ and covered with films of thicknesses $\ell_+$ and $\ell_-$, respectively, of the preferred fluid $A$. Moreover, the electrodes are assumed to be ideally polarised, i.e. electrochemical reactions do not occur. Even under these conditions the film thicknesses $\ell_+$ and $\ell_-$ can differ, if unequal partitioning of ions at the film-bulk fluid interfaces takes place. This is expected to occur in general due to generic differences in solubility contrasts [43] (see Sec. 2.1). The macroscopic distance $L$ between the substrates is typically the largest length scale such that only the limit $L \to \infty$ is considered in the following. Hence the effective interface potentials $\omega_+(\ell)$ and $\omega_-(\ell)$ at the substrates $S_+$ and $S_-$, respectively, are those of semi-infinite systems. For each substrate $S_\pm$ a coordinate axis in normal direction with the origin $z = 0$ at the substrate surface and the fluid at $z > 0$ is introduced (see Fig. 4.25(b)). The interface between the $A$-film and the bulk of phase $B$ is located at position $z = \ell_\pm$ and the electrode is at $z = -d$, where the electrostatic potential is $\Psi_\pm$ and the surface charge density is $\sigma_\pm$.

Considering the two bulk phases of fluids $F_1$ and $F_2$ outside the capacitor in Fig. 4.23 as particle reservoirs, one is naturally led to a grand-canonical description of the thermodynamic state. A starting point for the derivation of the effective interface potential $\omega_\pm(\ell)$ is the grand potential functional per thermal energy $k_BT = 1/\beta$ and per area $\mathcal{A}$ of the electrode [45]

$$\begin{aligned}\frac{\beta\Omega[\phi,\varrho_\pm]}{\mathcal{A}} = \frac{\beta\Omega_0[\phi]}{\mathcal{A}} + \frac{\beta d D(0)^2}{2\varepsilon_{\rm vac}\varepsilon_S} - \beta\Psi_\pm D(0) \\ + \int_0^\infty \mathrm{d}z \Big[ \sum_{i=\pm} \varrho_i(z) \Big( \ln\frac{\varrho_i(z)}{\zeta_i} - 1 + \beta V_i(\phi(z)) \Big) + \frac{\beta D(z)^2}{2\varepsilon_{\rm vac}\varepsilon(\phi(z))} \Big]\end{aligned} \tag{4.68}$$

in terms of the solvent composition profile $\phi$ and the $\pm$-ion number density profiles $\varrho_\pm$. Here the permittivity $\varepsilon_{\rm vac}$ of the vacuum, the relative permittivity $\varepsilon_S$ of the substrate $S_\pm$, and the fugacities $\zeta_\pm$ of $\pm$-ions are used. The density functional $\Omega_0[\phi]$ describes the grand potential of the pure, i.e. salt-free fluids, and $D(z)$ is the electric displacement.

For films of thicknesses $\ell_\pm > \xi$ it is natural to approximate the solvent composition profile $\phi$ in Eq. (4.68) within the sharp-kink approximation [107]

$$\varphi_\ell(z) := \begin{cases} \bar\phi_A, & z < \ell \\ \bar\phi_B, & z > \ell. \end{cases} \tag{4.69}$$

By minimising $\beta\Omega[\varphi_\ell, \Delta\varrho_\pm]/\mathcal{A}$ in Eq. (4.68) with respect to the deviations $\Delta\varrho_\pm(z)$ of the ion densities $\varrho_\pm(z)$ from the ionic strength one obtains the equilibrium profiles $\Delta\varrho_\pm^{(\ell)}$. Subtracting the bulk contribution $\beta\Omega_b(\bar\phi_B, I_B)/\mathcal{A}$ leads to the surface contribution to the grand potential [107]

$$\Omega_s(\ell) = \frac{\Omega(\ell, [\Delta\varrho_\pm^{(\ell)}]) - \Omega_b(\bar\phi_B, I_B)}{\mathcal{A}}. \tag{4.70}$$

Finally, the effective interface potential at substrate $S_\pm$ is given by $\omega_\pm(\ell) = \Omega_s(\ell) - \Omega_s(\infty)$ [107]. Hence, Eq. (4.67) can be written as [309]

$$\cos\vartheta_\pm(U) = \cos\vartheta_\pm(0) + \eta_\pm(U) \tag{4.71}$$

with the electrowetting number [45]

$$\eta_\pm(U) := p\frac{\omega_\pm(\ell_\pm;U) - \omega_\pm(\ell_\pm;0)}{\gamma_{12}}. \tag{4.72}$$

Whereas the full expression for the electrowetting number $\eta_\pm(U)$ depends on the five possibly largely different length scales $\lambda_A := 1/(\kappa_A\varepsilon_A)$, $\lambda_B := 1/(\kappa_B\varepsilon_B)$, $\lambda_S := d/\varepsilon_S$ and $\lambda_{\ell_\pm} := \ell_\pm/\varepsilon_A$, where $\kappa_\alpha^2 := 2\beta e^2 I_\alpha/(\varepsilon_{\rm vac}\varepsilon_\alpha)$ is the square of the inverse Debye length in the bulk of phase $\alpha \in \{A, B\}$, the latter two, corresponding to the thicknesses of the $A$-films at the substrates $S_+$ and $S_-$, respectively, are typically of similar magnitude: $\ell_+ \approx \ell_-$, i.e. $\lambda_{\ell_+} \approx \lambda_{\ell_-}$. This case $\ell_+ = \ell_- =: \ell$ is discussed here, for which the electrowetting number $\eta_\pm(U)$ simplifies to [45]

$$\eta_\pm(U) = \frac{p}{\gamma_{12}}\left(\frac{A(\ell)}{8}U^2 \pm \frac{B(\ell)}{2}\Big(\frac{A(\ell)}{F(\ell)} + 1\Big)U\right). \tag{4.73}$$

Moreover, the film thicknesses $\ell_+$ and $\ell_-$ are typically smaller than the Debye lengths $1/\kappa_A$ and $1/\kappa_B$ so that the limiting case $\lambda_\ell \ll \lambda_A, \lambda_B$ is considered throughout, within which [45]

$$A(\ell) \simeq \frac{\varepsilon_{\rm vac}}{Q(\ell)}\,\frac{\lambda_B - \lambda_A}{\lambda_B(\lambda_S + \lambda_A)} \tag{4.74}$$

$$B(\ell) = -\frac{\varepsilon_{\rm vac}}{Q(\ell)}\,\frac{\bar\psi_A - \bar\psi_B}{\lambda_B} \tag{4.75}$$

$$F(\ell) \simeq \frac{\varepsilon_{\rm vac}}{Q(\ell)}\left(\frac{\lambda_\ell}{\lambda_A^2} + \frac{1}{\lambda_B}\right) \tag{4.76}$$

$$Q(\ell) \simeq 1 + \frac{\lambda_S}{\lambda_B} + \frac{\lambda_\ell\lambda_S}{\lambda_A^2}. \tag{4.77}$$

Equation (4.73) is expected to be valid for sufficiently small voltages $|U|$. The electrowetting number $\eta_\pm(U)$ in Eq. (4.73) differs from those in the literature [309] in a number of aspects: The most obvious difference is the occurrence of a correction term $\sim U$, which vanishes exactly only if $B(\ell) = 0$ due to a vanishing Donnan potential (Galvani potential difference [2, 20, 121, 122]) $\bar\psi_A - \bar\psi_B$. For $\bar\psi_A - \bar\psi_B \neq 0$, i.e. $B(\ell) \neq 0$, the electrowetting number $\eta_\pm(U)$ is not minimal at and not symmetric with respect to $U = 0$. However, for a sufficiently large voltage $|U|$ the subleading term $\sim U$ is dominated by the leading term $\sim U^2$.

Before discussing the electrowetting number in Eq. (4.73) obtained within the density functional approach of Ref. [45], the traditional approach based on the assumption of electrowetting being an electrocapillarity effect [30, 51, 88, 93, 221, 232, 309, 350, 351, 370, 371, 411, 416, 417, 438, 469] is repeated. Here only the classical method based on Lippmann's equation is presented. However, calculations using alternative methods, e.g. based on Maxwell's stress tensor [224, 309], suffer from the same misconceptions.

The starting point is Young's equation (4.64) but with the *incorrect* assumption $\Omega_{s,\pm\alpha} = \gamma_{\pm\alpha}, \alpha \in \{F_1, F_2\}$. In order to obtain the $U$-dependence of the interfacial tension $\gamma_{\pm\alpha}$ one considers a semi-infinite fluid $\alpha$ bound by a planar substrate $S_\pm$. The interfacial tension $\gamma_{\pm\alpha}$ changes upon changing the electrostatic potential $\psi_{\pm\alpha}$ of substrate $S_\pm$ with respect to that of the bulk of phase $\alpha$ according to Lippmann's equation [164, 272]

$$\frac{\partial\gamma_{\pm\alpha}}{\partial\psi_{\pm\alpha}} = -\sigma_{\pm\alpha}, \tag{4.78}$$

where $\sigma_{\pm\alpha}$ is the surface charge density of substrate $S_\pm$ in contact with phase $\alpha$. Describing the $S_\pm$-$\alpha$ interface by means of the potential-independent differential capacitance $C_{S\alpha} = \partial\sigma_{\pm\alpha}/\partial\psi_{\pm\alpha}$, which is assumed to not depend on $S_\pm$ for chemically identical substrates, and integrating twice with respect to the electrostatic substrate potential $\psi_{\pm\alpha}$ using Lippmann's equation (4.78) leads to

$$\gamma_{\pm\alpha}(\psi_{\pm\alpha}) = \gamma_{\pm\alpha}(0) - \frac{C_{S\alpha}}{2}\psi_{\pm\alpha}^2. \tag{4.79}$$

Young's equation (4.64) in conjunction with the assumption $\Omega_{s,\pm\alpha} = \gamma_{\pm\alpha}$ reads

$$\begin{aligned}\gamma_{\pm2}(\psi_{\pm2}) &= \gamma_{\pm2}(0) - \frac{C_{S2}}{2}\psi_{\pm2}^2 \\ &= \gamma_{\pm1}(\psi_{\pm1}) + \gamma_{12}\cos\vartheta_\pm \\ &= \gamma_{\pm1}(0) - \frac{C_{S1}}{2}\psi_{\pm1}^2 + \gamma_{12}\cos\vartheta_\pm.\end{aligned} \tag{4.80}$$

Noting $\gamma_{\pm2}(0) - \gamma_{\pm1}(0) = \gamma_{12}\cos\vartheta_\pm(0)$ leads to

$$\cos\vartheta_\pm - \cos\vartheta_\pm(0) = \frac{C_{S1}}{2\gamma_{12}}\psi_{\pm1}^2 - \frac{C_{S2}}{2\gamma_{12}}\psi_{\pm2}^2. \tag{4.81}$$

Using $\sigma_{\pm\alpha} = C_{S\alpha}\psi_{\pm\alpha}$, one obtains $\psi_{\pm\alpha} = \pm U/2$ from $U = \psi_{+\alpha} - \psi_{-\alpha}$ and $\sigma_{+\alpha} + \sigma_{-\alpha} = 0$. This leads to the commonly used form of the electrowetting equation [30, 51, 88, 93, 221, 224, 232, 309, 350, 351, 370, 371, 411, 416, 417, 438, 469]

$$\cos\vartheta_\pm(U) - \cos\vartheta_\pm(0) = \frac{C_{S1} - C_{S2}}{8\gamma_{12}}U^2 =: \eta_{\mathrm{ec}}(U) \tag{4.82}$$

with the differential capacitances $C_{S\alpha}$ being those of a substrate in macroscopic contact with only one fluid phase $\alpha$. These differential capacitances $C_{S\alpha}$ can typically be interpreted as those of a capacitor of capacitance $C_S = \varepsilon_{\mathrm{vac}}\varepsilon_S/d$, representing substrate $S_\pm$, connected *in series* with a capacitor of capacitance $C_\alpha$, representing fluid $\alpha$: $1/C_{S\alpha} = 1/C_S + 1/C_\alpha$. If fluid $\alpha$ is an electrolyte solution the fluid capacitance is that of the electric double layer in a semi-infinite system, $C_\alpha = \varepsilon_{\mathrm{vac}}\kappa_\alpha\varepsilon_\alpha$, whereas for a non-conducting dielectric fluid $C_\alpha = \lim_{L\to\infty}\varepsilon_{\mathrm{vac}}\varepsilon_\alpha/L = 0$. Using the length scales defined above, this leads to

$$C_{S\alpha} = \begin{cases} \dfrac{\varepsilon_{\mathrm{vac}}}{\lambda_S + \lambda_\alpha}, & \alpha \text{ electrolyte solution} \\ 0, & \alpha \text{ non-conducting fluid.} \end{cases} \tag{4.83}$$

Equations (4.82) and (4.83) represent the interpretation of electrowetting as an electrocapillarity effect [309]. However, the crucial misconception underlying this interpretation is to use the approximation $\Omega_{s,\pm\alpha} = \gamma_{\pm\alpha}$ and hence the differential capacitance $C_{S\alpha}$, which corresponds to a semi-infinite system of a single phase $\alpha$ bound by substrate $S_\pm$, instead of accounting for the actual fluid structure at the substrate. The interfacial structure, and therefore surface quantities such as the surface contribution to the grand potential as well as the differential capacitance, of substrate $S_\pm$ in macroscopic contact with the bulk fluid $B$ depend significantly on whether the preferred fluid $A$ is present or not because an $A$-film forms in between the substrate $S_\pm$ and the bulk fluid $B$ in the former case whereas it does not in the latter case. In contrast, these structural properties are naturally accounted for within the density functional approach, which relates the contact angle to the effective interface potential (see Eq. (4.67)), a quantity which correctly describes the contact of a substrate with *both* fluids $A$ and $B$ [45].

The early investigations of electrocapillarity by Lippmann [272] and Pellat [350, 351] have been performed for metal electrodes without any dielectric coating. At that time for some decades mercury electrodes became the experimental standard for investigations of the electric double layer [164]. Pure metal electrodes can be considered as substrates with thickness $d$ being the smallest length scale: $\lambda_S \ll \lambda_\ell \ll \lambda_A, \lambda_B$.

For the case $\lambda_A \ll \lambda_B$, which is typically the case for water-adsorbing substrates, an aqueous electrolyte solution $F_1 = A$ (i.e. $p = +1$) and an oil $F_2 = B$, one obtains for the electrowetting number Eq. (4.73)

$$\begin{aligned}\eta_\pm(U) &\simeq \frac{\varepsilon_{\rm vac}}{8\gamma_{12}\lambda_A}U^2 \mp \frac{\varepsilon_{\rm vac}(\bar\psi_A - \bar\psi_B)}{2\gamma_{12}(\lambda_A + \lambda_\ell\lambda_B/\lambda_A)}U \\ &\simeq \frac{\varepsilon_{\rm vac}}{8\gamma_{12}\lambda_A}U^2, \quad \text{for } |U| \gg 4|\bar\psi_A - \bar\psi_B|. \end{aligned} \tag{4.84}$$

Hence, if the voltage $|U|$ is much larger than the Donnan potential (Galvani potential difference) $|\bar\psi_A - \bar\psi_B|$, the electrowetting number $\eta_\pm(U)$ agrees with that in Eq. (4.82), where $C_{S1} \simeq \varepsilon_{\rm vac}/\lambda_A, C_{S2} = 0$ due to Eq. (4.83).

Similarly, for the case $\lambda_A \gg \lambda_B$, which is typically the case for oil-adsorbing substrates, an oil $F_2 = A$ (i.e. $p = -1$) and an aqueous electrolyte solution $F_1 = B$, one obtains for the electrowetting number Eq. (4.73)

$$\begin{aligned}\eta_\pm(U) &\simeq \frac{\varepsilon_{\rm vac}}{8\gamma_{12}\lambda_B}U^2 \pm \frac{\varepsilon_{\rm vac}(\bar\psi_A - \bar\psi_B)}{2\gamma_{12}\lambda_A}U \\ &\simeq \frac{\varepsilon_{\rm vac}}{8\gamma_{12}\lambda_B}U^2, \quad \text{for } |U| \gg 4|\bar\psi_A - \bar\psi_B|. \end{aligned} \tag{4.85}$$

Again, if the voltage $|U|$ is much larger than the Donnan potential (Galvani potential difference) $|\bar\psi_A - \bar\psi_B|$, the electrowetting number $\eta_\pm(U)$ again agrees with that in Eq. (4.82), where $C_{S1} \simeq \varepsilon_{\rm vac}/\lambda_B, C_{S2} = 0$ due to Eq. (4.83).

Therefore, the formalism (Eqs. (4.73)–(4.77)) confirms the electrocapillarity-based form of the electrowetting number for the case of uncoated metal electrodes ($\eta_\pm(U) \simeq \eta_{\rm ec}(U)$), provided the voltage $|U|$ is sufficiently large as compared to the Donnan potential (Galvani potential difference) $|\bar\psi_A - \bar\psi_B|$. Interestingly, for uncoated metal electrodes it is irrelevant whether they are $F_1$-adsorbing (water-adsorbing) or $F_2$-adsorbing (oil-adsorbing).

However, a small voltage $|U| \ll |\bar\psi_A - \bar\psi_B|$ or $\lambda_A \approx \lambda_B$, e.g. for two immiscible electrolyte solutions, leads to electrowetting numbers $\eta_\pm(U) \sim U$, in contrast to $\eta_{\rm ec}(U) \approx 0$ in

Eq. (4.82) due to $C_{S1} \approx C_{S2}$ according to Eq. (4.83). Since these conditions are rather special, this scenario is not expected to be of practical relevance, but it might provide a test for the approach in Ref. [45].

In the last few decades most electrowetting settings used electrodes coated with an isolating dielectric for technical advantage [30]. Almost all of these studies used drops of an aqueous electrolyte solution $F_1$ placed on a hydrophobic ($\vartheta_\pm > \pi/2$) dielectric and an oil $F_2$ as the environmental fluid in order to achieve large contact angle ranges being covered by electrowetting [309]. Therefore, typically oil-adsorbing substrates are used, which, within the present notation, corresponds to $A = F_2$ (i.e. $p = -1$) and $B = F_1$. Since the thickness $\ell$ of the microscopic oil film on the substrates $S_\pm$ is typically smaller than the Debye length $1/\kappa_B$ of the dilute electrolyte solution $B = F_1$, which in turn is typically much smaller than the thickness $d$ of the dielectric substrates $S_\pm$, one identifies the case $\lambda_\ell \ll \lambda_B \ll \lambda_S \ll \lambda_A$, where a (practically) ion-free oil $A = F_2$ ($I_A \approx 0$) is assumed. For this regime Eq. (4.73) is given by [45]

$$\begin{aligned}\eta_\pm(U) &\simeq \frac{\varepsilon_{\rm vac}}{8\gamma_{12}\lambda_S}U^2 \pm \frac{\varepsilon_{\rm vac}(\bar\psi_A - \bar\psi_B)}{2\gamma_{12}\lambda_A}U \\ &\simeq \frac{\varepsilon_{\rm vac}}{8\gamma_{12}\lambda_S}U^2, \quad \text{for } |U| \gg 4\frac{\lambda_S}{\lambda_A}|\bar\psi_A - \bar\psi_B|.\end{aligned} \tag{4.86}$$

Since $\lambda_S/\lambda_A \ll 1$, the approximation in the second line of the previous equation almost always applies. It shows that the electrowetting number $\eta_\pm(U)$ for water on a oil-adsorbing dielectric in oil is also in agreement with $\eta_{\rm ec}(U)$ in Eq. (4.82) with $C_{S1} \simeq \varepsilon_{\rm vac}/\lambda_S, C_{S2} = 0$ due to Eq. (4.83).

Replacing the oil-adsorbing dielectric substrate by a water-adsorbing one leads to the case $A = F_1$ (i.e. $p = +1$), $B = F_2$ and $\lambda_\ell \ll \lambda_A \ll \lambda_S \ll \lambda_B$, where again a (practically) ion-free oil $B = F_2$ ($I_B \approx 0$) is assumed. For this regime Eq. (4.73) is of the form [45]

$$\begin{aligned}\eta_\pm(U) &\simeq \frac{1}{Q(\ell)}\left(\frac{\varepsilon_{\rm vac}}{8\gamma_{12}\lambda_S}U^2 \mp \frac{\varepsilon_{\rm vac}(\bar\psi_A - \bar\psi_B)}{2\gamma_{12}\lambda_B}\Big(\frac{1}{\lambda_S(\lambda_\ell/\lambda_A^2 + 1/\lambda_B)} + 1\Big)U\right) \\ &\simeq \frac{1}{Q(\ell)}\ \frac{\varepsilon_{\rm vac}}{8\gamma_{12}\lambda_S}U^2, \quad \text{for } |U| \gg 4|\bar\psi_A - \bar\psi_B|.\end{aligned} \tag{4.87}$$

Within the electrocapillarity approach one again expects an electrowetting number $\eta_{\rm ec}(U) = \varepsilon_{\rm vac}U^2/(8\gamma_{12}\lambda_S)$ (see Eqs. (4.82) and (4.83)). However, the electrowetting number $\eta_\pm(U)$ within the density functional approach in Eq. (4.87), for sufficiently large voltage $|U| \gg 4|\bar\psi_A - \bar\psi_B|$, is actually smaller than $\eta_{\rm ec}(U)$ by a factor $1/Q(\ell)$: $\eta_\pm(U) \simeq \eta_{\rm ec}(U)/Q(\ell)$.

It is apparent from Eq. (4.77) that $Q(\ell)$ is *not* necessarily close to unity, because the typically small value $\kappa_A\ell = \lambda_\ell/\lambda_A \ll 1$ is multiplied with the typically large value $\kappa_A d\varepsilon_A/\varepsilon_S = \lambda_S/\lambda_A \gg 1$. Assuming typical values of, e.g., dielectric layers of thicknesses $d = 1$ $\mu$m and dielectric constant $\varepsilon_S = 2$, a Debye length $1/\kappa_A = 10$ nm in the aqueous ($\varepsilon_A = 80$) electrolyte solution $F_1 = A$, and thicknesses $\ell = 1$ nm of the electrolyte films on the substrates, Eq. (4.77) leads to $Q(\ell) \approx 400$. Hence, for this example of electrowetting on a water-adsorbing dielectric, the analysis leads to electrowetting numbers $\eta_\pm(U)$ which are more than two orders of magnitude smaller than expected within the electrocapillarity approach: $\eta_\pm(U) \approx 0.0025\eta_{\rm ec}(U) \ll \eta_{\rm ec}(U)$.

It appears as if no experimental studies of electrowetting on water-adsorbing substrates have been reported so far. This is remarkable since the preparation of substrates with prescribed adsorption preferences is a standard procedure in surface science.

Finally, instead of considering an electrolyte solution and an oil, the case of two immiscible electrolyte solutions is discussed. This situation is characterised by $\lambda_\ell \ll \lambda_A, \lambda_B \ll \lambda_S$.

If electrolyte solutions $F_1$ and $F_2$ are defined by $\lambda_{F_1} \leq \lambda_{F_2}$, i.e. $\varepsilon_{F_1} I_{F_1} \geq \varepsilon_{F_2} I_{F_2}$, the following three cases have to be distinguished: (i) $A = F_1$ (i.e. $p = +1$) and $B = F_2$ with $\lambda_A \ll \lambda_B$, (ii) $A = F_2$ (i.e. $p = -1$) and $B = F_1$ with $\lambda_A \gg \lambda_B$ and (iii) $\lambda_A \approx \lambda_B$.

Case (i) leads to the electrowetting number Eq. (4.73) [45]

$$\begin{aligned} \eta_\pm(U) &\simeq \frac{1}{Q(\ell)} \left( \frac{\varepsilon_{\rm vac}}{8\gamma_{12}\lambda_S} U^2 \mp \frac{\varepsilon_{\rm vac}(\bar\psi_A - \bar\psi_B)}{2\gamma_{12}\lambda_B} U \right) \\ &\simeq \frac{1}{Q(\ell)} \ \frac{\varepsilon_{\rm vac}}{8\gamma_{12}\lambda_S} U^2, \quad \text{for } |U| \gg 4\frac{\lambda_S}{\lambda_B}|\bar\psi_A - \bar\psi_B|. \end{aligned} \tag{4.88}$$

Hence $\eta_\pm(U) \simeq \eta_{\rm ec}/Q(\ell)$, where, however, the depression factor $1/Q(\ell)$ here is typically much smaller than that for before because typically $\varepsilon_B \kappa_B d/\varepsilon_S \gg 1$ (see Eqs. (4.77)).

The electrowetting number of case (ii) is given by [45]

$$\begin{aligned} \eta_\pm(U) &\simeq \frac{\lambda_A}{\lambda_S} \left( \frac{\varepsilon_{\rm vac}}{8\gamma_{12}\lambda_S} U^2 \pm \frac{\varepsilon_{\rm vac}(\bar\psi_A - \bar\psi_B)}{2\gamma_{12}\lambda_A} U \right) \\ &\simeq \frac{\lambda_A}{\lambda_S} \ \frac{\varepsilon_{\rm vac}}{8\gamma_{12}\lambda_S} U^2, \quad \text{for } |U| \gg 4\frac{\lambda_S}{\lambda_A}|\bar\psi_A - \bar\psi_B|. \end{aligned} \tag{4.89}$$

This expression bears some resemblance to Eq. (4.86) except of the typically very small prefactor $\lambda_A/\lambda_S \ll 1$ here.

Therefore, electrowetting is also expected to be strongly suppressed for two immiscible electrolyte solutions with $\varepsilon_{F_1} I_{F_1} \not\approx \varepsilon_{F_2} I_{F_2}$, a condition which is typically fulfilled.

For completeness the rather special case (iii) is mentioned, for which the electrowetting number reads

$$\eta_\pm(U) \simeq \mp \frac{p\varepsilon_{\rm vac}(\bar\psi_A - \bar\psi_B)}{2\gamma_{12}\lambda_S} U. \tag{4.90}$$

The main conclusion is that that electrowetting is a consequence *not* of the voltage-dependence of the substrate-fluid interfacial tensions, i.e. electrowetting is *not* an electrocapillarity effect, *but* of the voltage-dependence of the depth of the effective interface potential. The traditional electrocapillarity approach to electrowetting is shown to be compromised by the reliance on the incorrect assumption that the surface structure of a fluid does not change upon bringing the system into contact with another fluid phase.

The analysis in Ref. [45] of Pellat's setup for electrowetting studies leads to effectively four length scales corresponding to the Debye lengths in both fluids, the thickness of the substrates and the film thicknesses, the latter being assumed to be approximately equal here, which serve to classify various relevant experimental situations, e.g. uncoated metal electrodes, water- or oil-adsorbing dielectric substrates or fluids comprising water+oil systems or immiscible electrolyte solutions. The dependence of the electrowetting number on these length scales renders electrowetting a general phenomenon with involved structure formation mechanisms of the underlying ionic complex fluid.

## 4.5 Wetting properties of charged colloidal platelets

Platelike colloidal particles play a decisive, constitutive role in fields like agriculture (soil), construction (concrete), filling (cosmetics, rubber, plastic, etc.), coating (paper) and oil-drilling (rheological fluids for oilrecovery). This wide range of applicability mirrors a very rich phase behaviour of suspensions of platelets, including liquid crystalline phases, sol-gel transitions, aging and flocculation, depending on numerous parameters such as size, shape, charge, polydispersity of the particles as well as on effective, solvent mediated interactions which can be tuned, e.g. by the choice of the solvent, ionic strength or *p*H-value.

On the experimental side, characterisation of bulk phases have been conducted for several model systems like natural clay [65, 249], laponite [148, 241, 266, 307, 308, 320, 321, 358, 362, 363, 386, 406], sterically stabilised gibbsite [439, 440, 442, 443, 451, 477] or nickel(II)hydroxide [67, 68] using methods like polarised light analysis [148, 439, 440, 442, 443], light scattering [241, 320, 321], small-angle scattering with neutrons or x-rays [67, 68, 241, 307, 355, 358, 406], rheological measurements [266, 307, 308] or NMR [362, 363]. For a review of these investigations see, e.g., Refs. [89, 316].

Computer simulations have been performed attempting to elucidate the experimental findings. In the pioneering work by Veerman and Frenkel [447] $NVT$ Monte Carlo simulations have been performed for a model of hard cut spheres in order to determine the phase diagram, which exhibits isotropic, nematic, columnar, cubatic and solid phases, for various aspect ratios. Later, the same model has been used for $NpT$ Monte Carlo simulations in Ref. [441] to study the influence of the gravitational field. In Ref. [111] $NVT$ Monte Carlo simulations of infinitely thin hard discs endowed with an electric quadrupolar moment to mimic distributed charges led to the observation of sol-gel transitions. A more elaborate model of hard discs with charges located in the equatorial plane has been used in Ref. [298, 299] to determine the effective interaction between two colloidal particles by means of $NVT$ Monte Carlo simulations. By means of bead models of charged colloidal platelets studied with Brownian dynamics simulations T-shaped configurations and a slowing down of self diffusion upon increasing the number density or the Debye length has been found in Ref. [324]. Finally, an extremely rich phase behaviour with isotropic, nematic, smectic, columnar, cubatic, parquet and solid phases has been found by means of $NpT$ Monte Carlo simulations of hard cuboids in Ref. [215].

Most theoretical work has been concentrated on the investigation of models of hard platelets [34, 85, 143, 182, 381, 471, 472] and anisotropically charged discs [4, 82, 178, 180, 268, 376, 377, 380, 435] in spatially homogeneous configurations. However, some theoretical investigations of colloidal platelets with *spatial inhomogeneities* such as interfaces, surfaces or due to external fields have been undertaken [34–36, 179, 181, 183, 305, 473]. Understanding the influence of surfaces is of particular importance as walls have a strong influence on this sort of material and electrodes are a common means to manipulate fluids of charged particles. An important theoretical step for understanding such surface properties requires to determine the corresponding surface phase diagrams which are well studied for simple fluids [94, 107, 407, 424] but less intensively for ionic complex fluids involving charges *and* anisotropically shaped particles [36].

The theoretical description of suspensions of charged platelets is rather complicated due to long-ranged, anisotropic interactions and many different length scales. Interfaces and surfaces in such systems add further difficulties induced by the partial loss of translational symmetry. Under these circumstances it is advisable to start with simplified models.

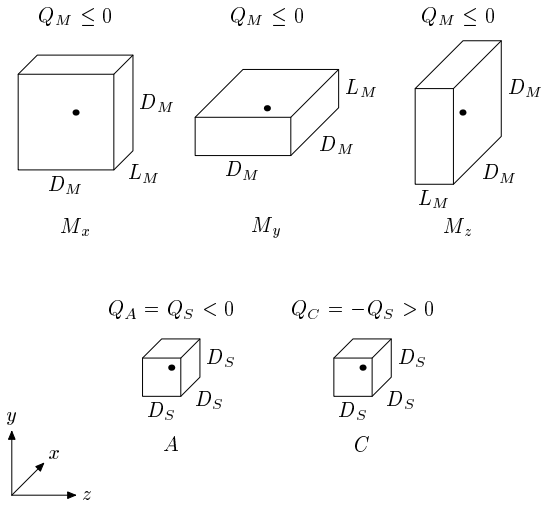


Figure 4.26: Macroions M are square cuboids of size $D_\mathrm{M} \times D_\mathrm{M} \times L_\mathrm{M}$, $D_\mathrm{M} \neq L_\mathrm{M}$ with charge $Q_\mathrm{M}$, whereas anions A and cations C are cubes of side length $D_\mathrm{S}$ with charges $Q_\mathrm{S}$ and $-Q_\mathrm{S}$, respectively. The pointlike charges (•) are localized in the centers of the cuboids. The macroions can adopt three possible orientations $\mathrm{M_x}$, $\mathrm{M_y}$, and $\mathrm{M_z}$ corresponding to the $L_\mathrm{M}$-edges being parallel to the $x$-, $y$-, and $z$-axis, respectively. (See Refs. [35, 36])

In the presented one, the particles are modeled as hard cuboids with pointlike charges concentrated in their center (see Fig. 4.26). Furthermore, the platelet orientations are restricted to three mutually perpendicular directions, which is commonly known as the Zwanzig model [492]. In Ref. [35] the density functional is constructed by functional integration of the two-particle density with respect to the interaction potential [131], which is the analogue to a Debye-charging process [91]. The two-particle density can be obtained, e.g. by interaction site model calculations [178, 180] or expressed in terms of the potential of mean force which may be approximated by effective pair potentials [380, 415, 435]. For reasons of computational advantages one can resort to an extension of the even simpler Debye-Hückel pair distribution function [91] in which the Debye screening factor is replaced by a spatially varying quantity.

Consider a ternary mixture of charged hard square cuboids with their edges required to be parallel to the Cartesian axes (Zwanzig model [492]) dissolved in a dielectric solvent (e.g. water) with dielectric constant $\varepsilon$. The solvent is treated as a continuum. For simplicity, the charges are fixed, monodisperse, and concentrated in the centers of the particles. The particles of the first component, representing the macroions M, have size $D_\mathrm{M} \times D_\mathrm{M} \times L_\mathrm{M}$, $D_\mathrm{M} \neq L_\mathrm{M}$, and charge $Q_\mathrm{M} \leq 0$. Within the Zwanzig approximation, macroions can take three different orientations, denoted as $\mathrm{M_x}$, $\mathrm{M_y}$, or $\mathrm{M_z}$ corresponding to whether the $L_\mathrm{M}$-edges are parallel to the $x$-, $y$-, or $z$-axis, respectively (see Fig. 4.26). The second component consists of salt anions A modeled as cubes of side length $D_\mathrm{A} := D_\mathrm{S}$ and charge $Q_\mathrm{A} := Q_\mathrm{S} < 0$ (see Fig. 4.26). Finally, the third component consists of salt cations C and counterions guaranteeing overall charge neutrality. They are also described by cubes with the same side length $D_\mathrm{C} := D_\mathrm{S}$ but opposite charge $Q_\mathrm{C} := -Q_\mathrm{S} > 0$ (see Fig. 4.26).

The number densities at point $\mathbf{r}$ of the centers of macroions with orientation $\mathrm{M_{x,y,z}}$, anions, and cations are denoted by $\varrho_i(\mathbf{r}), i \in \{\mathrm{M_x}, \mathrm{M_y}, \mathrm{M_z}, \mathrm{A}, \mathrm{C}\}$, respectively. Note that the position $\mathbf{r} \in V \subseteq \mathbb{R}^3$, with $V$ denoting the system volume, is a *continuous* variable

in contrast to the orientation of macroions, which varies within a *discrete* set. As an abbreviation, we introduce $\underline{\varrho}(\mathbf{r}) := (\varrho_{\mathrm{M_x}}(\mathbf{r}), \ldots, \varrho_{\mathrm{C}}(\mathbf{r}))$.

The system under consideration is coupled to two particle reservoirs: One supplies neutralised macroions (chemical formula $\mathrm{C}_k\mathrm{M}, k := \dfrac{Q_\mathrm{M}}{Q_\mathrm{S}}$) and the other neutral salt (chemical formula CA); $\mu_{\mathrm{C}_k\mathrm{M}}$ and $\mu_{\mathrm{CA}}$ denote the corresponding chemical potentials. Upon entering the solvent, these molecules dissociate:

$$\mathrm{C}_k\mathrm{M} \longrightarrow k\mathrm{C}^{Q_\mathrm{C}} + \mathrm{M}^{Q_\mathrm{M}}, \qquad \mathrm{CA} \longrightarrow \mathrm{C}^{Q_\mathrm{C}} + \mathrm{A}^{Q_\mathrm{A}}. \tag{4.91}$$

These equilibrium chemical reactions lead to the following relations between the reservoir chemical potentials ($\mu_{\mathrm{C}_k\mathrm{M}}$ and $\mu_{\mathrm{CA}}$) and the particle chemical potentials ($\mu_i, i \in \{\mathrm{M_x}, \mathrm{M_y}, \mathrm{M_z}, \mathrm{A}, \mathrm{C}\}, \mu_{\mathrm{M_x}} = \mu_{\mathrm{M_y}} = \mu_{\mathrm{M_z}}$):

$$\mu_{\mathrm{C}_k\mathrm{M}} = k\mu_\mathrm{C} + \mu_{\mathrm{M_{x,y,z}}}, \qquad \mu_{\mathrm{CA}} = \mu_\mathrm{C} + \mu_\mathrm{A}. \tag{4.92}$$

The configurations of this system are characterised by the set of number density profiles $\underline{\varrho}$. The equilibrium states minimise the grand canonical density functional [131]

$$\Omega[\underline{\varrho}] = \sum_i \int_V \mathrm{d}^3 r\, \varrho_i(\mathbf{r}) \left(\ln\left(\varrho_i(\mathbf{r})\right) - 1 - \mu_i^*\right) + F^\mathrm{ex}[\underline{\varrho}], \tag{4.93}$$

where $F^\mathrm{ex}$ is the free energy in excess over the ideal gas contribution. Here, the reduced particle chemical potentials $\mu_i^* := \mu_i - \ln\left(\Lambda_i^3\right)$ with the thermal de Broglie wavelength $\Lambda_i$ ($\Lambda_{\mathrm{M_x}} = \Lambda_{\mathrm{M_y}} = \Lambda_{\mathrm{M_z}}$) for particles of class $i$ have been introduced. With the reduced reservoir chemical potentials

$$\begin{aligned} \mu^*_{\mathrm{C}_k\mathrm{M}} &:= \mu_{\mathrm{C}_k\mathrm{M}} - \left(\ln\left(\Lambda^3_{\mathrm{M_{x,y,z}}}\right) + k\ln\left(\Lambda^3_\mathrm{C}\right)\right) \\ \mu^*_{\mathrm{CA}} &:= \mu_{\mathrm{CA}} - \left(\ln\left(\Lambda^3_\mathrm{A}\right) + \ln\left(\Lambda^3_\mathrm{C}\right)\right), \end{aligned} \tag{4.94}$$

Eq. (4.92) takes the form

$$\mu^*_{\mathrm{C}_k\mathrm{M}} = k\mu^*_\mathrm{C} + \mu^*_{\mathrm{M_{x,y,z}}}, \qquad \mu^*_{\mathrm{CA}} = \qquad\qquad \mu^*_\mathrm{C} + \mu^*_\mathrm{A}. \tag{4.95}$$

If $\underline{\varrho} = \underline{\varrho}^\mathrm{eq}$ minimises the density functional in Eq. (4.93), the grand potential $\Omega(T, V, \mu^*_{\mathrm{C}_k\mathrm{M}}, \mu^*_{\mathrm{CA}}) = -p(T, V, \mu^*_{\mathrm{C}_k\mathrm{M}}, \mu^*_{\mathrm{CA}})V$ with the osmotic pressure $p(T, V, \mu^*_{\mathrm{C}_k\mathrm{M}}, \mu^*_{\mathrm{CA}})$ equals $\Omega[\underline{\varrho}^\mathrm{eq}]$. Phase coexistence corresponds to different states with equal values of the pressure $p$, the chemical potential $\mu^*_{\mathrm{C}_k\mathrm{M}}$ of the reservoir of neutralised platelets and the chemical potential $\mu^*_{\mathrm{CA}}$ of the salt reservoir. In particular, coexistence does *not* imply equal values of the particle chemical potentials $\mu_i^*$, $i \in \{\mathrm{M_x}, \mathrm{M_y}, \mathrm{M_z}, \mathrm{A}, \mathrm{C}\}$. Rather, coexisting bulk phases give rise to a Donnan potential [2, 20, 121, 122] maintaining different chemical potentials $\mu_i^*$.

The interaction energy $U_{ij}(\mathbf{r}, \mathbf{r}')$ of a particle of class $i$ at position $\mathbf{r}$ with a particle of class $j$ at position $\mathbf{r}'$ comprises a hard-core potential $U^\mathrm{h}_{ij}(\mathbf{r}, \mathbf{r}')$, which prevents the particles from overlapping, and a contribution $U^\mathrm{c}_{ij}(\mathbf{r}, \mathbf{r}')$ due to the charges: $U = U^\mathrm{h} + U^\mathrm{c}$. No dispersion forces are considered here [209].

The interactions between the charges are approximated as [35, 36]

$$U^\mathrm{c}_{ij}(\mathbf{r}, \mathbf{r}') := \frac{Q_i Q_j}{\|\mathbf{r} - \mathbf{r}'\|_\infty}, \tag{4.96}$$

where the usual Euclidean norm $\|\mathbf{r}\|_2 = \sqrt{x^2+y^2+z^2}$ is replaced by the supremum norm $\|\mathbf{r}\|_\infty = \max(|x|,|y|,|z|)$ because of computational advantages. Since these two norms are equivalent, i.e. $\|\mathbf{r}\|_\infty \le \|\mathbf{r}\|_2 \le \sqrt{3}\,\|\mathbf{r}\|_\infty$, the results are not expected to change qualitatively due to this approximation. Furthermore, $\|\cdot\|_\infty$-spheres are cubes with their edges parallel to the Cartesian axes; therefore, the supremum norm is the most natural and adapted norm in the context of a Zwanzig model for cuboids.

According to Ref. [131], the excess free energy is given by

$$F^{\mathrm{ex}}[\underline{\varrho}] = \quad F^{\mathrm{ex,h}}[\underline{\varrho}] + \frac{1}{2}\sum_{ij}\int_V \mathrm{d}^3r \int_V \mathrm{d}^3r'\,\varrho_i(\mathbf{r})\varrho_j(\mathbf{r}')U_{ij}^{\mathrm{c}}(\mathbf{r},\mathbf{r}')\int_0^1 \mathrm{d}\eta\; g_{ij}^{(\eta)}(\mathbf{r},\mathbf{r}'), \qquad (4.97)$$

where $F^{\mathrm{ex,h}}$ is the excess free energy corresponding to the pure hard-core potential $U^{\mathrm{h}}$, and $g^{(\eta)}$ denotes the (inhomogeneous) pair distribution function for the pair potential $U^{(\eta)} := U^{\mathrm{h}} + \eta U^{\mathrm{c}}, \eta \in [0,1]$. In Ref. [35] $F^{\mathrm{ex,h}}$ is chosen as the fundamental measure functional introduced by Cuesta and Martínez-Ratón [83, 84].

As a first step in the investigation of the density functional above, bulk phase diagrams are determined for various macroion charges $Q_{\mathrm{M}}$ by solving the bulk Euler-Lagrange equations.

The macroion and the salt number densities are given by $\varrho_{\mathrm{M}} := \varrho_{\mathrm{M_x}} + \varrho_{\mathrm{M_y}} + \varrho_{\mathrm{M_z}}$ and $\varrho_{\mathrm{S}} := \varrho_{\mathrm{A}}$, respectively. In order to detect the formation of liquid crystalline phases of the macroions, the equilibrium nematic order parameter for the director oriented relative to the $z$-direction,

$$s_{\mathrm{M}} := \frac{3}{2}\frac{\varrho_{\mathrm{M_z}}}{\varrho_{\mathrm{M}}} - \frac{1}{2} \in \left[-\frac{1}{2}, 1\right], \qquad (4.98)$$

and the equilibrium biaxial order parameter,

$$q_{\mathrm{M}} := \frac{\varrho_{\mathrm{M_x}} - \varrho_{\mathrm{M_y}}}{\varrho_{\mathrm{M}}}, \qquad (4.99)$$

have been determined in Ref. [35]. The definition of $s_{\mathrm{M}}$ agrees with the well-known scalar liquid-crystal order parameter $S = \langle P_2(\cos\vartheta)\rangle = \frac{3}{2}\langle(\cos\vartheta)^2\rangle - \frac{1}{2}$ because within the Zwanzig model only macroion orientations $\mathrm{M_z}$ parallel ($\cos\vartheta = 1$) and $\mathrm{M_{x,y}}$ perpendicular ($\cos\vartheta = 0$) to the $z$-axis are possible. $s_{\mathrm{M}}$ vanishes in an isotropic phase ($\varrho_{\mathrm{M_x}} = \varrho_{\mathrm{M_y}} = \varrho_{\mathrm{M_z}}$), whereas it is positive in a nematic phase with director parallel to the $z$-axis ($\varrho_{\mathrm{M_z}} > \varrho_{\mathrm{M_x}}, \varrho_{\mathrm{M_y}}$). A discrimination of the orientation $\mathrm{M_z}$ leads to negative values of $s_{\mathrm{M}}$.

It turned out in Ref. [35] that the biaxial order parameter $q_{\mathrm{M}}$ vanishes throughout the whole inspected range of reduced chemical potentials $\mu^*_{\mathrm{C}_k\mathrm{M}}$ and $\mu^*_{\mathrm{CA}}$, whereas the nematic order parameter $s_{\mathrm{M}}$ indicates either an isotropic fluid ($s_{\mathrm{M}} = 0$) or a nematic fluid ($s_{\mathrm{M}} > 0$).

Figure 4.27 shows phase diagrams for the parameters (compare Fig. 4.26) $D_{\mathrm{M}} = 20\,\ell_B \approx 14\,\mathrm{nm}$, $L_{\mathrm{M}} = \ell_B \approx 0.72\,\mathrm{nm}$, $D_{\mathrm{S}} = \ell_B \approx 0.72\,\mathrm{nm}$, $Q_{\mathrm{S}} = -e$ with $Q_{\mathrm{M}} = 0$, $Q_{\mathrm{M}} = 0.25Q_{\mathrm{S}}$, $Q_{\mathrm{M}} = 0.5Q_{\mathrm{S}}$, $Q_{\mathrm{M}} = 0.75Q_{\mathrm{S}}$, and $Q_{\mathrm{M}} = Q_{\mathrm{S}}$ in terms of the macroion packing fraction $\eta_{\mathrm{M}} = \varrho_{\mathrm{M}} D_{\mathrm{M}}^2 L_{\mathrm{M}}$ and the salt density $\varrho_{\mathrm{S}}$. Note that the charges $Q_{\mathrm{M}}$ and $Q_{\mathrm{S}}$ have to be considered as effective ones [10] whose relation to real charges is unknown; a similar observation has been made in Ref. [299].

One isotropic phase ($I$) and one nematic phase ($N$) are found separated by first-order phase transitions. Whereas for coexisting phases $\eta_{\mathrm{M}}$ is always smaller in the isotropic phase than in the nematic phase, $\varrho_{\mathrm{S}}$ of coexisting phases is higher in the isotropic and

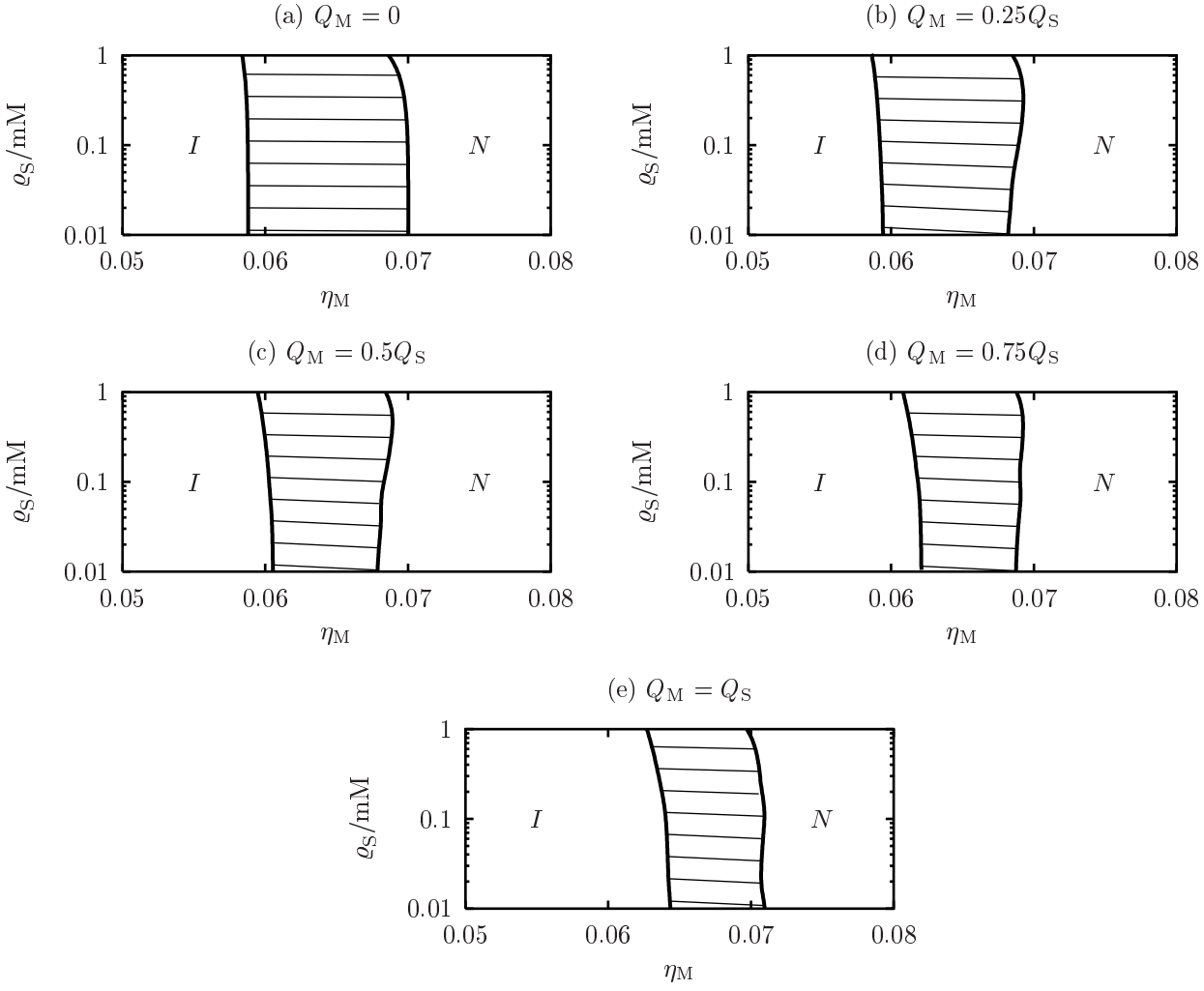


Figure 4.27: Bulk phase diagrams of mixtures of plate-like macroions ($D_M = 20\,\ell_B$, $L_M = \ell_B$) and monovalent salt ($D_S = \ell_B$, $Q_S = -e$) for macroion charges $Q_M = 0$ (a), $Q_M = 0.25Q_S$ (b), $Q_M = 0.5Q_S$ (c), $Q_M = 0.75Q_S$ (d), and $Q_M = Q_S$ (e) in terms of the platelet packing fraction $\eta_M = \varrho_M D_M^2 L_M$ and the salt density $\varrho_S$. Note that $\varrho_S = 1\,\text{mM}$ for $D_S = 0.72\,\text{nm}$ corresponds to a salt packing fraction $\varrho_S D_S^3 = 2.2 \cdot 10^{-4}$. Coexisting states are connected by (non-horizontal) tie lines. The model exhibits one isotropic ($I$) and one nematic ($N$) phase separated by first-order phase transitions. The salt density of coexisting phases is higher in the isotropic and lower in the nematic phase (Donnan effect [2, 20, 121, 122]) as can be inferred from the negative slope of the tie lines. For increasing macroion charge, the isotropic and the nematic binodals are shifted to larger macroion packing fractions $\eta_M$. With increasing salt density $\varrho_S$, the isotropic-nematic binodals for systems of charged macroions bend towards lower values of the macroion packing fraction. (See Ref. [35])

lower in the nematic phase. A similar displacement of salt from regions of large concentrations of charged macroions is known as Donnan effect [2, 20, 121, 122]. Whereas the original Donnan effect has been discovered in systems subdivided by membranes which are impermeable for macroions, here the density difference of the macroions occurs due

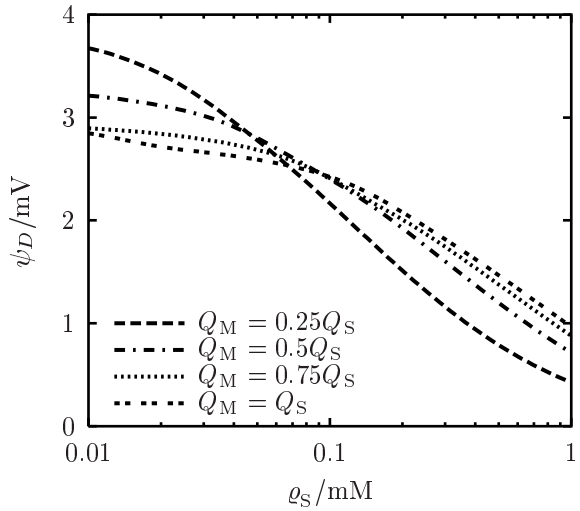


Figure 4.28: Donnan potential $\psi_D$ [2, 20, 121, 122] between the coexisting nematic ($N$) and isotropic ($I$) bulk phases in mixtures of platelike macroions and salt (see Fig. 4.27). For fixed macroion charge $Q_M$, the Donnan potential decreases with increasing salt density $\varrho_S$. For salt densities $\varrho_S \approx 0.01\,\mathrm{mM}$, $\psi_D$ decreases with increasing $|Q_M|$, whereas for salt densities $\varrho_S \approx 1\,\mathrm{mM}$, $\psi_D$ increases with increasing $|Q_M|$. (See Ref. [35])

to two coexisting bulk phases. As for the case of membrane equilibrium, here a Donnan potential $\psi_D$ maintains the density gradients between the coexisting phases. Figure 4.28 shows its dependence on the macroion charge $Q_M$ and the salt density $\varrho_S$. $\psi_D$ decreases with increasing salt density $\varrho_S$. This tendency is intuitively expected as the Donnan effect becomes more pronounced with increasing macroion charge whereas increasing the salt density gives rise to a stronger screening of the macroion charge. For fixed salt density $\varrho_S$ well below $\approx 0.1\,\mathrm{mM}$, $\psi_D$ decreases with increasing $|Q_M|$, whereas this behaviour is reversed for fixed salt density $\varrho_S$ above $\approx 0.1\,\mathrm{mM}$.

Upon an increase of the macroion charge $|Q_M|$, the isotropic and the nematic binodals are shifted to larger values of the macroion packing fraction $\eta_M$. This may be qualitatively understood by introducing the notion of an effective shape, which, in the present case, for macroions is given by a hard core surrounded by a soft $\|\cdot\|_\infty$-sphere, i.e. a cube, with its linear extension proportional to $Q_M^2$ due to the pairwise Coulomb repulsion. For small macroion charges, the effective shape is still platelike whereas for highly charged colloids, the effective shape tends towards a cube leading to a shift of the two-phase region to larger macroion packing fractions.

For fixed macroion charge as well as particle shape and increasing salt density $\varrho_S$, the isotropic-nematic binodals in Fig. 4.27 bend towards smaller macroion packing fractions. This behaviour is expected intuitively, because high ionic strength causes strong screening which in turn leads to effectively quasi-hard platelets (see Fig. 4.27(a)).

Based on the bulk properties, one is able to calculate the density profiles at the free interfaces between the coexisting isotropic and nematic phases by solving the spatially varying Euler-Lagrange equations. The density and order parameter profiles corresponding to the parameters used in Figs. 4.27 and 4.28 and to a nematic bulk salt density $\varrho_S^{(N)} = 2.2 \cdot 10^{-5} \mathrel{\widehat{=}} 0.1\,\mathrm{mM}$ are depicted in Figs. 4.29 and 4.30, respectively. The interface

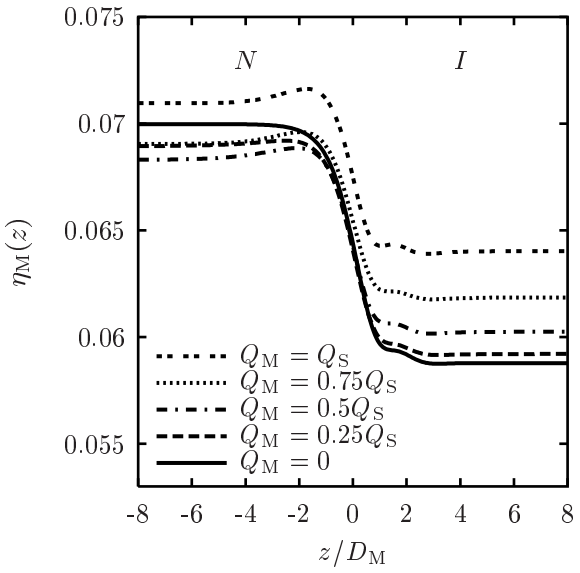


Figure 4.29: Macroion density profiles at the free interface between coexisting isotropic ($I$) and nematic ($N$) phases for the mixtures of platelike macroions and salt as studied in Fig. 4.27 at nematic bulk salt density $\varrho_S^{(N)} = 2.2 \cdot 10^{-5} \mathrel{\widehat{=}} 0.1\,\mathrm{mM}$. The interface position $z = 0$ is chosen such that $\varrho_M(0) = \frac{1}{2}\left(\varrho_M^{(I)} + \varrho_M^{(N)}\right)$. The interface width $\zeta$, inferred from the slope of the density profiles at the interface position $z = 0$ (see main text), the Debye length $\kappa^{-1}$ and the bulk correlation lengths $\xi$, inferred from the exponential decay of the density profiles, decrease monotonically with increasing macroion charge $|Q_M|$. The same behaviour is found for the interfacial tension $\gamma$. See also Fig. 4.30. (See Ref. [35])

position $z = 0$ is chosen such that $\varrho_M(0) = \frac{1}{2}\left(\varrho_M^{(I)} + \varrho_M^{(N)}\right)$.

First, and most important, the formalism described above renders stable free interfaces between coexisting bulk phases. This can be traced back to using the spatially varying screening factor $\kappa$ in the expression of $g^{(\eta)}$ in Eq. (4.97) (see also Refs. [255, 461] for alternative expressions); trials with spatially constant $\kappa$ are not successful [35].

For a given density profile $\varrho_M(z)$ (Fig. 4.29), the corresponding interface width $\zeta$ is defined as the spatial distance between the loci, where the tangent at the density profile at position $z = 0$ reaches the values of the nematic bulk density $\varrho_M^{(N)}$ and the isotropic bulk density $\varrho_M^{(I)}$, respectively. This interface width $\zeta$ decreases monotonically with increasing macroion charge from $\zeta = 1.8D_M$ for $Q_M = 0.25Q_S$ to $\zeta = 1.3D_M$ for $Q_M = Q_S$ (see Fig. 4.29). The Debye length $\kappa^{-1}$ decreases monotonically from $\kappa^{-1} = 1.5D_M$ for $Q_M = 0.25Q_S$ to $\kappa^{-1} = D_M$ for $Q_M = Q_S$. Finally, the bulk correlation lengths $\xi$ of the coexisting isotropic and nematic bulk phases, inferred from the exponential decay lengths of $\varrho_M(z) - \varrho_M^{(I,N)}$, also decrease monotonically upon increasing $|Q_M|$ and the values are by and large equal to those of $\kappa^{-1}$.

The nematic order parameter profiles $s_M(z)$ (Fig. 4.30) interpolate almost monotonically between $s_M(\infty) > 0$ in the nematic bulk phase ($N$) and $s_M(\infty) = 0$ in the isotropic bulk phase ($I$). Note that $s_M$ has been defined for a director in $z$-direction, i.e. platelets on the nematic side ($z < 0$) are preferably oriented parallel to the free interface. At a fixed position on the nematic side ($z < 0$), $s_M(z)$ decreases with increasing macroion charge

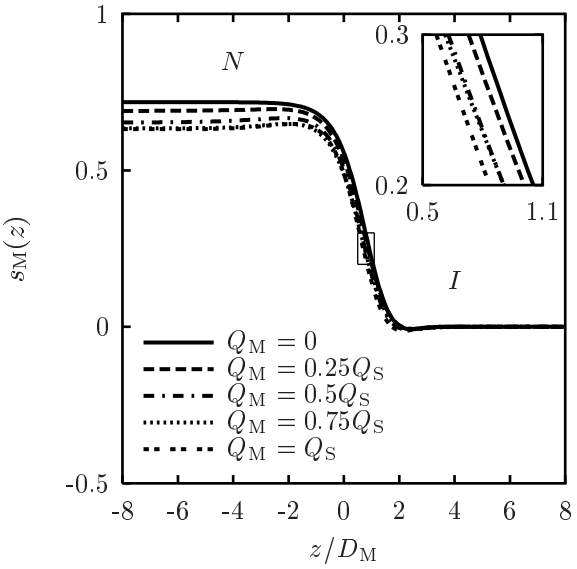


Figure 4.30: Macroion nematic order parameter profiles $s_M$ (Eq. (4.98)) at the free interface between coexisting isotropic ($I$) and nematic ($N$) phases for mixtures of platelike macroions and salt as shown in Fig. 4.27 at nematic bulk salt density $\varrho_S^{(N)} = 2.2 \cdot 10^{-5} \mathrel{\widehat{=}} 0.1\,\mathrm{mM}$. The position $z = 0$ is fixed by the choice $\varrho_M(0) = \frac{1}{2}\left(\varrho_M^{(I)} + \varrho_M^{(N)}\right)$ (see Fig. 4.29). On the nematic side of the free interface, most of the macroions lie parallel to the interface. For $z < 0$, $s_M(z)$ decreases with increasing macroion charge $|Q_M|$. The inset shows a detailed view of the steepest portions of the nematic order parameter profiles in the range $s_M(z) \in [0.2, 0.3]$ indicated by the frame. (See Ref. [35])

$|Q_M|$. This behaviour is consistent with the picture of an increasingly isotropic effective shape introduced before.

The interfacial tensions $\gamma$ of the interfaces shown in Fig. 4.29 decrease monotonically from $\gamma = 1.33 \cdot 10^{-5} \mathrel{\widehat{=}} 108\,\mathrm{nN \cdot m^{-1}}$ for $Q_M = 0.25Q_S$ to $\gamma = 6 \cdot 10^{-7} \mathrel{\widehat{=}} 5\,\mathrm{nN \cdot m^{-1}}$ for $Q_M = Q_S$, which are comparable to experimental findings for laponite suspensions [443]. The corresponding wetting parameters $\omega = (4\pi\gamma\xi^2)^{-1}$ [407] are in the range $6 \ldots 340$. If these values for $\gamma$ are indeed so small, the free isotropic-nematic interfaces are expected to be strongly affected by capillary wavelike fluctuations which are not captured by the present theory.

The charge density profiles $\varrho^Q(z) = \sum_i Q_i \varrho_i(z)$ displayed in Fig. 4.31 show deviations from local charge neutrality within the interfacial region $-4D_M \lesssim z \lesssim 4D_M$. A negative charge density occurs on the nematic side ($N$) and a positive charge density on the isotropic side ($I$). Such a local charging is necessary for the appearance of the non-vanishing Donnan potentials $\psi_D$ shown in Fig. 4.28. The full electrostatic potential profiles $\psi(z)$ are depicted in Fig. 4.32. They increase monotonically from the macroion-rich nematic phase $N$ to the macroion-poor isotropic phase $I$, maintaining the density gradients occurring in the interface region. The potential difference $\psi(\infty) - \psi(-\infty)$ equals the Donnan potential $\psi_D$ (see Fig. 4.28).

Hence, the general mechanism in ionic complex fluids of an unequal partitioning of (macro)ions at interfaces and consequently the occurrence of a Donnan potential between the coexisting bulk phases is not restricted to systems of molecular constitutents but

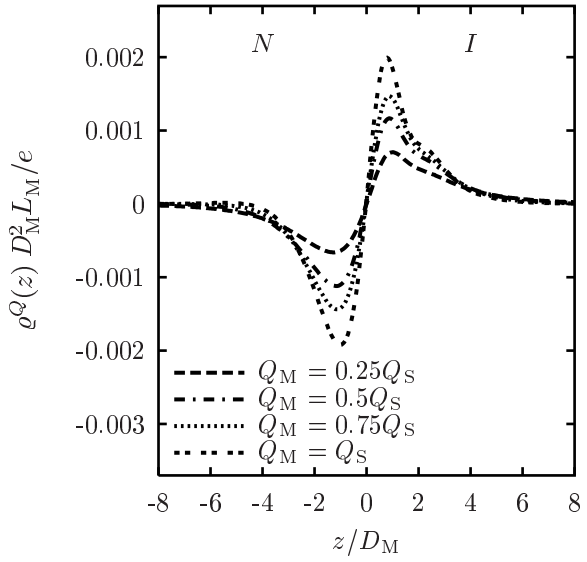


Figure 4.31: Local charge density profiles at the free isotropic-nematic interfaces shown in Figs. 4.29 and 4.30 using the same parameters and line code. Whereas *global* charge neutrality holds, deviations from *local* charge neutrality occur near the interface with a negative charge density on the nematic side ($N$) and a positive charge density on the isotropic side ($I$). The corresponding electrostatic potential profile is shown in Fig. 4.32. (See Ref. [35])

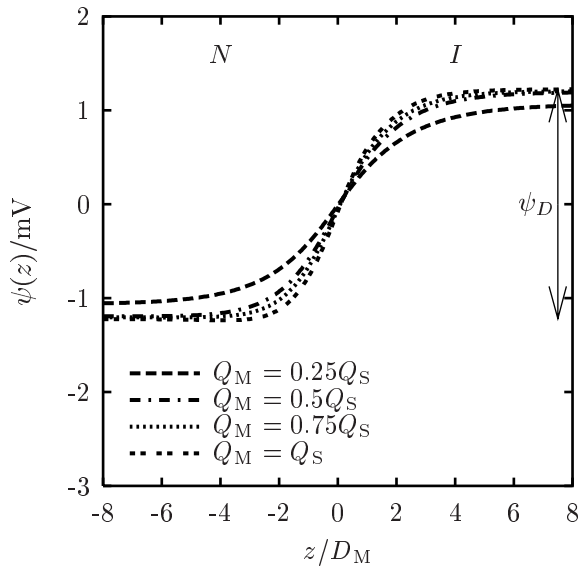


Figure 4.32: Electrostatic potential profiles at the free isotropic-nematic interfaces shown in Figs. 4.29-4.31. The potential difference between the nematic and the isotropic bulk is given by the Donnan potential $\psi_D$ displayed in Fig. 4.28; it is indicated for $Q_M = Q_S$. (See Ref. [35])

occurs equally well on colloidal length scales and between liquid crystalline phases.

In Ref. [36] the model fluid in Fig. 4.26 is studied in contact with a hard wall which

acquired charges upon releasing counterions into the fluid.

An intersting observation in Ref. [36] is an asymptotic decay of the density deviation $\Delta\varrho_i(z)$ from the bulk value *not faster* than proportional to $z^{-3}$. Moreover, it can be shown that the deviations $\Delta\varrho_i(z)$ exhibit a purely algebraic decay in leading order. Finally, one is led to the conclusion that the asymptotic Euler-Lagrange equations in conjunction with the Poisson equation leads to the properties $\Delta\varrho_i(z \to \infty) = \mathcal{O}(z^{-3})$, $\Delta\psi(z \to \infty) = \mathcal{O}(z^{-3})$, and $\varrho^Q(z \to \infty) = \mathcal{O}(z^{-5})$.

The asymptotic decay proportional to $z^{-3}$ of $\Delta\varrho_i(z)$ within the model for charged particles equals the corresponding one for systems governed by isotropic nonretarded van der Waals forces in Ref. [108]. This behaviour, which is generated by a coupling of electrostatic and steric interactions, is in sharp contrast to the results obtained within multicomponent Poisson-Boltzmann theories, where point-like ions are considered, which give rise to exponentially decaying density profiles [164].

Upon solving the Euler-Lagrange equations for mixtures of platelike macroions and monovalent salt in contact with a charged hard wall, one finds the equilibrium state of this system.

It turns out that the equilibrium states exhibit rotational symmetry with respect to the wall normal ($z$-axis), i.e. $\varrho_{M_x} = \varrho_{My}$. Therefore, the local equilibrium structure of the macroions is captured completely by the two densities $\varrho_{M_x}$ and $\varrho_{M_z}$. Equivalently, the (total) macroion density $\varrho_M := 2\varrho_{M_x} + \varrho_{M_z}$ and the nematic order parameter along the $z$-axis

$$s_M := \frac{3}{2}\frac{\varrho_{M_z}}{\varrho_M} - \frac{1}{2} \in \left[-\frac{1}{2}, 1\right] \tag{4.100}$$

may serve to identify various structures. The definition of $s_M$ coincides with the well-known scalar liquid-crystal order parameter $S = \langle P_2(\cos\vartheta)\rangle = \frac{3}{2}\langle(\cos\vartheta)^2\rangle - \frac{1}{2}$ for the special case of a Zwanzig model, within which the only possible macroion orientations are parallel ($M_z$, $\cos\vartheta = 1$) and perpendicular ($M_{x,y}$, $\cos\vartheta = 0$) to the $z$-axis. Therefore, structures with $s_M = 0$ and $s_M > 0$ are called *isotropic* and *nematic*, respectively.

Figure 4.33 displays the bulk and surface phase diagram for the surface charge density $\sigma = -0.4e/D_M^2$ in terms of the macroion charge $Q_M$ and the chemical potential difference $\Delta\mu^*_{C_kM} := \mu^*_{C_kM} - \mu^{*IN}_{C_kM}$. The solid line ($\Delta\mu^*_{C_kM} = 0$) denotes the states of bulk coexistence between the isotropic ($I$) phase and the nematic ($N$) phase, corresponding to the chemical potential $\mu^{*IN}_{C_kM}$ at coexistence. The bulk equilibrium states for $\Delta\mu^*_{C_kM} < 0$ and $\Delta\mu^*_{C_kM} > 0$ are isotropic and nematic, respectively.

At isotropic-nematic bulk coexistence with isotropic boundary conditions in the bulk ($\Delta\mu^*_{C_kM} = 0^-$), two first-order wetting transition points $W^-$ and $W^+$ have been found. The corresponding prewetting lines are so close to the coexistence line such that they could not be resolved numerically.

Complete wetting by the nematic phase occurs for approaching isotropic-nematic bulk coexistence from the isotropic side for $Q_M \in (Q_M^{W^-}, Q_M^{W^+})$. The phenomenon that only *partial* wetting is found for sufficiently large macroion charges $|Q_M|$ may be qualitatively understood as follows: The macroion number density profiles $\varrho_{M_x}$, $\varrho_{M_y}$, and $\varrho_{M_z}$ close to the surface are influenced by the hard-core interactions — which give rise to a preference of nematic order close to the wall —, the macroion-substrate Coulomb interactions proportional to $|Q_M|$, and the macroion-macroion Coulomb repulsion proportional to $|Q_M|^2$. The latter dominates for large macroion charges $|Q_M|$ leading to a depression of the values of the macroion number densities near the wall which in turn prevents the growth of a

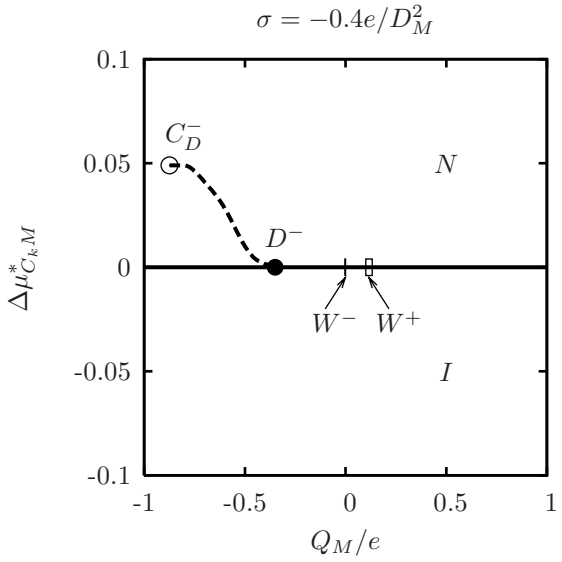


Figure 4.33: Bulk and surface phase diagram of mixtures of platelike macroions ($D_M = 20\ell_B, L_M = \ell_B$) and monovalent salt ($D_S = \ell_B, |Q_S| = e$) for salt density $\varrho_S = 0.1\,\mathrm{mM}$ in contact with a charged hard wall of surface charge density $\sigma = -0.4e/D_M^2$ in terms of macroion charge $Q_M$ and chemical potential difference $\Delta\mu^*_{C_kM}$. The bulk equilibrium states for $\Delta\mu^*_{C_kM} < 0$ and $\Delta\mu^*_{C_kM} > 0$ are isotropic ($I$) and nematic ($N$), respectively. Isotropic-nematic bulk coexistence corresponds to $\Delta\mu^*_{C_kM} = 0$ (solid line). For isotropic boundary conditions in the bulk at isotropic-nematic coexistence ($\Delta\mu^*_{C_kM} = 0^-$), two first-order wetting transition points $W^-$ (at $Q_M^{W^-} \in [-2 \times 10^{-3}e, 0]$) and $W^+$ (at $Q_M^{W^+} \in [0.1e, 0.132e]$) have been found. The tolerance intervals are indicated by frames of corresponding widths. Complete wetting by the nematic phase occurs for $Q_M \in (Q_M^{W-}, Q_M^{W+})$ upon approaching coexistence from the isotropic side. For nematic boundary conditions in the bulk at isotropic-nematic coexistence ($\Delta\mu^*_{C_kM} = 0^+$), a first-order drying transition point $D^-$ (at $Q_M^{D^-} = -0.35e$) has been found. The accompanying predrying line (dashed line) terminates at a critical point $C_D^-$ (at $Q_M^{C_D^-} = -0.87e, \Delta\mu^{*C_D^-}_{C_kM} = 0.049$). Complete drying by the isotropic phase occurs upon approaching coexistence from the nematic side for $Q_M < Q_M^{D^-}$. This implies that for $Q_M^{D^-} < Q_M < Q_M^{W^-}$ or $Q_M^{W^-} < Q_M < e$ there is neither complete wetting (by the nematic phase) nor complete drying (by the isotropic phase). A second drying transition point $D^+$ appears (not shown) for $Q_M$ sufficiently large and $\sigma$ sufficiently small so that there is reentrance of complete drying for large positive values of $Q_M$. (See Ref. [36])

nematic film. For small macroion charges $|Q_M|$, $\varrho_{M_x}$, $\varrho_{M_y}$, and $\varrho_{M_z}$ near the surface are determined by the balance between the hard-core interactions and the macroion-substrate interactions which lead to complete wetting for attractive walls.

In Fig. 4.33, a first-order drying transition point $D^-$ at $Q_M^{D^-} = -0.35e$ is found for isotropic-nematic bulk coexistence with nematic boundary conditions in the bulk ($\Delta\mu^*_{C_kM} = 0^+$). The first-order character of the drying transition at state point $D$ implies the existence of a predrying line (dashed line in Fig. 4.33), along which the excess

adsorption of macroions

$$\Gamma_M := \int_0^\infty \mathrm{d}z \, (\varrho_M(z) - \varrho_M(\infty)), \tag{4.101}$$

which is proportional to the thickness of the emerging film, exhibits a finite discontinuity. The predrying line is expected to meet the isotropic-nematic bulk coexistence line tangentially [186] and it terminates at a critical point $C_D^-$. Complete drying by the isotropic phase occurs for $Q_M < Q_M^{D^-}$ upon approaching isotropic-nematic bulk coexistence from the nematic side. As for the wetting scenario discussed above, the macroion-macroion repulsion will prevail over the macroion-surface interactions for a sufficiently large macroion charges $|Q_M|$. Therefore, for large $|Q_M|$, the formation of an isotropic film is initiated by the strongly depressed macroion number density close to the surface. Hence one expects complete drying for sufficiently large macroion charges $|Q_M|$. For a surface charge density $\sigma = -0.4e/D_M^2$ (see Fig. 4.33), *partial* drying is found for $Q_M \in (Q_M^{D^-}, e]$, i.e. the expected second drying transition point $D^+$ is located in the range $Q_M > e$. For smaller surface charge densities $\sigma$, indeed *two* drying transition points have been found within the range $Q_M \in [-e, e]$ [36].

Within the intervals $Q_M \in [Q_M^{D^-}, Q_M^{W^-}]$ and $Q_M \in [Q_M^{W^+}, Q_M^{D^+}]$ only partial wetting and drying occurs. In order to validate the topology of the bulk and surface phase diagram in Fig. 4.33, a modified version of the density functional Eq. (4.93) has been investigated in which coupling between electrostatics and particle shape has been omitted by setting $g^{(\eta)} = 1$ in Eq. (4.97). An asymptotic analysis leads to exponentially decaying profiles of $\Delta\underline{\varrho}$, $\Delta\psi$ and $\varrho^Q$. The corresponding phase diagram is qualitatively the same as in Fig. 4.33. In particular, there are also first-order wetting and drying transition points which are separated by intervals of only partial wetting *and* drying. Due to the exponentially decaying electrostatic potential, this modified model is similar to a model of hard rods interacting with an exponentially decaying wall potential [414]. Whereas Ref. [414] relied entirely on a numerical approach, which provided them only with *evidences* of first-order wetting transitions, it can be shown analytically that the wetting and drying transitions shown in Fig. 4.33 are of first order (see below).

First the wetting behaviour of the model fluid of platelike macroions and salt in contact with a charged hard wall is discussed. For a wetting scenario, the boundary conditions imposed on the solutions of the Euler-Lagrange equations require the isotropic bulk structure far from the wall. Isotropic-nematic coexistence with such boundary conditions is denoted as $\Delta\mu^*_{C_k M} = 0^-$.

The *effective interface potential* $\Omega^{\mathrm{eff}}(\zeta) := (\Omega[\underline{\varrho}_\zeta] - \Omega_b)/|A|$, where $\Omega_b$ denotes the *bulk* contribution to the grand potential and the density profiles $\underline{\varrho}_\zeta$ are the solutions of the Euler-Lagrange equations under the *constraint* of a prescribed film thickness $\zeta$ characterised by the position of the isotropic-nematic interface [107], has been determined approximately by considering the following subspace of density profiles [36, 108]:

$$\tilde{\varrho}_{i,\zeta}(z) := \begin{cases} \varrho_i^{\mathrm{wn}}(z) & , z \le \zeta/2 \\ \varrho_i^{\mathrm{ni}}(z-\zeta) & , z > \zeta/2 \end{cases}, \tag{4.102}$$

where $\underline{\varrho}^{\mathrm{wn}}(z)$ and $\underline{\varrho}^{\mathrm{ni}}(z)$ correspond to the wall-nematic and the free nematic-isotropic density profiles with the surface and the interface located at $z = 0$, respectively. Therefore, in the interval $z \in (-\infty, \zeta/2]$ the trial density profile $\underline{\tilde{\varrho}}_\zeta$ is described by the wall-nematic

profile whereas in the interval $z \in (\zeta/2, \infty)$ it is given by the free nematic-isotropic profile shifted to position $\zeta$. Due to $\varrho_i^{\mathrm{wn}}(\infty) = \varrho_i^{\mathrm{ni}}(-\infty)$, the discontinuity of $\underline{\tilde{\varrho}}_\zeta$ at $z = \zeta/2$ vanishes in the limit $\zeta \to \infty$. The transition regime around $z = \zeta/2$ does not contribute to the leading asymptotic terms of $\Omega^{\mathrm{eff}}(\zeta \to \infty)$ [108].

Substituting the trial density profiles $\underline{\tilde{\varrho}}_\zeta$ into the density functional in Eq. (4.93) and using the asymptotic behaviour of $\underline{\varrho}^{\mathrm{wn}}$ and $\underline{\varrho}^{\mathrm{ni}}$ leads to the effective interface potential [36]

$$\tilde{\Omega}^{\mathrm{eff}}(\zeta) = \gamma_{wn} + \gamma_{ni} - (\varrho_M^{\mathrm{ni}}(-\infty) - \varrho_M^{\mathrm{ni}}(\infty))\zeta\Delta\mu_M^* + a_2\zeta^{-2} + a_3\zeta^{-3} + \mathcal{O}(\zeta^{-4}) \qquad (4.103)$$

with the amplitudes $a_2$ and $a_3$ being independent of $\zeta$. Since the density profiles decay proportional to $z^{-3}$ towards the bulk values, the results of Ref. [108] can be used directly: $a_2$ depends only on the particle charges and bulk densities whereas $a_3$, in addition, contains contributions due to the wall-nematic and the free nematic-isotropic excess adsorption. The only difference between the density functional in Eq. (4.93) and the one investigated in Ref. [108] is the presence of the electrostatic term. It can be shown that it merely contributes a term $\mathcal{O}(\zeta^{-4})$ to $\tilde{\Omega}^{\mathrm{eff}}(\zeta)$ due to the more rapid asymptotic decay of the charge density $\varrho^Q(z \to \infty) = \mathcal{O}(z^{-5})$.

By inspection one recognises the *same* leading asymptotic decay of $\tilde{\Omega}^{\mathrm{eff}}(\zeta)$ in Eq. (4.103) as for systems governed by isotropic *nonretarded dispersion forces* [107, 407]. This result may appear surprising because the model does *not* include dispersion forces. The asymptotic behaviour $\sim z^{-3}$ in Eq. (4.103) is ultimately generated by the coupling of electrostatics and the steric interactions due to the cuboidal particles.

Minimising the effective interface potential $\Omega^{\mathrm{eff}}(\zeta)$ in Eq. (4.103) with respect to the interface position $\zeta$ leads to the (equilibrium) excess adsorption $\Gamma_M \sim (-\Delta\mu^*_{C_kM})^{-\frac{1}{3}} \nearrow \infty$ for $\Delta\mu^*_{C_kM} \nearrow 0$ as long as $a_2 > 0$. Evaluating the analytic expression for $a_2$ along the isotropic-nematic coexistence line, which depends only on bulk quantities (see Ref. [108]), one finds two wetting transition points — corresponding to $W^-$ and $W^+$ in Fig. 4.33 — with complete wetting, i.e. $a_2 > 0$, in between.

Figure 4.34 displays the excess adsorption $\Gamma_M$ (Eq. (4.101)) as a function of the chemical potential difference $\Delta\mu^*_{C_kM} < 0$ for fixed macroion charges $Q_M$. For $\Delta\mu^*_{C_kM} \nearrow 0$, isotropic-nematic bulk coexistence is approached along vertical thermodynamic paths in Fig. 4.33. In Fig. 4.34(a) the curves for $Q_M = 0$ and $Q_M = 0.1e$ suggest a divergence of $\Gamma_M$ in this limit, i.e. *complete wetting* of the surface by a nematic phase occurs for these macroion charges. On the other hand, for $Q_M \leq -0.01e$ the excess adsorption remains finite, i.e. *partial wetting* occurs. The complete wetting curves for $Q_M = 0$ and $Q_M = 0.1e$ in Fig. 4.34(a) exhibit *no discontinuity* in the shown range. Thus, the prewetting lines attached to the first-order wetting transition points $W^-$ and $W^+$ must be closer to the isotropic-nematic coexistence line than the numerically accessible values of $\Delta\mu^*_{C_kM}$.

Figure 4.34(b) compares the analytically obtained asymptotic behaviour for the case $Q_M = 0$ (dash-dotted line) with the corresponding numerical solution (dashed line). The differences between these curves indicate that the ultimate asymptotic regime is not yet reached within the numerically accessible range of undersaturations.

The order of the wetting transitions at state points $W^-$ and $W^+$ in Fig. 4.33 is determined by $\tilde{\Omega}^{\mathrm{eff}}(\zeta)$ for $\Delta\mu^*_{C_kM} = 0$. Critical wetting occurs for $a_2 = 0$, provided $a_3 > 0$; if $a_3 < 0$ the wetting transition is of first order and does not necessarily occur at the point given by $a_2 = 0$ [107, 108]. According to Ref. [108] the analytical expression for

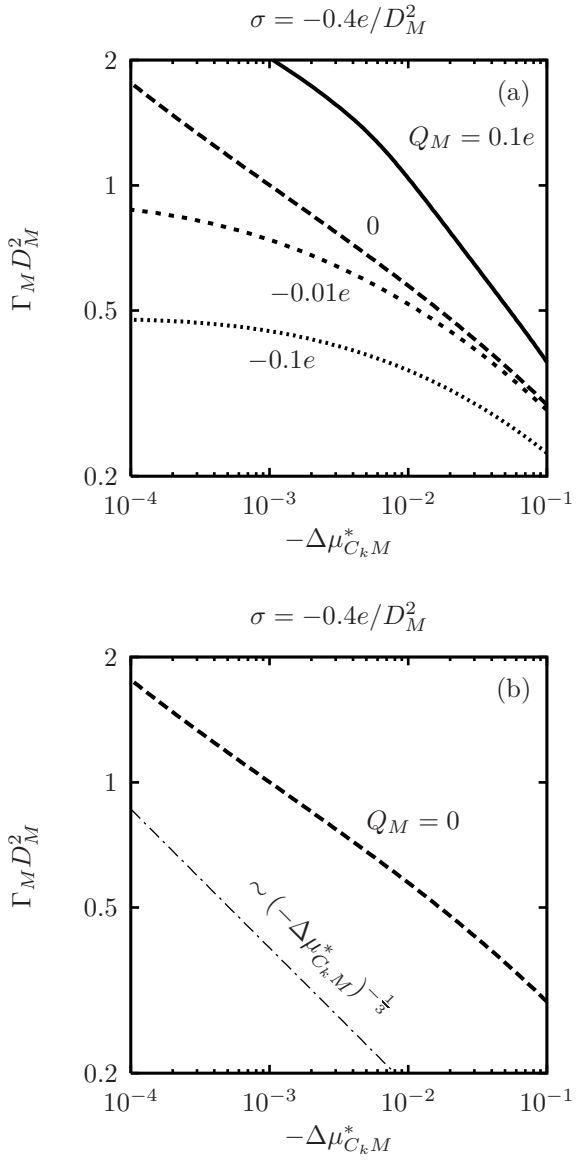


Figure 4.34: Excess adsorption $\Gamma_M$ of platelike macroions along vertical thermodynamic paths in Fig. 4.33 characterised by fixed macroion charges $Q_M$ and parameterised by the chemical potential difference $\Delta\mu^*_{C_kM} < 0$, which measures the thermodynamic distance from isotropic-nematic bulk coexistence. (a) The numerically determined excess adsorption $\Gamma_M$ remains finite upon $\Delta\mu^*_{C_kM} \nearrow 0$ for $Q_M \leq -0.01e$ (see also Fig. 4.35), whereas a divergence is suggested for the macroion charges $Q_M = 0$ and $Q_M = 0.1e$, i.e. there is complete wetting of the surface by a nematic film. (b) The comparison of the numerical solution for $Q_M = 0$ (dashed line) with the analytical asymptotic power law behaviour $\Gamma_M \sim (-\Delta\mu^*_{C_kM})^{-\frac{1}{3}}$ (dash-dotted line) (see main text) indicates that the asymptotic regime is not yet reached within the numerically accessible range of undersaturations. (See Ref. [36])

$a_3$ contains a contribution due to the wall-nematic excess adsorption, which is influenced by the surface charge density $\sigma$. Therefore, there is the possibility that the order of the

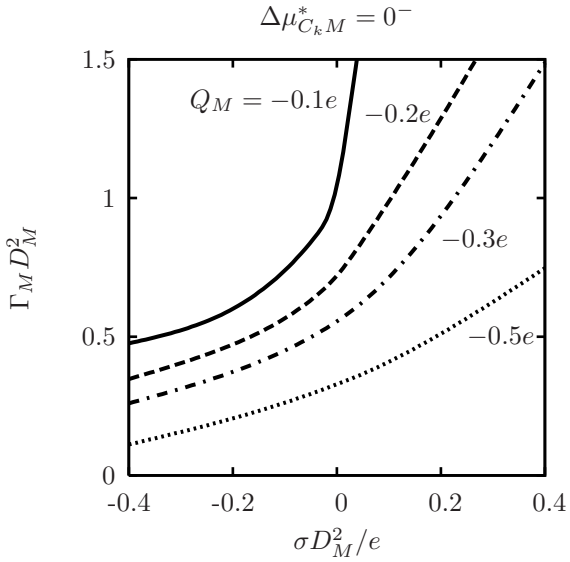


Figure 4.35: Excess adsorption $\Gamma_M$ of platelike macroions at isotropic-nematic coexistence with isotropic boundary conditions in the bulk ($\Delta\mu^*_{C_kM} = 0^-$) (see Fig. 4.33) in terms of the surface charge density $\sigma$. Curves for $Q_M = \overline{Q}_M$ and $Q_M = -\overline{Q}_M$ can be mapped upon each other by reflecting them at the axis $\sigma = 0$. For fixed macroion charge, the excess adsorption increases with increasing surface charge density. For fixed surface charge density, the excess adsorption *decreases* upon increasing $|Q_M|$, even for attractive walls. (See Ref. [36])

wetting transition depends on the surface charge density $\sigma$. For the values of $\sigma$ used in Ref. [36], however, $a_3 < 0$ has been found throughout, i.e. the wetting transitions at $W^-$ and $W^+$ are of first order.

Whereas the asymptotical analysis above is reliable with respect to the *order* of the wetting transitions at $W^-$ and $W^+$, this is not the case concerning the *location* of $W^-$ and $W^+$, because the wetting transitions are of first order [107]. Therefore, numerical methods have to be used.

In Fig. 4.35 the numerically determined excess adsorption at coexistence is shown as a function of the surface charge density $\sigma$. Without loss of generality, only curves for negative macroion charges $Q_M$ are displayed: since the density functional described is invariant under the simultaneous inversion of the signs of all charges ($Q_M$, $Q_S$, and $\sigma$), the curve for $Q_M = \overline{Q}_M$ is mapped onto the curve for $Q_M = -\overline{Q}_M$ by reflecting it at the axis $\sigma = 0$.

As expected, the excess adsorption $\Gamma_M$ of the macroions increases with increasing surface charge density $\sigma$ for fixed macroion charge $Q_M < 0$, because the surface becomes increasingly attractive (or decreasingly repulsive) for the macroions. However, for a fixed surface charge density $\sigma$ and sufficiently large macroion charges $|Q_M|$, $\Gamma_M$ decreases upon increasing $|Q_M|$, irrespective of the sign of $Q_M$, i.e. even for $\sigma Q_M < 0$, for which the wall attracts macroions. This depression of the macroion number density near the surface occurs because the macroion-macroion repulsion dominates the macroion-surface interactions. From Fig. 4.35 one can indeed infer that there is *partial* wetting for sufficiently large macroion charges $|Q_M|$.

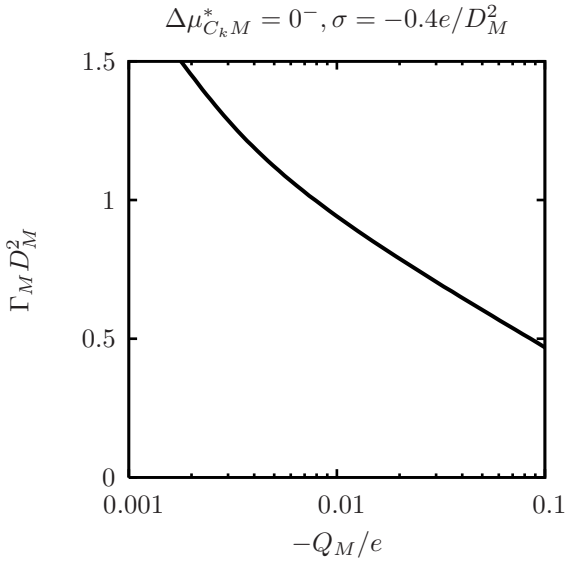


Figure 4.36: Excess adsorption $\Gamma_M$ of platelike macroions at isotropic-nematic coexistence with isotropic boundary conditions in the bulk ($\Delta\mu^*_{C_kM} = 0^-$) for a surface charge density $\sigma = -0.4e/D_M^2$ (see Fig. 4.33) as function of the macroion charge $Q_M$. It is finite within the range $-Q_M \geq 2 \times 10^{-3}e$ which implies the location of the lower wetting transition point $W^-$ (Fig. 4.33) to be within the range $Q_M \in [-2 \times 10^{-3}e, 0]$. (See Ref. [36])

The variation of the macroion excess adsorption $\Gamma_M$ upon $Q_M \nearrow 0$ along isotropic-nematic coexistence is shown in Fig. 4.36. $\Gamma_M$ is finite for $-Q_M \geq 2\times10^{-3}e$. On the other hand, $Q_M = 0$ corresponds to hard colloidal platelets for which the occurrence of complete wetting is well known [181]. Hence the lower wetting transition point $W^-$ in Fig. 4.33 is located within the range $Q_M^{W^-} \in [-2 \times 10^{-3}e, 0]$. In order to locate the upper wetting transition point $W^+$ one may use the fact that the true wetting transitions points $W^\pm$ can only be located *within* the interval $Q_M \in [-Q_M^*, Q_M^*]$, $Q_M^* = 0.1317165(5)e$, where $\pm Q_M^*$ are the locations of the wetting transition points inferred from the asymptotic analysis. This statement follows from the observation that $|Q_M| > Q_M^*$ leads to $a_2 < 0$ which renders $\zeta = \infty$ as a local *maximum* of $\Omega^{\text{eff}}(\zeta)$ [107]. Together with the numerically found complete wetting for $Q_M = 0.1e$ one concludes that the location of the upper wetting transition point $W^+$ lies within the range $Q_M^{W^+} \in [0.1e, 0.132e]$.

Finally, Fig. 4.37 displays the increase of nematic film thicknesses upon increasing $Q_M < 0$ in terms of the macroion density profiles $\varrho_M$.

Next the fluid composed of platelike macroions and salt in contact with a charged hard surface is studied for nematic boundary conditions at large distances from the wall. Isotropic-nematic coexistence with nematic boundary conditions in the bulk will be denoted as $\Delta\mu^*_{C_kM} = 0^+$.

A similar asymptotic analysis as before of the effective interface potential can be performed for drying [36]. By means of this analysis two first-order drying transition points $D^-$ and $D^+$ have been found. Due to the first-order character of the drying transitions, the loci of $D^-$ and $D^+$ have been determined numerically. Note that the upper drying transition point $D^+$ is not visible in Fig. 4.33 because it is located at $Q_M^{D^+} > e$. However, for sufficiently small surface charge densities $|\sigma|$ both drying transition points have been

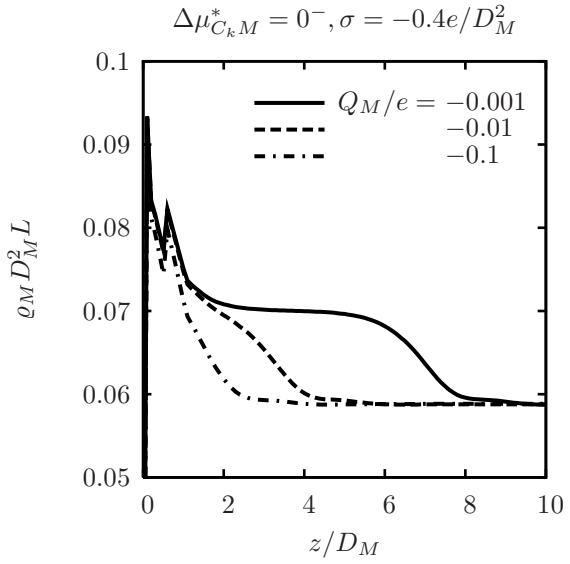


Figure 4.37: Macroion density profiles $\varrho_M$ of a mixture of platelike macroions and salt at isotropic-nematic coexistence with isotropic boundary conditions in the bulk ($\Delta\mu^*_{C_kM} = 0^-$) for a surface charge density $\sigma = -0.4e/D_M^2$ (see Fig. 4.33). Upon decreasing $|Q_M|$, i.e. upon approaching the wetting transition point $W^-$ in Fig. 4.33, a nematic-like film forms at the surface. (See Ref. [36])

found within the interval $Q_M \in [-e, e]$. In contrast to the wetting scenario above, one is able to numerically detect the discontinuity of the excess adsorption at the drying transitions. Moreover, the locations of the predrying lines in the phase diagrams (e.g. Fig. 4.33) could be numerically determined.

Figure 4.38 displays the macroion excess adsorption $\Gamma_M$ close to a charged hard wall with surface charge density $\sigma = -0.4e/D_M^2$ as a function of the macroion charge $Q_M \leq 0$. For $-0.35e = Q_M^{D^-} < Q_M \leq 0$, the excess adsorption is finite and bounded from below. It jumps to $-\infty$ at $Q_M = Q_M^{D^-}$. The *discontinuity* of $\Gamma_M$ corresponds to the occurrence of a first-order drying transition at $Q_M^{D^-}$, which is displayed as state point $D^-$ in Fig. 4.33.

A first-order drying transition is accompanied by a *predrying line* in the surface phase diagram (see the dashed line in Fig. 4.33), which connects the drying transition point $D^-$ with a critical point $C_D^-$. The predrying line may be parameterised in terms of, e.g. the macroion charge: $\Delta\mu^{*PD}_{C_kM}(Q_M)$ for $Q_M \in [Q_M^{C_D^-}, Q_M^{D^-})$ denotes the chemical potential difference $\Delta\mu^*_{C_kM}$ for which the excess adsorption $\Gamma_M$ as a function of $Q_M$ and $\Delta\mu^*_{C_kM}$ exhibits a *finite* discontinuity $\Delta\Gamma_M$.

Figure 4.39 displays this discontinuity as a function of the macroion charge $Q_M$ (solid line). It vanishes according to a power law $\Delta\Gamma_M \sim (Q_M - Q_M^{C_D^-})^\beta$ with the mean field critical exponent $\beta = \frac{1}{2}$ (dashed line). *Beyond* mean field theory, one expects an exponent $\beta = \frac{1}{8}$, corresponding to the two-dimensional Ising universality class.

Figure 4.40 depicts the formation of an isotropic film upon approaching isotropic-nematic coexistence for $\Delta\mu^*_{C_kM} > 0$ with macroion charge $Q_M = -0.6e$ and surface charge density $\sigma = -0.4e/D_M^2$. A *finite* discontinuity of the film thickness upon crossing the predrying line at $\Delta\mu^*_{C_kM} \approx 0.03$ can be inferred.

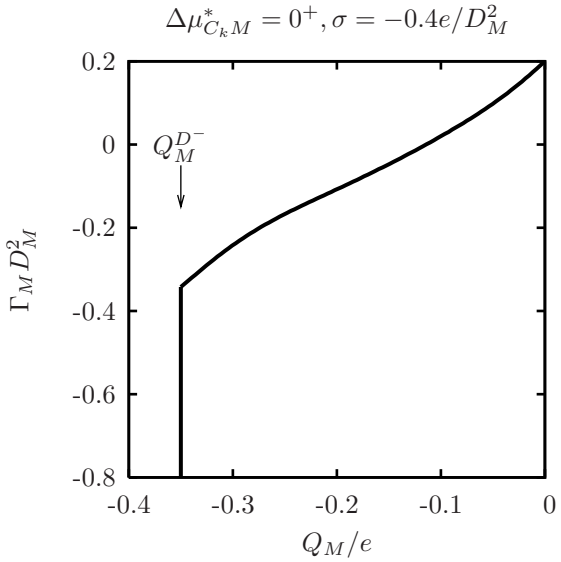


Figure 4.38: Excess adsorption $\Gamma_M$ of platelike macroions at isotropic-nematic coexistence with nematic boundary conditions ($\Delta\mu^*_{C_kM} = 0^+$) for surface charge density $\sigma = -0.4e/D_M^2$ (see Fig. 4.33) in terms of the macroion charge $Q_M$. The excess adsorption is finite and bounded from below for $Q_M > Q_M^{D^-} = -0.35e$, whereas at $Q_M = Q_M^{D^-}$ it jumps to $-\infty$. It has been verified by a comparison of surface tensions that the numerical solutions with finite excess adsorption correspond to equilibrium structures and not only to metastable states. The *discontinuity* of $\Gamma_M$ at $Q_M^{D^-}$ identifies state point $D^-$ in Fig. 4.33 as a *first-order* drying transition point. The latter conclusion can also be drawn from an asymptotic analysis of the effective interface potential (see main text). (See Ref. [36])

Figure 4.41 displays the salt ion density profile $\varrho_S$ and the counter ion density profile $\varrho_C$ for the case of macroions charge $Q_M = -0.1e$ and surface charge density $\sigma = -0.4e/D_M^2$ at isotropic-nematic bulk coexistence with nematic boundary conditions in the bulk ($\Delta\mu^*_{C_kM} = 0^+$). The positive counter ions $C$ are attracted and the negative salt ions $S$ are repelled by the negatively charged wall. This behaviour is found to be qualitatively independent of the chemical potential difference $\Delta\mu^*_{C_kM}$ and the boundary conditions (isotropic or nematic) in the bulk. Attraction and repulsion are reversed upon reversing the sign of $\sigma$. The number densities close to the charged hard wall follow from a balance between entropic contributions due to the hard cores as well as energetic contributions due to the Coulomb interaction. Hence it is not necessarily the ion species of maximal charge and minimal size which accumulates at the surface (compare the first peaks in Figs. 4.37, 4.40, and 4.41).

The rather strong variation of the salt and counter ion density profiles close to a strongly charged wall reveals limitations of the approximation of a *fixed* macroion charge $Q_M$ within the model of Refs. [35, 36] because actually macroion charges adapt according to the local electrolytic environment by means of charge regulation mechanisms. Therefore, macroion charges close to and far from a charged wall are expected to differ considerably. However, in Ref. [36] it is refrained from including a charge regulation model [56, 74, 90, 188, 191, 192, 385, 444].

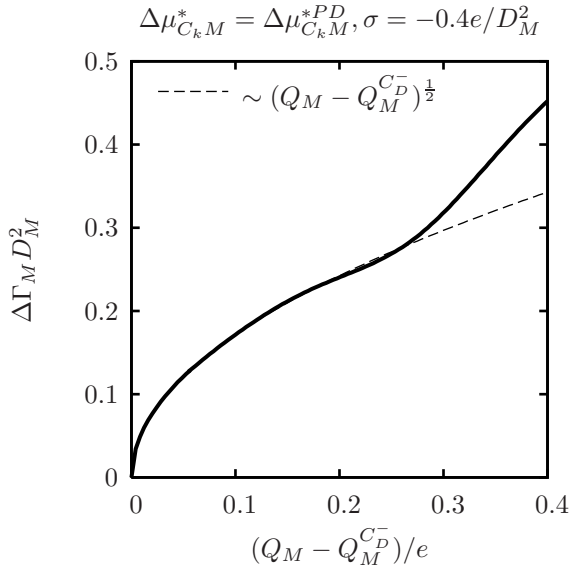


Figure 4.39: Excess adsorption discontinuity $\Delta\Gamma_M$ (solid line) of a mixture of platelike macroions and salt at the predrying line parameterized by the macroion charge $Q_M$ for a surface charge density $\sigma = -0.4e/D_M^2$ (see Fig. 4.33). The excess adsorption difference vanishes for $Q_M \searrow Q_M^{C_D^-} = -0.87e$ according to a power law $\Delta\Gamma_M \sim (Q_M - Q_M^{C_D^-})^\beta$ with the mean field critical exponent $\beta = \frac{1}{2}$ (dashed line). (See Ref. [36])

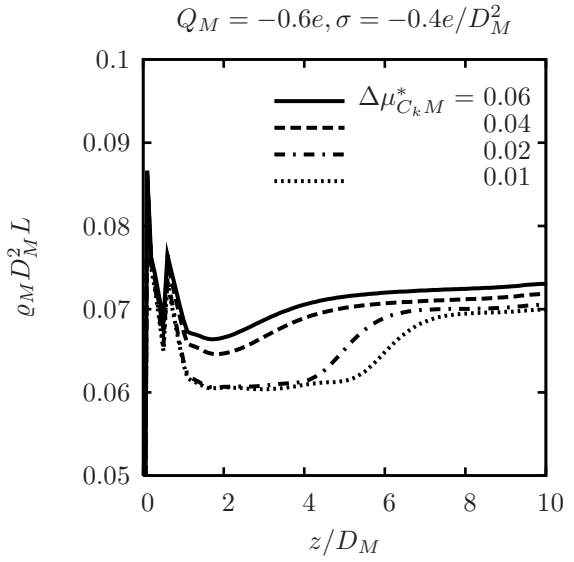


Figure 4.40: Macroion density profiles $\varrho_M$ of a mixture of platelike macroions with $Q_M = -0.6e$ and salt in contact with a surface of charge density $\sigma = -0.4e/D_M^2$ upon crossing the predrying line at $\Delta\mu^*_{C_kM} \approx 0.03$ (Fig. 4.33). At the predrying line, a quasi-isotropic film with *finite* thickness appears at the surface. (See Ref. [36])

Finally, after focussing on the fluid structure above, the electrostatic properties of the surface due to the contact with the fluid of charged particles is addressed.

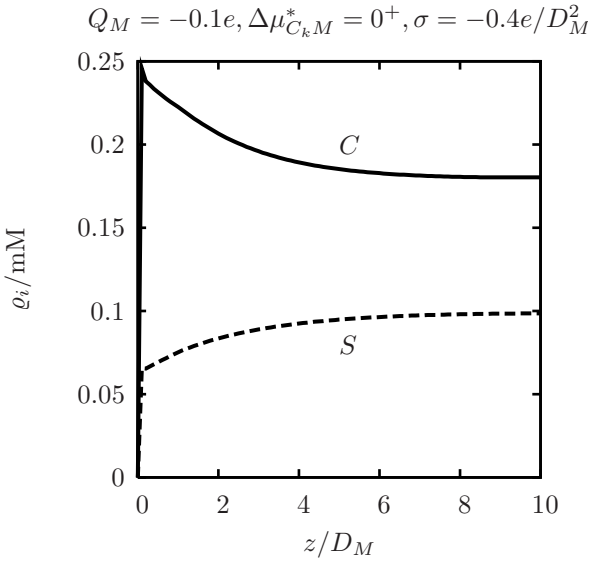


Figure 4.41: Salt ion ($S$) and counter ion ($C$) density profile in a mixture of platelike macroions with $Q_M = -0.1e$ and salt at isotropic-nematic bulk coexistence with nematic boundary conditions in the bulk ($\Delta\mu^*_{C_kM} = 0^+$) in contact with a charged substrate at $z \leq 0$ with surface charge density $\sigma = -0.4e/D_M^2$ (see Fig. 4.33). (See Ref. [36])

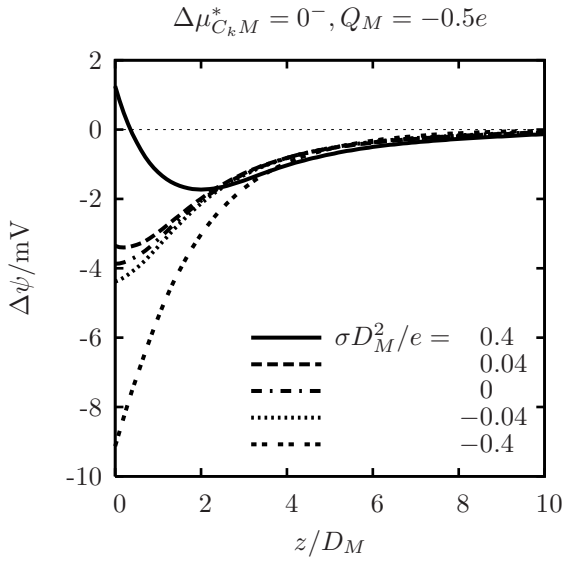


Figure 4.42: Electrostatic potential difference profiles $\Delta\psi$ relative to the electrostatic bulk potential in a mixture of platelike macroions with $Q_M = -0.5e$ and salt at isotropic-nematic bulk coexistence with isotropic boundary conditions in the bulk ($\Delta\mu^*_{C_kM} = 0^-$) (see Fig. 4.33). The slope of $\Delta\psi$ at the surface ($z = 0$) is governed by the surface charge density $\sigma$ whereas the bulk value $\Delta\psi(\infty) = 0$ is approached proportional to $z^{-3}$ from below. Hence upon increasing the surface charge, a crossover from monotonic to non-monotonic electrostatic potential profiles occurs. (See Ref. [36])

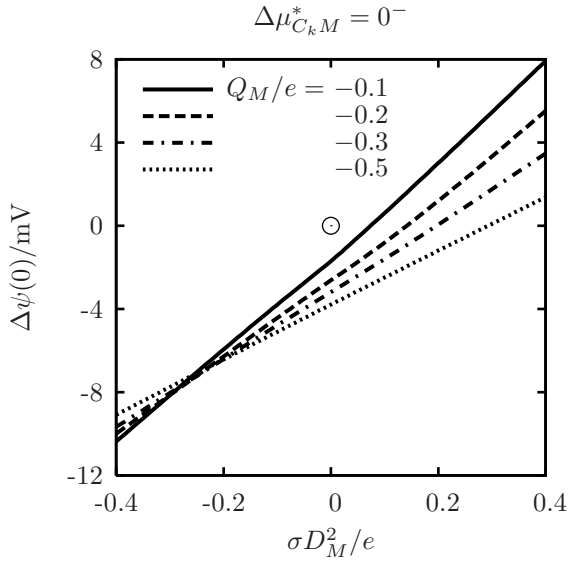


Figure 4.43: Electrostatic surface potential $\Delta\psi(0) = \psi(0) - \psi(\infty)$ as a function of the surface charge density $\sigma$ in a mixture of platelike macroions and salt at isotropic-nematic coexistence with isotropic boundary conditions in the bulk ($\Delta\mu^*_{C_kM} = 0^-$) (see Fig. 4.33). All curves are monotonically increasing but they do *not* pass through the origin ($\odot$) at ($\sigma = 0, \Delta\psi(0) = 0$) if $Q_M \neq 0$. Thus, the point of zero (surface) charge ($\sigma = 0$) does *not* coincide with the isoelectric point ($\Delta\psi(0) = 0$). Note that curves for $Q_M = \overline{Q}_M$ and $Q_M = -\overline{Q}_M$ can be mapped upon each other by reflecting them at the origin. (See Ref. [36])

The electrostatic potential profile difference $\Delta\psi(z) := \psi(z) - \psi(\infty)$ relative to the electrostatic bulk potential $\psi(\infty)$ for $Q_M = -0.5e$ at isotropic-nematic bulk coexistence with isotropic boundary conditions in the bulk ($\Delta\mu^*_{C_kM} = 0^-$) is shown in Fig. 4.42. For large distances $z$ from the surface, $\Delta\psi(z)$ decays proportional to $z^{-3}$. Upon increasing the surface charge density $\sigma$ a crossover from monotonic to non-monotonic electrostatic potential profiles occurs at $\sigma = 0$. The slope of the electrostatic potential difference at the wall is given by the surface charge density: $\Delta\psi'(0^+) = -8\sigma$. On the other hand, an electric double-layer is formed with a negatively charged layer on the nematic side and a positively charged layer on the isotropic side if a quasi-free interface between the isotropic bulk and a nematic film of finite thickness is present [35] (see Fig. 4.31). Thus $\Delta\psi$ approaches its bulk value 0 from below, i.e. $\Delta\psi'(z) > 0$ for large distances $z$ from the surface. Therefore, for $\sigma > 0$, i.e. $\Delta\psi'(0^+) < 0$, $\Delta\psi(z)$ is minimal at some finite distance $0 < z_0 < \infty$, whereas for $\sigma < 0$, i.e. $\Delta\psi'(0^+) > 0$, $\Delta\psi$ attains its minimal value at $z = 0$.

In the aforementioned case, a quasi-free isotropic-nematic interface is formed at isotropic-nematic coexistence for a state of partial wetting. Additionally, nematic films of finite thickness are present for states slightly below isotropic-nematic coexistence. Quasi-free isotropic-nematic interfaces also occur for nematic boundary conditions in the bulk close to complete drying. In the latter case, the electrostatic potential *decreases* upon approaching the bulk because $Q_M < 0$. Moreover, it has been found that the electrostatic potential is a *monotonic* function of the distance from the surface if *no* isotropic-nematic interfaces form [36].

Figure 4.43 displays the electrostatic surface potential $\Delta\psi(0)$ as a function of the surface charge density $\sigma$ at isotropic-nematic coexistence with isotropic boundary conditions in the bulk ($\Delta\mu^*_{C_kM} = 0^-$). Curves for $Q_M = \overline{Q}_M$ and $Q_M = -\overline{Q}_M$ can be mapped upon each other by reflecting them at the origin ($\odot$). As expected, the surface potential increases monotonically with the surface charge. However, the points of zero charge ($\sigma = 0$) do *not* coincide with the isoelectric points ($\Delta\psi(0) = 0$), i.e. the curves in Fig. 4.43 do *not* pass through the origin ($\odot$), in contrast to Poisson-Boltzmann theories [164]. This behaviour arises from the hard-core interaction of the particles, which leads to a depletion attraction of the larger macroions towards the wall on purely entropic grounds. Therefore, for a hard and uncharged wall ($\sigma = 0$), negatively charged macroions ($Q_M < 0$) are accumulated close to the surface leading to a negative electrostatic surface potential ($\Delta\psi(0) < 0$).

The findings of Ref. [36] show that the sign of the electrostatic surface potential $\Delta\psi(0)$ for vanishing surface charge density $\sigma = 0$ depends only on the sign of the macroion charge and not on the boundary conditions in the bulk or the chemical potential difference $\Delta\mu^*_{C_kM}$.

The discussion above shows that fluids of charged colloidal platelets and electrolyte solutions (Sec. 4.2) share many features of wetting and drying behaviour. However, in contrast to dilute electrolyte solutions, where the Debye length is larger than the ions, it is the opposite for colloidal suspensions. This reversed order of the relevant length scales leads to slight differences in the general characteristic properties of these ionic complex fluids: The properties of dilute electrolyte solutions are rather material-unspecific due to the dependence on the Debye length, whereas the properties of colloidal suspensions and RTILs (in particular ionic liquid crystals, see Sec. 2.3), are strongly dependent on the particle geometry.

## 4.6 Colloidal interactions in complex electrolyte solutions

Effective interactions among surfaces in contact with fluid media play a central role for a variety of topical fields in soft and condensed matter physics, cell biology, colloid and surface science, and nanotechnology. Since many relevant fluid media contain polar liquids such as water, their confining surfaces acquire an electric charge due to ion association or dissociation. As a result, electrostatic forces are known to contribute significantly to these effective interactions. In addition, a strong and highly temperature-sensitive solvent-mediated effective force arises upon approaching critical points of the solvent. This critical Casimir force [150, 239, 240, 408] has recently been reported for a single colloidal particle close to a wall and immersed in a binary liquid mixture near its critical demixing point [149, 189, 365]; it is expected to play also a role for the aggregation of colloidal suspensions [59, 151, 366] and to provide control of the spatial distribution of colloids in the presence of patterned substrates [152].

Motivated by previous experiments, the interplay between electrostatic and critical Casimir forces has been investigated in Ref. [42], which turns out to be responsible for rather unexpected effects in binary liquid mixtures with added salt. Colloids dispersed in such a solvent have been reported [59] to aggregate at temperatures further away from the critical demixing point as the ionic strength, i.e. the screening of the electrostatic forces, is increased. This observation has been confirmed experimentally also for a sin-

gle colloid near a wall [317]. While it was originally argued [59] that the aggregation could be completely explained in terms of a simple superposition of the critical Casimir and screened Coulomb forces (see, however, Ref. [151]), subsequent experimental results challenged this picture: An *attractive* colloid-wall interaction has been observed within a suitable temperature range even though *both* the electrostatic and the critical Casimir force are expected to be separately *repulsive* under these experimental conditions [317]. This observation posed a challenge because there was no obvious mechanism explaining the emergence of an attraction as salt is added to the solvent: Van-der-Waals attraction, which is typically rather weak already in the absence of salt [149, 189], is expected to become even weaker upon adding salt due to screening [385] and the formation of aggregates in the solvent, which might serve as depletion agents, has been ruled out experimentally [317]. All this pointed towards an important and little explored aspect of the coupling between electrostatics and the critical fluctuations of the medium. Certain features of ion-solvent coupling near critical points were investigated before, such as the possibility of a micro-heterogeneous phase [312–314] and the influence of criticality onto the solubility of ions [80, 334, 335]. The complementary point of view, i.e. the influence of ions onto the critical fluctuations of a solvent and therefore onto the critical Casimir effect offered the possibility of further insight [42].

In order to infer the mechanism responsible for the unexpected attraction mentioned above, one can derive an approximate Ginzburg-Landau-like description based on a suitable extension of standard models [29, 80, 334, 335] which, in contrast to the full original model, leads to an effective interaction potential between the confining surfaces which can be interpreted transparently [42]. It turns out that the leading correction to the simple superposition of critical Casimir and screened Coulomb forces is due to the interaction of the surface charges with electric double layers generated by the unequal partitioning of salt ions in a non-uniform solvent. Within this picture the experimental observations mentioned above can be consistently interpreted.

In Ref. [42] the model described in Sec. 2.1 is applied to an electrolyte solution in between two planar walls at distance $L$. The equilibrium profiles $\phi$, $\varrho_+$, and $\varrho_-$ minimise the approximate grand potential density functional $k_BT\Omega[\phi, \varrho_\pm]$,

$$\frac{\Omega[\phi, \varrho_\pm]}{A} = \int_0^L \mathrm{d}z \left\{ \omega_{\mathrm{sol}}(\phi(z)) + \frac{\chi(T)}{6}\phi'(z)^2 + \sum_{i=\pm} \left[ \omega_{\mathrm{ion}}^{(i)}(\varrho_i(z)) + \varrho_i(z) V_i(\phi(z)) \right] + 2\pi\ell_B D(z, [\varrho_\pm])^2 \right\} - h_0\phi(0) - h_L\phi(L). \tag{4.104}$$

While the model in Eq. (4.104) proved to be useful in certain previous investigations [29, 80, 334, 335], this form is not appropriate for understanding the influence of ion-solvent coupling on the effective wall-wall interaction potential, because its complexity precludes analytical approaches and the corresponding high-dimensional parameter space does not lend itself to numerical scans. Therefore Eq. (4.104) has been used as a starting point for systematic approximations which simplify the model and thus allows to identify the mechanism responsible for the leading order contribution of ion-solvent coupling to the effective wall-wall interaction potential. By analysing the full original model Eq. (4.104) numerically, one can verified that the approximations used do not alter the results qualitatively. Accordingly, the focus is on an approximate grand potential functional for the

solvent composition alone, which is obtained by expanding $\Omega[\phi, \varrho_\pm]$ in Eq. (4.104) in terms of the order parameter $\varphi := \phi - \phi_b$ and the ion density differences $\Delta\varrho_\pm := \varrho_\pm - I$ retaining quadratic contributions as well as terms proportional to $\varphi^3$ and $\varphi^4$ (see also Sec. 4.3). Here $\phi_b$ and $I = \varrho_{\pm b}$ denote the bulk solvent composition and the bulk ionic strength, respectively, corresponding to the chemical potentials $\mu_\phi$ and $\mu_\pm$. Similar to the Ginzburg-Landau theory for critical phenomena the expanded density functional no longer restricts the solvent composition $\phi_b+\varphi$ and the ion densities $I+\Delta\varrho_\pm$ to the ranges $[0, 1]$ and $[0, \infty)$, respectively; however, this feature of the approximate density functional is not expected to influence the resulting effective wall-wall interaction potential *qualitatively*, because the monotonicity of the profiles, which has been verified numerically for the full original model in Eq. (4.104), is preserved. The minimisation of the expanded density functional with respect to $\Delta\varrho_\pm$ leads to linear, analytically solvable Euler-Lagrange equations for $\Delta\varrho_{\pm\mathrm{eq}}(z, [\varphi])$, which are functionals of $\varphi$. Inserting these solutions into Eq. (4.104) one obtains a Ginzburg-Landau-type functional

$$\begin{aligned}\frac{\mathcal{H}[\varphi]}{A} = \int_0^L \mathrm{d}z \left\{U(z)\varphi(z) + \frac{t(T)}{2}\varphi(z)^2 + \frac{g}{24}\varphi(z)^4 + \frac{\chi(T)}{6}\varphi'(z)^2\right\} \\ - h_0\varphi(0) - h_L\varphi(L) + W(L) + \mathcal{O}((\Delta\gamma)^2)\end{aligned} \tag{4.105}$$

with the temperature-like variable $t(T) := 1/\phi_b + 1/(1-\phi_b) - 2\chi(T)$. Here it is assumed that the mixture is at its critical composition such that there is no $\varphi^3$-term. The electrostatic effects are contained in the coupling $g := 2/\phi_b^3 + 2/(1-\phi_b)^3 + 6I(\gamma_+^4 + \gamma_-^4), \gamma_\pm := V'_\pm(\phi_b)$ (see Eq. (2.3)), as well as in an "external" field generated by the surface charges $\sigma_{0,L}$ [42] (compare Eq. (4.56)):

$$\begin{aligned}U(z) := -\frac{\kappa\Delta\gamma}{2(1-\exp(-2\kappa L))}\big[(\sigma_0 + \sigma_L\exp(-\kappa L))\exp(-\kappa z) + \\ (\sigma_L + \sigma_0\exp(-\kappa L))\exp(-\kappa(L-z))\big]\end{aligned} \tag{4.106}$$

with the Debye screening length $\kappa^{-1} = (8\pi\ell_B I)^{-1/2}$ and $\Delta\gamma := \gamma_+ - \gamma_-$. The "direct", i.e. solely ion-mediated, electrostatic interaction between the walls is given by $W(L) := (4\pi\ell_B/\kappa)P(\kappa L, \sigma_0, \sigma_L)$ where

$$P(x, y_0, y_L) := \frac{2y_0y_L + (y_0^2 + y_L^2)\exp(-x)}{2\sinh(x)}. \tag{4.107}$$

The ion-solvent coupling affects the critical point only at order $\mathcal{O}((\Delta\gamma)^2)$ [43].

Upon approaching the critical point the dimensionless bulk correlation length $\xi = \widetilde{\xi}/\widetilde{a} = \sqrt{\chi(T)/(3t(T))}$, which characterises the exponential decay of the two-point correlation function, diverges. Accordingly, on the scale $\xi$, $U(z)$ is localised at the boundaries and therefore it merely modifies the surface fields $h_{0,L}$. Consequently $\mathcal{H}$ turns into a standard $\varphi^4$-theory, which describes the critical behaviour of the Ising universality class [349]. Thus, within the present model, electrostatic interactions do not affect the *universal* critical behaviour of the solvent.

The effective wall-wall interaction potential is defined by $\widetilde{\omega}(L) := \omega(L)k_BT\widetilde{a}^{-2}$ with $\omega(L) := (\mathcal{H}(L) - \mathcal{H}(\infty))/A$, where $\mathcal{H}(L)/A$ is the minimum of Eq. (4.105). In general, for the critical contribution one has $\omega(L) = \vartheta(L/\xi)/L^{d-1}$ with a universal scaling function

$\vartheta(x)$, which depends only on the relative *signs* of $h_{0,L}$ [240], with $\vartheta(x \to 0) = \text{const}$ and $\vartheta(x \to \infty) = Cx^{d-1}\exp(-x)$, where $C$ is a universal, boundary-condition-dependent constant [240].

For a sufficiently small bulk correlation length, i.e. if $\xi \ln \xi \ll L$, the term $\sim \varphi^4$ in Eq. (4.105) can be neglected relative to the term $\sim \varphi^2$. The resulting quadratic functional can be readily minimised and leads to the approximate effective wall-wall interaction [42]

$$\begin{aligned}\omega(L) = & -\frac{3\xi}{\chi(T)}P(L/\xi, h_0, h_L) + \frac{4\pi\ell_B}{\kappa}P(\kappa L, \sigma_0, \sigma_L) \\ & - \Delta\gamma\frac{3\kappa\xi^2}{\chi(T)}(Q_1(\kappa L, \kappa\xi)(h_0\sigma_L + h_L\sigma_0) + Q_2(\kappa L, \kappa\xi)(h_0\sigma_0 + h_L\sigma_L)) \\ & + \mathcal{O}((\Delta\gamma)^2)\end{aligned} \tag{4.108}$$

with the function, which is analytical for $y > 0$,

$$Q_k(x, y) := \frac{1}{y^2 - 1}\Big(\frac{y\exp(-kx/y)}{1 - \exp(-2x/y)} - \frac{\exp(-kx)}{1 - \exp(-2x)}\Big). \tag{4.109}$$

The approximate effective wall-wall interaction potential $\omega(L)$ in Eq. (4.108) has been found to agree qualitatively with that obtained numerically from the full original model in Eq. (4.104).

In Eq. (4.108) the term $\sim P(L/\xi, h_0, h_L)$ corresponds to the contribution of the surface fields to the wall-wall interaction in the absence of ion-solvent coupling ($\Delta\gamma = 0$) whereas the term $\sim P(\kappa L, \sigma_0, \sigma_L)$ is the direct electrostatic wall-wall interaction. The term $\sim (h_0\sigma_L + h_L\sigma_0)$ is the dominant correction to the effective wall-wall interaction potential, whereas the term $\sim (h_0\sigma_0 + h_L\sigma_L)$ is small. This dominant correction can be interpreted as the interaction of the electric double layer due to the unequal partitioning of ions ($\sim \Delta\gamma$) in the non-uniform order parameter close to one wall ($\sim h_{0,L}$) with the the electric double layer due to the surface charge on the *opposite* wall ($\sim \sigma_{L,0}$) (see Fig. 4.44).

The predictions of the model in Ref. [42] for two walls can be readily translated into those for the wall-sphere and sphere-sphere geometry by means of the Derjaguin approximation, which is applicable at separations much smaller than the sphere radii [385]. It turns out that assuming additivity of Casimir and screened Coulomb forces, i.e. independence of the order parameter from electrostatics, is in general insufficient to explain the experimental observations, whereas the present model, which includes ion-solvent coupling, leads to a consistent picture.

First symmetric boundary conditions, $(h_0, h_L) = (-, -)$, are considered for which the ion-solvent coupling is masked by the strong direct electrostatic repulsion. This situation has been investigated experimentally with a suspension of hydrophilic spherical colloids in a water-oil mixture [59] as well as with a single hydrophilic colloidal sphere in a similar water-oil mixture near a hydrophilic glass wall [317]. In the presence of salt aggregation [59] or strong wall-sphere attraction [317] has been observed upon approaching the critical point of the binary mixture already several Kelvin away from the critical point. Within the present model, this setting is described by $h_0 = h_L < 0$ and $\sigma_0 = \sigma_L < 0$ with the composition $\phi$ expressed as the mole fraction of the non-aqueous component. For a certain choice of parameters Fig. 4.45(a) displays the effective wall-wall interaction potential $\widetilde{\omega}(L)$. Since $\Delta\gamma \gtrless 0$ corresponds to $f_+ \gtrless f_-$, a negative ion-solvent coupling strength $\Delta\gamma < 0$ describes a salt the cations of which are slightly better soluble in oil than the anions,

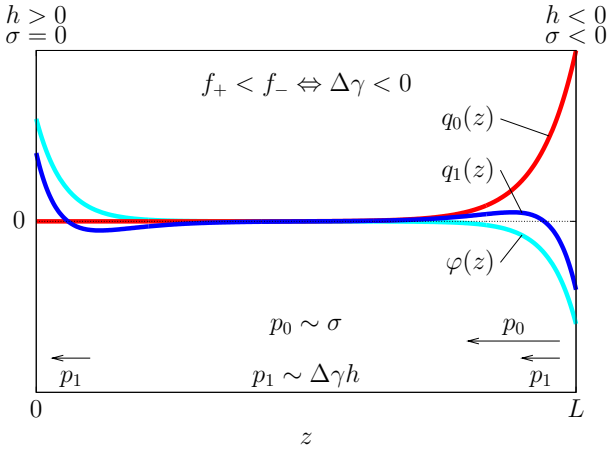


Figure 4.44: Schematic representation of the situation of an uncharged hydrophobic wall at $z = 0$ and a negatively charged hydrophilic wall at $z = L$ for $\Delta\gamma = \gamma_+ - \gamma_- < 0$, i.e. $f_+ < f_-$ (see Sec. 2.1). The curve $q_0(z)$ corresponds to the charge density which screens the surface charge of the wall. The curve $\varphi(z)$ denotes the order parameter, i.e. the deviation of the local composition $\phi(z)$ from the bulk value $\phi_b$. The non-uniformity of $\varphi(z)$ and the solubility contrast $\Delta\gamma \neq 0$ give rise to an ion partitioning with charge density $q_1(z)$. Charge density $q_0(z)$ leads to a dipolar layer of strength $p_0 \sim \sigma_L$ at the right wall, whereas $q_1(z)$ generates a dipolar layer of strength $p_1 \sim \Delta\gamma h_0$ at the left wall; the contribution of $q_1(z)$ to the dipolar strength at the right wall can be neglected as compared to the contribution of $q_0(z) \not\approx 0$. Since the directions of the dipoles are parallel and both dipolar layers are immersed in an electrolyte solution with Debye length $\kappa^{-1}$ and separated by a distance $\approx L$, an attraction occurs with strength proportional to $p_1 p_0 \exp(-\kappa L) \approx \Delta\gamma h_0 \sigma_L \exp(-\kappa L)$ (see the second line of Eq. (4.108)).

which is expected because the oils used in the experiments, 3-methylpyridine and 2,6-dimethylpyridine (2,6-lutidine), are Lewis bases [453]. The parameters used in Fig. 4.45 correspond to a critical water-2,6-lutidine mixture ($\widetilde{a} = 0.34\text{nm}, \ell_B = 2.82$) with 10mM salt ($1/\kappa = 7.73$). The value $\Delta\gamma = -0.2$ corresponds to conditions $f_- \gg f_+ = 3k_BT$, which are reasonable for Gibbs free energies of transfer [287]. Taking the renormalised surface charges $\sigma_0 = \sigma_L$ of the approximate, linearised electrostatics to be equal to the saturation value $\pm\sigma_{\text{sat}}$ corresponds to having large bare surface charges. Finally, due to the lack of a reliable microscopic theory, the values of the surface fields $h_{0,L}$ have been chosen without further analyses. It has been verified, however, that the shapes of the curves $\omega(L)$ do not change qualitatively over a wide range of choices for $h_{0,L}$. Far away from $T_c$ the effective wall-wall potential $\omega(L)$ exhibits a repulsion due to the direct electrostatic wall-wall interaction. Upon approaching $T_c$, $\omega(L)$ starts to develop an increasing attraction due to the critical Casimir effect. Since the change from repulsion to attraction occurs at $\kappa\xi \approx 1$, the attraction sets in only very close to the critical point if the ionic strength is small, whereas this change occurs already considerably far away from the critical point if the ionic strength is large. Due to the strong direct electrostatic wall-wall interaction between hydrophilic walls, the ion-solvent coupling does not qualitatively influence the effective wall-wall potential, so that the assumption of additivity of critical Casimir and screened Coulomb forces [59, 151] is justified.

The situation is different for antisymmetric boundary conditions, $(h_0, h_L) = (+, -)$, as

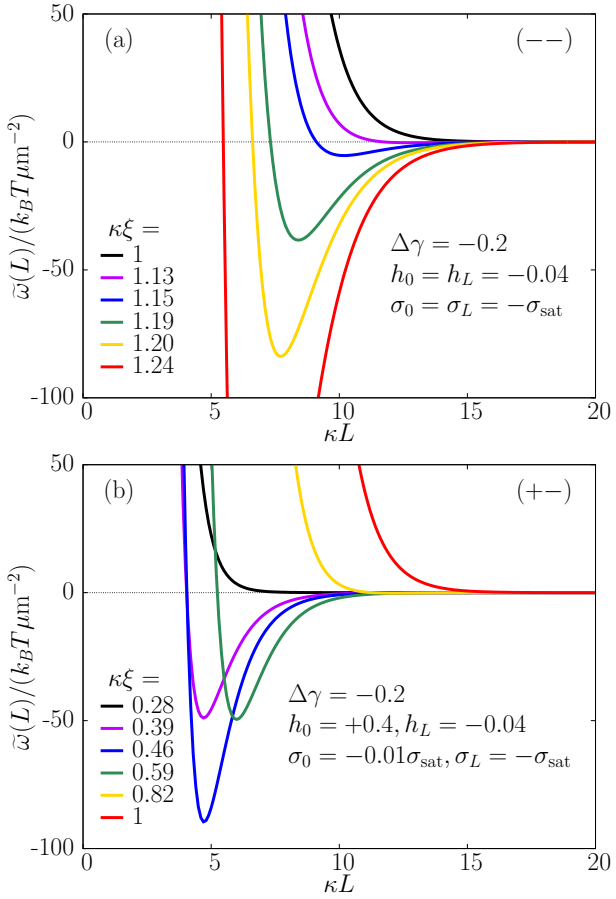


Figure 4.45: Effective wall-wall interaction potential $\widetilde{\omega}$ as a function of the scaled wall separation $\kappa L$ and the scaled bulk correlation length $\kappa\xi$ for (a) $(--)$ and (b) $(+-)$ boundary conditions; $\sigma_{\rm sat} = \kappa/(\pi\ell_B)$ is the saturation surface charge density. For symmetric $(--)$ boundary conditions $\widetilde{\omega}$ is repulsive far away from the critical point due to the direct electrostatic interaction between the like-charged walls whereas the Casimir force gives rise to an increasing attraction upon approaching the critical point. For antisymmetric $(+-)$ boundary conditions $\widetilde{\omega}$ is repulsive far away from as well as close to the critical point. Attraction ($\sim \Delta\gamma$) occurs in an intermediate temperature range due to the ion-solvent coupling induced by the difference between the solubility contrasts of cations and anions in the binary solvent. (See Ref. [42])

studied experimentally in Ref. [317] using a single hydrophilic colloid near a hydrophobic glass plate. Repulsion is observed far away from as well as close to the critical point, whereas within an intermediate temperature range a strong attraction is found. The near-critical repulsion is readily understood in terms of the critical Casimir effect for antisymmetric boundary conditions and the repulsion far away from the critical point is of electrostatic origin. However, the attraction occurring in the intermediate temperature range cannot be explained within a picture without ion-solvent coupling. Figure 4.45(b) shows $\widetilde{\omega}(L)$ for a particular choice of non-symmetric surface fields $h_0 > 0, h_L < 0$ and surface charge densities $\sigma_0, \sigma_L < 0, |\sigma_0| \ll |\sigma_L|$ corresponding to a weakly charged hydrophobic wall, in accordance with the experimentally observed trend of hydrophobic walls being weakly charged [384]. Far from ($\kappa\xi \leq 0.28$) and close to ($\kappa\xi \geq 0.82$) the

critical point $\widetilde{\omega}(L)$ is repulsive because in Eq. (4.108) the terms $\sim P$ dominate. Upon increasing $\kappa\xi$ beyond 0.28, i.e. en route towards $T_c$, attraction occurs (see $\kappa\xi = 0.39$), which for the chosen parameters is strongest around $\kappa\xi = 0.46$ and which weakens again closer to $T_c$ (see $\kappa\xi = 0.59$). This attraction is caused by the interaction of the electric double layer due to the unequal partitioning of ions ($\sim \Delta\gamma$) in the non-uniform order parameter close to the hydrophobic wall ($\sim h_0 > 0$) with the electric double layer due to the surface charge on the opposite, hydrophilic wall ($\sim \sigma_L < 0$). For the attraction to occur it is essential that the hydrophobic wall is sufficiently weakly charged ($|\sigma_0| \ll |\sigma_L|$). The same effect for symmetric boundary conditions but uncharged walls can be expected to lead to a repulsive interaction, which may stabilise colloidal dispersions [403].

Ion-solvent coupling manifests itself in yet another experiment described in Ref. [317], in which the surface preference of the solvent has been measured by surface plasmon resonance (see Sec. 4.3). It is reported that a hydrophilic surface ($h_0 < 0$) becomes less hydrophilic upon adding salt, whereas no changes have been detected for a hydrophobic surface ($h_0 > 0$). According to Eq. (4.105) the "external" field $U$ for a semi-infinite system ($L \to \infty$) acts like an additional, hydrophobic surface field $\delta h_0 = -\int_0^\infty \mathrm{d}z U(z) \exp(-z/\xi) = \Delta\gamma\sigma_0\kappa\xi/(2(1+\kappa\xi)) > 0$ if $\Delta\gamma, \sigma_0 < 0$. A hydrophilic surface becomes less hydrophilic by adding salt or for $T \to T_c$, whereas a hydrophobic surface is influenced only weakly as $|\sigma_0|$ is small.

This analysis demonstrates, as for critical adsorption in Sec. 4.3, that even though electrolytes do not alter the universal critical behaviour of polar solvents close to their critical point, the ion-solvent coupling is relevant further away, provided the direct electrostatic interaction is sufficiently weak. The crossover from an electrostatics- to a critical Casimir-dominated behaviour is expected to occur near that temperature at which the bulk correlation length becomes comparable with the Debye screening length. The analysis makes it transparent how the coupling of critical phenomena and electrostatics can generate counter-intuitive effects without violating the asymptotic universal behaviour.

A conceivable alternative mechanism for the emergence of an effective attraction in the case of antisymmetric boundary conditions has been proposed which is independent of differences in the solubility of cations and anions [364]. It has been argued within RPA that a charged wall (of either polarity) accumulates an increased number of ions compared to an uncharged wall. Due to this enhanced total density of ions (which are hydrophilic independent of their sign) a charged wall should, from a distance, appear increasingly hydrophilic upon adding salt such that for certain system parameters an underlying actually hydrophobic character of a wall might be overcompensated and turn into an effectively hydrophilic wall; actually hydrophilic walls remain so upon adding salt [364]. Such a salt-induced apparent hydrophilicity, which would occur on the surfaces of all dissolved colloids, would in turn lead to effectively symmetric boundary conditions and thus to attractive solvation forces. However, according to Fig. 4.22, even in the presence of salt the excess adsorption follows the actual preference of the surface field, also upon approaching $T_c$. Thus, within LDA Eq. (2.3), salt-induced apparent hydrophilicity does not occur (i.e. $\Gamma$ does not become negative). Therefore there is reason to expect that salt-induced apparent hydrophilicity is an artifact of the BCA and the RPA. In addition, by means of surface plasmon resonance it has been checked experimentally that the adsorption preference, in particularly of hydrophobic substrates, is not altered by adding salt [317]. Therefore, for antisymmetric boundary conditions of the order parameter, there are doubts that salt-induced apparent hydrophilicity can serve as an

explanation for the experimentally observed effective attraction within an intermediate temperature range.

Additional numerical studies within BCA have been performed suggesting that ion-induced "precipitation" [328] or non-linearities [402] influence the effective colloid-colloid interaction. However, the results of Ref. [43] concerning the reliability of BCA point towards the possibility that those proposed effects are artifacts of the BCA due to an overestimation of the ion-solvent coupling.

## 4.7 Colloids at electrolytic interfaces

Colloidal particles, trapped at fluid interfaces by adsorption energies much larger than the thermal energy, can form effectively two-dimensional colloidal monolayers [357]. During the last two decades these systems have received significant attention both in basic research as well as in applied sciences. On one hand, these monolayers serve as model systems for studying effective interactions, phase behaviour, structures, and the dynamics of condensed matter in reduced dimensionality [77, 113, 130, 213, 274, 285, 460]. On the other hand, self-assembled colloidal monolayers find applications in optical devices, molecular electronics, emulsion stabilization processes, and as templates in the fabrication of new micro- and nanostructured materials. Therefore, a reliable description of the lateral inter-particle interaction at all distances $r$, which governs the structure formation of colloids at fluid interfaces, is of primary importance.

In his pioneering work Pieranski [357] showed that the electrostatic *repulsion* of charged colloids at such interfaces is dominated by a long-ranged dipole-dipole interaction, due to an asymmetric counterion distribution in the two adjacent media, in addition to the screened Coulomb interaction also present in bulk systems. Later both the power-law and the exponential contributions have been calculated within the framework of linearized Poisson-Boltzmann theory assuming point-like particles [199]. It turned out that, whereas the interaction energy for charged particles always decays asymptotically $\sim 1/r^3$, the prefactor depends on whether the interaction originates from charges on the polar [344, 357] or on the apolar [16, 17] side of the fluid interface. In addition there are experimental indications of an *attractive* long-ranged lateral interaction which cannot be interpreted in terms of a van der Waals force [323, 418]. Attempts were made to explain it in terms of a deformation-induced capillary interaction, but a complete and final picture has not yet been reached [142, 325, 326, 480]. In Ref. [283] the focus is on the electrostatic contribution to the interaction.

Whereas Pieranski's work has been extended in numerous directions, almost all subsequent studies have discussed exclusively the case of colloidal particles being far away from each other. In this asymptotic limit the superposition approximation has been assumed to be reliable, according to which one approximates the actual electrostatic potential (or interfacial deformation) for a pair of particles by the sum of the potentials (or deformations) of the two single particles. However, for a dense system or during aggregation, particles can come close to each other such that this superposition approximation is no longer justified. For the deformation induced attractive part of the interaction, the validity of this approximation has been discussed for both large [117, 325, 480] and small [187] separations. For the repulsive electrostatic interaction, an investigation of small-distance deviations from the superposition approximation have been reported for the first time in

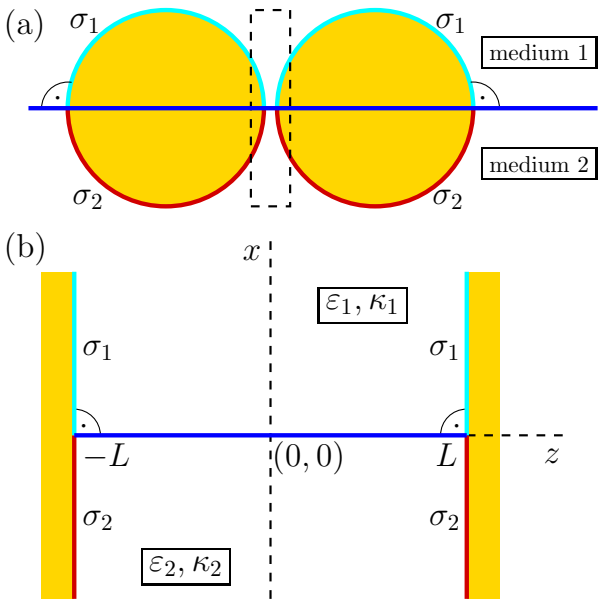


Figure 4.46: (a) Cross section of two identical spherical particles trapped at a fluid interface (horizontal blue line) close to each other and with contact angle 90°. (b) Magnified view of the boxed region in (a). The two adjacent fluids ("1", located at $x > 0$, and "2", located at $x < 0$) forming the interface have permittivities $\varepsilon_1$, $\varepsilon_2$ and inverse Debye lengths $\kappa_1$, $\kappa_2$, respectively. Since the surface-to-surface distance between the particles is small compared to their radii, the particle surfaces can be approximated by planes located at $z = \pm L$ which carry charge densities $\sigma_1$ and $\sigma_2$ at the surfaces in contact with fluid "1" and "2", respectively. According to the model the fluid structures vary steplike at the surfaces and at the interface. (See Ref. [283])

Ref. [283], although a systematic multipole expansion of the electrostatic potential around a single inhomogeneously charged particle trapped at an interface has been worked out before [118].

Considering a simplified problem allows one to assess the quality of the superposition approximation for the electrostatic interaction between two colloidal particles floating close to each other at an electrolyte interface (see Fig. 4.46) which offers the possibility to obtain exact analytic expressions [283]. Accordingly, first, the interface is assumed to be planar, i.e. no deformations of the fluid interface are considered, which are typically of the order of nanometers for micron-sized particles [251, 323, 418]. Second, due to the small particle-particle distances to be studied, the curvature of the colloidal particles is ignored in the spirit of a Derjaguin approximation [209, 385] by considering the effective interaction between two charged, planar, and parallel walls. Third, a liquid-particle contact angle of 90° is assumed; this value is encountered for actual systems [291]. An exact analytic expression for the electrostatic potential of this model has been derived in Ref. [283] within linearised Poisson-Boltzmann theory, which is then used to calculate the surface interaction energies per total surface area and the line interaction energy per total length of the two three-phase contact lines (Fig. 4.46). The main result is the observation of significant deviations between the exact values of these quantities and those obtained within the superposition approximation, both at small and even at large distances (see Figs. 4.48 and 4.49).

In Ref. [283] a three-dimensional Cartesian coordinate system is considered such that two charged planar walls, which mimic the colloidal particles, are located at $z = \pm L$ and the fluid interface is at $x = 0$ (Fig. 4.46(b)). The electrolyte solution present at $x > 0$ ($x < 0$) is denoted as medium "1" ("2"). For simplicity only binary monovalent electrolytes are considered. Generically the ions and the molecules are coupled such that the molecular and ion number densities vary on the scale of the bulk correlation length which is much smaller than the Debye length which sets the length scale for the variation of the charge density [43] (see Sec. 4.3). Thus the number densities in both media vary only close to the walls or to the fluid interface at distances of the order of the bulk correlation length, which, away from critical points, is of the order of the size of the fluid molecules and of the ions and falls below the length scale to be considered here. Accordingly, the permittivity $\varepsilon_1$ ($\varepsilon_2$) and the inverse Debye length $\kappa_1$ ($\kappa_2$) in medium "1" ("2") are uniform where $\kappa_i = (2I_i e^2/(\varepsilon_i k_B T))^{1/2}$, $i \in \{1, 2\}$, with bulk ionic strength $I_i$ (which is the bulk number density of each ionic species in medium $i$), Boltzmann constant $k_B$, temperature $T$, and elementary charge $e > 0$. The two walls are assumed to be chemically identical such that the surface charge densities at both half-planes in contact with medium "1" ("2") are given by $\sigma_1$ ($\sigma_2$). The local charge density of the ions is *not* uniform in media "1" or "2" because this quantity varies on the scale of the Debye lengths, which are typically much larger than molecular sizes. Since the slab formed by the two walls at $z = \pm L$ is a model of the space in between two colloidal particles trapped at the fluid interface, it is appropriate to describe the ions within a grand canonical ensemble, the reservoirs of which are given by the bulk electrolyte solutions far away from the fluid interface. Within a simple density functional theory, which (i) considers uniform solvents in the upper and the lower half space, (ii) assumes low ionic strength in the bulk (which facilitates the description of the ions as point-like particles), and (iii) describes deviations of the ion densities from the bulk ionic strengths only up to quadratic order, one derives the linearized Poisson-Boltzmann (PB) equation $(\Delta - \kappa_i^2)\Phi_i = 0$ to be fulfilled by the electrostatic potential $\Phi_i(x, z)$ in medium $i \in \{1, 2\}$. The corresponding boundary conditions are: (i) the electrostatic potential should remain finite for $x \to \pm\infty$, (ii) the electrostatic potential and the normal component of the electric displacement field at the fluid interface should be continuous, i.e. $\Phi_1(x = 0^+, z) = \Phi_2(x = 0^-, z)$ and $\varepsilon_1 \partial_x \Phi_1(x = 0^+, z) = \varepsilon_2 \partial_x \Phi_2(x = 0^-, z)$, and (iii) due to global charge neutrality the normal component of electric displacement field at the walls correspond to the surface charge densities, i.e. $\varepsilon_i \partial_z \Phi_i(x, z = \pm L) = \pm\sigma_i$. It is important to note that in this model the fluids are confined to the space between the two walls such that outside the fluid slab the electric field vanishes.

In order to determine the electrostatic potential one can split the whole problem into three sub-problems [283]: (i) only the fluid interface is present in the absence of any walls, (ii) two charged walls with homogeneous surface charge densities $\sigma_1$ and the uniform medium "1" in between, and (iii) two charged walls with homogeneous surface charge densities $\sigma_2$ and the uniform medium "2" in between. By adding the solution of problem (ii) and the solution of problem (i) for the upper half-space and by adding the solution of problem (iii) and the solution of problem (i) for the lower half-space, one obtains potentials in the two media which satisfy all the boundary conditions listed above except the continuity of the potential at the interface. In order to fulfill also the latter one, one can construct a correction function which (i) is a solution of the linearized PB equation, (ii) keeps all boundary conditions unchanged which are already satisfied, and (iii) leads to continuity of the potential at the interface [283]. This can be achieved by means of 2D

Fourier transform or Fourier series expansions [420]. The final expression for the *e*xact electrostatic potential (denoted by superscript "e") reads [283]

$$\Phi_i^e(x,z) = \Phi_{bi} + \sum_{j\in\{1,2\}}^{j\neq i} \frac{(-1)^j \kappa_j \varepsilon_j \Phi_D}{\kappa_1\varepsilon_1 + \kappa_2\varepsilon_2} e^{-\kappa_i|x|} + \Phi_i^{(0)} \frac{\cosh(\kappa_i z)}{\sinh(\kappa_i L)} + \sum_{j\in\{1,2\}}^{j\neq i} \frac{C_{ij}^{(0)}(L) e^{-a_i^{(0)}(L)|x|}}{2} + \sum_{j\in\{1,2\}}^{j\neq i} \sum_{n=1}^{\infty} C_{ij}^{(n)}(L) e^{-a_i^{(n)}(L)|x|} \cos\left(\frac{n\pi z}{L}\right), \quad (4.110)$$

where the explicit dependences of $\Phi_i^{(0)}$, $a_i^{(n)}(L)$ and $C_{ij}^{(n)}(L)$ on $n$, $L$, and the type of media $i$ and $j$ are given in Ref. [283]. The electrostatic bulk potential $\Phi_{bi}$ is defined as $\Phi_{b1} = 0$ and $\Phi_{b2} = \Phi_D$, with the Donnan potential (or Galvani potential difference [2, 20, 121, 122]) $\Phi_D$ between medium "2" and medium "1", which originates from the differences of the solubilities of the ions in the two media [37].

The first two terms on the right-hand side of Eq. (4.110) together represent the effect of the fluid interface in the absence of walls (sub-problem (i)) which corresponds to the limit $L \to \infty$ at any fixed position $z$. The third term describes the electrostatic potential of two uniformly and equally charged walls in the presence of a uniform electrolyte solution in between (sub-problem (ii) or (iii)). According to Eq. (4.110), up to the constant $\Phi_{bi}$, $\Phi_i^e(x,z)$ reduces to the third term in the limit $|x| \to \infty$, i.e. far away from the fluid interface. The fourth and the fifth term in Eq. (4.110) correspond to the correction function which describes the contact of the walls with the fluid interface. Due to the symmetry of the problem, $\Phi_i(x,z)$ has to be an even function of $z$, and $\Phi_2(-\infty,z) - \Phi_1(\infty,z) = \Phi_D$ for any fixed position $z$ in the limit of large wall separations $L \to \infty$. $\Phi_i^e(x,z)$ exhibits these properties.

By adding the electrostatic potentials of two single walls, each in contact with the fluid interface in a semi-infinite geometry with respect to $z$, one obtains the superposition approximation (denoted by superscript "$s$") [283]

$$\Phi_i^s(x,z) = 2\Phi_{bi} + \sum_{j\in\{1,2\}}^{j\neq i} \frac{2(-1)^j \kappa_j \varepsilon_j \Phi_D}{\kappa_1\varepsilon_1 + \kappa_2\varepsilon_2} e^{-\kappa_i|x|} + 2\Phi_i^{(0)} \cosh(\kappa_i z) e^{-\kappa_i L} + \sum_{j\in\{1,2\}}^{j\neq i} \int_0^\infty dq\; C_{ij}^s(q) \cos(qL) \cos(qz) e^{-\sqrt{q^2+\kappa_i^2}|x|}. \quad (4.111)$$

The explicit expression for $C_{ij}^s(q)$ is given in Ref. [283]. A comparison between the exact electrostatic potential $\Phi_i^e(x,z)$ and the superposition approximation $\Phi_i^s(x,z)$ at the plane of interface ($x = 0$) is displayed in Fig. 4.47. Moreover, $\Phi_i^s(x,z)$ does not satisfy the boundary condition which relates the electric displacement field at the walls to the surface charge densities and $\Phi_2^s(-\infty,z) - \Phi_1^s(\infty,z) \neq \Phi_D$ for any fixed position $z$ in the limit of large wall separations $L \to \infty$.

With the electrostatic potential given, the corresponding grand canonical potential can also be determined both exactly as well as within the superposition approximation. After subtracting the bulk free energy, the surface and interfacial tensions and the line tension contributions from the grand potential one obtains the $L$-dependent part of the grand potential,

$$\Delta\Omega(L) = A_1\omega_{\gamma,1}(L) + A_2\omega_{\gamma,2}(L) + \ell\omega_\tau(L), \quad (4.112)$$

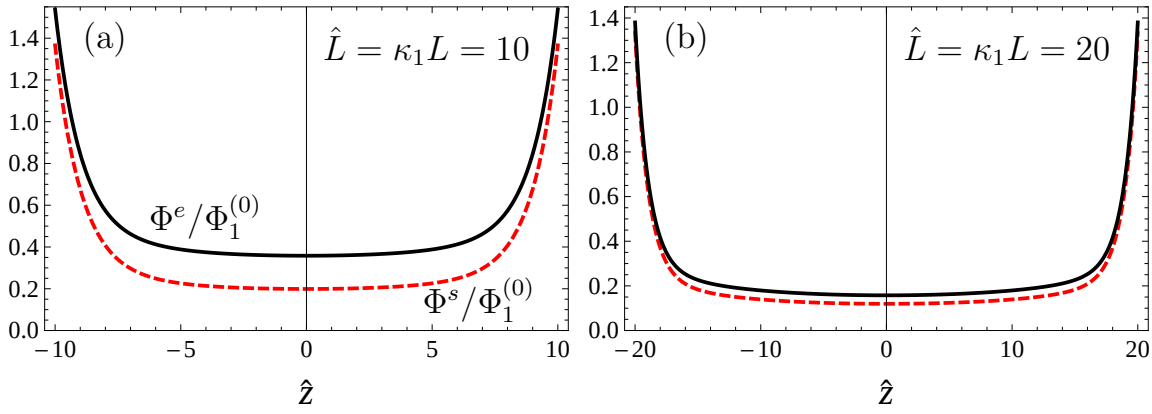


Figure 4.47: Comparison between the exact expression (superscript "e", black solid lines, see Eq. (4.110)) and the superposition approximation (superscript "s", red dashed lines, see Eq. (4.111)) of the electrostatic potential $\Phi(x,z)$ at the interfacial plane ($x = 0$) in units of $\Phi_1^{(0)} = \sigma_1/(\kappa_1\varepsilon_1)$ for varying $\hat{z} = \kappa_1 z$ and two slit widths: $\hat{L} = \kappa_1 L = 10$ (panel (a)) and $\hat{L} = \kappa_1 L = 20$ (panel (b)). For the plots typical parameter ratios $\kappa = \kappa_2/\kappa_1 = 0.025$, $\varepsilon = \varepsilon_2/\varepsilon_1 = 0.025$, $\sigma = \sigma_2/\sigma_1 = 0.1$, and $\Phi_D/\Phi_1^{(0)} = 1.3$ have been chosen. $\Phi^e$ and $\Phi^s$ differ significantly at narrow widths $L$, and the difference between the two expressions decreases upon increasing the slit width. In the limit $\hat{z} \to \pm\hat{L}$, both $\Phi^e$ and $\Phi^s$ remain finite. (See Ref. [283])

for the walls being a distance $2L$ apart, where $A_1$ and $A_2$ are the total areas of the two walls in contact with medium "1" and "2", respectively, and $\ell$ is the total length of the three-phase contact lines formed by medium "1", medium "2" and the walls; by construction $\Delta\Omega(L \to \infty) \to 0$. The surface interaction energy per total surface area $A_i$ ($\omega_{\gamma,i}$) in contact with medium $i \in \{1,2\}$ is exactly (superscript "e") given by [283]

$$\omega_{\gamma,i}^e(L) = \frac{\sigma_i^2}{2\kappa_i\varepsilon_i}\left(\coth(\kappa_i L) - 1\right), \tag{4.113}$$

and within the superposition approximation (superscript "s") by [283]

$$\omega_{\gamma,i}^s(L) = \frac{\sigma_i^2}{2\kappa_i\varepsilon_i}\left(2e^{-\kappa_i L}\cosh(\kappa_i L) - 1\right). \tag{4.114}$$

According to Eqs. (4.113) and (4.114), varying $\sigma_i$ and $\varepsilon_i$ influences only the amplitude of $\omega_{\gamma,i}$ whereas its decay rate is solely determined by $\kappa_i$. For large wall separations one has $\omega_{\gamma,i}^e(\kappa_i L \gg 1) \simeq \frac{\sigma_i^2}{\kappa_i\varepsilon_i}e^{-2\kappa_i L}$ and $\omega_{\gamma,i}^s(\kappa_i L \gg 1) \simeq \frac{\sigma_i^2}{2\kappa_i\varepsilon_i}e^{-2\kappa_i L}$, i.e. the superposition approximation correctly predicts the exponential decay in the large distance limit but, in contrast to common expectations, the corresponding prefactor is too small by a factor of 2. Moreover, the superposition approximation is qualitatively wrong for small wall separations (but still large on the molecular scale), because the exact surface interaction potential diverges in this limit as $\omega_{\gamma,i}^e(\kappa_i L \ll 1) = \frac{\sigma_i^2}{2\kappa_i\varepsilon_i}\left[\frac{1}{\kappa_i L} - 1 + \frac{\kappa_i L}{3} + \mathcal{O}((\kappa_i L)^3)\right]$, whereas the superposition approximation stays finite: $\omega_{\gamma,i}^s(\kappa_i L \ll 1) = \frac{\sigma_i^2}{2\kappa_i\varepsilon_i}\left[1 - 2\kappa_i L + \mathcal{O}((\kappa_i L)^2)\right]$.

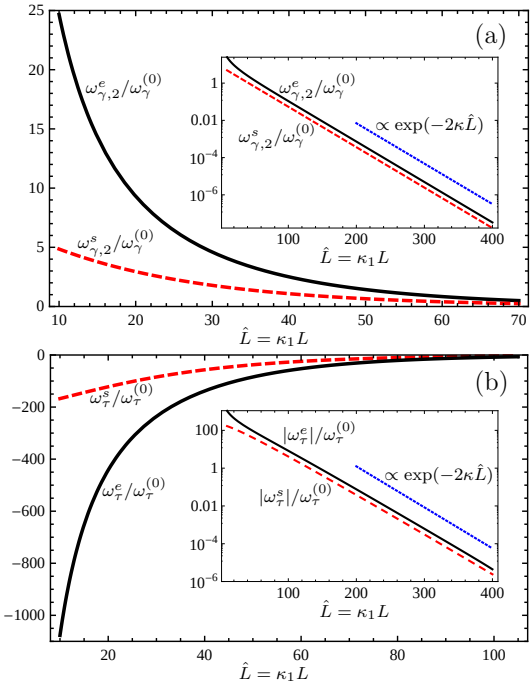


Figure 4.48: (a) Comparison between the exact expression (superscript "e", black solid lines, see Eq. (4.113)) and the corresponding superposition approximation (superscript "s", red dashed lines, see Eq. (4.114)) of the surface interaction energy $\omega_{\gamma,2}(L)$ per total surface area of contact between the walls and medium "2" in units of $\omega^{(0)}_\gamma = \sigma_1^2/(\kappa_1\varepsilon_1)$ as a function of $\hat{L} = \kappa_1 L$. Typical experimental values for the parameter ratios $\kappa = \kappa_2/\kappa_1 = 0.025$, $\varepsilon = \varepsilon_2/\varepsilon_1 = 0.025$, and $\sigma = \sigma_2/\sigma_1 = 0.1$ have been chosen for the plots [76, 87, 228, 323, 418]. Obviously $\omega^e_{\gamma,2}(L)$ and $\omega^s_{\gamma,2}(L)$ differ significantly at small distances, but even in the limit of large wall separations the superposition approximation is too small by a factor of 2 (see the offset between the two curve in the inset). A similar deviation is obtained for $\omega_{\gamma,1}(L)$, but due to its very small magnitude ($\approx 10^{-10} \times \omega_{\gamma,2}(L)$, for the above parameter choices) it is shown in Fig. 4.49. (b) Comparison of the exact expression (superscript "e", black solid lines) and the superposition approximation (superscript "s", red dashed lines) of the effective line interaction energy $\omega_\tau(L)$ per total length of the three-phase contact lines between media "1" and "2" and the walls in units of $\omega^{(0)}_\tau = \sigma_1^2/(\kappa_1^2\varepsilon_1)$ as a function of $\hat{L}$. In addition to the same parameters $\sigma$, $\varepsilon$, and $\kappa$ as in panel (a) the Donnan potential (Galvani potential difference) $\Phi_D/\Phi_1^{(0)} = 1.3$ is used. As for the surface interaction potential in panel (a), the superposition approximation of the line interaction potential deviates qualitatively from the exact result at small wall separations and its absolute value at large distances is too small by a factor of 2. (See Ref. [283])

Thus the superposition approximation underestimates $\omega_{\gamma,i}$ for all $L$. Since for dilute aqueous electrolyte solutions of, e.g. 1 mM ($\approx 0.0006\,\mathrm{nm}^{-3}$) ionic strength the Debye length ($1/\kappa_i \gtrsim 10\,\mathrm{nm}$) is much larger than typical molecular size (e.g. $L = 1\,\mathrm{nm}$), the exact surface interaction $\omega^e_{\gamma,i}(L)$ and the corresponding superposition approximation $\omega^s_{\gamma,i}(L)$ differ by at least one order of magnitude: $\omega^e_{\gamma,i}(L)/\omega^s_{\gamma,i}(L) \simeq 1/(\kappa_i L) \gtrsim 10$. Figures 4.48(a) and 4.49 display a comparison between the exact result (black solid lines) and the superposition approximation (red dashed lines) for a set of typical experimental values for the

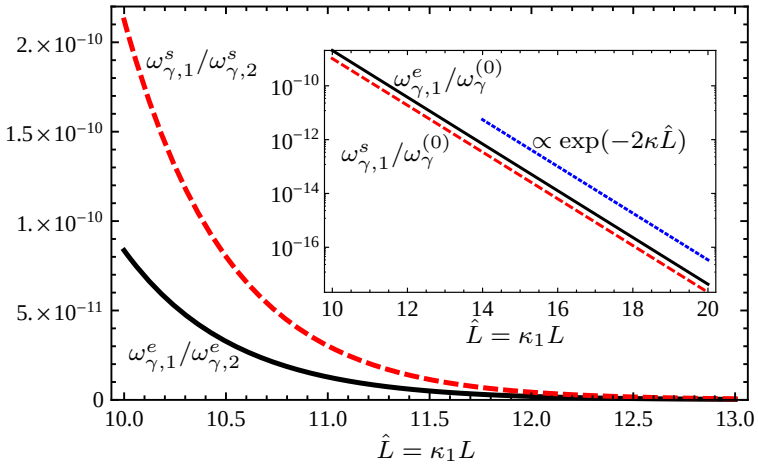


Figure 4.49: Comparison between the exact expression (superscript "e", black solid lines, see Eq. (4.113)) and the superposition approximation (superscript "s", red dashed lines, see Eq. (4.114)) for the surface interaction energy $\omega_{\gamma,1}(L)$ per total surface area of contact between the walls and medium "1" scaled by $\omega_{\gamma,2}(L)$ for varying $\hat{L} = \kappa_1 L$. Typical experimental values for the parameter ratios $\kappa = \kappa_2/\kappa_1 = 0.025$, $\varepsilon = \varepsilon_2/\varepsilon_1 = 0.025$, and $\sigma = \sigma_2/\sigma_1 = 0.1$ have been chosen for the plots. This data set is the same as the one used for Fig. 4.48, which displays the behaviour of $\omega^e_{\gamma,2}$ and $\omega^s_{\gamma,2}$. Obviously $\omega^e_{\gamma,i}(L)$ and $\omega^s_{\gamma,i}(L)$ differ significantly at small separation distances, but even in the limit of large wall separations the superposition approximation is too small by a factor of 2 (see the offset between the two curves in the inset). (See Ref. [283])

ratios $\sigma = \sigma_2/\sigma_1$, $\kappa = \kappa_2/\kappa_1$, and $\varepsilon = \varepsilon_2/\varepsilon_1$.

The line interaction potential $\omega_\tau(L)$ per total length of the three-phase contact line between media "1" and "2" and the walls has been calculated from Eqs. (4.110) and (4.111) (see Ref. [283] for explicit expressions). A comparison between the exact result $\omega^e_\tau(L)$ and the corresponding superposition approximation $\omega^s_\tau(L)$ is displayed in Fig. 4.48(b). Similar to the surface interaction potentials, $\omega^s_\tau(L)$ differs significantly from the exact result $\omega^e_\tau(L)$ at small wall separations $2L$. For large values of $L$, its absolute value is too small by a factor of 2, like the surface contribution.

In Ref. [283] the charge density at the surface of the colloids has been considered to be constant, forming a boundary condition. However, in actual systems the situation is slightly different. When two particles approach each other the electrostatic potential becomes deeper in the region between the particles. Due to that certain charged molecular surface groups recombine in order to adjust the electrostatic potential. Such a process can better be described by a charge regulation model [56, 74, 90, 188, 191, 192, 385, 444]. Keeping in mind the actual complexity of the system considered here, one can briefly discuss the implications of charge regulation by focusing on a simpler system which consists of an electrolyte between two charged walls without a liquid-liquid interface in between. For such a system, the electrostatic potential with a surface charge density $\sigma_{wi}(L)$ at the two walls (which is constant for any fixed $L$) is given by $\Phi^e_{wi} = \frac{\sigma^e_{wi}(L)}{\kappa_{wi}\varepsilon_{wi}} \frac{\cosh \kappa_{wi} z}{\sinh \kappa_{wi} L}$ for the *e*xact calculation (see Ref. [283]) and by $\Phi^s_{wi} = \frac{2\sigma^s_{wi}(L)}{\kappa_{wi}\varepsilon_{wi}} e^{-\kappa_{wi} L} \cosh(\kappa_{wi} z)$ within the *s*uperposition approximation. Here the subscript "*wi*" stands for the system *w*ithout *i*nterface and the quantities $\sigma_{wi}$, $\kappa_{wi}$ and $\varepsilon_{wi}$ indicate, respectively, the surface charge

density at the walls, the inverse Debye length, and the permittivity of the medium between the two planes in the absence of the horizontal interface. The dependence of the surface charge densities $\sigma^e_{wi}(L)$ and $\sigma^s_{wi}(L)$ on $L$ originates from the charge regulation. This leads to the following surface interaction energies per total surface area of both walls [283]:

$$\omega^e_{\gamma,wi}(L) = \frac{\left(\sigma^e_{wi}(L)\right)^2}{2\kappa_{wi}\varepsilon_{wi}} \left(\coth(\kappa_{wi}L) - 1\right) \tag{4.115}$$

and

$$\omega^s_{\gamma,wi}(L) = \frac{\left(\sigma^s_{wi}(L)\right)^2}{2\kappa_{wi}\varepsilon_{wi}} \left(2e^{-\kappa_{wi}L}\cosh(\kappa_{wi}L) - 1\right). \tag{4.116}$$

Note that Eqs. (4.115) and (4.116) are identical to Eqs. (4.113) and (4.114), respectively, except the fact that here the surface charge density varies with the thickness $L$ of the slab.

The two limiting cases of small and large $L$ are discussed separately. In the limit $\kappa_{wi}L \ll 1$ one has $\sigma^e_{wi}(L) \simeq -\mathrm{sign}(q)e\sqrt{2nKL}$ for the exact calculation and $\sigma^s_{wi}(L)$ is constant for the superposition approximation. $K$ (with units 1/volume) is the equilibrium constant for the association-dissociation reaction of the surface groups, $n$ denotes the total number of surface sites per cross-sectional area where a dissociation reaction can take place, and $q$ is the valency of the solvated ions due to the dissociation reaction at the wall surface. This implies $\omega^e_{\gamma,wi}(L \to 0) = \dfrac{e^2nKL}{\kappa_{wi}\varepsilon_{wi}}\left[\dfrac{1}{\kappa_{wi}L} - 1 + \dfrac{\kappa_{wi}L}{3} + \mathcal{O}((\kappa_{wi}L)^3)\right]$ which is nonzero for $L = 0$. On the other hand, the nonzero and finite limiting value $\sigma^s_{wi}(L \to 0) \neq 0$ within the superposition approximation is clearly unphysical because the charge density is expected to decrease upon decreasing the inter-particle separation distance $L$. If by fiat, in order to avoid this unphysical feature, in Eq. (4.116) one replaces $\sigma^s_{wi}(L)$ by $\sigma^e_{wi}(L)$, in the limit of small $L$ one finds $\omega^s_{\gamma,wi}(L \to 0) = \dfrac{e^2nKL}{\kappa_{wi}\varepsilon_{wi}}\left[1 - 2\kappa_{wi}L + \mathcal{O}((\kappa_{wi}L)^2)\right]$, which vanishes for $L \to 0$. In the opposite limit, i.e. for $\kappa_{wi}L \gg 1$, one finds $\omega^e_{\gamma,wi} \simeq \dfrac{\left(\sigma^e_{wi}(L)\right)^2}{\kappa_{wi}\varepsilon_{wi}} e^{-2\kappa_{wi}L}$ and, by using the same replacement as above, $\omega^s_{\gamma,wi} \simeq \dfrac{\left(\sigma^e_{wi}(L)\right)^2}{2\kappa_{wi}\varepsilon_{wi}} e^{-2\kappa_{wi}L} = \dfrac{\omega^e_{\gamma,wi}}{2}$ with $\sigma^e_{wi}(L)$ given in Ref. [283]. Thus for the simple slab system without a liquid-liquid interface, but with charge regulation, the exact calculation and the superposition approximation are also in disagreement by a factor of 2 in the large separation limit and they differ qualitatively in the small separation limit. For the more complicated system with a liquid-liquid interface, one can expect these discrepancies to persist.

The considerations above show that the effective interation between the two surfaces (colloids) is determined by the interplay of the Debye lengths $1/\kappa_1$ and $1/\kappa_2$ in both media and the Gouy-Chapman lengths $2k_BT\varepsilon_1/(e|\sigma_1|)$ and $2k_BT\varepsilon_2/(e|\sigma_2|)$ of the charged colloid-fluid interfaces. It has to be noted that this variety of length scales occurs due to the colloids being hosted at an interface between ionic complex fluids and not between inert structureless media.

# Chapter 5

# Conclusions

In the previous chapters several types of ionic complex fluids have been discussed which can be classified in terms of the relation of the Debye length to other relevant length scales. For electrolyte solutions the additional length scale is the bulk correlation length of the solvent, whereas in the absence of a solvent the Debye length competes with molecular or colloidal length scales.

For dilute electrolyte solutions the Debye length is competing with the bulk correlation length of the solvent. Far away from a critical point of the solvent the Debye length is the largest length scale so that the properties of the ionic complex fluid are rather material-independent and similar to those of a plasma. In particular the bulk structure (see Secs. 3.1 and 3.2) and the interfacial behaviour (see Secs. 4.1, 4.2, 4.3, 4.4 and 4.6) is characterised by the screening of charges. However, the bulk phase behaviour (see Sec. 2.1) is affected only marginally by the presence of a small amount of ions, as a consequence of the only short-ranged correlations.

Close to a critical point of the solvent an ionic complex fluids exhibits the universal critical behaviour of the pure solvent because then the Debye length takes the role of a "microscopic" length which is smaller than the bulk correlation length (see Secs. 3.1, 3.2, 4.3 and 4.6). It turned out that Kirkwood crossovers, i.e. crossovers between monotonic and damped oscillatory asymptotic decay of the pair correlation function, take place in between both regimes when the Debye length and the bulk correlation length are of similar magnitude (see Sec. 3.1).

In room temperature ionic liquids (RTILs), and particularly in ionic liquid crystals, no solvent is present and the properties are determined by an interplay between the Debye length and molecular lengths of the particles. For dense RTILs the Debye length is (much) smaller than the molecular size so that these systems behave to a large extent similar to non-ionic complex fluids with genuine short-ranged interactions due to, e.g., chemical bonding (see Sec. 3.4). Consequently formation of microheterogeneities due to the simultaneous presence of polar and apolar parts of the organic molecules and of mesophases of ionic liquid crystals (see Sec. 2.3) occurs. These features are sensitive to details of the chemical structure of the molecules. Only electrical observables, such as the dielectric function (see Sec. 3.3), exhibit material-independent plasma-like signatures of the freely moving ions at large length scales. In dilute RTILs (see Sec. 2.2) the Debye length is (much) larger than the particle size, which leads to a behaviour similar to a plasma of point-like particles.

In colloidal suspensions all three length scales (the size of the colloidal particles, the

Debye length and the bulk correlation length of the solvent) can be relevant. The size of the colloidal particles is typically the largest, which leads to the material-independent but geometry-dependent dominant behaviour of hard particles with characteristic phases of colloidal crystals (see Sec. 2.4) and liquid crystals (see Sec. 2.3). On the one hand, far away from a critical point of the solvent, screening of the colloidal surface charge on the scale of the Debye length provides the leading correction to the hard particle behaviour. This correction is again material-independent and it gives rise to similarities of colloidal suspensions with RTILs (e.g. ionic liquid crystals) and electrolyte solutions (see Sec. 4.5). On the other hand, close to the critical point of the solvent the critical Casimir force on the scale of the bulk correlation length dominates over the electrostatic interaction (see Sec. 4.6). However, under certain circumstances more complex structures form at the surfaces of colloids due to the coupling of ions and the solvent, such as the dipolar layers of unequally partitioned ions in composition gradients of the solvent, which give rise to involved effective interactions between colloidal particles (see Sec. 4.6), or the fluid structure in between colloidal particles trapped at an interface of immiscible ionic complex fluids, which gives rise to an effecive interaction of the colloids with contributions from the colloidal surfaces as well as from the fluid-fluid-colloid contact lines (see Sec. 4.7).

The considerations above suggest that the key to understand fine details of soft matter systems, to which advanced experimental techniques have given access in recent years, as well as some known but not yet fully understood phenomena, e.g. the aggregation in colloidal suspensions or the folding of proteins, is to recognise the ionic complex fluid properties, e.g. of the dispersion medium.

The present thesis is focussed on static general properties of ionic complex fluids, and it has been shown in the preceding chapters that the classification of static general properties of complex fluids in terms of competing length scales leads to ionic complex fluids being of particular interest, because the Debye length is largely material-independent and for the important case of dilute electrolyte solutions it happens to be well separated from the molecular length scale below and from the colloidal length scale above. For dynamic properties there are not only hierarchies of length but also of time scales which determine the properties. Examples of this situation are well-known for polymers [115, 383], interfaces of immiscible electrolyte solutions [156, 171, 374, 398–400, 458] and colloidal suspensions [38, 104, 166, 385]. Due to the multitude of time scales typically present it is common practice to study the dynamics of complex fluids on individual time scales. However, in contrast to the typical length scales relevant for static properties, the time scales relevant for the dynamics of a complex fluid depend sensitively on the system. This essentially precludes a general, i.e. system-independent, classification. Hence, the existence of three well-separated major length scale regimes to classify the general, i.e. system-indpendent, phenomena of complex fluids and the identification of ionic complex fluids as a material class representing all of them can be expected to be a peculiarity of static properties of soft matter systems.

# Kurzfassung in deutscher Sprache

## 1 Einführung

Unter der großen Vielzahl komplexer Fluide sind diejenigen mit ionischen Konstituenten von vorrangigem Interesse. Ionische komplexe Fluide beinhalten z.B. Elektrolytlösungen, "room temperature ionic liquids" (RTILs), ionische Flüssigkristalle, kolloidale Suspensionen und Polyelektrolyte. Das häufige Auftreten ionischer komplexer Fluide in Natur und Technik geht auf die Gegenwart von flüssigem Wasser zurück, das als hochpolares Lösungsmittel zur Dissoziation von Kationen und Anionen führt.

Die Bildung frei beweglicher Ionen in verdünnen Elektrolytlösungen, z.B. in physiologischen Fluiden wie dem Zytoplasma, ist essentiell für viele natürliche Prozess, z.B. den Zitronensäurezyklus des aeroben Zellstoffwechsels. Das Leben auf der Erde wäre nicht von der Art wie es heute anzutreffen ist, wenn die Ursuppe kein ionisches komplexes Fluid gewesen wäre. Der Charakter verdünnter Elektrolytlösungen als komplexe Fluide wird durch eine große Anzahl verschiedener Teilchen erzeugt, deren typischerweise unvollständige gegenseitige Mischbarkeit zu Entmischungsübergängen und Mikroheterogenitäten führt. Per Definition ist die Debye-Länge einer verdünnten Elektrolytlösung viel größer als die molekularen Größen der Konstituenten, sodass diese ionischen komplexen Fluide viele materialunabhängigen Eingenschaften besitzen (siehe Abschn. 2.1, 3.1, 3.2, 4.1, 4.2, 4.3 und 4.4).

Chemische Prozesse, die auf Redox-Reaktionen basieren, z.B. in Batterien, Brennstoffzellen und Solarzellen sowie bei Elektrolyse und Galvanisierung, spielen sich in ionischen komplexen Fluiden ab, die von den Reaktanden gebildet werden. Ein aktueller Trend in der Katalyseforschung ist es RTILs, d.h. (typischerweise organische) Salzschmelzen mit Schmelztemperaturen im Bereich der Raumtemperatur [457], als Reaktionsmedien zu untersuchen, die eine hochpolare fluide Umgebung für solche Anwendungen bereitstellen [7, 165, 464, 470, 481, 483]. RTILs werden ebenfalls als leistungsfähige Lösungsmittel in der chemischen Synthese verwendet, die wasserunlösliche Materialien, wie z.B. Holz (Zellulose), lösen, Enzyme stabilisieren [463] oder in der Verarbeitung von Biomasse [427] eingesetzt werden können. Auf Grund von Eigenschaften, wie z.B. einer hohen thermischen Stabilität und einen vernachlässigbaren Dampfdruck [31, 273, 346, 467], sind viele Anwendungen denkbar, z.B. als füssiges Medium unter Ultrahochvakuumbedingungen [31, 273, 425, 459]. All diese Eigenschaften von RTILs können als die ionischer komplexer Fluide betrachtet werden, die durch eine einzigartige Kombination aus elektrostatischer und sterischer Wechselwirkung sehr asymmetrischer Teilchen gekennzeichnet sind. Da RTILs keine Lösungen sondern Schmelzen sind, enthalten sie kein Lösungsmittel, sodass, im Gegensatz zu verdünnten Elektrolytlösungen, die Ionenstärke sehr hoch und daher die Debye-Länge sehr viel kleiner als die Teilchengröße ist. Allgemeine, d.h. materialun-

abhängige, Eigenschaften leiten sich von der hohen Ladungsdichte ab (siehe Abschn. 2.2, 3.3 und 3.4).

Während die vielfach untersuchten Imidazolium- und Pyridinium-basierten RTILs mit kurzen Alkylketten im Volumen isotrope Fluide sind, existieren auch ionische Flüssigkristalle, d.h. RTILs, die mesogenes Verhalten zeigen. Auf Grund ihrer selbstorganisierten Struktur sind letztere von Interesse für Anwendungen als anisotrope Leiter [1, 225, 332, 485] oder als Formvorlagen zur Synthese von Nanoteilchen [429, 430]. Verschiedene Arten ionischer Flüssigkristalle wurden hergestellt [19, 50], welche, z.B. smektische [61, 177, 193, 405], kolumnare [404, 486] und selbst kubische [318, 319] Mesophasen zeigen. Wie auch für isotrope RTILs zeigen ionische Flüssigkristalle hohe thermische und elektrochemische Stabilität [61, 103, 160, 237, 256, 419], was für manche Anwendungen von Vorteil ist. Der sterische Einfluss der ionischen Flüssigkristalle auf die Eigenschaften als komplexe Fluide ist jedoch stärker als bei isotropen RTILs, da die anisotropen Teilchenformen nicht nur zu den niedrigen Schmelztemperaturen, sondern auch zur Bildung von Mesophasen führen (siehe Abschn. 2.3).

Eine weitere Klasse ionischer komplexer Fluide, deren Teilchen größer als die Debye-Länge sind, sind kolloidale Suspensionen. Mit Hilfe entsprechender Präparationstechniken und experimenteller Bedingungen ist man in der Lage, die kolloidalen Wechselwirkungen in einem weiten Bereich einzustellen [169, 269, 368, 428]. Dementsprechend ist eine Vielzahl an Parametern festzulegen, z.B. Größe und Form der Kolloide sowie Stärke und funktionale Form des Wechselwirkungspotentials [112, 260, 413, 484]. Zudem nimmt die Zahl an Parametern dramatisch zu, wenn Mischungen verschiedener kolloidaler Spezies betrachtet werden. Es gibt zwei verschiedene Gesichtspunkte auf kolloidale Suspensionen im Kontext ionischer komplexer Fluide: Einerseits kann man das kolloidale Subsystem *als* ionisches komplexes Fluid betrachten und das Lösungsmittel als strukturloses, inertes und homogenes Medium behandeln, wie z.B. im Rahmen der DLVO-Theorie der Stabilität kolloidaler Dispersionen [209, 385]. In Abschn. 2.4 wird diskutiert, dass selbst binäre Mischungen geladener kolloidaler Kugeln mit gleichen Radien ein sehr komplexes Phasenverhalten zeigen, das lediglich durch die Reichweite der abgeschirmten elektrostatischen Wechselwirkung bestimmt wird, und in Abschn. 4.5, dass kolloidale Plättchen allgemeine Eigenschaften von verdünnten Elektrolytlösungen und ionischen Flüssigkristallen aufweisen. Andererseits kann man kolloidale Teilchen *in* einem ionischen komplexen Fluid als Medium suspendiert betrachten, z.B. bei Emulsionen zweier nicht mischbarer Flüssigkeiten, Suspensionen von Viren oder Ton und Makromolekülen wie DNA-Stränge und Proteine. Dieser Standpunkt führt zu der Frage nach der effektiven Wechselwirkung zwischen den kolloidalen Teilchen in Abhängigkeit von den Eigenschaften des ionischen komplex-fluiden Mediums; bekannte Beispiele sind der Abschirmeffekt elektrischer Ladungen durch frei bewegliche Ionen [75, 91, 92, 161, 162] und die salzspezifische Modifikation der Löslichkeit ("salting-in" oder "salting-out") von Proteinen in Elektrolytlösungen (Hofmeister-Effekt) [243]. Häufig auftretende Situationen in Systemen weicher Materie, deren Eigenschaften durch ionische komplex-fluide Medien bestimmt sind und die hier behandelt werden, sind die Bildung elektrostatisch stabilisierter Emulsionen zweier Flüssigkeiten (siehe Abschn. 4.1), die Wechselwirkung kolloidaler Teilchen in einer Elektrolytlösung nahe und weit weg von einem kritischen Punkt des Lösungsmittels (siehe Abschn. 4.6) und die Wechselwirkung kolloidaler Teilchen an einer Grenzfläche zwischen zwei Fluiden (siehe Abschn. 4.7).

Angesichts all dieser wichtigen Systeme, die Themen zahlreicher Forschungsgebiete und

technischer Anwendungen sind, ist es entscheidend, die Eigenschaften der ionischen komplexen Fluide zu verstehen, die einen wesentlichen Bestandteil dieser Systeme ausmachen. Obgleich es eine Vielfalt an ionischen komplexen Fluiden gibt, teilen sie allgemeine, d.h. materialunabhängige, Eigenschaften, die auf der Kopplung der beweglichen Ionen an weitere Freiheitsgrade des komplexen Fluids beruhen. Besonders zweckmäßig ist ein Klassifikationsschema, das bereits oben angewendet wurde und das eine Einteilung der relevanten Längenskalen vornimmt, wovon die Debye-Länge eine ist, die die Ionenstärke der geladenen Konstituenten quantifiziert. Die Kombination des ionischen Charakters mit, z.B., Orientierungsfreiheitsgraden, Größenpolydispersität oder Konformationsfreiheitsgraden führt zu einer reichhaltigen Phänomenologie ionischer komplexer Fluide, deren Verständnis dank Weiterentwicklungen der theoretischen Beschreibung, Computersimulationstechniken und experimentellen Methoden bedeutende Fortschritte gemacht hat. Ziel dieser Habilitationsschrift ist es die Beiträge des Autors zum Thema allgemeiner Eigenschaften ionischer komplexer Fluide aus den Arbeiten [24, 35–37, 39–45, 96, 203, 204, 236, 283, 487, 491] darzulegen und im Kontext aktueller Forschung zu diesem Thema zu diskutieren. Aus den zahllosen Möglichkeiten, allgemeine Eigenschaften der verschiedenen oben erwähnten ionischen komplexen Fluide zu diskutieren, wird in den folgenden Kapiteln eine Einteilung in die Kategorien “Phasenverhalten”, “Struktur im Volumen” und “Grenzflächen” gewählt. Jedes Kapitel beginnt mit einer Diskussion verdünnter Elektrolytlösungen, gefolgt von ionischen komplexen Fluiden hoher Ladungsdichte (RTILs) und / oder großer Teilchen (Kolloide).

Der Einfluss von ionischen Konstituenten auf das Phasenverhalten komplexer Fluide wird in Kap. 2 diskutiert. Die dort behandelten Phasenseparationen zweier Elektrolytlösungen in komplexen Lösungsmitteln (Abschn. 2.1) und die Gasphase von RTILs (Abschn. 2.2) repräsentieren die Situation kleiner Ionenstärke, d.h. einer Debye-Länge größer als die konstituierenden Moleküle. Die komplementäre Situation von Teilchengrößen größer als die Debye-Länge führt zu den mesogenen Eigenschaften ionischer Flüssigkristalle (Abschn. 2.3) und der reichhaltigen Phänomenologie kristalliner Phasen geladener Kolloide (Abschn. 2.4).

Der Einfluss von Ionen auf die Struktur komplexer Fluide im Volumen wird in Kap. 3 beschrieben. Die wichtigste Beobachtung für verdünnte Elektrolytlösungen ist hierbei, dass die Struktur dieser ionischer komplexer Fluide im Volumen durch die Debye-Länge bestimmt ist, ausgenommen in der Nähe eines kritischen Punkts des Lösungsmittels, wo die divergente Korrelationslänge zu einem interessanten Übergang von elektrolyt-ähnlichem Verhalten zum Verhalten des kritischen Lösungsmittels führt (Abschn. 3.1). Eine interessante allgemeine Beobachtung, die zu besprechen ist, ist die, dass ionische Verunreinigungen, im Gegensatz zu nichtionischen, die Lösungsmittelstruktur im Volumen verändern können (Abschn. 3.2). Bei dichten ionischen Fluiden führt die Konkurrenz zwischen der elektrostatischen Wechselwirkung und der sterischen Wechselwirkung auf Grund von Größe und Form der Teilchen zu einem Übergang zwischen plasma-ähnlichem und dipolar-fluidem Verhalten, das im Rahmen der statischen dielektrischen Funktion diskutiert werden wird (Abschn. 3.3). Gewöhnlich wird die Langreichweitigkeit der reinen Coulomb-Wechselwirkung für die Besonderheiten des Phasenverhaltens und der strukturellen Eigenschaften ionischer Systeme verantwortlich gemacht. Für dichte ionische Fluide kann jedoch gezeigt werden, dass das nicht zutrifft, d.h. dass dasselbe Phasenverhalten und dieselbe Struktur auch von einer geeigneten kurzreichweitigen Wechselwirkung erzeugt werden können (Abschn. 3.4).

Grenzflächeneigenschaften ionischer komplexer Fluide sind von besonderem Interesse für verschiedene Anwendungen, sodass Kap. 4 einer ausführlichen Diskussion von Grenzflächen gewidmet ist. Allgemeine Eigenschaften von Grenzflächen ionischer komplexer Fluide zeigen sich in der Grenzflächenspannung (Abschn. 4.1), dem Benetzungsverhalten (Abschn. 4.2), der kritischen Adsorption (Abschn. 4.3) und der Elektrobenetzung (Abschn. 4.4) in Elektrolytlösungen. Wiederum zeigt die Phänomenologie dieses Systemtyps weitgehende Materialunabhängigkeit, da die Debye-Länge als dominante Längenskala die molukulare Größe der Konstituenten überragt. Andererseits wird die Grenzflächenstruktur kolloidaler Suspensionen durch die Teilchengeometrie dominiert und die Debye-Länge führt lediglich zu einer Korrektur. Nichtsdestoweniger stellen sich die Benetzungseigenschaften kolloidaler Suspensionen als sehr ähnlich zu denen verdünnter Elektrolytlösungen und ionischer Flüssigkristalle heraus (Abschn. 4.5). Kolloidale Suspensionen können jedoch eine viel reichhaltigere Phänomenologie besitzen, falls mehrere Längenskalen gleichzeitig beitragen. Zu diskutierende Beispiele sind nichttriviale effektive Wechselwirkungen zwischen kolloidalen Teilchen im Volumen eines ionischen komplexen Fluids (Abschn. 4.6) oder an der Grenzfläche zwischen zwei nichtmischbaren ionischen komplexen Fluiden (Abschn. 4.7).

Ausgehend von den zuvor diskutierten Systemen werden in Kap. 5 allgemeine Schlussfolgerungen über die allgemeinen Eigenschaften ionischer komplexer Fluide gezogen. Es wird argumentiert, dass die in den Kap. 2–4 diskutierten ionischen komplexen Fluide nicht nur vom Anwendungsstandpunkt interessant sind, sondern dass sie auch einen vollständigen Satz von Repräsentanten der verschiedenen Klassen allgemeiner Eigenschaften darstellen.

# 2 Phasenverhalten

## 2.1 Elektrolytlösungen

Während im 19. Jahrhundert für Elektrolytlösungen nur die kolligativen Eigenschaften verstanden wurden [8] und Anfang des 20. Jahrhunderts die Ion-Ion-Korrelationen erkannt wurden [91, 296, 385], rückte in den letzten Jahren zunehmend die Kopplung zwischen Ionen und Lösungsmittel in den Fokus des Interesses. Untersuchungen befassen sich hierbei mit der Doppelschichtstruktur für komplexe Lösungsmittel nahe eines kritischen Punkts [42, 43, 80, 327, 328, 334, 335], mit möglichen salzinduzierte Strukturänderungen des komplexen Lösungsmittels [43, 44, 312–314, 388–392] und mit Effekten auf Grund von Inhomogenitäten der Permittivität in der Nähe von Grenzflächen [29, 329, 401, 436]. Die übergroße Mehrheit theoretischer Untersuchungen stützt sich dabei auf die sogenannte bilineare Kopplungsnäherung (BCA) der Ionen-Lösungsmittel-Wechselwirkung, d.h. einer lokalen Dichtenäherung mit freier Excessenergiedichte, die bilinear in den Teilchenzahldichten ist [29, 312–314, 327, 328, 334, 335, 401, 436]. Die "random-phase approximation" (RPA) [80, 329] stellt im Prinzip lediglich eine nichtlokale Variante der BCA dar, von der bekannt ist, dass sie nur für kleine Wechselwirkungsenergien anwendbar ist [176]. Typische Ionen-Lösungsmittel-Wechselwirkungsstärken betragen aber gewöhnlich einige $10\,k_BT$ [208, 286], sodass die Verwendung der BCA oder der RPA nicht gerechtfertigt ist. Tatsächlich wurde in Arbeit [43] im Rahmen einer Dichtefunktionaltheorie (siehe Gl. (2.1)) gezeigt, dass die BCA und die RPA zu qualitativ falschen Phasendiagrammen führen können (siehe Abb. 2.1). Außerdem wurde dort eine realistischere Kopplung, die

neben energetischen auch entropische Beiträge der Ionen-Lösungsmittel-Kopplung berücksichtigt, vorgeschlagen (siehe Gl. (2.3)). Diese verbesserte Beschreibung, im Gegensatz zur BCA und RPA, lässt für verdünnte Elektrolytlösungen auf einen nur schwachen Einfluss von Ionen auf das Phasenverhalten des Lösungsmittels schließen, was im Einklang mit der experimentellen Erfahrung steht [409].

## 2.2 Dampfdruck von RTILs

Eines der bemerkenswertesten und wahrscheinlich wichtigsten Eigenschaften von RTILs ist ein verschwindend kleiner Dampfdruck bei Raumtemperatur: Beispielsweise besitzt $[C_4mim][PF_6]$ bei 298 K einen Dampfdruck von ca. 100 pPa [346], während der von Wasser 3 kPa beträgt [258]. Dies bietet die Möglichkeit, RTILs als Lösungsmittel unter Ultrahochvakuumbedingungen zu verwenden [277, 462]. Bei höheren Temperaturen können RTILs allerdings destilliert werden [123] und ihr Dampfdruck und Verdampfungsenthalpie können gemessen werden [347, 488].

Verschwindend kleine Dampfdrücke nahe dem Tripelpunkt werden für alle aprotischen RTILs beobachtet, aber weder für nichtionische Flüssigkeiten (NILs), z.B. Wasser oder Benzol, noch für anorganische Salzschmelzen (IFSs) (siehe Tab. 2.1). Es stellt sich somit die Frage nach dem Grund für das Auftreten kleiner Tripelpunktdrücke genau für die Materialklasse der RTILs. Eine Begründung wurde in der Arbeit [40] in der *Kombination* eines niedrigen Schmelzpunkts ("room temperature") mit einer starken, ionischen Wechselwirkung ("ionic liquids") gefunden (siehe Abb. 2.4).

## 2.3 Ionische Flüssigkristalle

Qualitativ lässt sich das Phasenverhalten ionischer Flüssigkristalle bereits anhand eines einfachen Gittermodels (siehe Abb. 2.5) im Rahmen einer Dichtefunktionaltheorie reproduzieren (siehe Gl. (2.7)) mit Beiträgen der kurzreichweitigen sterischen Repulsion, der langreichweitigen Coulomb- und Van-der-Waals-Wechselwirkung und der kurzreichweitigen elektrostatischen Korrekturen wie in der MSA [454–456]. In Abb. 2.6 ist gezeigt, dass hiermit die Phasenübergänge zwischen isotroper Flüssigkeits- und Gasphase, sowie zwischen isotropen und anisotropen Phasen qualitativ mit experimentellen Resultaten, [372] bzw. [177], übereinstimmen.

Ein verfeinertes Modell (siehe Abb. 2.7) wurde in der Arbeit [236] untersucht, bei dem die nichtelektrostatischen Beiträge zur Wechselwirkung durch ein Gay-Berne Potential [25, 66, 97–99, 153] (siehe Gln. (2.9)–(2.11)) und die elektrostatische Wechselwirkung durch ein abgeschirmtes Coulomb-Potential (siehe Gln. (2.12)–(2.15)) beschrieben werden.

Die Phasendiagramme zeigen stets eine isotrope fluide Phase und eine smektische A-Phase (siehe Abb. 2.8). Abhängig von der Särke und der Position der elektrischen Ladungen kann auch eine nematische Phase auftreten (siehe Abb. 2.9 und 2.11–2.13). Mit zunehmender Anisotropie verschiebt sich der Übergang zwischen dem isotropen Fluid und den Mesophasen zu kleineren Packungsdichten und der Dichtesprung nimmt zu. Für zwei Ladungen an den Enden der Teilchen tritt eine nematische Phase auf, die bei Verschiebung der Ladungen Richtung Zentrum metastabil wird. Bei weiterer Annäherung und Zusammenführung der Ladungen im Zentrum verschiebt sich die smektische A-Phase zu größeren Packungsdichten, wodurch die nematische Phase wieder stabil wird.

## 2.4 Geladene Kolloide

Es ist aus Experimenten [260] und Computersimulationen [28, 53, 200, 201, 289, 489] bekannt, dass entgegengesetzt geladene Kolloide unter bestimmten Bedingungen kristalline Phasen bilden können statt die sonst übliche regellose Aggregation zu zeigen. Ziel der Arbeit [41] war es, das globale Phasendiagramm von binären Mischungen entgegengesetzt geladener kugelförmiger Kolloide mit gleichen Radien und Ladungsbeträgen zu bestimmen. Dazu wurde in Anlehnung an das Vorgehen der Arbeit [448] das Minimum der freien Enthalpie auf einer Menge von potentiellen Kristallstrukturen (siehe Tab. 2.2) bestimmt, wobei die verwendete Näherung der freie Enthalpie zwischen dem Limes harter Kugeln bei hohen Temperaturen und einer Beschreibung durch Madelung-Summen bei niedrigen Temperaturen interpoliert.

Die Phasendiagramme in Abb. 2.15–2.17 zeigen eine fluide Phase und kristalline rfcc- ("random face-centered cubic"), $Cu_3Au$-, CsCl-, CuAu- und NbP-Phasen. Die kristalline rfcc-Phase bei hohen Temperaturen reicht zu um so tieferen Temperaturen, je kleiner die Debye-Länge relativ zum Kugelradius ist. Ebenso hängt die Lage der kristallinen Phasen bei tiefen Temperaturen ($Cu_3Au$, CsCl, CuAu und NbP) empfindlich von diesem Parameter ab.

# 3 Struktur im Volumen

## 3.1 Struktur von Elektrolytlösungen in der Nähe kritischer Punkte

Die Struktur von Elektrolytlösungen im Rahmen des Dichtefunktionals in Gl. (2.1) (siehe Arbeit [43]) führt im Volumen auf die Dichte-Dichte-Korrelationsfunktionen $G_{ij}(r)$ mit $i,j \in \{\phi,+,-\}$ mit den Fouriertransformierten (partiellen Strukturfaktoren) in Gln. (3.1)–(3.3). Daraus folgt der (partielle) Strukturfaktor $\widehat{G}_{\phi\phi}(k)$ des Lösungsmittels in Gln. (3.4)–(3.6) und der Ladungs-Ladungs-Strukturfaktor $S_{ZZ}(k)$ in Gl. (3.7), wobei letzterer die für elektrostatische Abschirmung charakteristische Asymptotik $S_{ZZ}(k \to 0) \simeq (k/\kappa)^2$ zeigt. Aus den Positionen der Pole von $\widehat{G}_{\phi\phi}(k)$, d.h. der Nullstellen von $L(k)$ in Gl. (3.3), in der komplexen Ebene $k \in \mathbb{C}$ (siehe Abb. 3.1) kann das asymptotische Verhalten der Struktur der Elektrolytlösung bestimmt werden [134, 135]. Rein imaginäre Pole (siehe Abb. 3.1(a)) entsprechen der Superposition monoton abfallender Beiträge zu $G_{\phi\phi}(r \to \infty)$, während Pole mit nichtverschwindenden Realteilen (siehe Abb. 3.1(b)) oszillatorischen Abfall bedeuten. Monotoner Abfall von $G_{\phi\phi}(r \to \infty)$ findet sich weit weg von kritischen Punkten mit dem führenden, d.h. langreichweitigsten, Beitrag auf der Skala der Debye-Länge und in der Nähe kritischer Punkte auf der Skala der Ornstein-Zernike-Länge $\xi^{(\mathrm{OZ})}$ in Gl. (3.8) (siehe Abb. 3.3). Zwischen beiden Grenzfällen, wenn die Debye-Länge und die Ornstein-Zernike-Länge von ähnlicher Größe sind, tritt oszillatorischer Abfall der Korrelationsfunktion auf (siehe Abb. 3.3). Die Übergange zwischen monotonem und oszillatorischem Abfall von $G_{ij}(r \to \infty)$ sind durch Kirkwood-Übergänge [230, 259] (siehe Abb. 3.1(d)) gegeben, die im Phasendiagramm den schmalen Bereich oszillatorischen Abfalls begrenzen (siehe Abb. 3.2(b)–(d)). Es zeigt sich so insbesondere, dass die elektrostatische Wechselwirkung nicht das universelle Verhalten des Lösungsmittels in der Nähe eines kritischen Punkts verändert.

## 3.2 Struktur von Fluiden mit ionischen Verunreinigungen

Der Ausdruck Gl. (3.4) des Lösungsmittelstrukturfaktors $\widehat{G}_{\phi\phi}(k)$ einer Elektrolytlösung wurde im Rahmen des speziellen Modells aus Abschn. 2.1 (siehe die Arbeiten [43, 334]) hergeleitet. In der Arbeit [44] wurde die Situation vom allgemeineren Standpunkt eines Fluids mit Verunreinigungen betrachtet. Ohne Bezugnahme auf ein spezielles Modell oder Wechselwirkungspotenital konnte dort die allgemeine Form des Lösungsmittelstrukturfaktors hergeleitet werden (siehe Gln. (3.9)–(3.11)). Es zeigt sich damit, dass nichtionische Verunreinigungen keinen Einfluss auf die Struktur haben, ionische dagegen zu Mikroheterogenitäten führen können (siehe Abb. 3.4). Für ionische Verunreinigungen zeigen diejenigen die Bildung von Mikroheterogenitäten, die aus verschieden großen Ionen aufgebaut sind. Diese Interpretation findet ihre experimentelle Bestätigung in SANS-Messungen am System Wasser+3-Methylpyridin mit verschiedenen Salzen [388–390].

## 3.3 Dielektrische Eigenschaften dichter ionischer Fluide

Da RTILs eine breite Verwendung als Lösungsmittel finden, ist ihre Polarität eines der wichtigsten Charakteristika. Andererseits legten jüngst Messungen mit Hilfe eines "surface force appatus" (SFA) die Interpretation nahe, dass nur ein geringer Anteil eines RTILs tatsächlich als frei bewegliche Ionen vorliegt und der Rest aus temporär gebundenen Kation-Anion-Paaren besteht [154]. Während die Messdaten Kritik auf sich zogen [155, 352], wurde das theoretische Interesse an der Frage nach der Interpretation von RTILs als effektive verdünnte Elektrolytlösungen geweckt [257]. Die statische Dielektrizitätskonstante nichtleitender Fluide ist gut messbar (siehe z.B. die Arbeiten [32, 306]), wohingegen die dielektrische Funktion leitender, z.B. ionischer, Fluide wegen der Abschirmung elektrischer Ladungen auf großen Längenskalen divergiert [175, 422]. In der Arbeit [487] wurde demonstriert, dass die statische dielektrische Funktion ionischer Fluide auf kleinen Längenskalen, d.h. auf der Skala der Teilchengröße, nicht die eines Plasmas, sondern die einer dipolaren Flüssigkeit ist. Dazu wurde das "restricted primitive model" (RPM) geladener harter Kugeln gleicher Radien und Ladungsbeträge (siehe Abb. 3.5(a)) mit einem daraus abgeleiteten Modell eines dipolaren Fluids aus fest verbundenen Kationen-Anionen-Paaren (siehe Abb. 3.5(b)) verglichen. Es zeigte sich, dass die Orientierungspolarisation des RPM mit der des zugehörigen dipolaren Fluids übereinstimmt, während sich die Verschiebungspolarisation aus der Differenz der totalen Polarisation des RPM und des dipolaren Fluids ergibt (siehe Gl. (3.18)). Daraus ergab sich, dass auf großen Längenskalen die Verschiebungspolarisation, d.h. plasma-ähnliches Verhalten, dominiert, während auf der Skala der Teilchengröße die Orientierungspolarisation, d.h. Verhalten eines diplaren Fluids, dominiert (siehe Abb. 3.9). Der Übergang zwischen beiden Grenzfällen verschiebt sich mit zunehmender Packungsdichte und abnehmender Temperatur zu kleineren Längenskalen (siehe Abb. 3.10).

## 3.4 Effektive Wechselwirkung in dichten ionischen Fluiden

Bekanntermaßen ist das Coulomb-Potential repulsiv für gleichgeladene und attraktiv für entgegengesetztgeladene Ionen, und es fällt $\sim 1/r$ ab, d.h. es ist langreichweitig. Andererseits existiert für global ladungsneutrale Coulombsche Systeme der thermodynamische Limes [252, 271], da die Paarverteilungsfunktionen eines ionischen Fluids exponen-

tiell abklingen. Letztere Eigenschaft wird gewöhnlich in Form einer Stillinger-Lovett-Summenregel [176, 275, 421, 422] ausgedrückt, die eine notwendige Konsequenz der Langreichweitigkeit des Coulomb-Potentials ist [288, 304]. In der Arbeit [24] wurde für das "lattice restricted primitive model" (LRPM) gezeigt, dass das Phasenverhalten und die Struktur im Volumen dichter Systeme auch mit Hilfe eines geeignet gewählten kurzreichweitigen Potentials quantitativ reproduziert werden kann (siehe Abb. 3.16). Dies setzt einen nicht zu langsamen und nicht zu schnellen Abfall des kurzreichweitigen Potentials voraus (siehe Abb. 3.17). Selbst das Stillinger-Lovett-Abschirmverhalten wird reproduziert (siehe Abb. 3.18). Demnach ist die Langreichweitigkeit des Coulomb-Potentials für dichte ionische Fluide nicht notwendig. Wesentlich ist aber seine Valenzabhängigkeit, d.h. dass es für gleiches Vorzeichen der Ladungen repusiv und für entgegengesetzte attraktiv wirkt.

# 4 Grenzflächen

## 4.1 Grenzflächenspannung von Elektrolytlösungen

### Planare Elektrolytgrenzflächen

Im Gegensatz zur Oberflächenspannung einer Elektrolytlösung gegenüber einer Gasphase (Luft), in der Ionen praktisch unlöslich sind, was zur Zunahme mit der Ionenstärke führt [69, 116, 263–265, 284, 333], treten bei der Grenzflächenspannung zwischen zwei nichtmischbaren Elektrolytlösungen Partionierunseffekte auf Grund von Löslichkeitsunterschieden auf [37, 322, 335–337]. In der Arbeit [37] wurde gezeigt, dass daraus sehr allgemein drei mögliche asymptotische Abhängigkeiten der Grenzflächenspannungsänderung $\Delta\gamma$ gegenüber dem salzfreien Lösungsmittel von der Ionenstärke $I$ folgen (siehe Gln. (4.2) und (4.3)): $\Delta\gamma \sim I$, $\Delta\gamma \sim -I$ oder $\Delta\gamma \sim -\sqrt{I}$. Für Ionenstärken oberhalb eines Wertes $I^\times$ (siehe Gl. (4.4)) tritt eine lineare Abhängigkeit $\Delta\gamma \sim |I|$, während darunter $\Delta\gamma \sim -\sqrt{I}$ gilt. Letzterer Fall ist analog zum Jones-Ray-Effekt [216–220, 353, 354], der sich als Minimum der Grenzflächenspannung bei kleinen Ionenstärken zeigt. Die Ionenstärke $I^\times$ am Übergang dieser beiden Grenzfälle hängt stark von den Löslichkeitseigenschaften der Ionen ab (siehe Gl. (4.4)). So zeigt sich z.B. für den Fall einer Grenzfläche zwischen Wasser und cis-Decalin, dass durch geeignete Wahl der Anionen verschiedener Kaliumsalze alle Grenzfälle realisiert werden können (siehe Abb. 4.1).

### Gekrümmte Elektrolytgrenzflächen

Neben planaren Elektrolytgrenzflächen ist für die Untersuchung von Wasser-in-Öl- oder Öl-in-Wasser-Emulsionen die Grenzflächenspannung gekrümmter Grenzflächen von Interesse. Eine zur Arbeit [37] analoge Betrachtung [39] kugelförmiger Grenzflächen zwischen nichtmischbaren Elektrolytlösungen ergab Näherungsausdrücke für die Grenzflächenspannungsänderung (Gl. (4.9)) und die Oberflächenladung (Gl. (4.10)). Die Grenzflächenspannung hängt hierbei mit der Ionenstärke über eine Skalenfunktion (Gl. (4.8)) ab, die bis zu vier Grenzfälle (Gln. (4.13) und (4.14)) unterschiedlichen Skalenverhaltens aufweist (siehe Abb. 4.2). Die vier Grenzfälle werden durch drei Übergänge charakterisiert, welche sich durch Vergleich des Krümmungsradius mit den Debye-Längen beider Elektrolytlösungen sowie einer Längenskala auf Grund des Kontrasts der Dielektrizitätskonstanten ergeben.

Das abgeleitete Skalenverhalten des elektrostatischen Anteils der Grenzflächenspannung (Gl. (4.17)) ist in quantitativer Übereinstimmung mit Berechnungen im Rahmen einer (nichtlineren) Poisson-Boltzmann-Beschreibung [96] (siehe Abb. 4.3 und 4.4).

**Kristallisation von Wassertröpfchen**

Die gängigste Methode zur Stabilisierung von Öl-Wasser-Emulsionen ist die Verwendung von Emulgatoren, d.h. amphiphilen Molekülen, die durch Adsorption an die Grenzfläche eine Herabsetzung der Grenzflächenspannung oder eine Anhebung der Koaleszenzbarriere bewirken und so die Entmischungsrate reduzieren [49, 387]. Es wurde allerdings beobachtet, dass Emulsionen von Wassertröpfchen in leicht polaren Ölen auch ohne Zugabe von Emulgatoren sehr stabil sind [261] und dass sich die Wassertröpfchen in einem Kristallgitter anordnen [261, 262, 490]. Dieser Befund deutet auf eine langreichweitige Repulsion zwischen den Tröpfchen hin. In der Arbeit [491] wurde gezeigt, dass im Rahmen eines Modells einer abgeschirmten elektrostatischen Wechselwirkung (Gl. (4.22)) für Dielektrizitätskonstanten des Öls im Intervall $[4, 10]$ und Tröpfchenradien oberhalb 100 nm eine für Kristallisation genügend starke und genügend langreichweitige Wechselwirkung vorliegt (siehe Abb. 4.9).

## 4.2 Benetzungseigenschaften von Elektrolytlösungen

Die Benetzungseigenschaften von Elektrolytlösungen zeigen sich im Zusammenhang mit der effektiven Wechselwirkung zwischen zwei Oberflächen in einer elektrolytischen Umgebung [173, 248], der Stabilität von Benetzungsfilmen [102, 226, 227] und dem Phänomen der Elektrobenetzung [309]. Systematische Untersuchungen von Benetzungsübergängen in Elektrolytlösungen wurden allerdings erst kürzlich durchgeführt [101, 203, 204, 329, 330]. Problematisch an den Arbeiten [101, 329, 330] ist allerdings die Betrachtung im Rahmen der Poisson-Boltzmann-Theorie, d.h. einer Kontinuumsbeschreibung, die für dicke Benetzungsfilme sehr aufwendig ist und für dünne Benetzungsfilme kleine Debye-Längen, d.h. für die Poisson-Boltzmann-Theorie zu große Ionenstärken, verlangt. Zur Untersuchung allgemeiner Eigenschaften wurde daher in den Arbeiten [203, 204] auf ein Gittermodell (Gl. (4.25)) zurückgegriffen, das sehr dicke Benetzungsfilme zulässt. Im Rahmen dieses Modells zeigt das reine Lösungsmittel kontinuierliche Benetzungsübergänge (siehe Abb. 4.12 und 4.13) und Benetzungsübergänge erster Ordnung für nichtverschwindende Ionenstärke (siehe Abb. 4.14 und 4.16). Mit zunehmender Oberflächenladung bzw. abnehmender Ionenstärke sinkt die Benetzungstemperatur (siehe Abb. 4.15), was einer Vergrößerung der Attraktion des Lösungsmittels durch das Substrat entspricht. Die mit Benetzungsübergängen einhergehenden Vorbenetzungslinien (prewetting lines) dehnen sich mit zudehmender Wandladung in das Einphasengebiet des Gases aus (siehe Abb. 4.18).

Eine allgemeine Beobachtung, die in allen erwähnten Arbeiten [101, 203, 204, 329, 330] über Elektrolytlösungen gemacht wurde, ist die von Benetzungsübergängen erster Ordnung. Im Rahmen eines zu Gl. (2.1) ähnlichen Dichtefunktionals Gl. (4.29) wurde in der Arbeit [204] gezeigt, dass für kurzreichweitige Wechselwirkungen und nicht zu nahe an einem kritischen Punkt des Lösungsmittels der führende Beitrag zum effektiven Grenzflächenpotential durch die elektrostatische Wechselwirkung gegeben ist und auf der Skala der halben Debye-Länge abfällt (Gl. (4.32)). Nur in der Nähe kritischer Punkte

wird der führende Beitrag durch die kritische Adsorption wie im reinen Lösungsmittel bestimmt. Für die gleichzeitige Anwensenheit kurz- und langreichweitiger Wechselwirkungen des Lösungsmittels zeigt die Arbeit [204] die Möglichkeit eines unstetigen Übergangs zwischen zwei endlich dicken Benetzungsfilmen als Relikt des elektrostatisch induzierten Benetzungsübergangs erster Ordnung gefolgt von einem kontinuierlichen Benetzungsübergang auf Grund der langreichweitigen Wechselwirkung.

## 4.3 Kritische Adsorption in Elektrolytlösungen

Die Profile der Lösungsmittelkonzentration und des elektrostatischen Potentials an einem Substrat in Kontakt mit einer Elektrolytlösung lassen sich mit Hilfe des Dichtefunktionals Gl. (2.1) bestimmen [43] (siehe Abb. 4.20). Es zeigt sich [43], dass diese sehr gut durch bekannte funktionale Formen im Rahmen der Ginzburg-Landau- bzw. Poisson-Boltzmann-Theorie beschrieben werden (siehe Gln. (4.52) und (4.53)). Bei Annäherung an einen kritischen Punkt divergiert die Korrelationslänge, wodurch auch die Adsorption an einer Wand divergiert (kritische Adsorption). Dieses Phänomen, bei dem die Grenzflächenbreite divergiert, ist verschieden von einem Benetzungsübergang, bei dem ein Benetzungsfilm auftritt, dessen endlich breite Oberfläche sich makroskopisch weit vom Substrat entfernt. Um das Phänomen der kritischen Adsorption zu erfassen, wurde in der Arbeit [43] aus Gl. (2.1) ein Funktional vom Ginzburg-Landau-Typ (Gl. (4.55)) abgeleitet, in dem die elektrostatische Wechselwirkung in einem effektiven externen Feld auftritt (Gl. (4.56)). Der führende, universelle Beitrag zum Lösungsmitteldichteprofil in Gl. (4.57) ist identisch mit dem des reinen, salzfreien Lösungsmittels, während elektrostatische Einflüsse nur in den nachrangingen Beiträgen auftreten. Ähnliches gilt für die Adsorption Gl. (4.58)–(4.60), bei der der führende Beitrag auf universelle Skalenform gebracht werden kann und nur die nachfolgenden nichtuniversellen Beiträge Charakteristika, wie z.B. die Oberflächenladung, den Löslichkeitskontrast der Ionen und den Kontrast der Dielektrizitätskonstanten der Lösungsmittelkomponenten, enthalten. Diese nichtuniversellen Beiträge machen sich allerdings quantitativ bemerkbar (siehe Abb. 4.22). Insbesondere die Ionenlöslichkeit hat entscheidenden Einfluss auf das qualitative Verhalten, wie in der Arbeit [43] an Diskrepanzen der Vorhersagen im Rahmen der standardmäßigen BCA und der dort vorgeschlagenen Alternative (Gl. (2.3)) gezeigt wurde.

## 4.4 Elektrobenetzung

Elektrobenetzung wurde erstmals Ende des 19. Jahrhunderts von Lippmann [272] und Pellat [350, 351] beschrieben und man versteht heute darunter die Abhängigkeit des Kontaktwinkels eines Fluids an einem Substrat vom elektrostatischen Potential des Substrat [309]. In der Vergangenheit wurde Elektrobenetzung als Elektrokapillaritätseffekt, d.h. mit Hilfe einer Spannungsabhängigkeit der Substrat-Fluid-Grenzflächenspannung interpretiert [30, 51, 88, 93, 221, 232, 309, 350, 351, 370, 371, 411, 416, 417, 438, 469]. In der Arbeit [45] wurde dagegen argumentiert, dass diese Interpretation nicht mit der allgemeinen Theorie der Benetzungsphänomene konsistent ist und es wurden dort experimentelle Tests vorgeschlagen, um diese Frage zu entscheiden. Tatsächlich stimmen beide Interpretationen mit den ersten Experimenten von Lippmann und Pellat an Metalloberflächen und mit den heute gängigen Systemen von Elektroden, die mit einem hydrophoben Dielektrikum beschichtet sind [30], überein. Für Substrate, an die allerdings eine Elektrolytlösung

statt eines nichtleitenden Öls adsorbiert, wird nach der Interpretation von Arbeit [45] eine im Gegensatz zur tranditionellen Elektrokapillaritätsinterpretation verschwindend kleine Tendenz zur Elektrobenetzung erwartet. Experimentelle Realisierungen solcher Tests stehen aktuell noch aus.

## 4.5 Benetzungseigenschaften geladener kolloidaler Plättchen

Plättchenförmige kolloidale Teilchen spielen eine entscheidende Rolle, z.B. als Bestandteile des Erdbodens und von Beton, Füllmaterialien, Beschichtungen und rheologischen Fluiden zur Rohölförderung. Die weite Verbreitung dieser komplexen Fluide ist auf ein reiches Phasenverhalten, z.B. mit Flüssigkristallphasen und Sol-Gel-Übergängen, zurückzuführen. Neben experimentellen Untersuchungen verschiedener Suspensionen natürlicher und synthetischer Tonmineralien sowie Computersimulationen verschiedener Modellsysteme wurden v.a. theoretische Arbeiten über harte Plättchen und anisotrop geladene Scheiben unter räumlich homogenen Bedingungen untersucht. Ziel der Arbeiten [35, 36] war die Untersuchung räumlicher Inhomogenitäten elektrisch geladener Plättchen. Hierzu wurde ein vereinfachendes Modell quaderförmiger Teilchen mit diskreten Orientierungen betrachtet (siehe Abb. 4.26). Die Phasendiagramme zeigen eine isotrope und eine nematische Phase mit einem Phasenübergang erster Ordnung, dessen Position und Dichtedifferenz durch die Ionenstärke und die Plättchenladung festgelegt wird (siehe Abb. 4.27). An freien Grenzflächen zwischen der isotropen und der nematischen Phase (siehe Abb. 4.29 und 4.30) findet, wie an Grenzflächen nichtmischbarer Elektrolytlösungen (siehe Abschn. 4.1, eine Ladungstrennung statt (siehe Abb. 4.31), die sich in einem nichtkonstanten elektrostatischen Potential (siehe Abb. 4.32) äußert, dessen Potentialdifferenz zwischen den beiden Volumenphasen durch das Donnan-Potential (siehe Abb. 4.28) gegeben ist. Die Analogie zu verdünnten Elektrolytlösungen erstreckt sich aber auch auf Benetzungsphänomene (vgl. Abschn. 4.2), wobei geladene plättchenförmige Kolloide in Abhängigkeit von der elektrischen Ladung vollständige oder teilweise Benetzung eines Substrats durch einen isotropen Flüssigkeitsfilm (bei nematischer Volumenphase) oder durch einen nematischen Flüssigkeitsfilm (bei isotroper Volumenphase) zeigen (siehe Abb. 4.33). Die Benetzungsübergänge sind von erster Ordnung (vgl. Abschn. 4.2) und die Elektrostatik ist geprägt von Wechselspiel der elektrischen und der sterischen Wechselwirkung (siehe Abb. 4.42 und 4.43).

## 4.6 Kolloidale Wechselwirkungen in komplexen Elektrolytlösungen

Sieht man von der schwachen aber langreichweitigen Van-der-Waals-Wechselwirkung ab, so setzt sich die effektive Wechselwirkung zwischen kolloidalen Teilchen in einer komplexen Elektrolytlösung aus der elektrostatischen Wechselwirkung und der "solvation force" zusammen. Letztere resultiert bei Annäherung an einen kritischen Punkt der komplexen Elektrolytlösung (vgl. Abschn. 2.1) in der kritischen Casimir-Kraft [59, 149–152, 189, 239, 240, 365, 366, 408]. Experimentelle Untersuchungen [317] zeigen, dass die effektive Wechselwirkung nicht einfach eine Superposition aus elektrostatischer Wechselwirkung und "solvation force" ist: Zwei elektrisch negativ geladene Oberflächen, eine hydrophile und eine hydophobe, zeigten in einem Zwischentemperaturbereich eine attraktive effektive Wechselwirkung. In der Arbeit [42] wurde mit Hilfe des generischen

Dichtefunktionals Gl. (4.104) systematisch das effektive Grenzflächenpotential Gl. (4.108) hergeleitet, das die experimentellen Beobachtungen der Arbeit [317] qualitativ reproduzieren kann (siehe Abb. 4.45). Der die Attraktion erzeugende Mechanismus kann dadurch als die Bildung von dipolaren Schichten auf Grund einer ungleichmäßigen Partitionierung von Ionen in Lösungsmittelgradient an Wänden interpretiert werden (siehe Abb. 4.44). Ein solcher Mechanismus setzt ein ionisches komplexes Fluid als Medium voraus.

### 4.7 Kolloide an Elektrolytgrenzflächen

Kolloidale Teilchen können an Grenzflächen durch Adsorptionsenergien festgehalten werden, die die thermische Energie um mehrere Größenordnungen übersteigen [357]. Solche adsorbierten kolloidale Teilchen, die sich in lateraler Richtung frei bewegen können, bilden somit zweidimensionale Fluide. Eines der Hauptthemen im Kontext dieser zweidimensionalen Fluide ist die Strukturbildung und daher die Frage nach der (effektiven) Wechselwirkung zwischen den Kolloiden. Während der Wechselwirkungsbeitrag auf Grund der Grenzflächendeformation sowohl für große [117, 325, 480] wie auch für kleine [187] Abstände studiert wurde, wurde vor allem der Beitrag zur elektrostatischen Repulsion für große Distanzen untersucht. Der elektrostatische Beitrag für kleine Distanzen wurde erstmals in der Arbeit [283] bestimmt (siehe Abb. 4.46), nachdem in der Arbeit [118] das elektrostatische Potential um ein einzelnes Kolloid in einer Multipolentwicklung dargestellt wurde. Die exakte Lösung der linearisierten Poisson-Boltzmann-Gleichung für zwei planare Wände senkrecht zur Grenzfläche (Gl. (4.110)) kann mit der im Rahmen der Superpositionsapproximation (Gl. (4.111)) verglichen werden (siehe Abb. 4.47). Die daraus abgeleiteten Wechselwirkungen zwischen den Oberflächen und zwischen den Dreiphasenkontaktlinien zeigen markante Unterschiede zwischen den exakten Ausdrücken und denen im Rahmen der Superpositionsapproximation (siehe Abb. 4.48 und 4.49).

## 5 Schlussfolgerungen

In den vorangegangenen Kapiteln wurden verschiedene Typen ionischer komplexer Fluide besprochen, die sich mit Hilfe der Debye-Länge und anderer relevanter Längenskalen klassifizieren lassen. Bei Elektrolytlösungen ist die zusätzliche Längenskala die Korrelationslänge des Lösungsmittels, während bei Abwesenheit eines Lösungsmittels die Debye-Länge mit molekularen oder kolloidalen Längenskalen konkurriert.

In verdünnten Elektrolytlösungen konkurriert die Debye-Länge mit der Korrelationslänge des Lösungsmittels. Weit weg von einem kritischen Punkt des Lösungsmittels ist die Debye-Länge die größte Längenskala, sodass die Eigenschaften des ionischen komplexen Fluids weitgehend materialunabhängig sind und denen eines Plasma gleichen. Insbesondere sind die Struktur im Volumen (siehe Abschn. 3.1 und 3.2) und das Grenzflächenverhalten (siehe Abschn. 4.1, 4.2, 4.3, 4.4 und 4.6) durch die Abschirmung von Ladungen charakterisiert. Dahingegen wird das Phasenverhalten (siehe Abschn. 2.1), auf Grund der kurzreichweitigen Korrelationen, nur geringfügig durch die Gegenwart kleiner Mengen von Ionen beeinflusst.

In der Nähe eines kritischen Punkts des Lösungsmittels zeigt ein ionisches komplexes Fluid das universelle kritische Verhalten des reinen Lösungsmittels, da dann die Debye-Länge die Rolle einer “mikroskopischen” Länge spielt, die kleiner als die Korrelationslänge

ist (siehe Abschn. 3.1, 3.2, 4.3 und 4.6). Es zeigt sich, dass zwischen beiden Extremfällen, wenn die Debye-Länge und die Korrelationslänge von ähnlicher Größe sind, Kirkwood-Übergänge, d.h. Übergänge zwischen monotonem und gedämpft oszillatorischem Abfall der Paarkorrelationsfunktion, stattfinden (siehe Abschn. 3.1).

In "room temperature ionic liquids" (RTILs), und insbesondere in ionischen Flüssigkristallen, ist kein Lösungsmittel vorhanden und die Eigenschaften sind durch ein Wechselspiel zwischen der Debye-Länge und molekularen Längen der Teilchen bestimmt. Für dichte RTILs ist die Debye-Länge (viel) kleiner als die molekulare Größe, sodass sich diese Systeme größtenteils ähnlich zu nichtionischen komplexen Fluiden mit echten kurzreichweitigen Wechselwirkungen, z.B. auf Grund von chemischen Bindungen verhalten (siehe Abschn. 3.4). Eine Konsequenz ist die Bildung von Mikroheterogenitäten auf Grund der Gegenwart von polaren und unpolaren Teilen der organischen Moleküle und von Mesophasen ionischer Flüssigkristalle (siehe Abschn. 2.3). Diese hängen empfindlich von den Details der chemischen Struktur der Moleküle ab. Lediglich elektrische Observablen, wie z.B. die dielekrische Funktion (siehe Abschn. 3.3), weisen für große Längenskalen auf eine materialunabhängige plasmaähnliche freie Bewegung von Ionen hin. In verdünnten RTILs (siehe Abschn. 2.2) ist die Debye-Länge (viel) größer als die Teilchengröße, was zu einem Verhalten ähnlich eines Plasmas punktförmiger Teilchen führt.

In kolloidalen Suspensionen können alle drei Längenskalen (die Größe der kolloidalen Teilchen, die Debye-Länge und die Korrelationslänge des Lösungsmittels) relevant sein. Die Größe der kolloidalen Teilchen ist typischerweise die größte, was zu materialunabhängigem aber geometrieabhängigem dominantem Verhalten harter Teilchen mit charakteristischen Phasen kolloidaler Kristalle (siehe Abschn. 2.4) und Flüssigkristalle (siehe Abschn. 2.3) führt. Einerseits, weit weg von einem kritischen Punkt des Lösungsmittels, bewirkt die Abschirmung von kolloidalen Oberflächenladungen auf der Skala der Debye-Länge die führende Korrektur zu Verhalten harter Teilchen. Diese Korrektur ist wiederum materialunabhängig und sie bewirkt Ähnlichkeiten von kolloidalen Suspensionen zu RTILs (z.B. ionischen Flüssigkristallen) und Elektrolytlösungen (siehe Abschn. 4.5). Andererseits, in der Nähe kritischer Punkte des Lösungsmittels, dominiert die kritische Casimir-Kraft auf der Längenskala der Korrelationslänge gegenüber der elektrostatischen Wechselwirkung (siehe Abschn. 4.6). Unter bestimmten Umbständen bilden sich jedoch noch komplexere Strukturen, wie z.B. die dipolaren Schichten aus Ionen, die in Konzentrationsgradienten des Lösungsmittels ungleichmäßig partitioniert werden, welche zu einer verwickelten effektiven Wechselwirkung zwischen kolloidalen Teilchen führen (siehe Abschn. 4.6) oder die Fluidstruktur zwischen zwei kolloidalen Teilchen, die sich an der Grenzfläche zwischen zwei nichtmischbaren ionischen komplexen Fluiden befinden, welche eine effektive Wechselwirkung der Kolloide generiert, mit Beiträgen von den kolloidalen Oberflächen und den Dreiphasenkontaktlinien (siehe Abschn. 4.7).

Die obigen Betrachtungen weisen darauf hin, dass der Schlüssel zum Verständnis der feinen Details von Systemen weicher Materie, die durch Fortschritte in der experimentellen Technik zugänglich wurden, und einiger bekannter aber noch nicht vollständig verstandener Phänomene, wie z.B. die Aggregation kolloidaler Suspensionen oder die Faltung von Proteinen, die Berücksichtigung der Eigenschaften ionischer komplexer Fluide, z.B. des Dispersionsmediums, ist.

Die vorliegende Habilitationsschrift beschränkt sich auf statische allgemeine Eigenschaften ionischer komplexer Fluide, und es wurde in den vorangegangenen Kapiteln gezeigt, dass bei einer Klassifikation statischer allgemeiner Eigenschaften komplexer Fluide auf

Grund der konkurrierenden Längenskalen ionische komplexe Fluide von besonderem Interesse sind, da die Debye-Länge weitgehend materialunabhängig ist und im wichtigen Fall verdünnter Elektrolytlösungen klar nach unten hin gegenüber der molekularen Längenskala und nach oben hin gegenüber der kolloidalen Längenskala abgegrenzt ist. Für dynamische Eigenschaften gibt es nicht nur eine Hierarchie von Längen-, sondern auch von Zeitskalen, welche die Eigenschaften bestimmen. Bekannte Beispiele dieser Situation gibt es für Polymere [115, 383], Grenzflächen nichtmischbarer Elektrolytlösungen [156, 171, 374, 398–400, 458] und kolloidale Suspensionen [38, 104, 166, 385]. Auf Grund der Vielzahl an Zeitskalen ist es üblich, die Dynamik komplexer Fluide auf den einzelnen Zeitskalen zu studieren. Im Gegensatz zu den typischen Längenskalen, die für statische Eigenschaften relevant sind, hängen die relevanten Zeitskalen für die Dynamik eines komplexen Fluids stark vom System ab. Dies verhindert im Wesentlichen eine allgemeine, d.h. systemunabhängige, Klassifikation. Daher ist die Existenz von drei klar getrennten Längenskalenbereichen zur Klassifikation der allgemeinen, d.h. systemunabhängigen, Phänomene komplexer Fluide und die Identifikation ionischer komplexer Fluide als Materialklasse, die alle Fälle abdeckt, eine Besonderheit statischer Eigenschaften von Systemen weicher Materie.

# Bibliography


[1] D. Adam, P. Schuhmacher, J. Simmerer, L. Häussling, K. Siemensmeyer, K.H. Etzbach, H. Ringsdorf and D. Haarer, *Fast photoconduction in the highly ordered columnar phase of a discotic liquid crystal*, Nature **371**, 141 (1994).

[2] A.W. Adamson, *A textbook of physical chemistry* (Academic Press, New York, 1973).

[3] A.W. Adamson and A.P. Gast, *Physical chemistry of surfaces* (Wiley, New York, 1997).

[4] R. Agra, E. Trizac and L. Bocquet, *The interplay between screening properties and colloid anisotropy: Towards a reliable pair potential for disc-like charged particles*, Eur. Phys. J. E **15**, 345 (2004).

[5] M.P. Allen and D.J. Tildesley, *Computer simulation of liquids* (Oxford University Press, 1987).

[6] A.J. Archer, P. Hopkins and M. Schmidt, *Dynamics in inhomogeneous liquids and glasses via the test particle limit*, Phys. Rev. E **75**, 040501 (2007).

[7] M. Armand, F. Endres, D.R. MacFarlane, H. Ohno and B. Scrosati, *Ionic-liquid materials for the electrochemical challenges of the future*, Nature Mater. **8**, 621 (2009).

[8] S. Arrhenius, *Über die Dissociation der in Wasser gelösten Stoffe* Z. phys. Chem. **1**, 631 (1887).

[9] P.W. Atkins, *Physical chemistry* (Oxford University Press, Oxford, 1998).

[10] M. Aubouy, E. Trizac and L. Bocquet, *Effective charge versus bare charge: an analytical estimate for colloids in the infinite dilution limit*, J. Phys. A **36**, 5835 (2003).

[11] T. Aukrust and E.H. Hauge, *Nonuniversal $\nu$ from a van der Waals Theory of the Wetting Transition*, Phys. Rev. Lett. **54**, 1814 (1985).

[12] R. Aveyard and S.M. Saleem, *Interfacial tensions at alkane-aqueous electrolyte interfaces*, J. Chem. Soc. Faraday Trans. 1 **72**, 1609 (1976).

[13] R. Aveyard, B.P. Binks and J. Mead, *Interfacial tension minima in oil + water + surfactant systems — Effects of salt, temperature and alkane in systems containing ionic surfactants*, J. Chem. Soc. Faraday Trans. 1 **81**, 2169 (1985);

[14] R. Aveyard, B.P. Binks, S. Clark and J. Mead, *Interfacial tension minima in oil water surfactant systems — Behavior of alkane aqueous NaCl systems containing aerosol OT*, J. Chem. Soc. Faraday Trans. 1 **82**, 125 (1986);

[15] R. Aveyard, B.P. Binks and J. Mead, *Interfacial tension minima in oil water surfactant systems — Effects of alkane chain length and presence of normal alkanols in systems containing aerosol OT*, J. Chem. Soc. Faraday Trans. 1 **82**, 1755 (1986);

[16] R. Aveyard, J.H. Clint, D. Nees and V.N. Paunov, *Compression and structure of monolayers of charged latex particles at air/water and octane/water interfaces*, Langmuir **16**, 1969 (2000).

[17] R. Aveyard, B.P. Binks, J.H. Clint, P.D.I. Fletcher, T.S. Horozov, B. Neumann, V.N. Paunov, J. Annesley, S.W. Botchway, D. Nees, A.W. Parker, A.D. Ward and A.N. Burgess, *Measurement of long-range repulsive forces between charged particles at an oil-water interface*, Phys. Rev. Lett. **88**, 246102 (2002).

[18] R. Aveyard, B.P. Binks and J.H. Clint, *Emulsions stabilised solely by colloidal particles*, Adv. Colloid Interface Sci. **100-102**, 503 (2003);

[19] K.V. Axenov and S. Laschat, *Thermotropic Ionic Liquid Crystals*, Materials **4**, 206 (2011).

[20] V.S. Bagotsky, *Fundamentals of electrochemistry* (Wiley, Hoboken, 2006).

[21] C.D. Bain, *Studies of adsorption at interfaces by optical techniques: ellipsometry, second harmonic generation and sum-frequency generation*, Curr. Opin. Colloid Interface Sci. **3**, 287 (1998).

[22] J. Barrett, *First-order correction to classical nucleation theory: A density functional approach*, J. Chem. Phys. **111**, 5938 (1999).

[23] J.L. Barton and H. Bloom, *A boiling point method for determination of vapor pressures of molten salts*, J. Phys. Chem. **60**, 1413 (1956).

[24] H. Bartsch, O. Dannenmann and M. Bier, *Thermal and structural properties of ionic fluids*, Phys. Rev. E **91**, 042146 (2015).

[25] M.A. Bates and G.R. Luckhurst, *Computer simulation studies of anisotropic systems. XXX. The phase behavior and structure of a Gay-Berne mesogen*, J. Phys. Chem. **110**, 7087 (1999).

[26] S.H. Behrens and D.G. Grier, *The charge of glass and silica surfaces*, J. Chem. Phys. **115**, 6716 (2001).

[27] M.L. Bellac, *Quantum and Statistical Field Theory*, (Oxford University Press, 1991).

[28] A. Ben-Simon, H. Eshet and E. Rabani, *On the Phase Behavior of Binary Mixtures of Nanoparticles*, ACS Nano **7**, 978 (2013).

[29] D. Ben-Yaakov, D. Andelman, D. Harries and R. Podgornik, *Ions in Mixed Dielectric Solvents: Density Profiles and Osmotic Pressure between Charged Interfaces*, J. Phys. Chem. B **113**, 6001 (2009).

[30] B. Berge, *Électrocapillarité et mouillage de filmes isolants par l'eau*, C. R. Acad. Sci. II **317**, 157 (1993).

[31] M.D. Bermúdez, A.E. Jiménez, J. Sanes and F.J. Carrión, *Ionic Liquids as Advanced Lubricant Fluids*, Molecules **14**, 2888 (2009).

[32] R.D. Bezman, E.F. Casassa and R.L. Kay, *The temperature dependence of the dielectric constants of alkanols*, J. Mol. Liq. **73**, 397 (1997).

[33] H.L. Bianchi and M.L. Japas, *Phase equilibria of a near-critical ionic system. Critical exponent of the order parameter*, J. Chem. Phys. **115**, 10472 (2001).

[34] M. Bier, L. Harnau and S. Dietrich, *Bulk and interfacial properties of binary hard-platelet fluids*, Phys. Rev. E **69**, 021506 (2004).

[35] M. Bier, L. Harnau and S. Dietrich, *Free isotropic-nematic interfaces in fluids of charged platelike colloids*, J. Chem. Phys. **123**, 114906 (2005).

[36] M. Bier, L. Harnau and S. Dietrich, *Surface properties of fluids of charged platelike colloids*, J. Chem. Phys. **125**, 184704 (2006).

[37] M. Bier, J. Zwanikken and R. van Roij, *Liquid-liquid interfacial tension of electrolyte solutions*, Phys. Rev. Lett. **101**, 046104 (2008).

[38] M. Bier, R. van Roij, M. Dijkstra and P. van der Schoot, *Self diffusion of particles in complex fluids: temporary cages and permanent barriers*, Phys. Rev. Lett. **101**, 215901 (2008).

[39] M. Bier, J. de Graaf, J. Zwanikken and R. van Roij, *Curvature dependence of the electrolytic liquid-liquid interfacial tension*, J. Chem. Phys. **130**, 024703 (2009).

[40] M. Bier and S. Dietrich, *Vapour pressure of ionic liquids*, Mol. Phys. **108**, 211 (2010) [Corrigendum: Mol. Phys. **108**, 1413 (2010)].

[41] M. Bier, R. van Roij and M. Dijkstra, *Phase diagrams of binary mixtures of oppositely charged colloids*, J. Chem. Phys. **133**, 124501 (2010).

[42] M. Bier, A. Gambassi, M. Oettel and S. Dietrich, *Electrostatic interactions in critical solvents*, EPL **95**, 60001 (2011).

[43] M. Bier, A. Gambassi and S. Dietrich, *Local theory for ions in binary liquid mixtures*, J. Chem. Phys. **137**, 034504 (2012).

[44] M. Bier and L. Harnau, *The Structure of Fluids with Impurities*, Z. Phys. Chem. **226**, 807 (2012).

[45] M. Bier and I. Ibagon, *Density functional theory of electrowetting*, Phys. Rev. E **89**, 042409 (2014).

[46] K. Binder and D.P. Landau, *Wetting and layering in the nearest-neighbor simple-cubic Ising lattice: A Monte Carlo investigation*, Phys. Rev. B **37**, 1745 (1988).

[47] K. Binder, D.P. Landau and S. Wansleben, *Wetting transitions near the bulk critical point: Monte Carlo simulations for the Ising model*, Phys. Rev. B **40**, 6971 (1989).

[48] B.P. Binks, W.G. Cho, P.D.I. Fletcher, D.N. Petsev, *Stability of oil-in-water emulsions in a low interfacial tension system* Langmuir **16**, 1025 (2000).

[49] B.P. Binks, *Particles as surfactants — similarities and differences*, Curr. Opinion Colloid Interface Sci. **7**, 21 (2002).

[50] K. Binnemans, *Ionic liquid crystals*, Chem. Rev. **105**, 4148 (2005).

[51] T.D. Blake, A. Clarke, and E.H. Stattersfield, *An investigation of electrostatic assist in dynamic wetting*, Langmuir **16**, 2928 (2000).

[52] E.M. Blokhuis and D. Bedeaux, *Derivation of microscopic expressions for the rigidity constants of a simple liquid vapor interface*, Physica A **184**, 42 (1992).

[53] D. Bochicchio, A. Videcoq and R. Ferrando, *Kinetically driven ordered phase formation in binary colloidal crystals*, Phys. Rev. E **87**, 022304 (2013).

[54] L. Bocquet, E. Trizac and M. Aubouy, *Effective charge saturation in colloidal suspensions*, J. Chem. Phys. **117**, 8138 (2002).

[55] C.J.F. Böttcher, *Theory of Electric Polarization* (Elsevier, Amsterdam, 1973).

[56] G.H. Bolt and W.H. van Riemsdijk, *Ion adsorption on inorganic variable charge constituents*, in *Soil Chemistry. B. Physico-chemical Models*, edited by G.H. Bolt (Elsevier, Amsterdam, 1982), p. 459.

[57] D. Bonn and D. Ross, *Wetting transitions*, Rep. Prog. Phys. **64**, 1085 (2001).

[58] D. Bonn, J. Eggers, J. Indekeu, J. Meunier and E. Rolley, *Wetting and spreading*, Rev. Mod. Phys. **81**, 739 (2009).

[59] D. Bonn, J. Otwinowski, S. Sacanna, H. Guo, G. Wegdam and P. Schall, *Direct Observation of Colloidal Aggregation by Critical Casimir Forces* Phys. Rev. Lett. **103**, 156101 (2009).

[60] M. Born, *Volumen und Hydratationswärme der Ionen*, Z. Phys. **1**, 45 (1920).

[61] A.E. Bradley, C. Hardacre, J.D. Holbrey, S. Johnston, S.E.J. McMath and M. Nieuwenhuyzen, *Small-angle X-ray scattering studies of liquid crystalline 1-alkyl-3-methylimidazolium salts*, Chem. Mater. **14**, 629 (2002).

[62] K. Breitsprecher, P. Košovan and C. Holm, *Coarse-grained simulations of an ionic liquid-based capacitor: I. Density, ion size, and valency effects*, J. Phys.: Condens. Matter **26**, 284108 (2014).

[63] K. Breitsprecher, P. Košovan and C. Holm, *Coarse-grained simulations of an ionic liquid-based capacitor: II. Asymmetry in ion shape and charge localization*, J. Phys.: Condens. Matter **26**, 284114 (2014).

[64] K. Breitsprecher, K. Szuttor and C. Holm, *Electrode Models for Ionic Liquid-Based Capacitors*, J. Phys. Chem. C **119**, 22445 (2015).

[65] British Ceramic Society, *Clay and other colloidal systems*, Proc. Brit. Ceramic Soc. **13** (British Ceramic Society, Stoke-on-Trent, 1969).

[66] J.T. Brown, M.P. Allen, E.M. del Rio and E. de Miguel, *Effects of elongation on the phase behavior of the Gay-Berne fluid*, Phys. Rev. E **57**, 6685 (1998).

[67] A.B.D. Brown, S.M. Clarke and A.R. Rennie, *Ordered phase of platelike particles in concentrated dispersions*, Langmuir **14**, 3129 (1998).

[68] A.B.D. Brown, C. Ferrero, T. Narayanan and A.R. Rennie, *Phase separation and structure in a concentrated colloidal dispersion of uniform plates*, Eur. Phys. J. B **11**, 481 (1999).

[69] F.P. Buff and F.H. Stillinger, *Surface tension of ionic solutions*, J. Chem. Phys. **25**, 312 (1956).

[70] J.W. Cahn and J.E. Hilliard, *Free Energy of a Nonuniform System. I. Interfacial Free Energy*, J. Chem. Phys. **28**, 258 (1958).

[71] P.J. Camp, C.P. Mason, M.P. Allen, A.A. Khare and D.A. Kofke, *The isotropic-nematic phase transition in uniaxial hard ellipsoid fluids: Coexistence data and the approach to the Onsager limit*, J. Phys. Chem. **105**, 2837 (1996).

[72] D.N. Card and J.P. Valleau, *Monte Carlo Study of the Thermodynamics of Electrolyte Solutions*, J. Chem. Phys. **52**, 6232 (1970).

[73] P.M. Chaikin and T.C. Lubensky, *Principles of Condensed Matter Physics* (Cambridge University Press, 2000).

[74] D. Chan, J.W. Perram, L.R. White and T.W. Healy, *Regulation of surface potential at amphoteric surfaces during particle-particle interaction*, J. Chem. Soc.: Faraday Trans. I **71**, 1046 (1975).

[75] D.L. Chapman, *A Contribution to the Theory of Electrocapillarity*, Philos. Mag. **25**, 475 (1913).

[76] W. Chen, S. Tan, Y. Zhou, T.-K. Ng, W.T. Ford and P. Tong, *Attraction between weakly charged silica spheres at a water-air interface induced by surface-charge heterogeneity*, Phys. Rev. E **79**, 041403 (2009).

[77] Q. Chen, S.C. Bae and S. Granick, *Directed self-assembly of a colloidal kagome lattice*, Nature **469**, 381 (2011).

[78] N.V. Churaev and Z.M. Zorin, *Wetting films*, Adv. Colloid Interface Sci. **40**, 109 (1992).

[79] N.V. Churaev, *Surface forces in wetting films*, Adv. Colloid Interface Sci. **103**, 197 (2003).

[80] A. Ciach and A. Maciołek, *Distribution of ions near a charged selective surface in critical binary solvents*, Phys. Rev. E **81**, 041127 (2010).

[81] D.J. Cleaver, C.M. Care, M.P. Allen and M.P. Neal, *Extension and generalization of the Gay-Berne potential*, Phys. Rev. E **54**, 559 (1996).

[82] D. Costa, J.-P. Hansen and L. Harnau, *Structure and equation of state of interaction site models for disc-shaped lamellar colloids*, Mol. Phys. **103**, 1917 (2005).

[83] J.A. Cuesta and Y. Martínez-Ratón, *Dimensional crossover of the fundamental-measure functional for parallel hard cubes*, Phys. Rev. Lett. **78**, 3681 (1997).

[84] J.A. Cuesta and Y. Martínez-Ratón, *Fundamental measure theory for mixtures of parallel hard cubes. 1. General formalism*, J. Chem. Phys. **107**, 6379 (1997).

[85] J.A. Cuesta and R.P. Sear, *Phase transitions in simple models of rod-like and disc-like micelles*, Eur. Phys. J. B **8**, 233 (1999).

[86] C. Daguenet, P.J. Dyson, I. Krossing, A. Oleinikova, J. Slattery, Ch. Wakai and H. Weingärtner, *Dielectric response of imidazolium-based room-temperature ionic liquids*, J. Phys. Chem. B **110**, 12682 (2006).

[87] K.D. Danov, P.A. Kralchevsky and M.P. Boneva, *Electrodipping force acting on solid particles at a fluid interface*, Langmuir **20**, 6139 (2004).

[88] C.D. Daub, D. Bratko, and A. Luzar, *Nanoscale Wetting Under Electric Field from Molecular Simulations*, in *Multiscale molecular methods in applied chemistry*, Top. Curr. Chem. **307**, edited by B. Kirchner and J. Vrabec (Springer, Berlin 2012), p. 155.

[89] P. Davidson and J.-Ch.P. Gabriel, *Mineral liquid crystals*, Curr. Opin. Colloid Interface Sci. **9**, 377 (2005).

[90] J.A. Davis, R.O. James and J.O. Leckie, *Surface ionization and complexation at oxide-water interfaxce. 1. Computation of electrical double-layer properties in simple electrolytes*, J. Colloid Interface Sci. **63**, 480 (1978).

[91] P. Debye and E. Hückel, *Zur Theorie der Elektrolyte*, Phys. Z. **24**, 185 (1923).

[92] P. Debye and E. Hückel, *Zur Theorie der Elektrolyte. II*, Phys. Z. **24**, 305 (1923).

[93] C. Decamps and J. De Coninck, *Dynamics of spontaneous spreading under electrowetting conditions*, Langmuir **16**, 10150 (2000).

[94] P.G. de Gennes, *Wetting: statics and dynamics*, Rev. Mod. Phys. **57**, 827 (1985).

[95] P.-G. de Gennes, F. Brochard-Wyart, and D. Queré, *Capillarity and Wetting Phenomena* (Springer, New York, 2004).

[96] J. de Graaf, J. Zwanikken, M. Bier, A. Baarsma, Y. Oloumi, M. Spelt and R. van Roij, *Spontaneous Charging and Crystallization of Water Droplets in Oil*, J. Chem. Phys. **129**, 194701 (2008).

[97] E. de Miguel, L.F. Rull, M.K. Chalam and K.E. Gubbins, *Liquid crystal phase diagram of the Gay-Berne fluid*, Mol. Phys. **74**, 405 (1991).

[98] E. de Miguel, E.M. del Rio, J.T. Brown and M.P. Allen, *Effect of the attractive interactions on the phase behavior of the Gay-Berne liquid crystal model*, J. Phys. Chem. **105**, 4234 (1996).

[99] E. de Miguel and C. Vega, *The global phase diagram of the Gay-Berne model*, J. Phys. Chem. **117**, 6313 (2002).

[100] N.A. Denesyuk and J.-P. Hansen, *A mean-field theory of wetting by ionic solutions*, Europhys. Lett. **63**, 261 (2003).

[101] N.A. Denesyuk and J.-P. Hansen, *Wetting transitions of ionic solutions*, J. Chem. Phys. **121**, 3613 (2004).

[102] B.V. Derjaguin and N.V. Churaev, *Structural component of disjoining pressure*, J. Colloid Interface Sci. **49**, 249 (1974).

[103] J. de Roche, C.M. Gordon, C.T. Imrie, M.D. Ingram, A.R. Kennedy, F. Lo Celso and A. Triolo, *Application of complementary experimental techniques to characterization of the phase behavior of [C(16)mim][PF6] and [C(14)mim][PF6]*, Chem. Mater. **15**, 3089 (2003).

[104] J.K.G. Dhont, *An introduction to dynamics of colloids* (Elsevier, Amsterdam 1996).

[105] R. Dickman and G. Stell, *Phase diagram of the lattice restricted primitive model*, AIP Conf. Proc. **492**, 225 (1999).

[106] S. Dietrich and M. Schick, *Critical wetting of surfaces in systems with long-range forces*, Phys. Rev. B **31**, 4718 (1985).

[107] S. Dietrich, *Wetting Phenomena*, in *Phase Transitions and Critical Phenomena*, Vol. 12, edited by C. Domb and J.L. Lebowitz (Academic Press, London, 1988), p. 1.

[108] S. Dietrich and M. Napiórkowski, *Analytical results for wetting transitions in the presence of van der Waals tails*, Phys. Rev. A **43**, 1861 (1991).

[109] S. Dietrich and A. Haase, *Scattering of x-rays and neutrons at interfaces*, Phys. Rep. **260**, 1 (1995).

[110] R. Digilov, *Charge-induced modification of contact angle: The secondary electrocapillary effect*, Langmuir **16**, 6719 (2000).

[111] M. Dijkstra, J.-P. Hansen and P.A. Madden, *Statistical model for the structure and gelation of smectite clay suspensions*, Phys. Rev. E **55**, 3044 (1997).

[112] M. Dijkstra, *Computer simulations of charge and steric stabilised colloidal suspensions*, Curr. Opin. Colloid Interface Sci. **6**, 372 (2001).

[113] A.D. Dinsmore, M.F. Hsu, M.G. Nikolaides, M. Márquez, A.R. Bausch and D.A. Weitz, *Colloidosomes: Selectively permeable capsules composed of colloidal particles*, Science **298**, 1006 (2002).

[114] Z. Dogic and S. Fraden, *Phase Behavior of Rod-Like Viruses and VirusSphere Mixtures*, in *Soft Matter*, Vol. 2, edited by G. Gompper and M. Schick (Wiley, Berlin, 2006), p. 1.

[115] M. Doi and S.F. Edwards, *The theory of polymer dynamics* (Oxford University Press, 1998).

[116] M. Dole, *A theory of surface tension of aqueous solutions*, J. Am. Chem. Soc. **60**, 904 (1938).

[117] A. Domínguez, M. Oettel and S. Dietrich, *Theory of capillary-induced interactions beyond the superposition approximation*, J. Chem. Phys. **127**, 204706 (2007).

[118] A. Domínguez, D. Frydel and M. Oettel, *Multipole expansion of the electrostatic interaction between charged colloids at interfaces*, Phys. Rev. E **77**, 020401(R) (2008).

[119] F. Dommert, K. Wendler, R. Berger, L. Delle Site and C. Holm, *Force Fields for Studying the Structure and Dynamics of Ionic Liquids: A Critical Review of Recent Developments*, ChemPhysChem **13**, 1625 (2012).

[120] F. Dommert, K. Wendler, B. Qiao, L. Delle Site and C. Holm, *Generic force fields for ionic liquids*, J. Mol. Liq. **192**, 32 (2014).

[121] F.G. Donnan, *Theorie der Membrangleichgewichte und Membranpotentiale bei Vorhandensein von nicht-dialysierenden Elektrolyten. Ein Beitrag zur physikalisch-chemischen Physiologie*, Z. Elektrochem. **17**, 572 (1911).

[122] F.G. Donnan, *The theory of membrane equilibria*, Chem. Rev. **1**, 73 (1924).

[123] M.J. Earle, J.M.S.S. Esperança, M.A. Gilea, J.N. Canongia Lopes, L.P.N. Rebelo, J.W. Magee, K.R. Seddon and J.A. Widegren, *The distillation and volatility of ionic liquids*, Nature **439**, 831 (2005).

[124] C. Ebner, *Film formation on a weakly attractive substrate within the lattice-gas model*, Phys. Rev. A **22**, 2776 (1980).

[125] C. Ebner, *Evidence for the roughening and wetting transitions in the lattice-gas model of adsorption from Monte Carlo simulations*, Phys. Rev. A **23**, 1925 (1981).

[126] C. Ebner, W.F. Saam and A.K. Sen, *Critical and multicritical wetting phenomena in systems with long-range forces*, Phys. Rev. B **31**, 6134 (1985).

[127] E.L. Eckfeldt and W.W. Lucasse, *The liquid-liquid phase equilibria of the system cyclohexane-methyl alcohol in the presence of various salts as third components* J. Phys. Chem. **47**, 164 (1943).

[128] E. Eggen, M. Dijkstra and R. van Roij, *Effective shape and phase behavior of short charged rods*, Phys. Rev. E **79**, 041401 (2009).

[129] V.N. Emel'yanenko, S.P. Verevkin and A. Heintz, *The gaseous enthalpy of formation of the ionic liquid 1-butyl-3-methylimidazolium dicyanamide from combustion calorimetry, vapor pressure measurements and ab initio calculations*, J. Am. Chem. Soc. **129**, 3930 (2007).

[130] D. Ershov, J. Sprakel, J. Appel, M.A. Cohen Stuart and J. van der Gucht, *Capillarity-induced ordering of spherical colloids on an interface with anisotropic curvature*, Proc. Natl. Acad. Sci. USA **110**, 9220 (2013).

[131] R. Evans, *The nature of the liquid-vapour interface and other topics in the statistical mechanics*, Adv. Phys. **28**, 143 (1979).

[132] R. Evans, *Microscopic theories of simple fluids and their interfaces*, in *Les Houches, Session XLVIII, 1988 — Liquides aux interfaces / Liquids at interfaces*, edited by J. Charvolin, J.F. Joanny and J. Zinn-Justin (North-Holland, Amsterdam, 1988), p. 1.

[133] R. Evans, *Density Functionals in the Theory of Nonuniform Fluids*, in *Fundamentals of Inhomogeneous Fluids*, edited by D. Henderson (Marcel Dekker, New York, 1992), p. 85.

[134] R. Evans, J.R. Henderson, D.C. Hoyle, A.O. Parry, and Z.A. Sabeur, *Asymptotic decay of liquid structure — oscillatory liquid-vapor density profiles and the Fisher-Widom line*, Mol. Phys. **80**, 755 (1993)

[135] R. Evans, R.J.F. Leote de Carvalho, J.R. Henderson, and D.C. Hoyle, *Asymptotic decay of correlations in liquids and their mixtures*, J. Chem. Phys. **100**, 591 (1994).

[136] D.H. Everett, *Basic Principles of Colloid Science*, RSC Paperbacks (The Royal Society of Chemistry, London, 1988).

[137] P.P. Ewald, *Die Berechnung optischer und elektrostatischer Gitterpotentiale*, Ann. Physik **369**, 253 (1921).

[138] M. Fedorov and A.A. Kornyshev, *Ionic liquid near a charged wall: Structure and capacitance of electrical double layer*, J. Phys. Chem. B **112**, 11868 (2008).

[139] M.P.A. Fisher and M. Wortis, *Curvature corrections to the surface tension of fluid drops — Landau theory and scaling hypothesis*, Phys. Rev. B **29**, 6252 (1984).

[140] M.E. Fisher, *The story of Coulombic Critiality*, J. Stat. Phys. **75**, 1 (1994).

[141] G. Flöter and S. Dietrich, *Universal amplitudes and profiles for critical adsorption*, Z. Physik B **97**, 213 (1995).

[142] L. Foret and A. Würger, *Electric-field induced capillary interaction of charged particles at a polar interface*, Phys. Rev. Lett. **92**, 058302 (2004).

[143] P.A. Forsyth, S. Marčelja, D.J. Mitchell and B.W. Ninham, *Ordering in colloidal systems*, Adv. Colloid Interface Sci. **9**, 37 (1978).

[144] M. Franco-Melgar, A.J. Haslam and G. Jackson, *A generalisation of the Onsager trial-function approach: describing nematic liquid crystals with an algebraic equation of state*, Mol. Phys. **106**, 649 (2008).

[145] C.P. Fredlake, J.M. Crosthwaite, D.G. Hert, S. N.V.K. Aki and J.F. Brennecke, *Thermophysical properties of imidazolium-based ionic liquids*, J. Chem. Eng. Data **49**, 954 (2004).

[146] D. Frenkel and B. Smit, *Understanding molecular simulation: from algorithms to applications* (Academic Press, San Diego, 2002).

[147] S. Fuller, N.N. Shinde and G.J.T. Tiddy, *Thermotropic and lyotropic mesophase behavior of amphitropic diammonium surfactants*, Langmuir **12**, 1117 (1996).

[148] J.-Ch.P. Gabriel, C. Sanchez and P. Davidson, *Observation of nematic liquid-crystal textures in aqueous gels of smectite clays*, J. Phys. Chem. **100**, 11139 (1996).

[149] A. Gambassi, A. Maciołek, C. Hertlein, U. Nellen, L. Helden, C. Bechinger and S. Dietrich, *Critical Casimir effect in classical binary liquid mixtures*, Phys. Rev. E **80**, 061143 (2009).

[150] A. Gambassi, *The Casimir effect: from quantum to critical fluctuations*, J. Phys.: Conf. Ser. **161**, 012037 (2009).

[151] A. Gambassi and S. Dietrich, *Colloidal Aggregation and Critical Casimir Forces*, Phys. Rev. Lett. **105**, 059601 (2010).

[152] A. Gambassi and S. Dietrich, *Critical Casimir forces steered by patterned substrates*, Soft Matter **7**, 1247 (2011).

[153] J.G. Gay and B.J. Berne, *Modification of the overlap potential to mimic a linear site-site potential*, J. Phys. Chem. **74**, 3316 (1981).

[154] M.A. Gebbie, M. Valtiner, X. Banquy, E.T. Fox, W.A. Henderson and J.N. Israelachvili, *Ionic liquids behave as dilute electrolyte solutions*, Proc. Nat. Acad. Sci. USA **110**, 9674 (2013).

[155] M.A. Gebbie, M. Valtiner, X. Banquy, W.A. Henderson and J.N. Israelachvili, *Reply to Perkin et al.: Experimental observations demonstrate that ionic liquids form both bound (Stern) and diffuse electric double layers*, Proc. Nat. Acad. Sci. USA **110**, E4122 (2013).

[156] G. Geblewicz, Z. Figaszewski, and Z. Koczorowski, *Study of the impedance of the water- 1,2-dichloroethane interface — Influence of the picrate ion transfer*, J. Electroanal. Chem. **177**, 1 (1984).

[157] T. Getta and S. Dietrich, *Line tension between fluid phases and a substrate*, Phys. Rev. E **57**, 655 (1998).

[158] J.W. Gibbs, *The scientific papers*, Vol. 1 (Longmans, London, 1961).

[159] H.H. Girault and D.J. Schiffrin, *Thermodynamic surface excess of water and ionic solvation at the interface between immiscible liquids*, J. Electroanal. Chem. **150**, 43 (1983).

[160] C.M. Gordon, J.D. Holbrey, A.R. Kennedy and K.R. Seddon, *Ionic liquid crystals: hexafluorophosphate salts*, J. Mater. Chem. **8**, 2627 (1998).

[161] M. Gouy, *Sur la constitution de la charge électrique à la surface d'un électrolyte*, C. R. Acad. Sci. **149**, 654 (1909(.

[162] M. Gouy, *Sur la constitution de la charge électrique à la surface d'un électrolyte*, J. Physique **9**, 457 (1910).

[163] H. Graf and H. Löwen, *Phase diagram of tobacco mosaic virus solutions*, Phys. Rev. E **59**, 1932 (1999).

[164] D.C. Grahame, *The electrical double layer and the theory of electrocapillarity*, Chem. Rev. **41**, 441 (1947).

[165] T.L. Greaves and C.J. Drummond, *Protic Ionic Liquids: Properties and Applications*, Chem. Rev. **108**, 206 (2008).

[166] E. Grelet, M.P. Lettinga, M. Bier, R. van Roij and P. van der Schoot, *Dynamical and structural insights into the smectic phase of rod-like particles*, J. Phys.: Condens. Matter **20**, 494213 (2008).

[167] B. Groh, R. Evans and S. Dietrich, *Liquid-vapor interface of an ionic fluid*, Phys. Rev. E **57**, 6944 (1998).

[168] W.L. Guest and W.C.M. Lewis, *The effect of electrolytes upon the interfacial tension between water and dekalin (trans-decahydronaphtalene)*, Proc. Roy. Soc. London A **170**, 501 (1939).

[169] P. Habdas and E.R. Weeks, *Video microscopy of colloidal suspensions and colloidal crystals*, Curr. Opin. Colloid Interface Sci. **7**, 196 (2002).

[170] T. Hahn and S. Hardt, *Concentration and Size Separation of DNA Samples at Liquid-Liquid Interfaces*, Anal. Chem. **83**, 5476 (2011).

[171] P. Hájková, D. Homolka, V. Mareček, and Z. Samec, *The double layer at the interface between 2 immiscible electrolyte solutions — Capacity of the water - 1,2-dichloroethane interface*, J. Electroanal. Chem. **151**, 277 (1983).

[172] B.J. Hales, G.L. Bertrand and L.G. Hepler, *Effects of 3rd components on critical mixing in water-triethylamine system*, J. Phys. Chem. **70**, 3970 (1966).

[173] A.C. Hall, *Optical studies of thin films on surfaces of fused quartz*, J. Phys. Chem. **74**, 2742 (1970).

[174] S. Hamaguchi, R.T. Farouki and D.H.E. Dubin, *Triple point of Yukawa systems*, Phys. Rev. E **56**, 4671 (1997).

[175] J.-P. Hansen and I.R. McDonald, *Statistical mechanics of dense ionized matter. 4. Density and charge fluctuations in a simple molten salt*, Phys. Rev. A **11**, 2111 (1975).

[176] J.-P. Hansen and I.R.McDonald, *Theory of Simple Liquids*, 2nd ed. (Academic Press, San Diego, 1986).

[177] C. Hardacre, J.D. Holbrey, P.B. McCormac, S.E.J. McMath, M. Nieuwenhuyzen and K.R. Seddon, *Crystal and liquid crystalline polymorphism in 1-alkyl-3-methylimidazolium tetrachloropalladate(II) salts*, J. Mater. Chem. **11**, 346 (2001).

[178] L. Harnau, D. Costa and J.-P. Hansen, *A solvable interaction site model for lamellar colloids*, Europhys. Lett. **53**, 729 (2001).

[179] L. Harnau and S. Dietrich, *Fluids of platelike particles near a hard wall*, Phys. Rev. E **65**, 021505 (2002).

[180] L. Harnau and J.-P. Hansen, *Colloid aggregation induced by oppositely charged polyions*, J. Chem. Phys. **116**, 9051 (2002).

[181] L. Harnau and S. Dietrich, *Wetting and capillary nematization of binary hard-platelet and hard-rod fluids*, Phys. Rev. E **66**, 051702 (2002).

[182] L. Harnau, D. Rowan and J.-P. Hansen, *Thermodynamics and phase behavior of the lamellar Zwanzig model*, J. Chem. Phys. **117**, 11359 (2002).

[183] L. Harnau and S. Dietrich, *Bulk and wetting phenomena in a colloidal mixture of hard spheres and platelets*, Phys. Rev. E **71**, 011504 (2005).

[184] L. Harnau and S. Dietrich, *Inhomogeneous Platelet and Rod Fluids*, in *Soft Matter*, Vol. 3, edited by G. Gompper and M. Schick (Wiley, Berlin, 2007), p. 159.

[185] L. Harnau, *Structure and thermodynamics of platelet dispersions*, Mol. Phys. **106**, 1975 (2008).

[186] E.H. Hauge and M. Schick, *Continuous and 1st-order wetting transition from the van der Waals theory of fluids*, Phys. Rev. B **27**, 4288 (1983).

[187] A. He, K. Nguyen and S. Mandre, *Capillary interactions between nearby interfacial objects*, EPL **102**, 38001 (2013).

[188] T.W. Healy and L.R. White, *Ionizable surface group models of aqueous interfaces*, Adv. Colloid Interface Sci. **9**, 303 (1978).

[189] C. Hertlein, L. Helden, A. Gambassi, S. Dietrich and C. Bechinger, *Direct measurement of critical Casimir forces*, Nature **451**, 172 (2008.

[190] V. Hessel, H. Ringsdorf, R. Festag and J.H. Wendorff, *Ionic thermotropic liquid crystals formed by monomeric dipolar and polymeric multipolar amphiphiles with pyridinium head groups*, Makromol. Chem. Rapid Commun. **14**, 707 (1993).

[191] T. Hiemstra, W.H. van Riemsdijk and M.G.M. Bruggenwert, *Proton adsorption mechanism at the gibbsite and aluminium oxide solid-solution interface*, Neth. J. Agric. Sci. **35**, 281 (1987).

[192] T. Hiemstra, W.H. van Riemsdijk and G.H. Bolt, *Multisite proton adsorption modeling at the solid-solution interface of (hydr)oxides — a new approach. 1. Model description and evaluation of intrinsic reaction constants*, J. Colloid Interface Sci. **133**, 91 (1989).

[193] J.D. Holbrey and K.R. Seddon, *The phase behaviour of 1-alkyl-3-methylimidazolium tetrafluoroborates; ionic liquids and ionic liquid crystals*, J. Chem. Soc. Dalton Trans. **13**, 2133 (1999).

[194] J.D. Holbrey, W.M. Reichert, M. Nieuwenhuyzen, S. Johnston, K.R. Seddon and R.D. Rogers, *Crystal polymorphism in 1-butyl-3-methylimidazolium halides: supporting ionic liquid formation by inhibition of crystallization*, Chem. Commun. **2003**, 1636.

[195] F.J. Holly, *Contact angle of sessile drops as an indicator of surface polarization*, J. Colloid Interface Sci. **61**, 435 (1977).

[196] B. Hou, N. Laanait, H. Yu, W. Bu, J. Yoon, B. Lin, M. Meron, G. Luo, P. Vanýsek and M.L. Schlossman, *Ion Distributions at the Water / 1,2-Dichloroethane Interface: Potential of Mean Force Approach to Analyzing X-ray Reflectivity and Interfacial Tension Measurements*, J. Phys. Chem. B **117**, 5365 (2013).

[197] R.J. Hunter, *Zeta potential in colloid science* (Academic Press, London, 1981).

[198] R.J. Hunter, *Foundations of colloid science* (Oxford University Press, 2001).

[199] A.J. Hurd, *The electrostatic interaction between interfacial colloidal particles* J. Phys. A **18**, L1055 (1985).

[200] A.-P. Hynninen and M. Dijkstra, *Phase diagrams of hard-core repulsive Yukawa particles*, Phys. Rev. E **68**, 021407 (2003).

[201] A.-P. Hynninen, M.E. Leunissen, A. van Blaaderen and M. Dijkstra, *CuAu structure in the restricted primitive model and oppositely charged colloids*, Phys. Rev. Lett. **96**, 018303 (2006).

[202] A.-P. Hynninen, C. G. Christova, R. van Roij, A. van Blaaderen and M. Dijkstra, *Prediction and observation of crystal structures of oppositely charged colloids*, Phys. Rev. Lett. **96**, 138308 (2006).

[203] I. Ibagon, M. Bier and S. Dietrich, *Wetting in electrolyte solutions*, J. Chem. Phys. **138**, 214703 (2013).

[204] I. Ibagon, M. Bier and S. Dietrich, *Order of wetting transitions in electrolyte solutions*, J. Chem. Phys. **140**, 174713 (2014).

[205] J.O. Indekeu, *Thin-thick adsorption phase transitions and competing short-range forces*, Europhys. Lett. **10**, 165 (1989).

[206] J.O. Indekeu, K. Ragil, D. Bonn, D. Broseta and J. Meunier, *Wetting of alkanes on water from a Cahn-type theory: Effects of long-range forces*, J. Stat. Phys. **95**, 1009 (1999).

[207] J.O. Indekeu, *Must thin-thick transitions precede long-range critical wetting?*, Phys. Rev. Lett. **85**, 4188 (2000).

[208] H.D. Inerowicz, W. Li, and I. Persson, *Determination of the transfer thermodynamic functions for some monovalent ions from water to n,n-dimethylthioformamide and for some anions from water to methanol, dimethyl-sulfoxide, acetonitrile and pyridine and standard electrode-potentials of some M+/M(s) couples in n,n-dimethylthioformamide*, J. Chem. Soc. Faraday Trans. **90**, 2223 (1994).

[209] J.N. Israelachvili, *Intermolecular and surface forces*, 2nd ed. (Academic Press, London, 1991).

[210] J.D. Jackson, *Classical Electrodynamics*, 3rd ed. (Wiley, New York, 1999).

[211] A.K. Jain and D.P. Landau, *Monte Carlo study of the fcc Blume-Capel model*, Phys. Rev. B **22**, 445 (1980).

[212] G.J. Janz, *Molten salts handbook* (Academic Press, New York, 1967).

[213] J.D. Joannopoulos, *Self-assembly lights up*, Nature **414**, 257 (2001).

[214] K. Johansson and J.C. Eriksson, *$\gamma$ and $d\gamma/dT$ measurements on aqueous solutions of 1,1-electrolytes*, J. Colloid Interface Sci. **49**, 469 (1974).

[215] B.S. John and F.A. Escobedo, *Phase behavior of colloidal hard tetragonal parallelepipeds (cuboids): A Monte Carlo simulation study*, J. Phys. Chem. B **109**, 23008 (2005).

[216] G. Jones and W.A. Ray, *The surface tension of solutions*, J. Am. Chem. Soc. **57**, 957 (1935).

[217] G. Jones and W.A. Ray, *The surface tension of solutions of electrolytes as a function of the concentration. I. A differential method for measuring relative surface tension*, J. Am. Chem. Soc. **59**, 187 (1937).

[218] G. Jones and W.A. Ray, *The Surface Tension of Solutions of Electrolytes as a Function of the Concentration II*, J. Am. Chem. Soc. **63**, 288 (1941).

[219] G. Jones and W.A. Ray, *The Surface Tension of Solutions of Electrolytes as a Function of the Concentration. III. Sodium Chloride*, J. Am. Chem. Soc. **63**, 3262 (1941).

[220] G. Jones and W.A. Ray, *The Surface Tension of Solutions of Electrolytes as a Function of the Concentration. IV. Magnesium Sulfate*, J. Am. Chem. Soc. **64**, 2744 (1942).

[221] T.B. Jones, K.-L. Wang, and D.-J. Yao, *Frequency-dependent electromechanics of aqueous liquids: Electrowetting and dielectrophoresis*, Langmuir **20**, 2813 (2004).

[222] U. Kaatze and D. Woermann, *Dielectric study of a binary aqueous mixture with a lower critical point*, J. Phys. Chem. **88**, 284 (1984).

[223] C. Kalidas, G. Hefter and Y. Marcus, *Gibbs energies of transfer of cations from water to mixed aqueous organic solvents*, Chem. Rev. **100**, 819 (2000).

[224] K.H. Kang, *How electrostatic fields change contact angle in electrowetting*, Langmuir **18**, 10318 (2002).

[225] T. Kato, *Self-assembly of phase-segregated liquid crystal structures*, Science **295**, 2414 (2002).

[226] R.F. Kayser, *Effect of Surface Ionization on Wetting Layers*, Phys. Rev. Lett. **56**, 1831 (1986).

[227] R.F. Kayser, *Wetting layers in electrolyte solutions*, J. Physique **49**, 1027 (1988).

[228] R. Kesavamoorthy, C.B. Rao and B. Raj, *Instability of a 2-dimensional colloidal crystal at a water-air interface*, J. Phys.: Condens. Matter **5**, 8805 (1993).

[229] Y.C. Kim and M.E. Fisher, *Discretization Dependence of Criticality in Model Fluids: A Hard-Core Electrolyte*, Phys. Rev. Lett. **92**, 185703 (2004).

[230] J.G. Kirkwood, *Statistical mechanics of liquid solutions*, Chem. Rev. **19**, 275 (1936).

[231] J.G. Kirkwood and F.P. Buff, *The statistical mechanical theory of surface tension*, J. Chem. Phys. **17**, 338 (1949).

[232] D. Klarman and D. Andelman, *A Model of Electrowetting, Reversed Electrowetting, and Contact Angle Saturation*, Langmuir **27**, 6031 (2011).

[233] V. Kobelev, A.B. Kolomeisky, M.E. Fisher, *Lattice models of ionic systems*, J. Chem. Phys. **116**, 7589 (2002).

[234] P.-M. König, R. Roth, and K.R. Mecke, *Morphological thermodynamics of fluids: Shape dependence of free energies* Phys. Rev. Lett. **93**, 160601 (2004).

[235] A. Kokkinia and C.M. Paleos, *Liquid-crystalline behavior of some bipolar quaternary ammonium salts and phosphate amphiphiles*, Mol. Cryst. Liq. Cryst. **186**, 239 (1990).

[236] S. Kondrat, M. Bier and L. Harnau, *Phase behavior of ionic liquid crystals*, J. Chem. Phys. **132**, 184901 (2010).

[237] P.H.J. Kouwer and T.M. Swager, *Synthesis and mesomorphic properties of rigid-core ionic liquid crystals*, J. Am. Chem. Soc. **129**, 14042 (2007).

[238] E.M. Kramer and J. Herzfeld, *Avoidance model for soft particles. II. Positional ordering of charged rods*, Phys. Rev. E **61**, 6872 (2000).

[239] M. Krech, *The Casimir effect in critical systems* (World Scientific, Singapore, 1994).

[240] M. Krech, *Casimir forces in binary liquid mixtures*, Phys. Rev. E **56**, 1642 (1997).

[241] M. Kroon, W.L. Vos, and G.H. Wegdam, *Structure and formation of a gel of colloidal disks*, Phys. Rev. E **57**, 1962 (1998).

[242] W. Kung, F.J. Solis and M. Olvera de la Cruz, *Thermodynamics of ternary electrolytes: Enhanced adsorption of macroions as minority component to liquid interfaces*, J. Chem. Phys. **130**, 044502 (2009).

[243] W. Kunz, J. Henle and B.W. Ninham, *'Zur Lehre von der Wirkung der Salze' (about the science of the effect of salts): Franz Hofmeister's historical papers* Curr. Opin. Colloid Interface Sci. **9**, 19 (2004).

[244] N. Laanait, M. Mihaylov, B. Hou, H. Yu, P. Vanýsek, M. Meron, B. Lin, I. Benjamin and M.L. Schlossman, *Tuning ion correlations at an electrified soft interface*, Proc. Natl. Acad. Sci. USA **109**, 20326 (2012).

[245] L. Lafuente and J.A. Cuesta, *Cluster density functional theory for lattice models based on the theory of Möbius functions*, J. Phys.: Condens. Matter **38**, 7461 (2005).

[246] L.D. Landau and E.M. Lifshitz, *Fluid mechanics (Volume 6 of Course of Theoretical Physics)* (Elsevier, Amsterdam, 2005).

[247] G. Langie and J.O. Indekeu, *Phase transitions between partial wetting states in the Landau theory and the van der Waals theory of adsorbed fluids*, J. Phys. Condens. Matter **3**, 9797 (1991).

[248] I. Langmuir, *Repulsive forces between charged surfaces in water and the cause of the Jones-Ray effect*, Science **88**, 430 (1938).

[249] I. Langmuir, *The role of attractive and repulsive forces in the formation of tactoids, thixotropic gels, protein crystals and coacervates*, J. Chem. Phys. **6**, 873 (1938).

[250] A.S. Larsen, J.D. Holbrey, F.S. Tham and C.A. Reed, *Designing ionic liquids: Imidazolium melts with inert carborane anions*, J. Am. Chem. Soc. **122**, 7264 (2000).

[251] A.D. Law, M. Auriol, D. Smith, T.S. Horozov and D.M.A. Buzza, *Self-Assembly of Two-Dimensional Colloidal Clusters by Tuning the Hydrophobicity, Composition and Packing Geometry*, Phys. Rev. Lett. **110**, 138301 (2013).

[252] J.L. Lebowitz and E.H. Lieb, *Existence of Thermodynamics for Real Matter with Coulomb Forces*, Phys. Rev. Lett. **22**, 631 (1969).

[253] S.D. Lee, *A numerical investigation of nematic ordering based on a simple hard-rod model*, J. Chem. Phys. **87**, 4972 (1987).

[254] B.P. Lee and M.E. Fisher, *Density Fluctuations in an Electrolyte from Generalized Debye-Hückel Theory*, Phys. Rev. Lett. **76**, 2906 (1996).

[255] B.P. Lee and M.E. Fisher, *Charge oscillations in Debye-Huckel theory*, Europhys. Lett. **39**, 611 (1997).

[256] K.-M. Lee, Y.-T. Lee and I.J.B. Lin, *Supramolecular liquid crystals of amide functionalized imidazolium salts*, J. Mater. Chem. **13**, 1079 (2003).

[257] A.A. Lee, D. Vella, S. Perkin and A. Goriely, *Are Room-Temperature Ionic Liquids Dilute Electrolytes?*, J. Phys. Chem. Lett. **6**, 159 (2015).

[258] E.W. Lemmon, M.O. McLinden and D.G. Friend, *Thermophysical Properties of Fluid Systems*, in NIST Chemistry WebBook, NIST Standard Reference Database Number 69, edited by P.J. Linstrom and W.G. Mallard, `http://webbook.nist.gov`

[259] R.J.F. Leote de Carvalho and R. Evans, *The decay of correlations in ionic fluids*, Mol. Phys. **83**, 619 (1994).

[260] M.E. Leunissen, C.G. Christova, A.-P. Hynninen, C.P. Royall, A.I. Campbell, A. Imhof, M. Dijkstra, R. van Roij, and A. van Blaaderen, *Ionic colloidal crystals of oppositely charged particles*, Nature **437**, 235 (2005).

[261] M.E. Leunissen, J. Zwanikken, R. van Roij, P.M. Chaikin and A. van Blaaderen, *Ion partitioning at the oil-water interface as a source of tunable electrostatic effects in emulsions with colloids*, Phys. Chem. Chem. Phys. **9**, 6405 (2007).

[262] M.E. Leunissen, A. van Blaaderen, A.D. Hollingsworth, M.T. Sullivan and P.M. Chaikin, *Electrostatics at the oil-water interface, stability and order in emulsions and colloids*, Proc. Natl. Acad. Sci. USA **104**, 2585 (2007).

[263] Y. Levin, *Interfacial tension of electrolyte solutions*, J. Chem. Phys. **113**, 9722 (2000).

[264] Y. Levin and J.E. Flores-Mena, *Surface tension of strong electrolytes*, Europhys. Lett. **56**, 187 (2001).

[265] Y. Levin, *Thermodynamics of surface tension: Application to electrolyte solutions*, J. Stat. Phys. **110**, 825 (2003).

[266] P. Levitz, E. Lécolier, A. Mourchid, A. Delville and S. Lyonnard, *Liquid-solid transition of Laponite suspensions at very low ionic strength: Long-range electrostatic stabilisation of anisotropic colloids*, Europhys. Lett. **49**, 672 (2000).

[267] J. Leys, D. Subramanian, E. Rodezno, B. Hammouda and M.A. Anisimov, *Mesoscale phenomena in solutions of 3-methylpyridine, heavy water, and an antagonistic salt*, Soft Matter **9**, 9326 (2013).

[268] L. Li, L. Harnau, S. Rosenfeldt and M. Ballauff, *Effective interaction of charged platelets in aqueous solution: Investigations of colloid laponite suspensions by static light scattering and small-angle x-ray scattering*, Phys. Rev. E **72**, 051504 (2005).

[269] Y. Liang, N. Hilal, P. Langston, and V. Starov, *Interaction forces between colloidal particles in liquid: Theory and experiment*, Adv. Colloid Interface Sci. **134-135**, 151 (2007).

[270] D.R. Lide (Ed.), *CRC Handbook of Chemistry and Physics* (CRC Press, Boca Raton, 1998).

[271] E.H. Lieb and J.L. Lebowitz, *The constitution of matter: Existence of thermodynamics for systems composed of electrons and nuclei*, Adv. Math. **9**, 316 (1972).

[272] G. Lippmann, *Relations entre les phénomènes électriques et capillaires*, Ann. Chim. Phys. **5**, 494 (1875).

[273] W. Liu, C. Ye, Q. Gong, H. Wang and P. Wang, *Tribological performance of room-temperature ionic liquids as lubricant*, Tribol. Lett. **13**, 81 (2002).

[274] J.C. Loudet, A.M. Alsayed, J. Zhang and A.G. Yodh, *Capillary interactions between anisotropic colloidal particles*, Phys. Rev. Lett. **94**, 018301 (2005).

[275] R. Lovett and F.H. Stillinger, *Ion-Pair Theory of Concentrated Electrolytes. II. Approximate Dielectric Response Calculation*, J. Chem. Phys. **48**, 3869 (1968).

[276] T.C. Lubensky and M. Rubin, *Critical phenomena in semi-infinte systems. 2. Mean-field theory*, Phys. Rev. B **12**, 3885 (1975).

[277] R. Ludwig and U. Kragl, *Do we understand the volatility of ionic liquids?*, Angew. Chem. Int. Ed. **46**, 6582 (2007).

[278] M.Y. Lui, L. Crowhurst, J.P. Hallett, P.A. Hunt, H. Hiedermeyer and T. Welton, *Salts dissolved in salts: ionic liquid mixtures*, Chem. Sci. **2**, 1491 (2011).

[279] E. Luijten, M.E. Fisher and A.Z. Panagiotopoulos, *Universality Class of Criticality in the Restricted Primitive Model Electrolyte*, Phys. Rev. Lett. **88**, 185701 (2002).

[280] G.M. Luo, S. Malkova, J. Yoon, D.G. Schultz, B.H. Lin, M. Meron, I. Benjamin, P. Vanysek and M.L. Schlossman, *Ion distributions near a liquid-liquid interface*, Science **311**, 216 (2006).

[281] J. Lyklema, *Fundamentals of interface and colloid science, Vol. I* (Academic Press, London, 1991).

[282] J. Lyklema, *Fundamentals of interface and colloid science, Vol. II* (Academic Press, London, 1995).

[283] A. Majee, M. Bier and S. Dietrich, *Electrostatic interaction between colloidal particles trapped at an electrolyte interface*, J. Chem. Phys. **140**, 164906 (2014).

[284] M. Manciu and E. Ruckenstein, *Specific ion effects via ion hydration: I. Surface tension*, Adv. Colloid Interface Sci. **105**, 63 (2003).

[285] X. Mao, Q. Chen and S. Granick, *Entropy favours open colloidal lattices*, Nature Materials **12**, 217 (2013).

[286] Y. Marcus, *Thermodynamic functions of transfer of single ions from water to non-aqueous and mixed solvents. 1. Gibbs free energies of transfer to non-aqueous solvents*, Pure Appl. Chem. **55**, 977 (1983).

[287] Y. Marcus, *Gibbs energies of transfer of anions from water to mixed aqueous organic solvents*, Chem. Rev. **107**, 3880 (2007).

[288] P.A. Martin and C. Gruber, *A new proof of the Stillinger-Lovett complete shielding condition*, J. Stat. Phys. **31**, 691 (1983).

[289] G.R. Maskaly, R.E. García, W.C. Carter, and Y.-M. Chiang, *Ionic colloidal crystals: Ordered, multicomponent structures via controlled heterocoagulation*, Phys. Rev. E **73**, 011402 (2006).

[290] T.G. Mason, J.N. Wilking, K. Meleson, C.B. Chang, S.M. Graves, *Nanoemulsions: formation, structure, and physical properties*, J. Phys.: Condens. Matter **18**, R635 (2006).

[291] K. Masschaele, B.J. Park, E.M. Furst, J. Fransaer and J. Vermant, *Finite Ion-Size Effects Dominate the Interaction between Charged Colloidal Particles at an Oil-Water Interface*, Phys. Rev. Lett. **105**, 048303 (2010).

[292] N. Matubayasi, H. Matsuo, K. Yamamoto, S. Yamaguchi and A. Matuzawa, *Thermodynamic Quantities of Surface Formation of Aqueous Electrolyte Solutions. I. Aqueous Solutions of NaCl, $MgCl_2$ and $LaCl_3$*, J. Colloid Interface Sci. **209**, 398 (1999).

[293] P. J. McGonigal, *Concerning critical constants of sodium choloride and potassium chloride*, J. Phys. Chem. **67**, 1931 (1963).

[294] S.C. McGrother, D.C. Williamson and G. Jackson, *A re-examination of the phase diagram of hard spherocylinders*, J. Phys. Chem. **104**, 6755 (1996).

[295] E. McLaughlin, M.A. Shakespeare and A.R. Ubbelohde, *Pre-freezing phenomena in relation to liquid crystal formation*, Trans. Faraday Soc. **60**, 25 (1964).

[296] D.A. McQuarrie, *Statistical Mechanics* (University Science Books, Sausalito, 2000).

[297] N. Metropolis, A.W. Rosenbluth, M.N. Rosenbluth, A.H. Teller and E. Teller, *Equation of State Calculations by Fast Computing Machines*, J. Chem. Phys. **21**, 1087 (1953).

[298] S. Meyer, P. Levitz and A. Delville, *A (N,V,T) Monte Carlo study of the long-range electrostatic coupling between a large collection of charged colloidal platelets*, J. Phys. Chem. B **105**, 9595 (2001).

[299] S. Meyer, P. Levitz and A. Delville, *Influence of the relative orientation of two charged anisotropic colloidal particles on their electrostatic coupling: A (N,V,T) Monte Carlo study*, J. Phys. Chem. B **105**, 10684 (2001).

[300] M. Mezger, H. Schröder, H. Reichert, S. Schramm, J.S. Okasinski, S. Schöder, V. Honkimäki, M. Deutsch, B.M. Ocko, J. Ralston, M. Rohwerder, M. Stratmann and H. Dosch, *Molecular Layering of Fluorinated Ionic Liquids at a Charged Sapphire (0001) Surface*, Science **322**, 424 (2008).

[301] M. Mezger, S. Schramm, H. Schröder, H. Reichert, M. Deutsch, E.J. De Souza, J.S. Okasinski, B.M. Ocko, V. Honkimäki and H. Dosch, *Layering of* $[BMIM]^+$*-based ionic liquids at at charged sapphire interface*, J. Chem. Phys. **131**, 094701 (2009).

[302] M. Mezger, B.M. Ocko, H. Reichert and M. Deutsch, *Surface layering and melting in an ionic liquid studied by resonant soft X-ray reflectivity*, Proc. Natl. Acad. Sci. USA **110**, 3733 (2013).

[303] D. Michler, N. Shahidzadeh, M. Westbroek, R. van Roij and D. Bonn, *Are Antagonistic Salts Surfactants?*, Langmuir **31**, 906 (2015).

[304] D.J. Mitchell, D.A. McQuarrie, A. Szabo and J. Groeneveld, *On the second-moment condition of Stillinger and Lovett*, J. Stat. Phys. **17**, 15 (1977).

[305] B.G. Moore and W.E. McMullen, *A finite-density calculation of the surface tension of isotropic-nematic interfaces*, J. Phys. Chem. **96**, 3374 (1992).

[306] M. Mohsen-Nia and H. Amiri, *Measurement and modelling of static dielectric constants of aqueous solutions of methanol, ethanol and acetic acid at T=293.15 K and 91.3 kPa*, J. Chem. Thermod. **57**, 67 (2013).

[307] A. Mourchid, A. Delville, J. Lembard, E. Lécolier and P. Levitz, *Phase diagram of colloidal dispersions of anisotropic charged particles — Equilibrium properties, structure and rheology of laponite suspensions*, Langmuir **11**, 1942 (1995).

[308] A. Mourchid, E. Lécolier, H. van Damme, and P. Levitz, *On viscoelastic, birefringent, and swelling properties of Laponite clay suspensions: Revisited phase diagram*, Langmuir **14**, 4718 (1998).

[309] F. Mugele and J.-C. Baret, *Electrowetting: from basics to applications*, J. Phys.: Condens. Matter **17**, R705 (2005).

[310] F. Mugele, B. Bera, A. Cavalli, I. Siretanu, A. Maestro, M. Duits, M. Cohen-Stuart, D. van der Ende, I. Stocker and I. Collins, *Ion adsorption-induced wetting transition in oil-water-mineral systems*, Sci. Rep. **5**, 10519 (2015).

[311] T. Murphy, R. Atkin and G.G. Warr, *Scattering from ionic liquids*, Curr. Opin. Colloid Interface Sci. **20**, 282 (2015).

[312] V.M. Nabutovskii, N.A. Nemov and Y.G. Peisakhovich, *Charge density and order parameter waves in liquid and solid electrolytes in the vicinity of the critical point*, Phys. Lett. A **79**, 98 (1980).

[313] V.M. Nabutovskii, N.A. Nemov and Y.G. Peisakhovich, *Correlation functions for the electrolyte near the critical point of pure solvent*, Mol. Phys. *54*, 979 (1985).

[314] V.M. Nabutovskii and N.A. Nemov, *Electric structure of the interface in an electrolyte near the critical point*, J. Colloid Interface Sci. **114**, 208 (1986).

[315] H. Nakanishi and M.E. Fisher, *Multicriticality of Wetting, Prewetting and Surface Transitions*, Phys. Rev. Lett. **49**, 1565 (1982).

[316] T. Nakato and N. Miyamoto, *Liquid Crystalline Behavior and Related Properties of Colloidal Systems of Inorganic Oxide Nanosheets*, Materials **2**, 1734 (2009).

[317] U. Nellen, J. Dietrich, L. Helden, S. Chodankar, K. Nygård, J.F. van der Veen and C. Bechinger. Soft Matter **7**, 5360 (2011).

[318] F. Neve, A. Crispini, S. Armentano, O. Francescangeli, *Synthesis, structure and thermotropic mesomorphism of layered N-alkylpyridinium tetrahalopalladate(II) salts*, Chem. Mater. **10**, 1904 (1998).

[319] F. Neve, O. Francescangeli, A. Crispini and J. Charmant, *A(2)[MX4] copper(II) pyridinium salts. From ionic liquids to layered solids to liquid crystals*, Chem. Mater. **13**, 2032 (2001).

[320] T. Nicolai and S. Cocard, *Light scattering study of the dispersion of laponite*, Langmuir **16**, 8189 (2000).

[321] T. Nicolai and S. Cocard, *Structure of gels and aggregates of disk-like colloids*, Eur. Phys. J. E **5**, 221 (2001).

[322] A. L. Nichols III and L. R. Pratt, *Salt effects on the surface tensions of dilute electrolyte solutions — The influence of nonzero relative solubility of the salt between the coexistign phases*, J. Chem. Phys. **80**, 6225 (1984).

[323] M.G. Nikolaides, A.R. Bausch, M.F. Hsu, A.D. Dinsmore, M.P. Brenner, C. Gay and D.A. Weitz, *Electric-field-induced capillary attraction between like-charged particles at liquid interfaces*, Nature **420**, 299 (2002).

[324] G. Odriozola, M. Romero-Bastida and F.D. Guevara-Rodríguez, *Brownian dynamics simulations of Laponite colloid suspensions*, Phys. Rev. E **70**, 021405 (2004).

[325] M. Oettel, A. Domínguez and S. Dietrich, *Attractions between charged colloids at water interfaces*, J. Phys.: Condens. Matter **17**, L337 (2005).

[326] M. Oettel, A. Domínguez and S. Dietrich, *Effective capillary interaction of spherical particles at fluid interfaces*, Phys. Rev. E **71**, 051401 (2005).

[327] R. Okamoto and A. Onuki, *Precipitation in aqueous mixtures with addition of a strongly hydrophilic or hydrophobic solute*, Phys. Rev. E **82**, 051501 (2010).

[328] R. Okamoto and A. Onuki, *Charged colloids in an aqueous mixture with a salt*, Phys. Rev. E **84**, 051401 (2011).

[329] A. Oleksy and J.-P. Hansen, *Microscopic density functional theory of wetting and drying of a solid substrate by an explicit solvent model of ionic solutions*, Mol. Phys. **107**, 2609 (2009).

[330] A. Oleksy and J.-P. Hansen, *Wetting of a solid substrate by a "civilized" model of ionic solutions*, J. Chem. Phys. **132**, 204702 (2010).

[331] M.J. de Oliveira and R.B. Griffiths, *Lattice-gas model of multiple layer adsorption*, Surf. Sci. **71**, 687 (1978).

[332] M. O'Neill and S.M. Kelly, *Liquid crystals for charge transport, luminescence and photonics*, Adv. Mater. **15**, 1135 (2003).

[333] L. Onsager and N.N.T. Samaras, *The Surface Tension of Debye-Huckel Electrolytes*, J. Chem. Phys. **2**, 528 (1934).

[334] A. Onuki and H. Kitamura, *Solvation effects in near-critical binary mixtures*, J. Chem. Phys. **121**, 3143 (2004).

[335] A. Onuki, *Ginzburg-Landau theory of solvation in polar fluids: Ion distribution around an interface*, Phys. Rev. E **73**, 021506 (2006).

[336] A. Onuki, *Surface tension of electrolytes: Hydrophilic and hydrophobic ions near an interface*, J. Chem. Phys. **128**, 224704 (2008).

[337] A. Onuki, *Nonionic and ionic surfactants at an interface*, EPL **82**, 58002 (2008).

[338] A. Onuki, R. Okamoto and T. Araki, *Phase Transitions in Soft Matter Induced by Selective Solvation*, Bull. Chem. Soc. Jpn. **84**, 569 (2011).

[339] A.A.H. Pádua, M.F. Costa Gomes and J.N.A. Canongia Lopes, *Molecular solutes in ionic liquids: A structural, perspective*, Acc. Chem. Res. **40**, 1087 (2007).

[340] A.Z. Panagiotopoulos and S.K. Kumar, *Large Lattice Discretization Effects on the Phase Coexistence of Ionic Fluids*, Phys. Rev. Lett. **83**, 2981 (1999).

[341] A.Z. Panagiotopoulos, *Critical parameters of the restricted primitive model*, J. Chem. Phys. **116**, 3007 (2002).

[342] R. Pandit, *Systematics of multilayer adsorption phenomena on attractive substrates*, Phys. Rev. B **26**, 5112 (1982).

[343] R. Pandit and M. Wortis, *Surfaces and interfaces of lattice models: Mean-field theory as an area-preserving map*, Phys. Rev. B **25**, 3226 (1982).

[344] B.J. Park, J.P. Pantina, E.M. Furst, M. Oettel, S. Reynaert and J. Vermant, *Direct measurements of the effects of salt and surfactant on interaction forces between colloidal particles at water-oil interfaces*, Langmuir **24**, 1686 (2008).

[345] J.D. Parsons, *Nematic ordering in a system of rods*, Phys. Rev. A **19**, 1225 (1979).

[346] Y.U. Paulechka, G.J. Kabo, A.V. Blokhin, O.A. Vydrov, J.W. Magee and M. Frenkel, *Thermodynamic Properties of 1-Butyl-3-methylimidazolium Hexafluorophosphate in the Ideal Gas State*, J. Chem. Eng. Data **48**, 457 (2003).

[347] Y.U. Paulechka, D.H. Zaitsau, G.J. Kabo and A.A. Stechan, *Vapor pressure and thermal stability of ionic liquid 1-butyl-3-methylimidazolium Bis(trifluoromethylsulfonyl)amide*, Thermochim. Acta **439**, 158 (2005).

[348] Y.U. Paulechka, A.V. Blokhin, G.J. Kabo and A.A. Stechan, *Thermodynamic properties and polymorphism of 1-alkyl-3-methylimidazolium bis(triflamides)*, J. Chem. Thermodyn. **39**, 866 (2007).

[349] A. Pelissetto and E. Vicari, Phys. Rep. **368**, 549 (2002).

[350] M.H. Pellat, *Force agissant à la surface de séparation de deux diélectriques*, C. R. Hebd. Séances Acad. Sci. **119**, 675 (1894).

[351] M.H. Pellat, *Mesure de la force agissant sur un diélectrique non électrisé, placé dans un champ électrique*, C. R. Hebd. Séances Acad. Sci. **121**, 938 (1895).

[352] S. Perkin, M. Salanne, P. Madden and R. Lynden-Bell, *Is a Stern and diffuse layer model appropriate to ionic liquids at surfaces?*, Proc. Nat. Acad. Sci. USA **110**, E4121 (2013).

[353] P.B. Petersen, J.C. Johnson, K.P. Knutsen, R.J. Saykally, *Direct experimental validation of the Jones-Ray effect*, Chem. Phys. Lett. **397**, 46 (2004).

[354] P.B. Petersen and R.J. Saykally, *Adsorption of ions to the surface of dilute electroyte solutions: The Jones-Ray effect revisited* J. Am. Chem. Soc. **127**, 15446 (2005).

[355] A.V. Petukhov, J.-M. Meijer and G.J. Vroege, *Particle shape effects in colloidal crystals and colloidal liquid crystals: Small-angle X-ray scattering studies with microradian resolution*, Curr. Opin. Colloid Interface Sci. **20**, 272 (2015).

[356] J. Piasecki and E.H. Hauge, *A new generalization of the Sullivan model for wetting transitions*, Physica A **143**, 87 (1987).

[357] P. Pieranski, *Two-dimensional interfacial colloidal crystals*, Phys. Rev. Lett. **45**, 569 (1980).

[358] F. Pignon, A. Magnin, J.-M. Piau, B. Cabane, P. Lindner and O. Diat, *Yield stress thixotropic clay suspension: Investigation of structure by light, neutron, and x-ray scattering*, Phys. Rev. E **56**, 3281 (1997).

[359] N.V. Plechkova and K.R. Seddon, *Applications of ionic liquids in the chemical industry*, Chem. Soc. Rev. **37**, 123 (2008).

[360] M. Plischke and B. Bergersen, *Equilibrium statistical physics*, 3rd ed. (World Scientific, Singapore, 2006).

[361] M.G. Pollack, R.B. Fair and A.D. Shenderov, *Electrowetting-based actuation of liquid droplets for microfluidic applications*, Appl. Phys. Lett. **77**, 1725 (2000).

[362] P. Porion, M. Al Mukhtar, S. Meyer, A.M. Faugère, J.R.C. van der Maarel and A. Delville, *Nematic ordering of suspensions of charged anisotropic colloids detected by Na-23 nuclear magnetic resonance*, J. Phys. Chem. B **105**, 10505 (2001).

[363] P. Porion, M. Al-Mukhtar, A.-M. Faugère, S. Meyer and A. Delville, *Nematic ordering of suspension of charged anisotropic colloids detected by multinuclear quadrupolar spectra and H-1 PGSE-NMR measurements*, Eur. Phys. J. E **12**, S17 (2003).

[364] F. Pousaneh and A. Ciach, *The origin of the attraction between like charged hydrophobic and hydrophilic walls confining a near-critical binary aqueous mixture with ions*, J. Phys.: Condens. Matter **23**, 412101 (2011).

[365] F. Pousaneh, A. Ciach and A. Maciołek, *Effect of ions on confined near-critical binary aqueous mixture*, Soft Matter **8**, 3567 (2012).

[366] F. Pousaneh, A. Ciach and A. Maciołek, *How ions in solution can change the sign of the critical Casimir potential*, Soft Matter **10**, 470 (2014).

[367] F. Pousaneh and A. Ciach, *The effect of antagonistic salt on a confined near-critical mixture*, Soft Matter **10**, 8188 (2014).

[368] V. Prasad, D. Semwogerere and E.R. Weeks, *Confocal microscopy of colloids*, J. Phys.: Condens. Matter **19**, 113102 (2007).

[369] C. Quilliet and B. Berge, *Electrowetting: a recent outbreak*, Curr. Opin. Colloid Interface Sci. **6**, 34 (2001).

[370] A. Quinn, R. Sedev, J. Ralston, *Influence of the electrical double layer in electrowetting*, J. Phys. Chem. B **107**, 1163 (2003).

[371] A. Quinn, R. Sedev, J. Ralston, *Contact angle saturation in electrowetting*, J. Phys. Chem. B **109**, 6268 (2005).

[372] L.P.N. Rebelo, J.N. Canongia Lopes, J.M.S.S. Esperanca and E. Filipe, *On the critical temperature, normal boiling point and vapor pressure of ionic liquids*, J. Phys. Chem. B **109**, 6040 (2005).

[373] P.A. Redhead, *Vacuum science and technology: 1950-2003*, J. Vac. Sci. Technol. A **21**, S12 (2003).

[374] A. Reindl and M. Bier, *Impedance spectroscopy of ions at liquid-liquid interfaces*, Phys. Rev. E **88**, 052312 (2013).

[375] R. Ren, C.J. O'Keeffe and G. Orkoulas, *Simulation of symmetric tricritical behavior in electrolytes*, J. Chem. Phys. **125**, 124504 (2006).

[376] Y. Rosenfeld and W.M. Gelbart, *On the statistical thermodynamics of interacting charged particles of arbitrary shape and concentration*, J. Chem. Phys. **81**, 4574 (1984).

[377] Y. Rosenfeld and L. Blum, *Statistical thermodynamics of charged objects*, J. Phys. Chem. **89**, 5149 (1985).

[378] Y. Rosenfeld, *Scaled field particle theory of the structure and the thermodynamics of isotropic hard particle fluids*, J. Chem. Phys. **89**, 4272 (1988).

[379] Y. Rosenfeld, *Free-energy model for the inhomogeneous hard-sphere fluid mixture and density-functional theory of freezing*, Phys. Rev. Lett. **63**, 980 (1989).

[380] D.G. Rowan, J.-P. Hansen and E. Trizac, *Screened electrostatic interactions between clay platelets*, Mol. Phys. **98**, 1369 (2000).

[381] D.G. Rowan and J.-P. Hansen, *Salt-induced ordering in lamellar colloids*, Langmuir **18**, 2063 (2002).

[382] J.S. Rowlinson and B. Widom, *Molecular Theory of Capillarity* (Dover, Mineola, 2002).

[383] M. Rubinstein and R.H. Colby, *Polymer Physics* (Oxford University Press, 2004).

[384] D. Rudhardt, C. Bechinger and P. Leiderer, *The interaction between colloidal particles and differently treated glass surfaces studied with evanescent wave scattering*, Prog. Colloid Polym. Sci. **110**, 37 (1998).

[385] W.B. Russel, D.A. Saville and W.R. Schowalter, *Colloidal dispersions* (Cambridge University Press, Cambridge, 1989).

[386] B. Ruzicka, L. Zulian and G. Ruocco, *More on the phase diagram of laponite*, Langmuir **22**, 1106 (2006).

[387] S. Sacanna, W.K. Kegel and A.P. Philipse, *Thermodynamically stable pickering emulsions*, Phys. Rev. Lett. **98**, 158301 (2007).

[388] K. Sadakane, H. Seto and M. Nagao, *Long-range periodic structure induced by coupling of the solvation effect and concentration fluctuation in water and 3-methylpyridine with salts*, Chem. Phys. Lett. **426**, 61 (2006).

[389] K. Sadakane, H. Seto, H. Endo and M. Kojima, *Mesoscopic structure in near-critical mixtures of D2O and 3-methylpyridine with salts*, J. Appl. Cryst. **40**, s527 (2007).

[390] K. Sadakane, H. Seto, H. Endo and M. Shibayama, *A periodic structure in a mixture of D2O/3-methylpyridine/NaBPh4 induced by solvation effect*, J. Phys. Soc. Jpn. **76**, 113602 (2007).

[391] K. Sadakane, A. Onuki, K. Nishida, S. Koizumi and H. Seto, *Multilamellar Structures Induced by Hydrophilic and Hydrophobic Ions Added to a Binary Mixture of D2O and 3-Methylpyridine*, Phys. Rev. Lett. **103**, 167803 (2009).

[392] K. Sadakane, N. Iguchi, M. Nagao, H. Endo, Y.B. Melnichenko and H. Seto, *2D-Ising-like critical behavior in mixtures of water and 3-methylpyridine including antagonistic salt or ionic surfactant*, Soft Matter **7**, 1334 (2011).

[393] K. Sadakane, M. Nagao, H. Endo and H. Seto, *Membrane formation by preferential solvation of ions in mixtures of water, 3-methylpyridine, and sodium tetraphenylborate*, J. Chem. Phys. **139**, 234905 (2013).

[394] K. Sadakane, H. Endo, K. Nishida and H. Seto, *Lamellar/Disorder Phase Transition in a Mixture of Water / 2,6-Dimethylpyridine / Antagonistic Salt*, J. Sol. Chem. **43**, 1722 (2014).

[395] S.A. Safran, *Statistical Thermodynamics of Surfaces, Interfaces and Membranes* (Westview, Boulder, 2003).

[396] K. Sainath and P. Ghosh, *Stabilization of Silicone Oil-in-Water Emulsions by Ionic Surfactant and Electrolytes: The Role of Adsorption and Electric Charge at the Interface*, Ind. Eng. Chem. Res. **52**, 15808 (2013).

[397] A. Samborski, G.T. Evans, C.P. Mason and M.P. Allen, *The isotropic to nematic liquid crystal transition for hard ellipsoids — an onsager-like theory and computer simulations*, Mol. Phys. **81**, 263 (1994).

[398] Z. Samec, V. Mareček, and D. Homolka, *The double layer at the interface between 2 immiscible electrolyte solutions. 1. Capacity of the water-nitrobenzene interface*, J. Electroanal. Chem. **126**, 121 (1981).

[399] Z. Samec, V. Mareček, K. Holub, S. Račinský, and P. Hájková, *The double layer at the interface between 2 immiscible electrolyte solutions. 3. Capacity of the water - 1,2-dichloroethane interface*, J. Electroanal. Chem. **225**, 65 (1987).

[400] Z. Samec, *Electrochemistry at the interface between two immiscible electrolyte solutions*, Pure Appl. Chem. **76**, 2147 (2004).

[401] S. Samin and Y. Tsori, *Attraction between like-charge surfaces in polar mixtures*, EPL **95**, 36002 (2011).

[402] S. Samin and Y. Tsori, *The interaction between colloids in polar mixtures above $T_c$*, J. Chem. Phys. **136**, 154908 (2012).

[403] S. Samin and Y. Tsori, *Stabilization of charged and neutral colloids in salty mixtures*, J. Chem. Phys. **139**, 244905 (2013).

[404] S. Sauer, N. Steinke, A. Baro, S. Laschat, F. Giesselmann, and W. Kantlehner, *Guanidinium chlorides with triphenylene moieties displaying columnar mesophases*, Chem. Mater. **20**, 1909 (2008).

[405] S. Sauer, S. Saliba, S. Tussetschläger, A. Baro, W. Frey, F. Giesselmann, S. Laschat and W. Kantlehner, *p-Alkoxybiphenyls with guanidinium head groups displaying smectic mesophases*, Liq. Cryst. **36**, 275 (2009).

[406] J.M. Saunders, J.W. Goodwin, R.M. Richardson and B. Vincent, *A small-angle X-ray scattering study of the structure of aqueous laponite dispersions*, J. Phys. Chem. B **103**, 9211 (1999).

[407] M. Schick, *Introduction to wetting phenomena*, in *Les Houches, Session XLVIII, 1988 — Liquides aux interfaces / Liquids at interfaces*, edited by J. Charvolin, J.F. Joanny and J. Zinn-Justin (North-Holland, Amsterdam, 1988), p. 415.

[408] F. Schlesener, A. Hanke, and S. Dietrich, *Critical Casimir forces in colloidal suspensions*, J. Stat. Phys. **110**, 981 (2003).

[409] C.Y. Seah, C.A. Grattoni and R.A. Dawe, *The effect of halides on the lower critical solution temperature of the 2,6-lutidine-water system*, Fluid Phase Equil. **89**, 345 (1993).

[410] K.R. Seddon, *Ionic liquids for clean technology*, J. Chem. Tech. Biotechnol. **68**, 351 (1997).

[411] R. Sedev, *Electrowetting: Electrocapillarity, saturation, and dynamics*, Eur. Phys. J. Special Topics **197**, 307 (2011).

[412] N. Shahidzadeh, D. Bonn, K. Ragil, D. Broseta and J. Meunier, *Sequence of two wetting transitions induced by tuning the Hamaker constant*, Phys. Rev. Lett. **80**, 3992 (1998).

[413] E.V. Shevchenko, D.V. Talapin, N.A. Kotov, S. O'Brien, and C.B. Murray, *Structural diversity in binary nanoparticle superlattices*, Nature **439**, 55 (2006).

[414] K. Shundyak and R. van Roij, *Hard colloidal rods near a soft wall: Wetting, drying and symmetry breaking*, Europhys. Lett. **74**, 1039 (2006).

[415] I.S. Sogami, T. Shinohara and M.V. Smalley, *Effective interaction of highly charged plates in an electrolyte*, Mol. Phys. **74**, 599 (1991).

[416] J.A.M. Sondag-Huethorst and L.G.J. Fokkink, *Potential-dependent wetting of octadecanethiol-modified polycrystalline gold electrodes*, Langmuir **8**, 2560 (1992).

[417] M.J. Sparnaay, *On the electrostatic contribution to the interfacial tension of semiconductor-gas and semiconductor-electrolyte interfaces*, Surf. Sci. **1**, 213 (1964).

[418] D. Stamou, C. Duschl and D. Johannsmann, *Long-range attraction between colloidal spheres at the air-water interface: The consequence of an irregular meniscus*, Phys. Rev. E **62**, 5263 (2000).

[419] D. Ster, U. Baumeister, J. Lorenzo Chao, C. Tschierske and G. Israel, *Synthesis and mesophase behaviour of ionic liquid crystalst*, J. Mater. Chem. **17**, 3393 (2007).

[420] F.H. Stillinger, *Interfacial solutions of Poisson-Boltzmann equation*, J. Chem. Phys. **35**, 1584 (1961).

[421] F.H. Stillinger and R. Lovett, *Ion-Pair Theory of Concentrated Electrolytes. I. Basic Concepts*, J. Chem. Phys. **48**, 3858 (1968).

[422] F.H. Stillinger and R. Lovett, *General Restriction on the Distribution of Ions in Electrolytes*, J. Chem. Phys. **49**, 1991 (1968).

[423] D.E. Sullivan, *Van der Waals model of adsorption*, Phys. Rev. B **20**, 3991 (1979).

[424] D.E. Sullivan and M.M. Telo da Gama, *Wetting Transitions and Multilayer Adsorption at Fluid Interfaces*, in *Fluid Interfacial Phenomena*, edited by C.A. Croxton (Wiley, Chichester, 1986), p. 65.

[425] A. Suzuki, Y. Shinka and M. Masuko, *Tribological Characteristics of Imidazolium-based Room Temperature Ionic Liquids Under High Vacuum*, Tribol. Lett. **27**, 307 (2007).

[426] V. Talanquer and D.W. Oxtoby, *Density-functional analysis of phenomenological theories of gas-liquid nucleation*, J. Phys. Chem. **99**, 2865 (1995).

[427] S. Tan and D.R. MacFarlane, *Ionic Liquids in Biomass Processing*, in *Ionic Liquids*, Topics in Current Chemistry Vol. 290 (Springer, Berlin, 2010), p. 311.

[428] B.V.R. Tata and S.S. Jena, *Ordering, dynamics and phase transitions in charged colloids*, Solid State Commun. **139**, 562 (2006).

[429] A. Taubert, *CuCl nanoplatelets from an ionic liquid-crystal precursor*, Angew. Chem. Int. Ed. **43**, 5380 (2004).

[430] A. Taubert, P. Steiner and A. Mantion, *Ionic liquid crystal precursors for inorganic particles: Phase diagram and thermal properties of a CuCl nanoplatelet precursor*, J. Phys. Chem. B **109**, 15542 (2005).

[431] D.J. Tobias, A.C. Stern, M.D. Baer, Y. Levin and C.J. Mundy, *Simulation and Theory of Ions at Atmospherically Relevant Aqueous Liquid-Air Interfaces*, Annu. Rev. Phys. Chem. **64**, 339 (2013).

[432] H. Tokuda, K. Hayamizu, K. Ishii, M.A. Bin Hasan Susan and M. Watanabe, *Physicochemical properties and structures of room temperature ionic liquids. 2. Variation of alkyl chain length in imidazolium cation*, J. Phys. Chem. B **109**, 6103 (2005).

[433] R.C. Tolman, *The effect of droplet size on surface tension*, J. Chem. Phys. **17**, 333 (1949).

[434] G.M. Torrie and J.P. Valleau, *A Monte Carlo study of an electrical double layer*, Chem. Phys. Lett. **65**, 343 (1979).

[435] E. Trizac, L. Bocquet, A. Agra, J.-J. Weis and M. Aubouy, *Effective interactions and phase behaviour for a model clay suspension in an electrolyte*, J. Phys.: Condens. Matter **14**, 9339 (2002).

[436] Y. Tsori and L. Leibler, *Phase-separation in ion-containing mixtures in electric fields*, Proc. Natl. Acad. Sci. **104**, 7348 (2007).

[437] O.D. Velev, B.G. Prevo and K.H. Bhatt, *On-chip manipulation of free droplets*, Nature **426**, 515 (2003).

[438] M. Vallet, B. Berge, and L. Vovelle, *Electrowetting of water and aqueous solutions on poly(ethylene terephthalate) insulating films*, Polymer **37**, 2465 (1996).

[439] D. van der Beek and H.N.W. Lekkerkerker, *Nematic ordering vs. gelation in suspensions of charged platelets*, Europhys. Lett. **61**, 702 (2003).

[440] D. van der Beek and H.N.W. Lekkerkerker, *Liquid crystal phases of charged colloidal platelets*, Langmuir **20**, 8582 (2004).

[441] D. van der Beek, T. Schilling and H.N.W. Lekkerkerker, *Gravity-induced liquid crystal phase transitions of colloidal platelets*, J. Chem. Phys. **121**, 5423 (2004).

[442] F.M. van der Kooij and H.N.W. Lekkerkerker, *Formation of nematic liquid crystals in suspensions of hard colloidal platelets*, J. Phys. Chem. B **102**, 7829 (1998).

[443] F.M. van der Kooij, D. van der Beek and H.N.W. Lekkerkerker, *Isotropic-nematic phase separation in suspensions of polydisperse colloidal platelets*, J. Phys. Chem. B **105**, 1696 (2001).

[444] W.H. van Riemsdijk, G.H. Bolt, L.K. Koopal, and J. Blaakmeer, *Electrolyte adsorption on heterogeneous surfaces — adsorption models*, J. Colloid Interface Sci. *109*, 219 (1986).

[445] R. van Roij, P. Bolhuis, B. Mulder and D. Frenkel, *Transverse interlayer order in lyotropic smectic liquid crystals*, Phys. Rev. E **52**, 1277 (1995).

[446] O.S. Vaulina and S.A. Khrapak, *Scaling law for the fluid-solid phase transition in Yukawa systems (dusty plasmas)*, J. Exp. Theo. Phys. **90**, 287 (2000).

[447] J.A.C. Veerman and D. Frenkel, *Phase behavior of disk-like hard-core mesogens*, Phys. Rev. A **45**, 5632 (1992).

[448] C. Vega, F. Bresme, and J.L.F. Abascal, *Fluid-solid equilibrium of a charged hard-sphere model*, Phys. Rev. E **54**, 2746 (1996).

[449] E.J.W. Verwey and K.F. Niessen, *The electrical double layer at the interface of two liquids*, Phil. Mag. **28**, 435 (1939).

[450] P.S. Vincett, *Generalization of Trouton rule to dissociative and associative evaporation — Calculation of heat and entropy of evaporation for group 2-6 compounds and for alkali-halides*, J. Phys. Chem. **82**, 2797 (1978).

[451] M. Vis, H.H. Wensink, H.N.W. Lekkerkerker and D. Kleshchanok, *Nematic and lamellar liquid-crystalline phases in suspensions of charged silica-coated gibbsite platelets*, Mol. Phys. **113**, 1053 (2015).

[452] A.G. Volkov, D.W. Deamer, D.L. Tanelian, V.S. Markin, *Electrical double layers at the oil/water interface*, Prog. Surf. Sci. **53**, 1 (1996).

[453] L.G. Wade, *Organic Chemistry* (Prentice-Hall, Upper Saddle River, 2006).

[454] E. Waisman and J.L. Lebowitz, *Exact solution of an integral equation for structure of a primitive model of electrolytes*, J. Chem. Phys. **52**, 4307 (1970).

[455] E. Waisman and J.L. Lebowitz, *Mean spherical model integral equation for charged hard spheres. 1. Method of solution*, J. Chem. Phys. **56**, 3086 (1972).

[456] E. Waisman and J.L. Lebowitz, *Mean spherical model integral equation for charged hard spheres. 2. Results*, J. Chem. Phys. **56**, 3093 (1972).

[457] P. Walden, *Ueber die Molekulargrösse und elektrische Leitfähigkeit einiger geschmolzenen Salze*, Bull. Acad. Imp. Sci. St.-Petersbourg **8**, 405 (1914).

[458] T. Wandlowski, V. Mareček, and Z. Samec, *Adsorption of phospholipids at the interface between 2 immiscible electrolyte solutions. 1. Equilibrium adsorption of phosphatidylcholines at the water nitrobenzene interface*, J. Electroanal. Chem. **242**, 277 (1988).

[459] H. Wang, Q. Lu, C. Ye, W. Liu and Z. Cui, *Friction and wear behaviors of ionic liquid of alkylimidazolium hexafluorophosphates as lubricants for steel/steel contact*, Wear **256**, 44 (2004).

[460] Y. Wang, Y. Wang, D.R. Breed, V.N. Manoharan, L. Feng, A.D. Hollingsworth, M. Weck and D.J. Pine, *Colloids with valence and specific directional bonding*, Nature **491**, 51 (2012).

[461] P.B. Warren, *A theory of void formation in charge-stabilized colloidal suspensions at low ionic strength*, J. Chem. Phys. **112**, 4683 (2000).

[462] P. Wasserscheid and W. Keim, *Ionic liquids - New ßolutionsffor transition metal catalysis*, Angew. Chem. Int. Ed. **39**, 3773 (2000).

[463] P. Wasserscheid and T. Welton (Eds.), *Ionic liquids in synthesis* (Wiley, Weinheim, 2003).

[464] P. Wasserscheid and T. Welton (Eds.), *Ionic Liquids in Synthesis, Vol. 2* (Wiley, Weinheim, 2007).

[465] H. Weingärtner, A. Knocks, W. Schrader and U. Kaatze, *Dielectric spectroscopy of the room temperature molten salt ethylammonium nitrate*, J. Phys. Chem. A **105**, 8646 (2001).

[466] H. Weingärtner, *The static dielectric constant of ionic liquids*, Z. Phys. Chem. **220**, 1395 (2006).

[467] H. Weingärtner, *Understanding ionic liquids at the molecular level: Facts, problems, and controversies*, Ang. Chem. Int. Ed. **47**, 654 (2008).

[468] P.K. Weissenborn and R.J. Pugh, *Surface tension of aqueous solutions of electrolytes: Relationship with ion hydration, oxygen solubility, and bubble coalescence*, J. Colloid Interface Sci. **184**, 550 (1996).

[469] W.J.J. Welters and L.G.J. Fokkink, *Fast electrically switchable capillary effects*, Langmuir **14**, 1535 (1998).

[470] T. Welton, *Room-temperature ionic liquids. Solvents for synthesis and catalysis*, Chem. Rev. **99**, 2071 (1999).

[471] H.H. Wensink, G.J. Vroege and H.N.W. Lekkerkerker, *Isotropic-nematic density inversion in a binary mixture of thin and thick hard platelets*, J. Phys. Chem. B **105**, 10610 (2001).

[472] H.H. Wensink and G.J. Vroege, *Demixing in binary mixtures of anisometric colloids*, J. Phys.: Condens. Matter **16**, S2015 (2004).

[473] H.H. Wensink and H.N.W. Lekkerkerker, *Sedimentation and multi-phase equilibria in mixtures of platelets and ideal polymer*, Europhys. Lett. **66**, 125 (2004).

[474] S. Wiegand, J.M.H. Levelt Sengers, K.J. Zhang, M.E. Briggs and R.W. Gammon, *Discrepancies in turbidity measurements in the ionic binary mixture triethyl n-hexyl ammonium triethyl n-hexyl boride in diphenyl ether*, J. Chem. Phys. **106**, 2777 (1997).

[475] S. Wiegand, R.F. Berg and J.M.H. Levelt Sengers, *Critical viscosity of the ionic mixture triethyl n-hexyl ammonium triethyl n-hexyl borate in diphenyl ether*, J. Chem. Phys. **109**, 4533 (1998).

[476] S. Wiegand, M.E. Briggs, J.M.H. Levelt Sengers, M. Kleemeier and W. Schröer, *Turbidity, light scattering and coexistence curve data for the ionic binary mixture triethyl n-hexyl ammonium triethyl n-hexyl borate in diphenyl ether*, J. Chem. Phys. **109**, 9038 (1998).

[477] J.E.G.J. Wijnhoven, D.D. van't Zand, D. van der Beek and H.N.W. Lekkerkerker, *Sedimentation and phase transitions of colloidal gibbsite platelets*, Langmuir **21**, 10422 (2005).

[478] M. Witala, R. Nervo, O. Konovalov and K. Nygård, *Microscopic segregation of hydrophilic ions in critical binary aqueous solvents*, Soft Matter **11**, 5883 (2015).

[479] J. Wu, *Density functional theory for chemical engineering: From capillarity to soft materials*, AIChE Journal **52**, 1169 (2006).

[480] A. Würger and L. Foret, *Capillary attraction of colloidal particles at an aqueous interface*, J. Phys. Chem. B **109**, 16435 (2005).

[481] N. Yamanaka, R. Kawano, W. Kubo, N. Masaki, T. Kitamura, Y. Wada, M. Watanabe and S. Yanagida, *Dye-Sensitized TiO2 Solar Cells Using Imidazolium-Type Ionic Liquid Crystal Systems as Effective Electrolytes*, J. Phys. Chem. B **111**, 4763 (2007).

[482] Q. Yan and J.J. de Pablo, *Phase equilibria and clustering in size-asymmetric primitive model electrolytes*, J. Chem. Phys. **114**, 1727 (2001).

[483] T. Yasuda and M. Watanabe, *Protic ionic liquids: Fuel cell applications*, MRS Bull. **38**, 560 (2013).

[484] A. Yethiraj and A. van Blaaderen, *A colloidal model system with an interaction tunable from hard sphere to soft and dipolar*, Nature **421**, 513 (2003).

[485] M. Yoshio, T. Mukai, K. Kanie, M. Yoshizawa, H. Ohno and T. Kato, *Layered ionic liquids: Anisotropic ion conduction in new self-organized liquid-crystalline materials*, Adv. Mater. **14**, 351 (2002).

[486] M. Yoshio, T. Mukai, H. Ohno and T. Kato, *One-dimensional ion transport in self-organized columnar ionic liquids*, J. Am. Chem. Soc. **126**, 994 (2004).

[487] G. Zarubin and M. Bier, *Static dielectric properties of dense ionic fluids*, J. Chem. Phys. **142**, 184502 (2015).

[488] D.H. Zaitsau, G.J. Kabo, A.A. Strechan, Y.U. Paulechka, A. Tschersich, S.P. Verevkin and A. Heintz, *Experimental vapor pressures of 1-alkyl-3-methylimidazolium bis(trifluoromethylsulfonyl) imides and a correlation scheme for estimation of vaporization enthalpies of ionic liquids*, J. Phys. Chem. A **110**, 7303 (2006).

[489] R. Zhang, P.K. Jha and M. Olvera de la Cruz, *Non-equilibrium ionic assemblies of oppositely charged nanoparticles*, Soft Matter **9**, 5042 (2013).

[490] J. Zwanikken and R. van Roij, *Charged colloidal particles and small mobile ions near the oil-water interface: Destruction of colloidal double layer and ionic charge separation*, Phys. Rev. Lett. **99**, 178301 (2007).

[491] J. Zwanikken, J. de Graaf, M. Bier and R. van Roij, *Stability of additive-free water-in-oil emulsions*, J. Phys.: Condens. Matter **20**, 494238 (2008). DOI:10.1088/0953-8984/20/49/494238

[492] R. Zwanzig, *First-order phase transitions in a gas of long thin rods*, J. Chem. Phys. **39**, 1714 (1963).

# Related publications by the author

This thesis is related to the following publications by the author:


[24] H. Bartsch, O. Dannenmann and M. Bier, *Thermal and structural properties of ionic fluids*, Phys. Rev. E **91**, 042146 (2015).

[35] M. Bier, L. Harnau and S. Dietrich, *Free isotropic-nematic interfaces in fluids of charged platelike colloids*, J. Chem. Phys. **123**, 114906 (2005).

[36] M. Bier, L. Harnau and S. Dietrich, *Surface properties of fluids of charged platelike colloids*, J. Chem. Phys. **125**, 184704 (2006).

[37] M. Bier, J. Zwanikken and R. van Roij, *Liquid-liquid interfacial tension of electrolyte solutions*, Phys. Rev. Lett. **101**, 046104 (2008).

[39] M. Bier, J. de Graaf, J. Zwanikken and R. van Roij, *Curvature dependence of the electrolytic liquid-liquid interfacial tension*, J. Chem. Phys. **130**, 024703 (2009).

[40] M. Bier and S. Dietrich, *Vapour pressure of ionic liquids*, Mol. Phys. **108**, 211 (2010) [Corrigendum: Mol. Phys. **108**, 1413 (2010)].

[41] M. Bier, R. van Roij and M. Dijkstra, *Phase diagrams of binary mixtures of oppositely charged colloids*, J. Chem. Phys. **133**, 124501 (2010).

[42] M. Bier, A. Gambassi, M. Oettel and S. Dietrich, *Electrostatic interactions in critical solvents*, EPL **95**, 60001 (2011).

[43] M. Bier, A. Gambassi and S. Dietrich, *Local theory for ions in binary liquid mixtures*, J. Chem. Phys. **137**, 034504 (2012).

[44] M. Bier and L. Harnau, *The Structure of Fluids with Impurities*, Z. Phys. Chem. **226**, 807 (2012).

[45] M. Bier and I. Ibagon, *Density functional theory of electrowetting*, Phys. Rev. E **89**, 042409 (2014).

[96] J. de Graaf, J. Zwanikken, M. Bier, A. Baarsma, Y. Oloumi, M. Spelt and R. van Roij, *Spontaneous Charging and Crystallization of Water Droplets in Oil*, J. Chem. Phys. **129**, 194701 (2008).

[203] I. Ibagon, M. Bier and S. Dietrich, *Wetting in electrolyte solutions*, J. Chem. Phys. **138**, 214703 (2013).

[204] I. Ibagon, M. Bier and S. Dietrich, *Order of wetting transitions in electrolyte solutions*, J. Chem. Phys. **140**, 174713 (2014).

[236] S. Kondrat, M. Bier and L. Harnau, *Phase behavior of ionic liquid crystals*, J. Chem. Phys. **132**, 184901 (2010).

[283] A. Majee, M. Bier and S. Dietrich, *Electrostatic interaction between colloidal particles trapped at an electrolyte interface*, J. Chem. Phys. **140**, 164906 (2014).

[487] G. Zarubin and M. Bier, *Static dielectric properties of dense ionic fluids*, J. Chem. Phys. **142**, 184502 (2015).

[491] J. Zwanikken, J. de Graaf, M. Bier and R. van Roij, *Stability of additive-free water-in-oil emulsions*, J. Phys.: Condens. Matter **20**, 494238 (2008). DOI:10.1088/0953-8984/20/49/494238

# Acknowledgements

A thesis such as the present one primarily serves the purpose to summarise the author's research activity and to put it into a larger context. At the same time it documents the completion of a research programme, which, in the present case, has been carried out at the Max Planck Institute for Metals Research / Intelligent Systems in the department of Prof. S. Dietrich. I owe him a great dept of gratitude for the many years of support, inspiration, trust and generosity.
I wish to thank all former and present colleagues at the Dietrich department for the nice and professional atmosphere. Particularly I want to thank Hendrik Bartsch, Oliver Dannenmann, Dr. Ingrid Ibagon, PD Dr. Ludger Harnau, Dr. Svyatoslav Kondrat, Dr. Arghya Majee, Andreas Reindl and Grigory Zarubin for their effort put into the research projects together with me on ionic complex fluids. Moreover, I am grateful to Anke Geigle, Simone Blümlein and the computer service group for their indispensable assistence.
Some precursor work on electrolyte solutions has been performed during my postdoc period at Utrecht University (Netherlands). I want to thank my collaborators there, Dr. Joost de Graaf, Arnold Jansen, Prof. René van Roij and Prof. Jos Zwanikken.
During a visit of the Ian Wark Research Institute of the University of South Australia in Adelaide, I enjoyed the hospitality of Dr. Mihail N. Popescu and Prof. John Ralston. Moreover, I acknowledge insightful discussions with Dr. Vera N. Lockett and Prof. Rossen Sedev on experimental aspects of RTILs at interfaces.
For their hospitality during a research stay at the Brookhaven National Laboratory, Upton (USA), in the framework of the Marie Curie International Research Staff Exchange Scheme grant "Complex Liquids At Structured Surfaces", I wish to thank Dr. Antonio Checco and Dr. Benjamin M. Ocko.
Collaboration with JP Dr. Markus Mezger from the Max Planck Institute for Polymer Research in Mainz on microheterogeneities in ionic complex fluids is acknowledged. Moreover, I thank Dr. Koichiro Sadakane from Doshisha University, Kyoto (Japan), for discussions on his experimental work on the same topic.
I am indebted to Prof. Robert Evans from the University of Bristol (UK) for countless extended discussions, short conversations and quick chats on various topics related to the theory of fluids.
I am grateful to Prof. Andrea Gambassi from SISSA, Trieste (Italy), and Prof. Martin Oettel from the University of Tübingen for various discussions.
Finally I want to express my gratitude to the mentors group as well as to the referees of the present thesis for their assessment.

Markus Bier
Stuttgart, Januar 2016